Universitat Autònoma de Barcelona

Development of resolution-enhanced NMR techniques for improved small-molecules structural analysis

Núria Marcó García

Universitat Autònoma de Barcelona

Development of resolution-enhanced NMR techniques for improved small-molecules structural analysis

Núria Marcó García

Doctoral thesis

PhD. in Chemistry

Director: Dr. Teodor Parella Coll

Tutor: Dr. Albert Virgili Moya

Chemistry Department

Faculty of Science

2018

Universitat Autònoma de Barcelona

Memòria presentada per aspirar al Grau de Doctor per Núria Marcó García

Vist i plau,

Dr. Teodor Parella Coll Dr. Albert Virgili Moya Núria Marcó García

Bellaterra, 7 de maig de 2018

TABLE OF CONTENTS

ACKNOWLEDGEMENTS

I would like to thank the financial support for this research provided by:

♦ Ministerio de Economía, Industria y Competitividad (MINECO) for providing me with the scholarship BES-2013-066034 to do this PhD, and also the EEBB-I-17-11908 grant that allows me a two-month stay in Carnegie Mellon University (Pittsburgh).

♦ The research projects CTQ2012-32436 and CTQ2015-64436-P, "New Methodologies in Nuclear Magnetic Resonance (Parts IV and V)" from the MINECO. IP: Dr. Teodor Parella Coll.

♦ Servei de Ressonància Magnètica Nuclear (SeRMN) for offering me optimum working conditions and the use of all its equipment and facilities.

♦ Universitat Autònoma de Barcelona (UAB), especially to the Chemistry Department, for all the help related to the doctoral program.

♦ Grupo Especializado de Resonancia Magnética Nuclear (GERMN), belonging to the RSEQ, for the travel grants received to assist to Small Molecule NMR Conference (SMASH)

Esta tesis la firmo yo, pero he de reconocer que lleva tantos hombros arrimados que no sé si me cabrán todos los gracias en una página.

Mi primer enorme GRACIAS es para ti, Alex, por estar tanto a mi lado que casi deberías contar como compañero de trabajo. Por compartir los buenos días, y nunca fallar en los malos. Porque no negaré, que sin ti mis tuppers hubieran sido mucho más malos y porque los lunes son menos duros si los domingos los pasas bruncheando en la mejor compañía.

Sin lugar a dudas no habría llegado hasta aquí de no ser por mi fantástica familia. Mama, mil gracias por todos los esfuerzos, las broncas y la paciencia. Por las verduras, los panes y los miles de chocolates. Somos un poco más gordos por ti, pero también un poco más felices. Papa, gràcies per ensenyar-me que les dones també podem penjar quadres, canviar bombetes i estudiar ciències. Per inculcar-me el teu amor a la química i seguir sempre ensenyant-me tant. I a la meva sestra Silvia, ets la nostra bateria. Gràcies per ajudar-me a desdramatitzar-ho tot, per totes les cançons que han animat la meva tesis i per saber que mai em faltarà una amiga. Yaya, gracias por todo tu cariño y por escucharme siempre; tus ganas de aprender, incluso sobre esta tesis, son inspiradoras.

Blanca, em falten gràcies, per cada audio matiner que em fa començar el dia amb bon humor, per cada teràpia, cada copa de vi, mojito i café, per apuntar-te a totes les meves aventures i per seguir estant sempre tan aprop com si fossim veïnes, ojalà algún dia ho siguem.

A mis químicos, Marta, Mangi, Dani Mo y Javi, y en especial a Dani Q por siempre ver la parte buena de todo el mundo y apuntarse a mis frikadas. Ana, se merece un punto aparte, gracias por dar siempre tanto, por escucharme y por los millones de tonterías que siempre me hacen reír, no cambies nunca ret.

Gràcies als meus companys de SeRMN. A Teo, moltes gràcies per donar-me la direcció, per tota la teva paciència, i per fer sempre el que és millor per nosaltres. Miquel, gràcies per estar-hi sempre per tot, si alguna cosa falla no passa res, sempre està el Miquel, i si la burocràcia es torna pesada ens quedarà algún dels teus mails per treure'ns un somriure. Especial mención a mi despacho; André, son lo más gordos los que dejan mayor espacio cuando se van, gracias por ser un gran amigo y pasar por esto codo con codo, esta tesis es muy tuya; Kumar, gracias por ser la alegría del despacho. I com no a l'Albert Virgili, al Pau, la Míriam, la Silvia i l'Eva, gràcies per estendre'm una mà quan ho he necessitat.

No puedo terminar sin agradecer a Roberto por todo su cariño durante mi estancia en CMU. Gracias por la oportunidad, y por todo lo que me enseñaste, tu motivación y amor por este trabajo son contagiosos. Me diste el chute de energía que necesitaba para terminar esta tesis. And of course to the Schulz family for hosting me during the stay and make me feel at home, especially to Karl for all the good moments, for being not just a coworker or a roommate, but a friend, for helping me with the english and reminding me how important is to a scientist to always remain curious. Without you this stay wouldn't have been the same.

Probablemente me haya dejado algún hombro arrimado, a los que falten, muchas gracias.

Nos vemos en la siguiente etapa.

ACRONYMS

BIRD	**BI**linear **R**otation **D**ecoupling
CPMG	**C**arr-**P**urcell-**M**aiboom-**G**ill
CLIP	**CL**ean **I**n-**P**hase
CPD	**C**omposite **P**ulse **D**ecoupling
COSA	**C**omputer-**O**ptimized **S**pectral **A**liasing
COSY	**CO**rrelation **S**pectroscop**Y**
DQC	**D**ouble **Q**uantum **C**oherence
EA	**E**cho/**A**nti-echo
E.COSY	**E**xclusive **CO**rrelation **S**pectroscop**Y**
EFG	**E**lectric **F**ield **G**radient
FT	**F**ourier **T**ransformation
FID	**F**ree **I**nduction **D**ecay
HETLOC	**HET**ero nuclear **LO**ng-range **C**oupling
HECADE	**HE**teronuclear **C**ouplings from **A**SSCI-**D**omain experiments with **E**.COSY-type cross peaks
HMBC	**H**eteronuclear **M**ultiple **B**ond **C**orrelation
HMQC	**H**eteronuclear **M**ultiple **Q**uantum **C**orrelation
HSQC	**H**eteronuclear **S**ingle **Q**uantum **C**orrelation,
HSQMBC	**H**eteronuclear **S**ingle **Q**uantum **M**ultiple **B**ond **C**orrelation
HOBS	**HO**modecoupled **B**and-**S**elective
HOBB	**HO**modecoupled **B**road**B**and
IPAP	**I**n-**P**hase **A**nti-**P**hase
INEPT	**I**nsensitive **N**uclei **E**nhanced by **P**olarization **T**ransfer
LC	**L**iquid **C**rystal
ME	**M**ultiplicity **E**dited
MDD	**M**odel of multi-**D**imensional **D**ecomposition
NUS	**N**on-**U**niform **S**ampling
NMR	**N**uclear **M**agnetic **R**esonance
NOE	**N**uclear **O**verhauser **E**ffect
PDMS	**P**oly-**D**i**M**ethyl**S**iyloxane
PMMA	**P**oly-**M**ethyl **M**ethacryl**A**te

PS	**P**oly-**S**tyrene
PBLG	**P**oly-γ-**B**enzyl-**L**-**G**lutamate
PELG	**P**oly-γ-**E**thyl-**L**-**G**lutamate
PCBLL	**P**oly-ε-**C**arbo**B**enzyloxy-**L**-**L**ysin
PEP	**P**reservation of **E**quivalent **P**athways
PFG	**P**ulsed **F**ield **G**radients
PIP	**P**ure **I**n-**P**hase
PSYCHE	**P**ure **S**hift **Y**ielded by **CH**irp **E**xcitation
RCSA	**R**esidual **C**hemical **S**hift **A**nisotropy
RDC	**R**esidual **D**ipolar **C**oupling
RQC	**R**esidual **Q**uadrupolar **C**oupling
SAG	**S**trained **A**ligning **G**els
TMS	**T**etra**M**ethyl**S**ilane
TOCSY	**TO**tal **C**orrelation **S**pectroscop**Y**
VASS	**V**ariable-**A**ngle **S**ample **S**pinning
ZS	**Z**angger **S**terk
ZQC	**Z**ero **Q**uantum **C**oherence
ZQF	**Z**ero-**Q**uantum **F**ilter

1. INTRODUCTION

Nuclear Magnetic Resonance (NMR) spectroscopy has proven to be an essential analytical tool to obtain atomic-resolution information about the structure, the dynamics and/or the chemical composition for samples of different origin and nature. Its universality relies on the fact that it can provide both qualitative and quantitative information. This technique started its development in 1938 with the first studies of Rabi *et al.*[1]. That opened the doors to its successful application to liquid and solid samples, for which Bloch and Purcell won the Nobel Prize in 1952. One of the most important advances in NMR was the implementation of the Fourier transformation (FT) in the 1960s. This approach transforms the time-domain dependent signal into a frequency-domain representation, speeding up data acquisition by signal averaging after radio-frequency pulsed methods. The design of multiple pulse sequences facilitated the development of two-dimensional (2D) NMR from the 70s and higher-multidimensional (3D, 4D…) NMR in the 90s. These experiments made possible to obtain unequivocal structural and dynamic molecular information and expanded the potential use of NMR to more complex systems (mixture analysis, biomolecular NMR, intermolecular interactions…) in a vertiginous way.

1.1. 2D NMR spectroscopy

2D NMR experiments are designed to correlate two different frequencies which depend on the type of experiment done. A general 2D NMR pulse scheme consists of several sequential steps (Figure 1). It starts with an initial *preparation period* that converts the original longitudinal magnetization (I_z) into transversal magnetization (I_x or I_y). This excitation can be achieved by a simple 90º pulse or from more complicated NMR building blocks combining pulses and delays. Then, this transverse magnetization can be monitored during the *evolution t_1 period* which consists of a variable incremented time. Magnetization is transferred between different spins during the subsequent *mixing period* where it becomes an observable signal. The nature of this mixing time defines the NMR properties (coupling constant, chemical exchange, relaxation…) to be transferred and the experiment to be performed. The signal is finally recorded during the *detection t_2 period*.

The NMR signal is recorded as a 2D matrix data where the Free Induction Decay (FID) obtained for each indirect, non-detected t_1 period is digitized as a function of the

directly detected t_2 period. The first row corresponds to the t_2 data acquired for $t_1 = 0$; the second is for $t_1 = \Delta$; the third equals to $t_1 = 2*\Delta$; and so on… where the increment Δ is 1/(2*SW), and SW is the spectral width monitored during t_1. The time-domain (t_1,t_2) data is converted to a frequency-domain (ν_1,ν_2) spectrum by applying FT sequentially in each independent dimension. The result is a 2D NMR spectrum showing cross-peaks that correlates the frequencies along two orthogonal axes (indirect F1 and direct F2 dimensions).

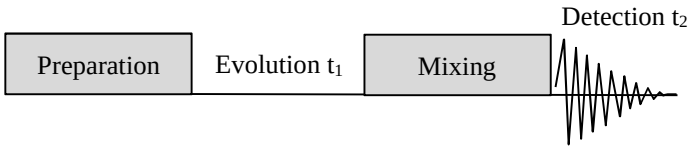

Figure 1: General pulse scheme of a 2D NMR experiment. Four different steps are sequentially executed: preparation, evolution (t_1), mixing and detection (t_2). The detected signal is encoded as a function of two different time periods that after Fourier transformation will be observed as a 2D cross-peak at the frequencies (ν_1,ν_2).

2D NMR experiments provide a wide variety of spectral and chemical information depending on the mixing periods used. One example is the homonuclear correlation experiment, which correlates frequencies of the same nucleus, like ^{1}H vs ^{1}H. The essential Correlation Spectroscopy (COSY) experiment uses a simple ^{1}H pulse as mixing to correlate signals which are through-bond connected with a scalar J_{HH} coupling.[2] As an extension of this experiment, a complete ^{1}H *J*-coupled subspin systems can be correlated with the Total Correlation Spectroscopy (TOCSY) experiment which uses somewhat complicated MLEV or DIPSI pulse trains as a mixing process.[3] In a complementary way, Nuclear Overhauser Enhancement spectroscopy (NOESY) affords through-space ^{1}H-^{1}H connectivities by using a 90º-delay-90º element as a mixing.

The Heteronuclear Multiple-Quantum Correlation (HMQC) experiment[4] and the Heteronuclear Single-Quantum Correlation (HSQC) experiment[5] are the most famous heteronuclear correlations NMR pulse sequences. These experiments correlate the frequencies of two different nuclei, for instance ^{1}H and X, where X is typically an NMR active heteronuclei like ^{13}C ^{15}N, or ^{31}P, among others. Despite the robustness to experimental imperfections of HMQC, HSQC provides better resolution, performance and more flexibility and simplicity for pulse sequence developments.

1.1.1. The 2D HSQC experiment

The HSQC experiment provides a 2D spectrum where each cross-peak correlates a ^{1}H resonance with its directly-attached heteronucleus (commonly ^{13}C or ^{15}N). The basic HSQC pulse sequence contains four defined steps (Figure 2).

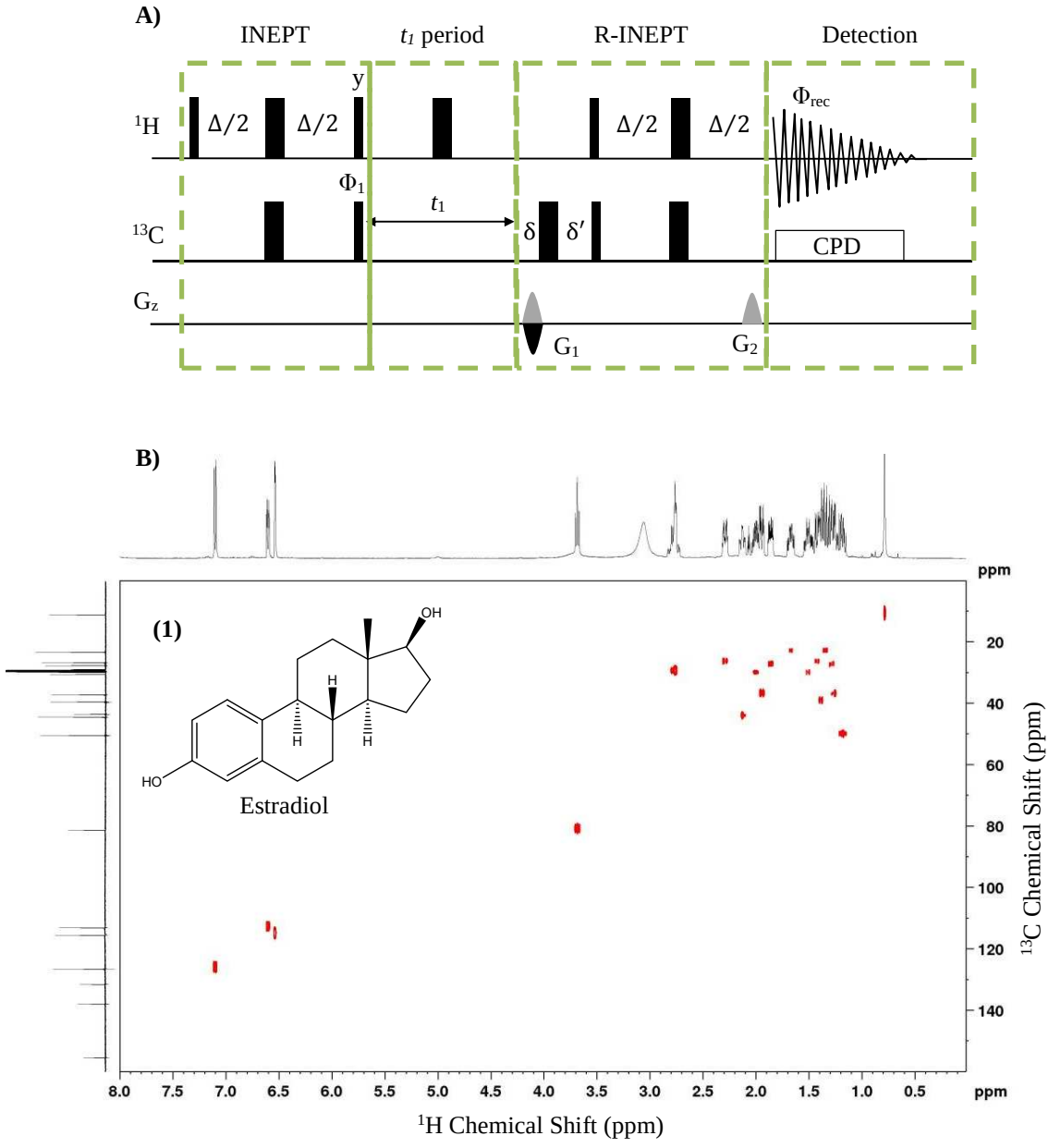

Figure 2: A) Basic pulse sequence scheme of the 2D HSQC experiment. Thin and thick vertical rectangles represent 90º and 180º hard pulses, respectively. The delay Δ should be set to $1/(2^{1}J_{CH})$ and δ represents the duration of the PFG and its recovery delay. The gradient pair G1:G2 ratio is 4:1 while applying the echo-antiecho approach. A basic two-step phase cycling is executed with ϕ_1= x,-x and ϕ_{rec}= x,-x. B) 2D ^{1}H-^{13}C HSQC spectrum of the steroid Estradiol (1).

The initial *Insensitive Nuclei Enhanced by Polarization Transfer* (INEPT) step transfers ^{1}H magnetization to the heteronucleus.[6] For an isolated CH spin system, the product operator (PO) description is summarized as:

$$H_z \xrightarrow{INEPT} -2H_zC_ys$$

Eq. 1

where $c = \cos(\pi J_{CH}\Delta)$, $s = \sin(\pi J_{CH}\Delta)$ and $\Delta/2$ is the interpulse delay.
In the optimum case that $\Delta = 1/(2 * {}^{1}J_{CH})$, Eq. 1 is simplified to $-2H_zC_y$ that represents Anti-phase (AP) ^{13}C magnetization. During the subsequent *t_1 period*, ^{13}C chemical shift evolves while $^{1}J_{CH}$ is refocused due to the central 180º ^{1}H pulse:

$$-2H_zC_ys \xrightarrow{t_1} -2H_zC_y\,sc' + 2H_zC_x\,ss'$$

Eq. 2

where $c' = \cos(\Omega_c t_1)$ and $s' = \sin(\Omega_c t_1)$.

Then, the ^{13}C AP magnetization is transferred back to detectable In-Phase (IP) ^{1}H magnetization through a *retro-INEPT (R-INEPT)* block. After the refocusing period, the detectable ^{1}H signal is a mixture of IP and AP ^{1}H magnetization components:

$$-2H_zC_y\,sc' + 2H_zC_x\,ss' \xrightarrow{R-INEPT} -H_x\,s^2c' + 2H_yC_z\,scc'$$

Eq. 3

During the last *^{1}H detection period*, ^{13}C broadband heteronuclear composite pulse decoupling (CPD) is applied to remove the $^{1}J_{CH}$ splitting. Under these conditions, the second AP term in Eq. 3 becomes not observable.

The use of pulsed field gradients (PFG) for coherence selection represents a significant improvement in the elimination of unwanted coherence pathways and the obtention of high-quality spectra without the interference of ^{1}H-^{12}C magnetization.[7] In the example of Figure 2A, a defocusing gradient G1 is applied during ^{13}C single-quantum coherence evolution whereas a second refocusing gradient G2 is placed just before ^{1}H acquisition. The echo/anti-echo (EA) procedure (separate acquisition of echo and anti-echo data followed by combined data processing) affords phase-sensitive data, optimizing pure absorption lineshapes, sensitivity and signal resolution. A G1:G2 = ± 4:1 ratio fulfils the gradient refocusing condition $p_{C*}\gamma_{c*}G_1 - \gamma_{H*}G_2 = 0$, where p_C is the active coherence order during the gradient G1.

The 2D HSQC pulse sequence has been extensively modified to improve its performance. For instance, the incorporation of a ^{13}C spin-echo period when ^{13}C magnetization is in the transverse plane (step 2) affords a widely used multiplicity-edited HSQC (ME-HSQC) experiment where CH/CH_3 signals present a relative opposite phase concerning CH_2 groups.[8] Other developments have been focused on achieving fast data acquisition. The Acceleration by Sharing Adjacent Polarization (ASAP) HSQC experiment uses a shorter PFG-flanked period of 40 ms as a relaxation delay and a 90º (^1H) pulse with -x phase at the beginning of the mixing period, to use a short repetition rate between experiments.[9] On the other hand, a more sophisticated strategy based on a single-scan Ultrafast (UF) HSQC uses spatially encoding elements during the ^{13}C evolution period and an echo-planar imaging acquisition mode to obtain HSQC data in, theoretically, less than one second.[10–12] Other modifications of the sequence have been focused on the quantitative determination cross-peak volumes (quantitative HSQC), determination of proton-carbon coupling constants or to study longer-range heteronuclear correlations.[13–15]

1.1.1.1. $^1J_{XH}$ Measurements from F2-coupled HSQC

Any HSQC pulse scheme can be used to determine $^1J_{CH}$ quantitatively. In the most straightforward approach, this measurement can be achieved by omitting the heteronuclear decoupling during ^1H acquisition in Figure 2A. In this case, each cross-peak shows a large doublet along the F2 dimension due to $^1J_{CH}$. However, the AP term $2H_yC_z\ scc'$ of Eq. 3 is active when removing CPD, causing some signal distortion. Also, the effect of J_{HH} must be evaluated. The analysis of a CH_1-H_2 spin system (defined with the corresponding $^1J_{CH}$ and $^3J_{H1H2}$ coupling constants) shows that, just before the acquisition, the ^1H magnetization is determined by the following 4 terms;

$$H_{1x}\,c^{*2}s^2\ \textbf{\textit{(I)}} - 2H_{1y}C_z\,csc^{*2}\ \textbf{\textit{(II)}} + 2H_{1y}H_{2z}\,c^2c^*s^*\ \textbf{\textit{(III)}} + 4H_{1x}H_{2z}\,C_z\,csc^*s^*\ \textbf{\textit{(IV)}}$$

Eq. 4

where $c = \cos(\pi J_{CH}\Delta)$, $s = \sin(\pi J_{CH}\Delta)$, $c' = \cos(\Omega_c t_1)$, $s' = \sin(\Omega_c t_1)$, $c^* = \cos(\pi J_{HH}\Delta)$ and $s^* = \sin(\pi J_{HH}\Delta)$.

In practice, these signals can present strong phase distortions due to the J_{CH} and J_{HH} modulations. These distortions represent a severe drawback to obtain reliable

measurements. The term I represent IP ^{1}H magnetization whereas Terms II, III and IV correspond to AP ^{1}H magnetization, being the term III is a mixture of homonuclear Zero- (ZQC) and Double-Quantum coherences (DQC). These AP terms cause distortions and, therefore, inaccuracy in the determination of J_{CH} and J_{HH} and/or the quantification of cross-peak volume via peak integration. Some improved HSQC versions like the Clean In-Phase (CLIP)-HSQC,[16] the Perfect-HSQC[17] or the Pure in-Phase (PIP)-HSQC[18] experiments have been proposed to obtain the desired IP component without unwanted distortions.

1.1.1.1.1. CLIP-HSQC

The phase distortions from terms II and IV in eq. 1 are produced by the mismatching between $^{1}J_{CH}$ and the experimental interpulse delay optimization (Δ). Some of these AP contributions can be efficiently removed by the CLIP-HSQC experiment (Figure 3), where a purging 90º ^{13}C pulse is applied before the acquisition to convert AP contributions from terms II and IV to undetectable multiple-quantum terms.[16]

$$Eq.4 \xrightarrow{CLIP-HSQC} H_{1x}s^2c^{*2}(\boldsymbol{I}) + 2H_{1y}C_Yc^{*2}sc(\boldsymbol{II}) + 2H_{1y}H_{2z}c^{*}ss^{*2}(\boldsymbol{III}) - 4H_{1x}H_{2z}C_ycsc^{*}s^{*}(\boldsymbol{IV})$$

Eq. 5

The CLIP-HSQC sequence is widely used for the determination of scalar $^{1}J_{CH}$ and residual dipolar $^{1}D_{CH}$ couplings. Despite its utility minimizing phase distortions and its straightforward implementation, it still provides some interferences that can complicate the accurate measurement of $^{1}J_{CH}$/$^{1}D_{CH}$ due to the evolution of J_{HH} (Term III).

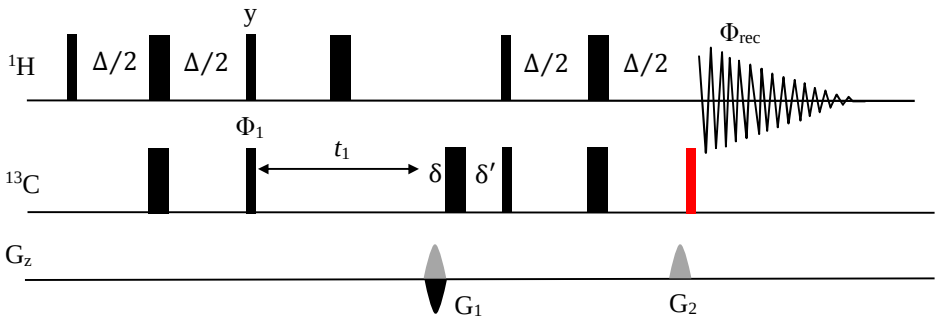

Figure 3: General pulse scheme of the F2-heterocoupled CLIP-HSQC pulse sequence. The red rectangle defines the key 90º (^{13}C) CLIP pulse.

1.1.1.1.2. Perfect-HSQC

During the INEPT and retro-INEPT blocks, the evolution of J_{HH} couplings takes place as observed with term III in Eq. 4, causing additional antiphase distortions that can preclude a reliable *J* measurement.

For an H_1-H_2 spin system, the conventional spin-echo experiment (Δ – 180º - Δ) (Figure 4A) produces AP terms that can cause signal phase distortion (Eq. 6)

$$-H_{1y} - H_{2y} \xrightarrow{\Delta-180-\Delta} -H_{1y}c^* + 2H_{1x}H_{2z}s^* \\ -H_{2y}c^* + 2H_{2x}H_{1z}s^*$$

Eq. 6

where c*= cos($\pi J_{HH}\Delta$) and s* = sin($\pi J_{HH}\Delta$).

The concept of perfect-echo was reported to avoid this J_{HH} evolution into a spin-echo period.[19] The perfect-echo consists of a double spin-echo scheme separated with a 90^o_y (^{1}H) (Figure 4B) with the interpulse delay set to $\Delta < 1/J_{HH}$ to refocus AP terms (Eq. 7).

$$Eq.6 \xrightarrow{90(y)} -H_{1y}c^* - 2H_{1z}H_{2x}s^* - H_{2y}c^* + 2H_{2z}H_{1x}s^* \xrightarrow{\Delta-180-\Delta} -H_{1y}c^{*2} \\ + 2H_{1x}H_{2z}c^*s^* - 2H_{1z}H_{2x}c^*s^* - H_{2y}s^{*2} - H_{2y}c^{*2} + 2H_{2x}H_{1z}c^*s^* \\ - 2H_{2z}H_{1x}\,c^*s^* - H_{1y}s^{*2} = -H_{1y} - H_{2y}$$

Eq. 7

This methodology was implemented in the typical INEPT block, converting it into a perfect-INEPT block involving a double spin-echo period (Figure 4C and D).[20] The signal amplitude in the conventional INEPT block is modulated by the effect of both J_{CH} and J_{HH}. However, the signal in perfect-INEPT is only modulated by the effect of J_{CH}. In this block, the first homonuclear spin-echo makes evolve J_{HH}. Then, when the second INEPT is applied, J_{HH} is refocused while J_{CH} evolves. The product operator at the end of the block is defined by two terms free from homonuclear *J*-modulations:

$$2H_{1z}C_y\,s^* + 2H_{2z}C_y\,s^*$$

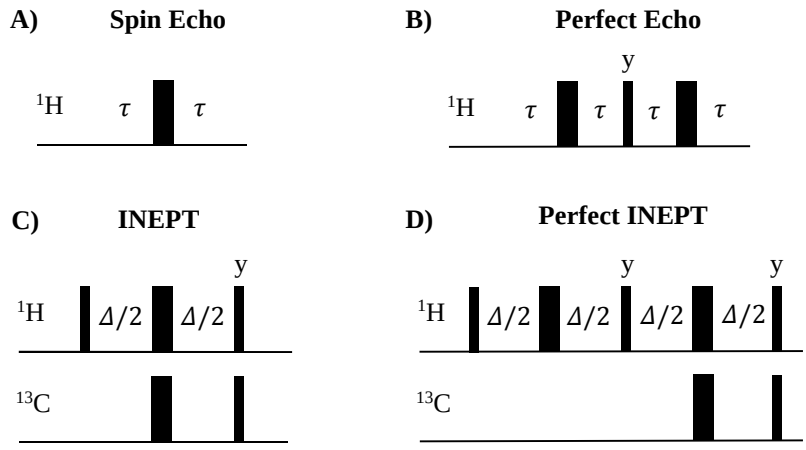

Figure 4: Schematic representation of NMR building blocks: A) Spin-Echo, B) Perfect Echo, C) INEPT and D) Perfect INEPT.

Perfect-echo INEPT can be implemented into the HSQC scheme by substituting the corresponding INEPT and R-INEPT periods. The perfect-HSQC sequence (Figure 5A) affords PIP signals without J_{HH} modulation, allowing a better quantification of peak volumes, improving integrations and phase corrections and also facilitating more accurate peak picking (Figure 6).

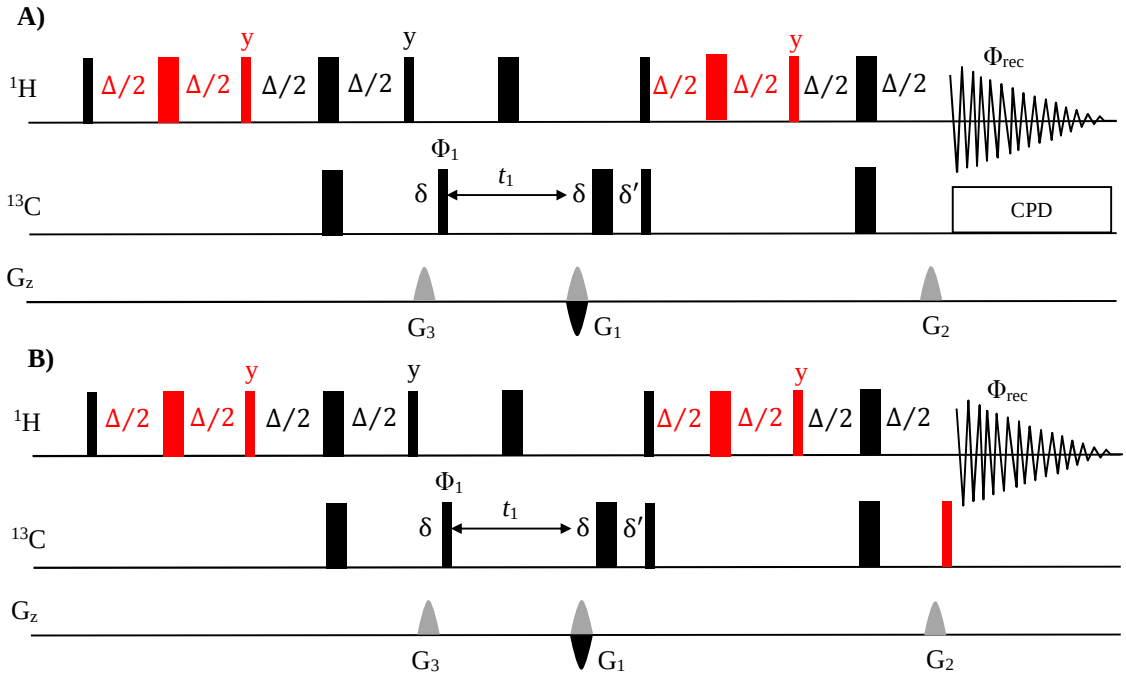

Figure 5: General pulse schemes of the (A) perfect-HSQC experiment and (B) F2-heterocoupled perfect CLIP-HSQC experiments. The red rectangles correspond to the new additional pulses in relation with the basic HSQC sequence of Figure 2A.

Perfect-HSQC can be easily adapted to determine $^{1}J_{XH}$ just by disabling CPD and adding the characteristic 90º ^{13}C pulse of the CLIP technique before the acquisition (Figure 5B). The resulting F2-coupled perfect CLIP-HSQC spectrum provides $^{1}J_{XH}$ without distortions of either J_{HH} or J_{CH}. Both experiments are robust, easy to implement and especially useful when the sample studied present large J_{HH} magnitudes. The use of long echoes and therefore the potential sensitivity loss by T_2 relaxation is minimized in the case of small molecules that have longer T_2 relaxation times.

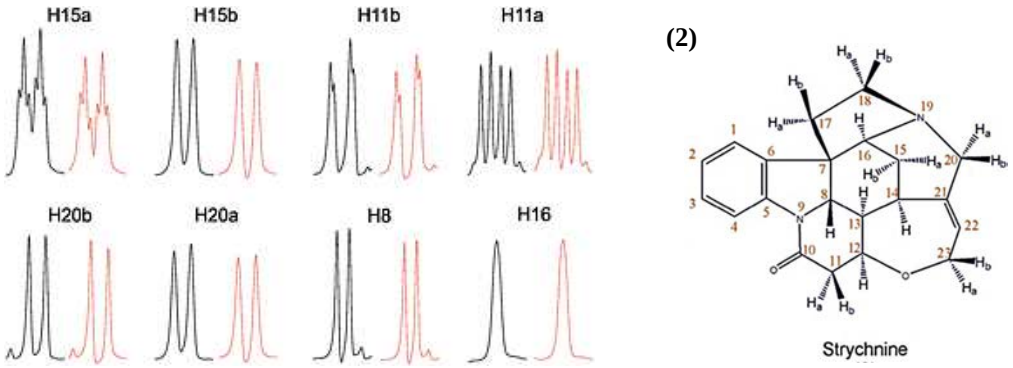

Figure 6: Comparison of some cross-peaks extracted from perfect-HSQC (black) and conventional HSQC (red) spectra of the alkaloid strychnine (2). Figure extracted from the reference[4]

1.1.1.1.3. PIP-HSQC

The PIP-HSQC experiment is another interesting approach for obtaining HSQC spectra without phase distortions.[18] This sequence adds a Zero-Quantum Filter (ZQF) to remove any AP contribution and a refocusing perfect-echo period just before the acquisition (Figure 7), providing PIP cross-peaks. That ZQF is a z-filter involving the simultaneous application of an adiabatic 180º ^{1}H pulse and a purging encoding gradient, showing a significant capacity in removing homo- and heteronuclear AP interferences.[16,21–25]

Just before the ZQF, the magnetization is formed by four components (Eq. 4). After the 90º ^{1}H pulse:

$$Eq.4 \rightarrow -H_{1z}s^2c^{*2}(\boldsymbol{I}) + 2H_{1y}C_zc^{*2}sc(\boldsymbol{II})$$
$$+2H_{1y}H_{2z}c^{*}ss^{*2}(\boldsymbol{III}) - 4H_{1z}H_{2x}C_zcsc^{*}s^{*}(\boldsymbol{IV})$$

Eq. 8

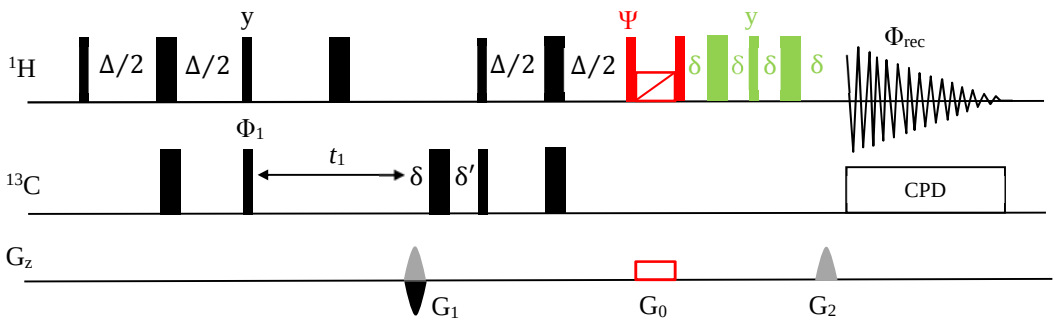

Figure 7: General pulse scheme of PIP-HSQC experiment. The red and green pulses and delays are the novelties in comparison with the basic HSQC scheme of Figure 2A. The ZQF is formed by a z-filter with an adiabatic 180º (^{1}H) pulse and a spatial-encoding gradient G0 (marked in red). The final perfect-echo element is marked in green.

In Eq 8, the terms II and IV correspond to transverse AP heteronuclear magnetization, and the term III represents a mixture of homonuclear ZQC and DQC. These three undesirable terms are efficiently removed with the use of the ZQF, remaining just the IP term I. This sequence is beneficial for the accurate extraction of $^1J_{XH}$ coupling constants, and its efficiency has been demonstrated with anisotropic samples to get residual dipolar couplings (RDCs). In case of signal overlap, the In-Phase/Anti-Phase (IPAP) technique affords the separation of each component in two spin-state selective spectra, the IP+AP and IP-AP components of the doublet, to simplify the measurement.[26–28]

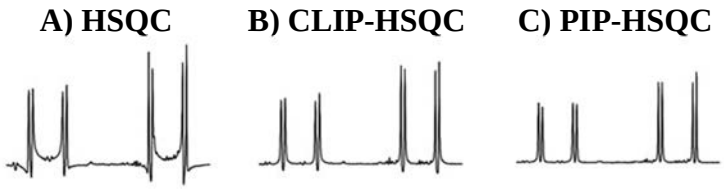

Figure 8: Comparison of the 1D traces corresponding to the methylene H20 protons extracted from the A) HSQC, B) CLIP-HSQC and C) PIP-HSQC spectra of (2). Figure extracted from the reference.[18]

1.1.1.2. $^1J_{XH}$ Measurements from F1-coupled HSQC

The extraction of $^1J_{CH}$ along the direct F2 dimension can entail the loss of accuracy in the measurement due to the complex multiplet patterns of ^{1}H signals. Even with the improvements explained in the section *1.1.1.1*, there are some situations where others factors can distort this measurement, like the existence of RDCs when working with

anisotropic samples, or the presence of strong coupling effects and broad linewidths. IT has been reported that $^{1}J_{CH}$ can also be determined from the F1 dimension of HSQC spectra. A comparison of several NMR methods for the measurement of $^{1}J_{CH}$ along the different F1 or F2 dimensions was reported.[29]

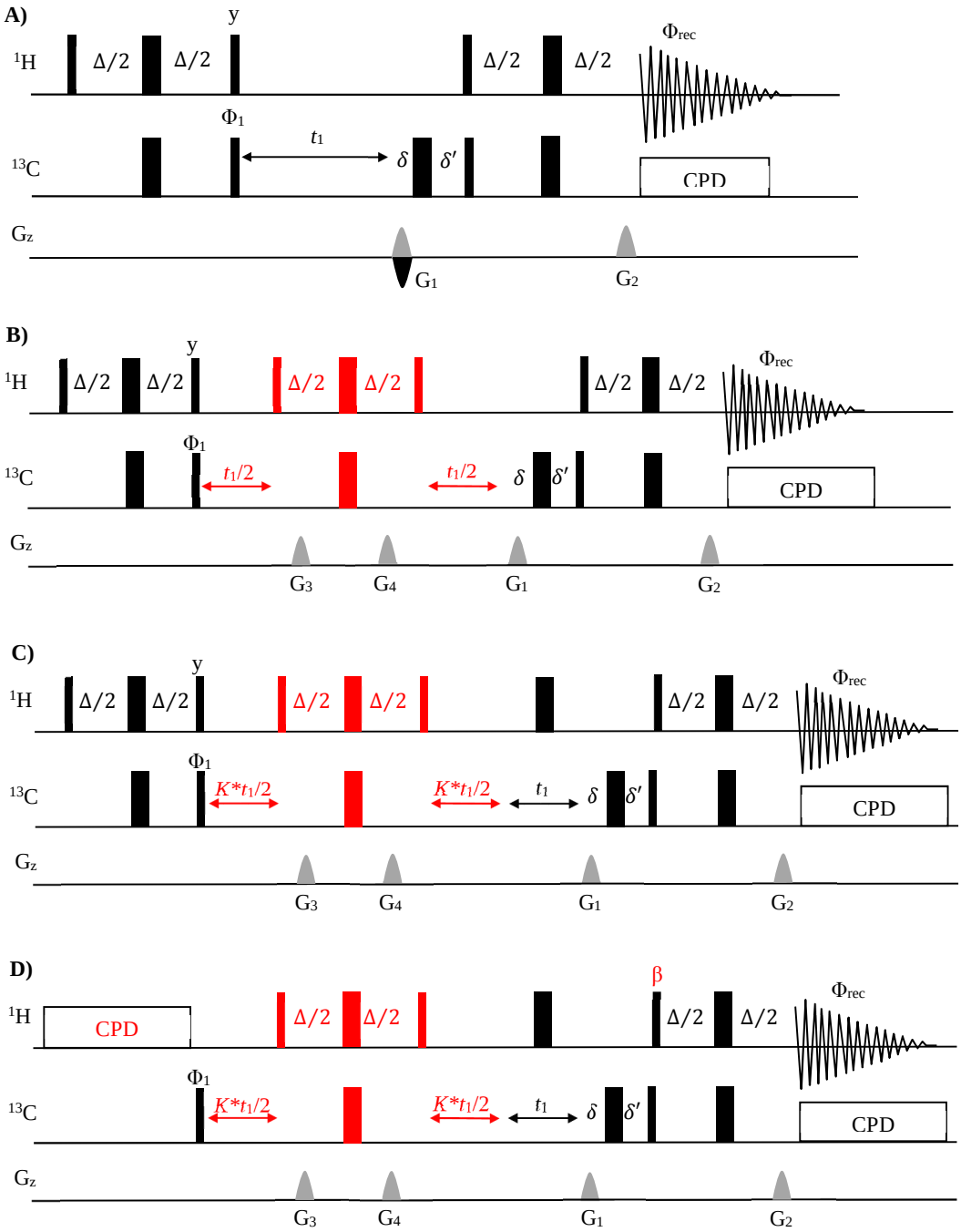

Figure 9: Several HSQC pulse schemes to measure $^{1}J_{CH}$ along the F1 dimension. A) F1-HSQC, B) F1-coupled HSQC incorporating a G-BIRD element, C) JSB-HSQC and D) F1-iINEPT (β=36º).

Taking the basic HSQC pulse sequence of Figure 2 as a starting point, the simplest way to get the heteronuclear coupling in F1 is just by removing the 180º ^{1}H pulse

situated in the center of the t_1 period. This simple F1-HSQC experiment (Figure 9A) provides a conventional heteronuclear correlation spectrum showing the splitting due to $^1J_{XH}$ in F1.[30] One drawback of this approach is the line broadening because of the simultaneous evolution of long-range heteronuclear couplings.

Following with this idea, the *J*-scaled bilinear rotation decoupling (BIRD) HSQC (*J*SB-HSQC) experiment[31] (Figure 9C) was developed, derived from the F1-coupled HSQC with G-BIRD (Figure 9B).[32] This experiment allows the accurate measurement of $^1J_{CH}$ by a *J*-scaling method to avoid the use of a large number of t_1 increments. This sequence uses a separate, *J*-scaled t_1-incrementable BIRD-element to allow the exclusive evolution of $^1J_{XH}$, whereas ^{13}C chemical shift is refocused. This experiment is very efficient for CH and CH_3 systems. However, it does not differentiate between $^1J_{CHa}$ and $^1J_{CHb}$ in prochiral CH_2 groups. $^1J_{CH}$ is related to the *s* character of this bond and the electronegativity effects of the substituents and its surrounding. Thus, the magnitudes of $^1J_{CH}$ in a CH_2 group can provide information about equatorial and axial ^{1}H positions and help in the assignment of their relative stereoselectivity. The application of Non-Uniform Sampling (NUS) in *J*SB-HSQC experiment was reported to allow high-resolution improvements without sacrificing experimental time as it is going to be explained in more detail in the section *1.1.3*. .[31]

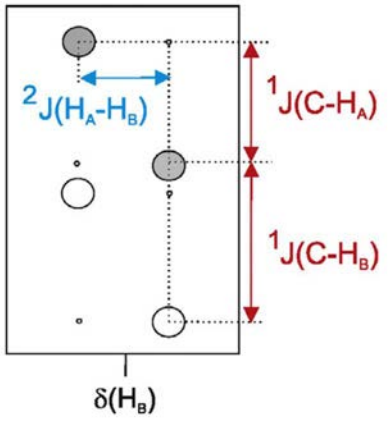

Figure 10: Characteristic E.COSY coupling pattern obtained for a prochiral H_A-C-H_B group in a F1-iINEPT spetrum. Figure adapted from reference.[72]

The F1-iINEPT experiment (Figure 9D) was proposed to solve the inaccuracy derived from having to divide by 2 the value of $^1J_{CH}$ in diastereotopic groups.[33] In this experiment, the initial INEPT is avoided and the sequence starts from the ^{13}C Boltzmann polarization. The flip angle of the first ^{1}H pulse of the R-INEPT can be set to 36º instead of the typical 90º. The corresponding four-component exclusive correlation spectroscopy (E.COSY) cross-peak allows the separated measurement of the magnitude of J_{CHa} from J_{CHb} as well as the magnitude and sign of $^2J_{Ha\text{-}Hb}$ (Figure 10).

Resolution improvements in the F1 dimension can be achieved by reducing the ^{13}C spectral width. This reduction of the spectral width is generally realized in 2D *J*-resolved experiments where each proton only display the scalar J_{HH} coupling information along F1, symmetric to the central F1=0 axis.[34] The *J*-resolved HSQC

experiment was developed based on this idea, avoiding the use of an extra delay for ^{13}C evolution and improving digital F1 resolution.[35] It is a very useful experiment to measure J_{CH} free from signal overlap and, combined with homodecoupling techniques, can provide substantial improvements in spectral quality, sensitivity, and both signal and digital resolution enhancements.

1.1.2. The HSQMBC Experiment

The Heteronuclear Single Quantum Multiple Bond Correlation (HSQMBC) experiment corresponds to a long-range optimized version of the HSQC, which affords heteronuclear correlations that are further away than a one-bond distance.[36] This experiment is beneficial in the structural determination since it allows the observation of the correlations between quaternary carbons and protons.

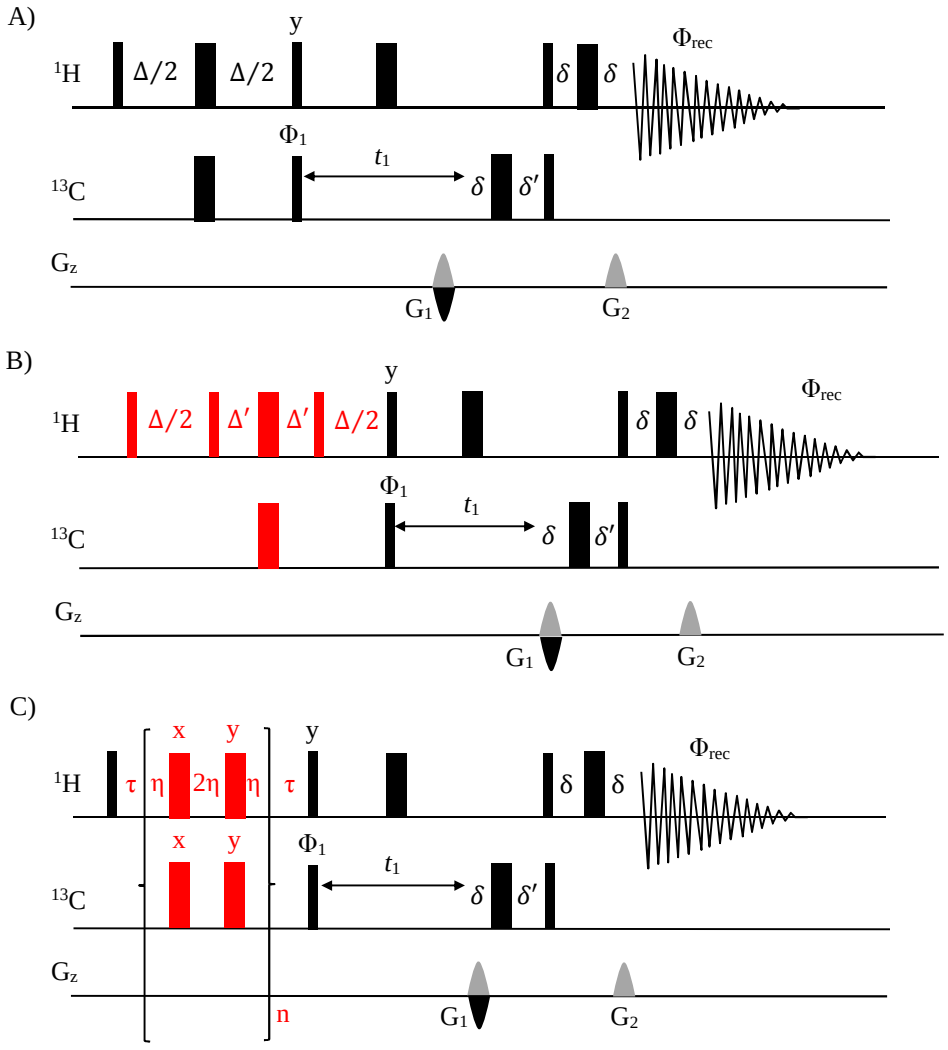

Figure 11: Pulse sequence schemes of several non-refocused HSQMBC sequences, A) standard HSQMBC, B) BIRD-HSQMBC, and C) CPMG-HSQMBC experiments.

The Δ delay in HSQMBC has to be optimized to a long-range heteronuclear coupling value, close to 5 to 8 Hz, that implies the lengthening of the sequence (Δ is about 50 o 70 ms). Regarding sensitivity, this can give losses by relaxation for samples with short T_2. The non-refocused HSQMBC scheme is commonly used avoiding the refocusing INEPT step to prevent further relaxation losses (Figure 11A).

A drawback of the HSQMBC is the simultaneous evolution of J_{HH} during Δ, which have similar sizes than $^{n}J_{CH}$. These additional modulations cause distortions in the phase and the intensity of cross-peak, as well as to facilitate partial or full signal cancellation. Some approaches have been developed to avoid these problems, for instance, implementing a BIRD block in the middle of the INEPT period to differentiate $^{n}J_{XH}$ vs $^{1}J_{XH}$ evolution (BIRD-HSQMBC) (Figure 11B). Another improvement was the incorporation of a Carr-Purcell-Maiboom-Gill (CPMG) composite π pulses block during the INEPT period (Figure 11C) to minimize J_{HH} modulations, by adjusting the delay between 90º pulses to a value shorten than $1/2 \cdot \sqrt{J^2 + \Delta\upsilon^2}$.[37] It approaches to $1/2 \cdot \Delta\upsilon_{max}$ in cases of weak coupling (small *J*), being $\Delta\upsilon_{max}$ the biggest difference between chemical shifts in coupled proton partners. Unfortunately, this option can cause probehead heating by fast pulsing due to the required short interpulse delays to remove completely J_{HH} for all spin systems. Both enhancements can be joint in a BIRD-CPMG-HSQMBC experiment to get a spectrum with the minimum amount of distortions, but still remaining some of the problems due to relaxation and sample heating.[38] The incorporation of the CLIP and PIP concepts, previously explained for the HSQC, into the HSQMBC affords the related CLIP-HSQMBC[39] and PIP-HSQMBC experiments,[18] which yield undistorted IP cross-peaks, making the measurement of small coupling constants more accurate and easy. It is also possible to apply the IPAP methodology to HSQMBC experiments (IPAP-HSQMBC) to overcome overlapped signals.[27]

1.1.2.1. Other long-range heteronuclear correlation experiments

HSQMBC is not the only option to trace out heteronuclear long-range correlations. Just as the HSQMBC is the long-range of the HSQC, the long-range version of HMQC, the Heteronuclear Multiple Bond Correlation (HMBC), is also routinely used (Figure 13A). HMBC provides NMR spectra with good sensitivity, but it shows important phase and intensities modulations arising from J_{HH} evolution. HMBC has been extensively

modified by incorporating, for instance, z-filters,[21,40] constant-time periods[41] or EA coherence selection.[40,42,43]

Another very interesting experiment is the long-range HSQMBC (LR-HSQMBC). [44–46] This experiment consists of a refocused HSQMBC scheme optimized for very small $^{n}J_{CH}$ values of 2-4 Hz. It affords good results in challenging structures, but it can be critical in molecules with short T_2 relaxation times because of the long INEPT periods.

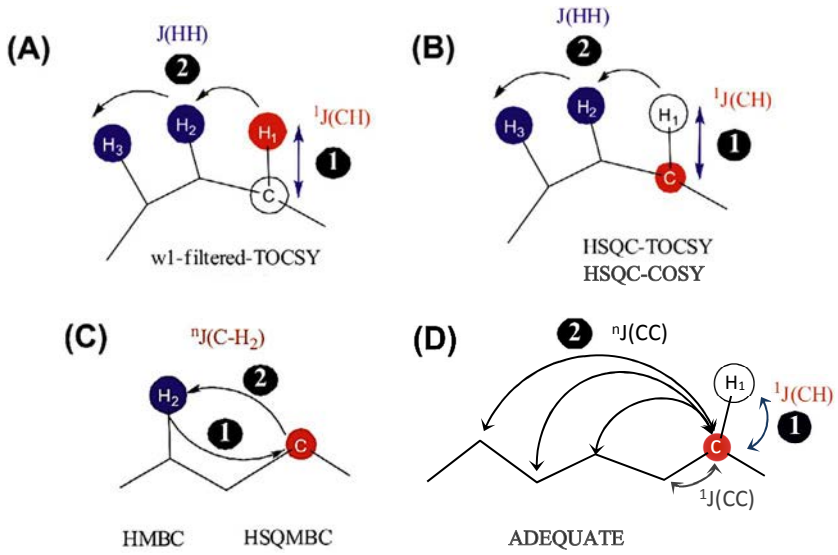

Figure 12: Spin coupling topologies and *J*-coupling transfer mechanisms involved in some long-range heteronuclear NMR experiments. White circles represent intermediate spins that are not observed, red/blue circles represent observed spins. Figure adapted from reference.[37]

Another family of long-range heteronuclear experiments use additional ^{1}H-^{1}H mixing blocks, like COSY and TOCSY (Figure 12B). The most straightforward approach is the HSQC-COSY (Figure 13B), where the long-range connectivity is traced out by to the ^{1}H-^{1}H COSY transfer. In the same way, 2D HSQC-TOCSY (Figure 13C) provides similar patterns, but ^{1}H-^{1}H transfer can arrive further away. [47] Both HSQC-COSY and HSQC-TOCSY sequences have been modified from the basic scheme of Bax *et al*. on several occasions to improve their spectral features. In the case of spectra with poorly resolved multiplets, IPAP methodology simplifies the measurement of $^{n}J_{CH}$.[25,41,48–50] On the other hand, PEP element increases the sensitivity for CH groups[49] whereas the addition of a ZQF provides cleaner spectra by removing AP contributions.[25] Nevertheless, any of this improvement can change the major drawback that this family of sequences experience; they do not work for non-protonated carbons.

On the other hand, the extended transfer mechanism through carbon-carbon correlations in the ADEQUATE experiment has been also explored (Figure 12D).[51] This experiment was adapted to long-range versions optimizing the evolution period for small long-range carbon-carbon coupling values in the initial transfer.[52] ADEQUATE experiments are particularly interesting for proton-deficient molecules since it can provide information between non-protonated carbons, but they suffer from very low sensitivity.

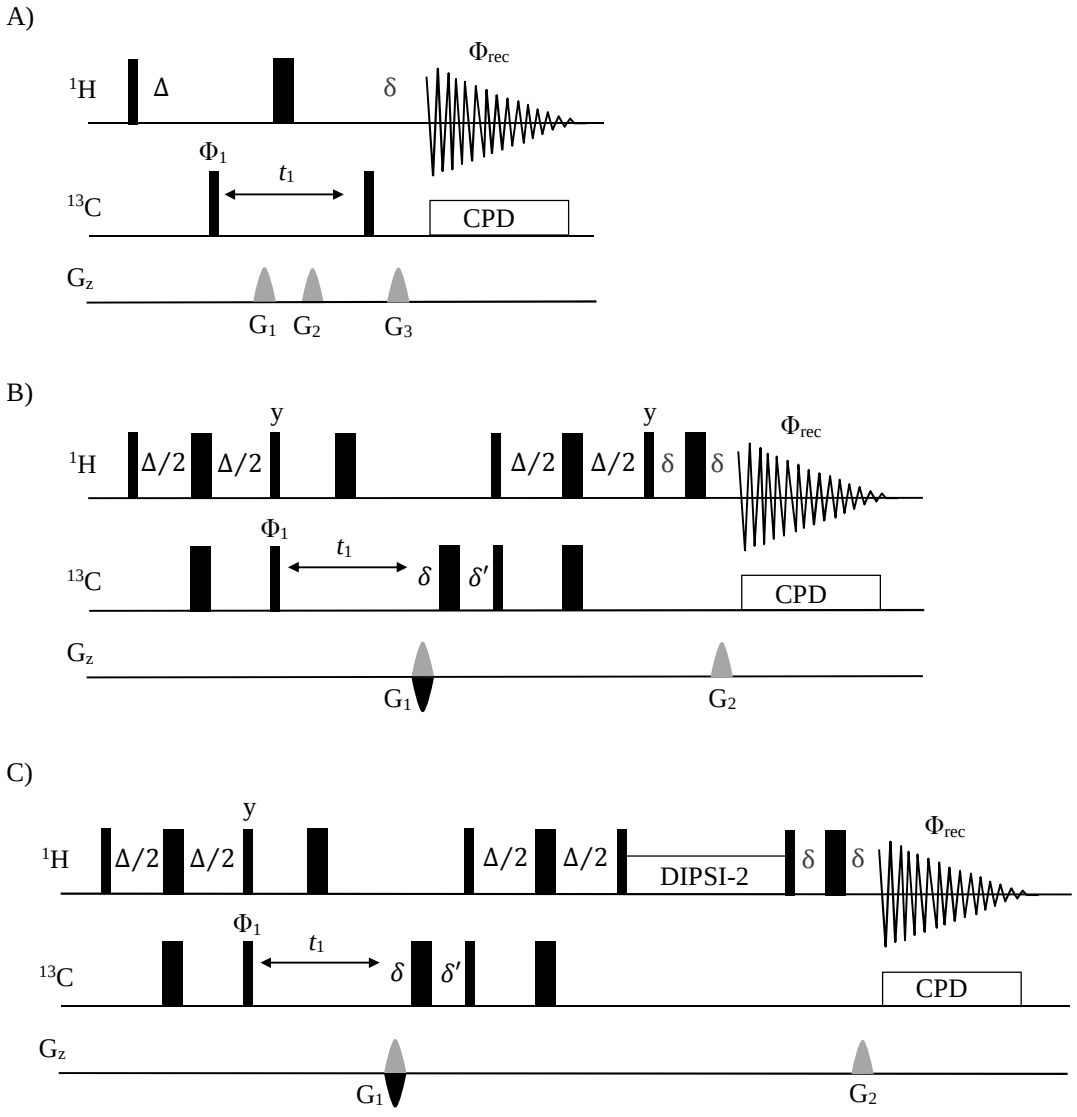

Figure 13: Pulse sequence scheme of some long range heteronuclear correlation experiments: A) HMBC, B) HSQC-COSY, and C) HSQC-TOCSY.

1.1.3. Resolution-enhanced NMR

The improvement of the digital and/or the signal resolution is one of the most interesting topics in modern NMR spectroscopy. A better resolution facilitates more accurate measurements and improves signal overlap. Some resolution-enhanced NMR techniques are now available for these purposes. For instance, broadband homodecoupling techniques afford simplified multiplet patterns, whereas spectral aliasing (SA) or NUS can achieve better digital resolution per time unit, economizing spectrometer time.

1.1.3.1. Pure-shift NMR Spectroscopy

Despite the use of high magnetic fields, the range of ^{1}H chemical shift is small (typically 10ppm; 6000 Hz at 600MHz) and frequently leads to signals overlap due to the multiplicity J_{HH} pattern splitting of each proton resonance (around 10-40 Hz). The development of novel homodecoupling techniques has been explored in the last years, improving signal resolution and doing some measurements and assignments easier and more straightforward.

The traditional homodecoupling method used frequency-selective continuous-wave irradiation on a specific signal during the acquisition.[53] Modern homodecoupling methods are based on the original Zangger-Sterk (ZS) experiment.[54] This experiment uses a pseudo-2D acquisition mode, where a decoupling block consists of a hard 180º pulse and a slice-selective element (simultaneous application of a selective 180º pulse and a weak encoding gradient) applied in the middle of a variable t_1 delay. A post-processing protocol generates a new homodecoupled 1D FID joining the first data chunk of each collected FID. Real-time ZS methods have also been reported where the mentioned homodecoupling block is repeatedly applied during the FID period.[55] In general terms, real-time 2D experiments provide better signal-to-noise ratios (SNR) but they suffer from lower spectral quality. Pseudo-2D ZS experiments afford better spectral quality at the expense of longer acquisition times. Both acquisition modes have been applied to a plethora of NMR experiments, both offering advantages and drawbacks depending on their implementation (Figure 14).

Some homodecoupling blocks are available, all including a hard 180º ^{1}H pulse to the passive spins and a selective inversion element to the chosen active spins. They can be separated into three groups: isotopic editing by a BIRD module, frequency-selective 180º pulses, and spatially encoded elements.

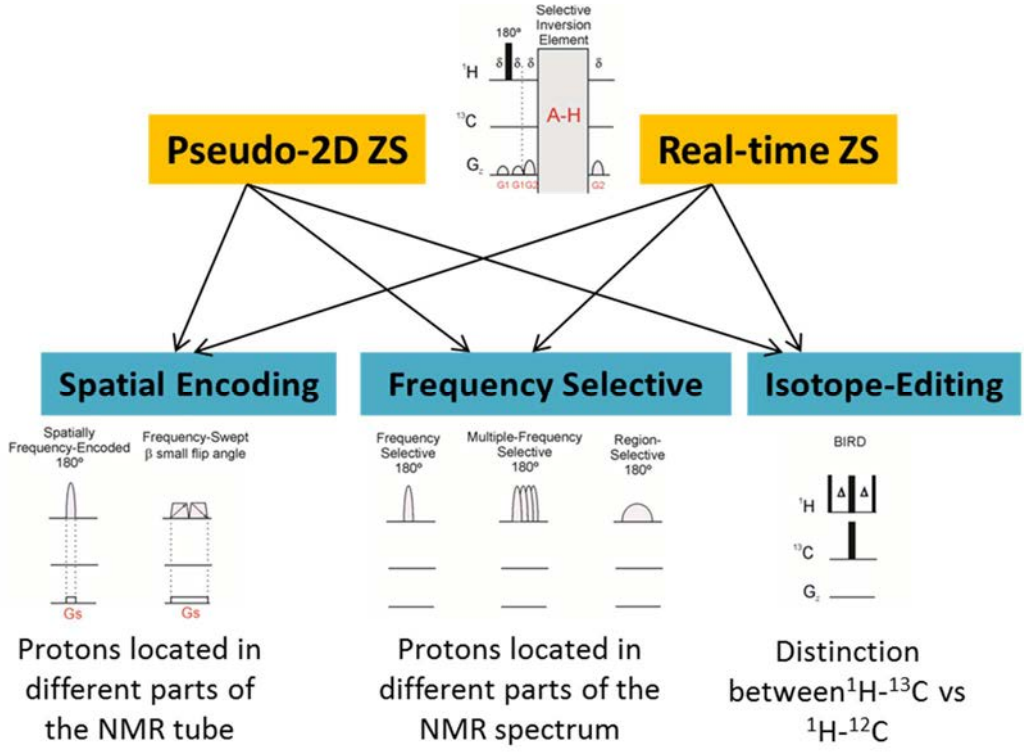

Figure 14: Different approaches to obtain homodecoupled NMR spectra depending on the acquisition mode and the chosen homodecoupling block.

a) Spatially encoded elements

Slice-selective NMR experiments involve the application of selective or adiabatic 180º ^{1}H pulses simultaneously with a PFG having both the same duration. The PFG makes the magnetic field spatially inhomogeneous along the dimension where it is applied (z-axis). Under these conditions, spins will be excited depending on their position along the NMR tube, providing a spatial dependence frequency shift. These experiments give excellent results in weakly coupled signals although it can fail for strongly coupled spin systems. The major drawback is the low sensitivity (about 1-5% of the conventional ^{1}H sensitivity), as just a small part of the entire sample (z-slice) is getting excited by each frequency. Some sensitivity improvements have been reported to circumvent this inconvenient.[56–60]

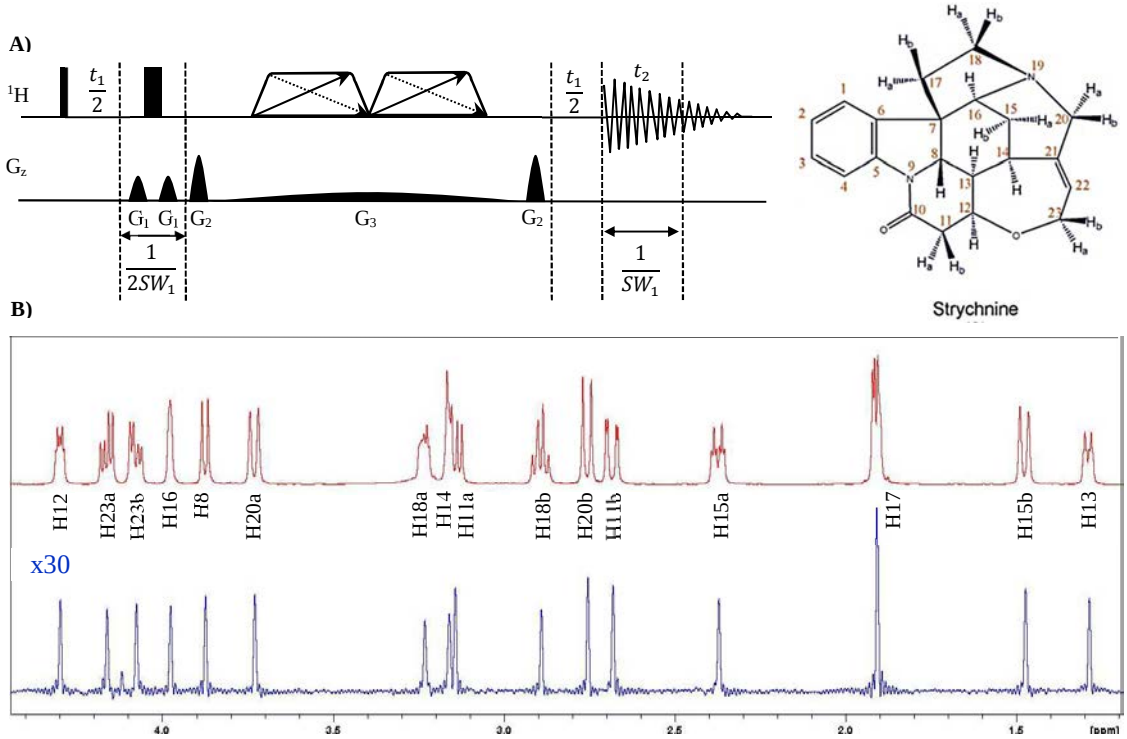

Figure 15: A) Pulse scheme of the PSYCHE experiment. B) Comparison between the conventional ^{1}H spectrum (red) and the PSYCHE spectrum acquired with two chirp pulses of 15 ms of the alkaloid strychnine. The PSYCHE spectrum has been enlarged by a factor of 30 to show the same signal than the conventional spectrum.

The original ZS experiment is based on this methodology, achieving the homodecoupling spectrum with the use of a slice-selective pulse timing combined with a pseudo-2D acquisition.[54] A similar approach was applied in a real-time ZS version where PFGs suppress strong signals from passive spins. Currently, the most commonly used experiment with real-time homodecoupling is the homodecoupled broadband (HOBB) technique,[61] whereas the pure-shift yielded by chirp excitation (PSYCHE) experiment is the preferred as a pseudo-2D ZS method (Figure 15).[62,63–65] The spatial encoding in PSYCHE is achieved thanks to the simultaneous application of a pair of low-flip angle swept-frequency pulses with a PFG. It is possible to obtain a fully broadband homodecoupled spectrum by adjusting the pulse flip angle of the adiabatic pulse. The significant advantage of PSYCHE lies in its sensitivity, almost one order of magnitude better than conventional pseyudo-2D ZS or BIRD-based experiments (Figure 15B).

b) Frequency-selective 180º pulse

Another homodecoupling block uses a hard 180º pulse and a frequency-selective inversion element. It is the same approach as the above encoding method but without using the encoding gradient. These experiments allow the excitation of well isolated ^{1}H signals by the application of a selective 180º pulse, and they can be used to excite a single frequency, a region, or multiple frequencies. The major advantage of this approach is its full sensitivity whereas the only practical requirement is to have well-isolated proton resonances.

The homodecoupled band-selective (HOBS) strategy was developed based on the real-time ZS experiment from Meyer and Zangger.[61] This approach affords full sensitivity thanks to avoiding the simultaneous application of the spatially encoding gradient with the selective 180º ^{1}H pulse. [66–68]

c) BIRD module

The BIRD cluster developed by the group of Pines is based on a differential $^{12}C/^{13}C$ isotope behaviour.[69] The homodecoupling BIRD module consists of a hard 180º ^{1}H pulse followed by a $BIRD^{d,X}$ element, which inverts direct $^{1}H,^{13}C$ while $^{1}H,^{12}C$ is not affected. This block minimizes the problem of the strong J_{HH} coupling but is not able to decouple germinal $^{2}J_{HH}$ because both protons are attached to the same ^{13}C nucleus. Due to the selectivity of the ^{13}C in front of the ^{12}C, the sensitivity decreases to the natural abundance of that isotope, 1.1%. However, in experiments that already selects $^{1}H\{^{13}C\}$ magnetization, as in the case of HSQC, the application of this homodecoupling block does not introduce an additional sensitivity penalty. This module has been used both with the real-time[55] and pseudo-2D acquisition modes.[70]

1.1.3.2. Spectral aliasing

A simple approach to increase the resolution of a 2D spectrum is by increasing the number of points in the F1 dimension until the limit of T_2 relaxation, and with the consequence of a significant increase of overall experimental time.

SA was proposed to solve that problem a straightforward and elegant solution. This methodology consists in the reduction of the spectral width in the indirect dimension; by doing this, the signals that remain outside the spectral size are repositioned in the new spectrum (Figure 16).

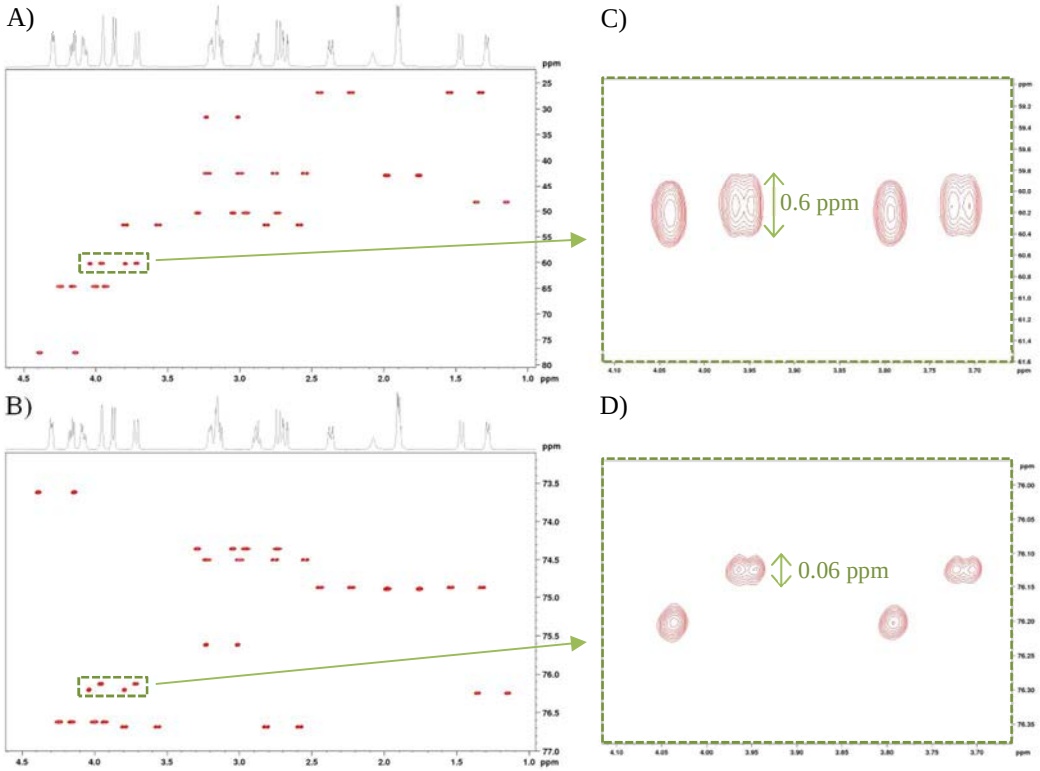

Figure 16: Application of spectral aliasing in a F2-coupled HSQC experiment of strychnine. A) Without aliasing, SW(^{13}C) = 180 ppm. B) Aliased to SW(^{13}C) = 4 ppm. C-D) Expanded signals corresponding to H16 and H8 protons. It is observed how the resolution improves one order of magnitude for the aliased spectrum maintaining the same values for t_1 and the same experimental time.

In 1D experiments, aliased/folded signals are digitally filtered out and will not appear in the spectrum. But this filter applies only in the direct dimension, so, it is possible to take advantage of that phenomenon in the indirect dimension of a 2D experiment. The lost of information of the ^{13}C chemical shift can be determined from $\delta = \delta_{exp} \pm K * SW_a$ where δ is the actual chemical shift, δ_{exp} is the chemical shift in the aliased spectrum, SW_a is the spectral width in the aliased spectrum, and K is the aliasing order and corresponds to a positive or negative integer value that has to be determined to know δ. To find K several solutions has been proposed, one of them requires the combination of the aliased spectrum with other spectra. One of the options consists of

taking the coordinates of any signal in the aliased spectrum and looking for its corresponding signal in the full spectrum of a ^{13}C spectrum or a low-resolved HSQC.[71–74] Other more complexes solutions provide the information of the aliasing order encoded in the aliasing spectrum, causing differences in the phase or multiplets for each signal along the F1 dimension with a distance proportional to the chemical shift. It is also possible to simplify the calculation by the use of the computer program Computer-Optimized Spectral Aliasing (COSA).[75]

This technique depends on the quadrature detection used in the indirect dimension. If TPPI is used, instead of achieving an aliased spectrum, a folded spectrum is obtained. As can be seen in Figure 17, while in SA the spectrum behaves as if it were rolling in on itself, placing the signals that are outside the window at the opposite end of the window. In spectral folding, these signals are located on the same end, changing the phase and following the edge of the end as an axis of symmetry. That behaviour implies that, in contrast with spectral folding, SA maintains the phase properties of the full spectrum. SA has been widely used in both hetero- and homonuclear 2D experiments,[76,77] and even in 3D experiments.[78]

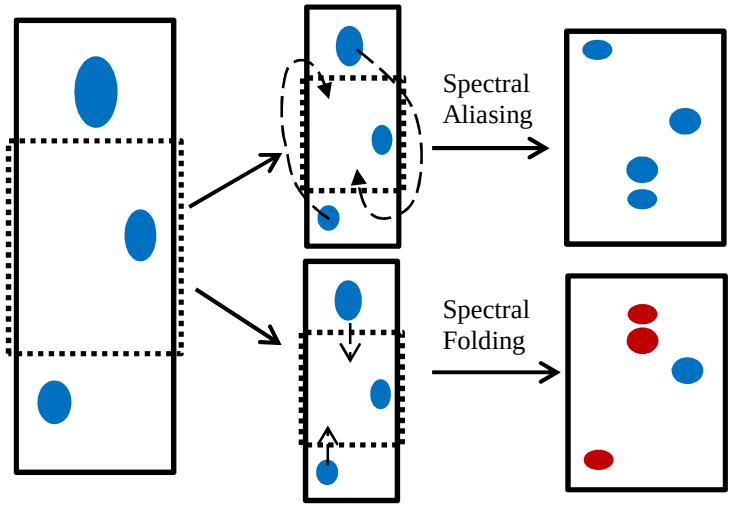

Figure 17: Schematic representation of spectral aliasing and spectral folding. The color red of the signals in spectral folding represents the change of phase.

1.1.3.3. Non-uniform sampling

Another attractive alternative to getting a high-resolved spectrum without compromising the experimental time consists in avoiding the Nyquist condition. The

Nyquist condition explains that the rate of the sampling (dwell time) has to be at least twice the wavelength. For a traditional experiment with M dimensions and N points, this sampling rate entails an experimental time $T = N^{M-1} \cdot 2^{M-1} \cdot T^{FID}$, where T^{FID} is the time required for the measurement of a single data point. With the NUS technique, the selection of the data points is made in non-equal random intervals to reconstruct the spectrum with a much smaller amount of data.[79,80] A special processing algorithm is needed to reconstruct the spectrum, for instance, multi-dimensional decomposition (MDD)[81] or compressed sensing (CS).[80,82] The quality of the final spectra depends on the processing algorithm chosen and the sampling schedule. CS process separately each 2D spectrum in a series (forming pseudo-3D data) giving cleaner spectra. MDD treats all data together, affording faster reconstruction.

NUS can reduce significantly the time needed to obtain high-resolved 2D, 3D and higher dimensional NMR experiments. Thus, using a 50% NUS, it is possible to obtain the same spectrum with the same resolution in the half of the time. It is also possible to improve the resolution without compromising the experimental time. For example, a reduction of the ^{13}C linewidth from 200 Hz (without NUS) to 6 Hz (with NUS) has been reported for HSQC at the same time and without altering the spectral quality.[83]

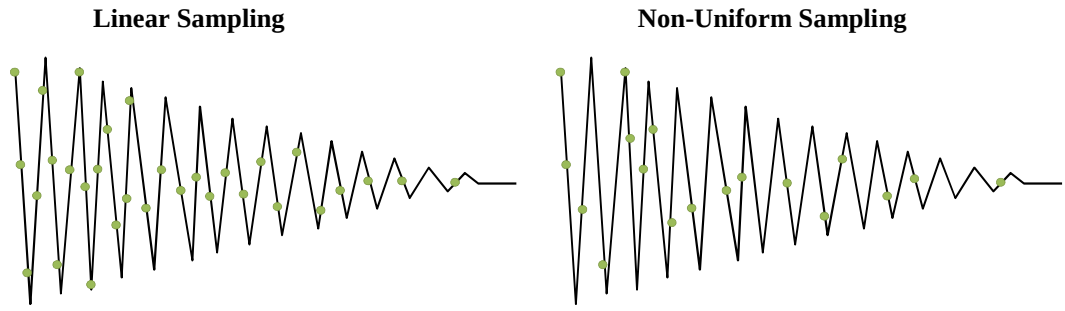

Figure 18: Schematic representation of uniform sampling and non-uniform sampling to a FID.

1.2. NMR in anisotropic media

The determination of relative configurations is one of the main objectives in structure elucidation by NMR spectroscopy. There are three general NMR strategies that helps to determine the 3D structure of molecules: i) from dihedral angles determined by $^3J_{HH}$ via the Karplus equation,[84] ii) determination of nuclear Overhauser effects (NOE) to obtain internuclear distances,[85,86] and iii) the obtention of anisotropic NMR parameters, namely dipolar couplings, chemical shift anisotropies and quadrupolar couplings.[87–90]

The limitation of $^3J_{HH}$ is that they cannot distinguish positive from negative dihedral angles due to its *J* cosine dependence. On the other hand, the use of NOE has been extensively applied since the first conformational studies realized by Anet and Bourn in 1965.[85] NOE can be defined as a local parameter because of its direct relationship with the distance between nuclei, and therefore it shows limitation when atoms are too far one of the other.

On the other hand, anisotropic NMR parameters can be defined as global restraints and can relate atoms from any part of the molecule, no matter the distance between them. The properties of these parameters depend on the molecular orientation and they are measurable when working in an anisotropic medium. Anisotropic parameters were observed for the first time in the 60s decade by Saupe and Englert when they studied the alignment of molecules in oriented media.[91] 40 years later, in 2003, the first configurational analysis of small molecules in strained crosslinked polyacrylamide gels were reported.[92,93]

1.2.1. Anisotropic NMR parameters

Dipolar couplings (D_{ij}) results of the interaction between two nuclei (i and j) with spin different from zero in an anisotropic medium. D_{ij} depend on the distance between the two nuclei (r_{ij}), on the angle between them and the magnetic field (θ), moreover on the gyromagnetic ratios, according to:

$$D_{ij} = \frac{K}{r_{ij}}\left(cos^2\theta - \frac{1}{3}\right)$$

Eq. 9

Where $K = \frac{3}{8\pi^2}\gamma_i\gamma_j\mu_0\hbar$ and γ correspond to the gyromagnetic constant, μ_0 is the vacuum permeability constant and □ the Planck constant divided by 2π.

D_{ij} is the most important parameter involved in solid-state NMR spectroscopy for nuclei with spin ½. However, these interactions cause undesired line broadening due to all the possible molecular orientations. In liquid-state conditions, these orientations are averaged to zero and therefore D_{ij} is not observed because of the Brownian isotropic motion. In a mid-point state, a little degree of orientation can be achieved by exposing molecules to a weakly anisotropic medium, allowing the observation and measurement of a fraction of the dipolar coupling, known as RDC. Other anisotropic parameters that can be observed under these sample conditions are the residual chemical shift anisotropy (RCSA) and the residual quadrupolar coupling (RQC).

1.2.1.1. Residual Dipolar Couplings

In isotropic media, NMR signals show a splitting due to indirect spin–spin couplings, are also known as scalar coupling. In a weakly aligned media, the splitting experienced a variation due to the effect of dipolar interaction. The resulting RDCs are the variation experimented for each signal between a weakly aligned and a not aligned sample. Thus, it is necessary to determine both the isotropic (scalar coupling; *J*) and the anisotropic (total coupling; *T*) values to measure RDCs.

$$^1T_{CH} = {}^1J_{CH} + {}^1D_{CH}$$

Eq. 10

RDCs provide structural information about the relative orientation of two internuclear vectors so that they can help in the determination of relative configurations, no matter the distance between the stereocenters.

The measurement of ^{1}H-^{1}H RDCs has been reported by using different versions of the COSY sequence.[94,95] However, $^1D_{CH}$ has proven to be the most commonly determined RDC by using HSQC-type spectra.[96–99] These experiments measure $^1J_{CH}$ and $^1T_{CH}$ along the F2 dimension because of the simplicity, the speed and the excellent resolution obtained. Some examples are the F2-heterocoupled CLIP-HSQC,[16] Perfect-HSQC[17] and PIP-HSQC[18] experiments. Despite these improvements, the complex multiplet pattern and broad linewidths obtained for anisotropic signals due to the

presence of both J_{HH} and D_{HH} can introduce considerable errors in the measurements along F2. Broadband homodecoupled techniques have been proposed to partially solving this problem, such as real-time BIRD-based homodecouped HSQC experiments.[31,62,67,100,32,101] However, signal distortions can still be observed due to the presence of large $^2J_{HH}$ and $^2D_{HH}$ in diastereotopic CH_2 groups. Alternatively, the *J*SB-HSQC experiment has been proposed for the measurement of $^1J_{CH}$ and $^1T_{CH}$ along the F1 dimension.[31,102]

1.2.1.1.1. Theory of Residual Dipolar Couplings

To deeply understand the meaning of RDCs and how to work with them it is essential to focus on some equations. For simplicity, it can be assumed that the molecule is rigid, so there are not internal dynamics and the internuclear distance is constant. *D*ij is needed to solve the term $cos^2\theta$ which means that the knowledge on the probability of the orientational distribution for the couple of nucleus is required. This probability, as it was explained in the paper of Kramer et al.,[103] can be expressed as the 3x3 matrix $\hat{P}$ where the components define the probabilities of finding the magnetic external field in the fixed frame of reference in the molecule. Instead of this probability tensor, represented by *P*, the term alignment tensor A can be found in some references.[103,104] The relation between both is simply given by: $\hat{\mathrm{A}} = \hat{\mathrm{P}} - \frac{1}{3}\hat{1}$ where $\hat{1}$ is a unitary diagonal tensor. On the other hand, the concept of Saupe tensor $\hat{S}$ ($\hat{S} = \frac{3}{2}\hat{A}$.) can also be found in some cases. [91]

The matrix $\hat{P}$ can be expressed as:

$$\overline{\cos^2\theta} = \vec{r}^T\hat{P}\vec{r} = \begin{pmatrix} x & y & z \end{pmatrix}\begin{pmatrix} P_{xx} & P_{xy} & P_{xz} \\ P_{yx} & P_{yy} & P_{yz} \\ P_{zx} & P_{zy} & P_{zz} \end{pmatrix}\begin{pmatrix} x \\ y \\ z \end{pmatrix}$$

Eq. 11

Where $\vec{r}$ is the internuclear vector and x, y and z correspond to its coordinates in the molecular frame. The matrix has a trace value of 1 ($P_{xx} + P_{yy} + P_{zz} = 1$) and it is symmetrical ($P_{xy} = P_{yx}$, $P_{zy} = P_{yz}$ and $P_{zx} = P_{xz}$). That allow to reduce the number of unknowns to just five, that means that with five equations we are going to be able to get the value of the probability, alignment and Saupe tensor. In order to obtain those

equations, we need five values of RDCs, non-parallel among them. It is important that those vectors are not parallel because then they would have the same value of $\cos^2\theta$ and give us the same information.

With those five parameters, it is already possible to diagonalize the matrix through the Singular-value decomposition algorithm (SVD), as it is shown in the nice paper of Prestegard.[105] SVDs provides a very optimal least-squares fit between the experimental and calculated values, although other methodologies are feasible such as TRAMITES[106] or Almond-Axelsen.[107] The most commonly employed computer programs which implement this algorithm for RDCs data analysis are PALES[108] and MSpin.[109] These programs provide the value of the Cornilescu's Q factor which scales for the fitting of our experimental RDCs with the selected structure. The closer to zero the Q is, the better the fitting with the structure.

$$Q = \sqrt{\frac{\sum\left(D_i^{exp} - D_j^{calc}\right)^2}{\sum D_i^{exp}}}$$

Eq. 12

1.2.1.2. Residual Chemical Shift Anisotropy

RCSAs are based on the difference observed between the isotropic and the anisotropic chemical shift values and, therefore, depends on the relative orientation of the chemical shielding tensor. In contrast to RDCs, RCSAs are usually measured from 1D ^{13}C NMR spectra because both protonated and mainly non-protonated RCSA carbons are usually required.[110,111]

To measure RCSA, the peak that we expect has nothing or the small RCSA is used as a reference. Sometimes, Tetramethylsilane (TMS) is used as a reference because its symmetry makes RCSA negligible, although it may not be the best option for all cases.[112] During alignment processes the environment of the sample change and produce changes in isotropic chemical shift of the reference. To avoid that drawback, several solutions have been developed. For instance, the use of a specific device to get variable-angle sample spinning (VASS) [113,114] or variable-angle NMR spectroscopy[115]. Unfortunately, the technology necessary to obtain a variable angle is not common in many laboratories. Kuchel and his coworkers studied a rubber-based stretching

apparatus. [116] This apparatus, although improved by the group of Luy,[117] still shows some limitations at solving the inaccuracies in the chemical shift. Without the use of any device , Gil *et al*. find a solution by making the approximation of the ΔΔRCSA calculation,[118] where the differences of differences in the chemical shift of the same peak must be measured under two aligning conditions, 1 and 2:

$$\Delta\Delta\text{RCSA} = (\delta_i^{aniso} - \delta_{ref}^{aniso})^1 - (\delta_i^{aniso} - \delta_{ref}^{aniso})^2$$

Eq. 13

The effects on the reference coming from the changes in the environment of the atoms, also affect each of the signals. These changes do not affect the measurements of RDCs, but they do for RCSA. To solve that, a post-acquisition correction that compensated this isotropic shift has been proposed by Gil who use a certain amount of isotropic signal as an internal reference that always remains present in the compression device.[111] Without having to acquire any other spectrum, the correction is performed by measuring the difference between the ^{13}C signals of inside and outside the gel. It is based on the Eq. 14:

$$(\delta_i^{max} - \delta_{ref}^{max}) - (\delta_i^{min} - \delta_{ref}^{min}) = \Delta RCSA_i + (k_i - k_{ref}) \cdot (r^{max} - r^{min})$$

Eq. 14

Where "$(k_i - k_{ref})$" is a constant that characterizes the isotropic contribution and "r" refers to the ratio gel/analyte.

1.2.1.3. Residual Quadrupolar Couplings

RQCs are the splitting observed in the signals of the NMR spectra of nuclei with spin larger than ½ dissolved in an anisotropic media. ^{2}H is the most common nucleus to be studied for this purpose.

Quadrupolar nuclei do not have a spherical electron density distribution of charge (Figure 19) This non-spherical distribution causes a gradient in the electric field that interacts with the nuclear charge, producing an unequally shift in the nuclear energy levels. The biggest the anisotropy, the biggest the RQC.

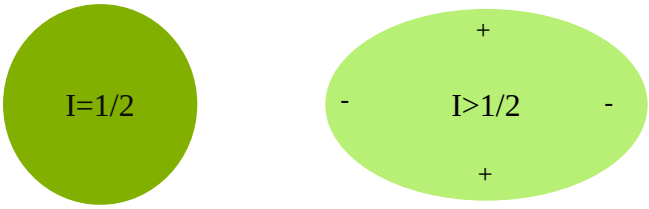

Figure 19: Electric distribution in nuclei with spin equal and different from ½.

RQCs are usually an order of magnitude higher than $^{1}D_{CH}$ RDCs and they are used to study the degree of alignment in the anisotropic media (Figure 20). RQCs depends on the electric field gradient (EFG). If the molecule is highly symmetric, the EFG vanishes and nuclei act similarly as a spin ½ one.

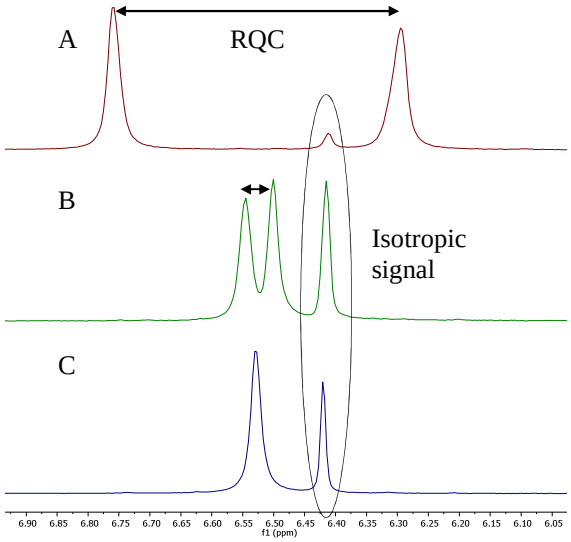

Figure 20: ^{2}H NMR spectra of PMMA gel with different compression: The most compressed sample is A) whereas spectrum C) shows the sample without compression.

1.2.2. Weak alignment media

To measure any anisotropic NMR restraint, it is necessary to use a suitable alignment medium to create the required anisotropy. Alignment NMR media can be sorted into three major groups: liquid crystals (LC), paramagnetic susceptibility and strained aligning gels (SAG).

1.2.2.1. Liquid crystals

LCs were the first alignment media studied by NMR by Saupe and Englert.[91] A proper alignment was achieved with a nematic LC which gave an extraordinary strong alignment and lead to obtaining too large RDCs and very broad signals. To avoid the broadening, current NMR experiments are done with lyotropic LC. Lyotropic LC were applied as oriented media in 2003 by the groups of Griesinger, Courtieu, and Thiele almost at the same time.[43,119,120] This kind of LC are formed by two components, the builder and the solvent. By modifying the proportion of both components it is possible to manipulate, within some limits, the alignment obtained. Despite that, the lower degree of alignment achievable can still be very high causing undesired broad signals.

LC are enantioselective, becoming the only chiral orienting media for organic solvents. Also, the high molecular weight of LC contributes to making their signals less visible, because of their fastest T_2 relaxation.

Besides the well-known homopolypeptides-based LC developed by Aroulanda in 2001 et al. (PBLG, PELG or PCBLL) there are plenty of other interesting options in this field, as summarized in Table 1 .[121]

LC	Solvent	Commercial Availability
PBLG (Poly-γ-benzyl-$_L$-glutamate) [43,119–124]	$CDCl_3$, CD_2Cl_2, DMF, THF, Dioxane	√
PELG (Poly-γ-ethyl-$_L$-glutamate) [29,121]	$CDCl_3$, CD_2Cl_2	√
PCBLL (Poly-ε-carbobenzyloxy-$_L$-lysin)[121,123]	$CDCl_3$, CD_2Cl_2	X
Polyguanidines[125]	$CDCl_3$	X
Helical β-peptides[126]	$CDCl_3$	X
Polyisocianides[127]	$CDCl_3$	X
Polyacetylenes[128]	D_2O	X
Disodium cromoglycate[129]	D_2O	√
Cetylpyridinium Chloride[130]	D_2O	√
C12E5 (Pentaehtylene glycol monodecyl ether)[131]	Mixture D_2O-DMSO	√

Table 1: Liquid crystals more used to align organic molecules.

1.2.2.2. Paramagnetic susceptibility

This methodology is based on the use of some paramagnetic ions to orient the sample. The paramagnetic ions are weakly attracted by an external magnetic field, leading to internal induced magnetic fields. This approach has been executed in biomacromolecules, but it has not been developed in the field of small molecules because of the excessive broadening signals observed in near nuclei. [132–134]

1.2.2.3. Strained Aligning Gels

The SAG method consists in the use of a polymer gel that can be mechanically compressed or stretched, within certain limitations, to align the sample that has been diffused inside it. One of the main strengths that this method is its simplicity. These polymer gels can be acquired dry and only has to be swollen into the same NMR tube with the sample and the chosen solvent. The polymerization is carried out with the desired monomer in the presence of a cross-linker and a radical initiator. A washing procedure consisting of pumping, softly, clean solvent into the gel can be required to release the monomer remaining inside the gel.

The study of the anisotropic properties of elastic polymers was started to study in 1980 by Samulski and Deloche were they swell a polyisoprene based elastomer with benzene sample to see the differences observed in ^{2}H NMR spectra.[135] This work opened the way to the innovative works of the Tycko group in 2000 about the mechanical alignment of gels,[136] followed by Grzesiek et al..[137]

The most interesting advantage that this alignment media offers is the ability to have different degrees of alignment, without any lower limit, just by changing the mechanical compression. However, this technique still has an important way to go in the area of apolar solvents.

The physical explanation for this alignment is simple. The gel is formed by cavities that, in the presence of some mechanical movement (compression or stretching), become asymmetric, manipulating the orientation probabilities of the sample in the space (Figure 21).

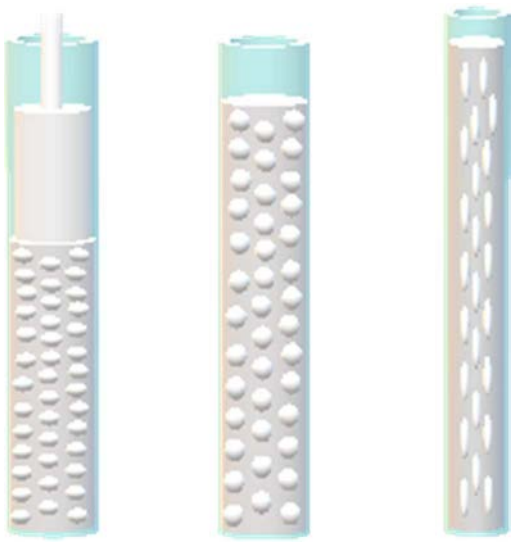

Figure 21: Representative scheme of the shape of the cavities formed in the gel depending of their compression.

1.2.2.3.1. Devices used for SAG methodology

There are two families of devices used in SAG methodology depending on the kind of mechanical movement realized, stretching or compression. Many devices have been developed in the field of stretched gels, highlighting one of the group of Luy,[117] the device of Liu and Prestegard,[138] the design by Kuchel et al.[116] and the novel adaptation of Gil and coworkers[112] derived from the one of the group of Bax.[139]

The good point of stretched gels is the fact that the isotropic signals are completely removed, and therefore the isotropic shift interferences do not disturb the measurements of RCSAs. The main drawback of this technique is that only one alignment can be obtained each time.

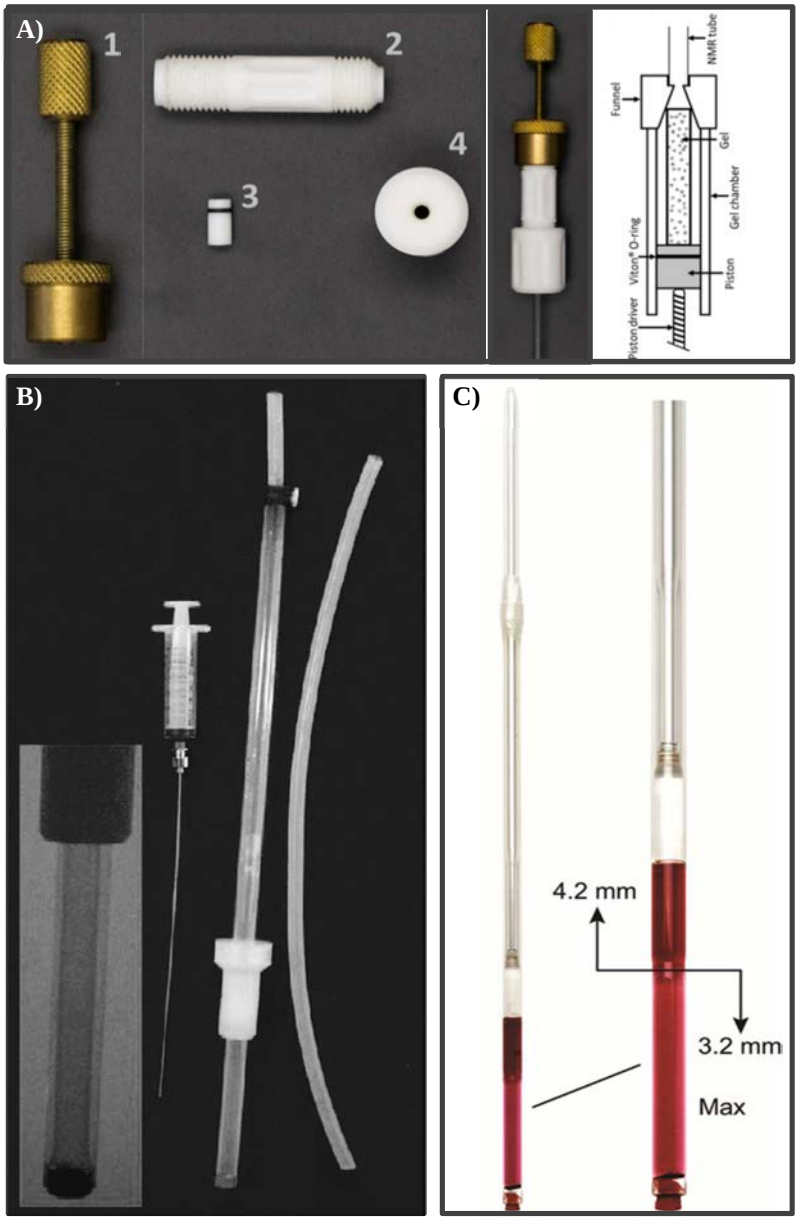

Figure 22: Different stretching devices used to align organic molecules. A) The one developed by the group of Gil (Figure reproduced from the reference[112]). B) Device from Kuchel (Figure adapted from reference [116]) C) The solution proposed by Prestegard where it is possible to observe the gel colored in red. (Figure extracted from the reference[111])

The most common device for gel compression is the Shigemi plunger (Figure 23A), explained very well by Gil et al..[118] The preparation with this traditional method is going to be described in the section *1.2.2.3.3.1.*. However, this device it is quite rudimentary and inaccurate. Nowadays, a more novel and precise device, supplied by New Era Enterprises Inc.,[140] is made of a special tube modified for compression applications and a Teflon plunge (Figure 23B).[112]

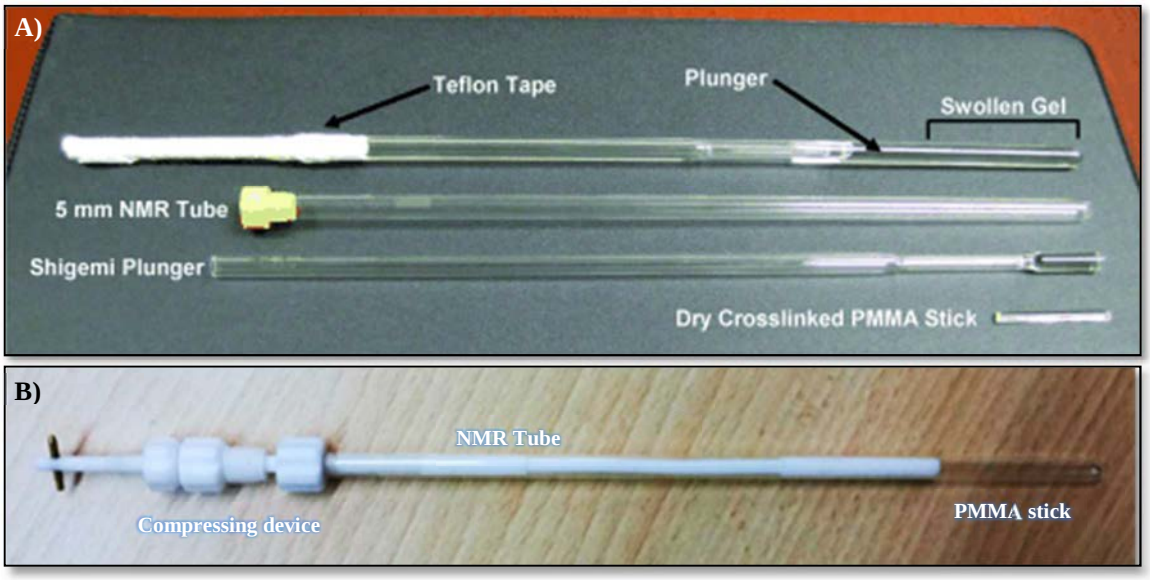

Figure 3: The most common devices used to compress the gel: A) Shigemi plunger method (Figure extracted from the reference [118]) and B) the newly device from Gil.[112]

1.2.2.3.2. Gel types

There are a significant amount of possibilities in the area of SAG depending on the characteristics of the sample that is going to be analyzed. However, to our knowledge, nowadays just the dry sticks of polymethyl methacrylate (PMMA) are commercially available. In Table 2 are described most of the actual SAG gels.

SAG	Solvent	Commercial Availability	Remarks
PMMA (Polymethyl metacrylate)[98,118]	$CDCl_3$, CD_2Cl_2	√	Easy to prepare
Polyacrylamide[136,137]	D_2O	X	
PH.PDMAA (Dimethylacrylamide copolymers) [141,142]	D_2O, DMSO	X	
PAN (Polyacrylonitrile)[143,144]	DMSO	X	Clean Spectra

PVAc (Polyvinylacetate)[145]	$CDCl_3$, CD_2Cl_2, CD_3OD, CD_3CN, DMSO, DMF, C_6D_6, Acetone, THF, AcOEt, Dioxane	X	
PS (Polystyrene)[146,147]	$CDCl_3$, CD_2Cl_2, C_6D_6, THF, Dioxane	X	Long time for diffusion
PDMS (Polydimethylsyloxane)[148]	$CDCl_3$, CD_2Cl_2, C_6D_6, THF, Dioxane, n-Hexane	X	Clean Spectra
Gelatin[149]	D_2O, Mixture D_2O-DMSO	X	Chiral
$\bar{e}$ - Gelatin[150]	D_2O, DMSO	X	Chiral

Table 2: List of common SAG used to align organic molecules in different solvents.

1.2.2.3.3. PMMA as an anisotropic medium

The development of good SAG that can be used with dissolved samples in $CDCl_3$ is of high interest for organic molecule$_s$. Of all the available gels, including polystyrene (PS) and poly-dimethylsiloxane (PDMS), the cross-linked PMMA, synthesized by the group of Gil, is the one that shows better properties to align small molecules in $CDCl_3$.[98]

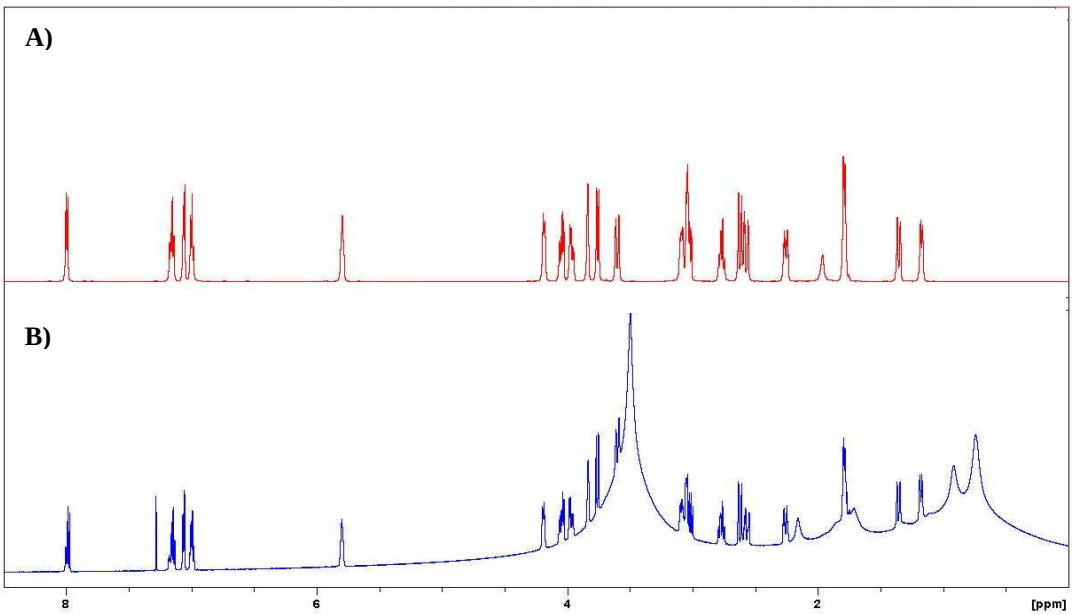

Figure 24: ^1H spectrum of strychnine in A) isotropic $CDCl_3$ and B) in relaxed PMMA gel dissolved in $CDCl_3$. Note the broad signals corresponding to the gel in B.

PMMA is a polymer of the monomer Methyl methacrylate done using ethylene glycol dimethacrylate (EGDMA, 98%) as a cross-linker. The different amount of cross-linker used will provide a different degree of alignment. Also of being able to select a more significant or lower degree of alignment through the density of the crosslinker, it is also possible to refine this alignment by using compression devices, as in the case of the other SAGs. PMMA shows very good alignment properties with no important background signals (Figure 24) and, unlike PS, none of them in the aromatic part. The preparation of PDMS requires the use of β-rays from an electron generator; instead, PMMA gels have an affordable preparation.

1.2.2.3.3.1. Preparation of the PMMA/$CDCl_3$ sample

The preparation of the sample can depend on the gel to be used. There are two procedures to get the PMMA gel swollen in $CDCl_3$:

The first procedure consists in the introduction of the dry gel-stick into the NMR tube with $CDCl_3$ until the stick is covered and the solvent exceeds it by 2 mm. Then, a Shigemi plunger is inserted until the upper part of the gel-stick. The plunger is fixed at the beginning of the tube with some Teflon to avoid that the gel swells vertically but allowing some flexibility (as it is seen in Figure 25). The stick is swollen in 24h and then it has to be washed by pumping some clean $CDCl_3$ as many times as necessary until, in a fast ^1H NMR experiment, we stop seeing the residual monomer that remains from the synthesis (usually it is accomplished with 5–7 washings with about 200 ml of fresh solvent). There is also the option of just, letting the gel with some $CDCl_3$ overnight and without needing to pump it, the gel will be cleaned.

The second method consists in a previous pre-swollen by letting overnight the dry cross-linked gel-stick in a 40:60 acetone-methanol solution that moisturizes the gel, preventing a too fast swelling that could break the gel. Once the PMMA stick has been pre-swollen. it is put it in some container with $CDCl_3$ and, without needing the use of a Shigemi plunger, it will fully swell perfectly exchanging the acetone and the methanol for $CDCl_3$. After that, it can be transferred to another container with clean $CDCl_3$ and keep it there, ready to be used. In that case, the monomer is being washed while it is in the solution of acetone-methanol so it has much less amount of monomer when it will be used.

Once it is verified that there is no monomer inside of the gel by ^{1}H NMR, the degree of alignment is monitored by observing the RQC by ^{2}H NMR.

To introduce the sample into the gel, the excess of solvent is removed from the NMR tube. Then, the sample dissolved in a small amount of $CDCl_3$ (100-200 µl.) is added and gently pumped to help the introduction into the tube. Now, the sample is ready for NMR measurements.

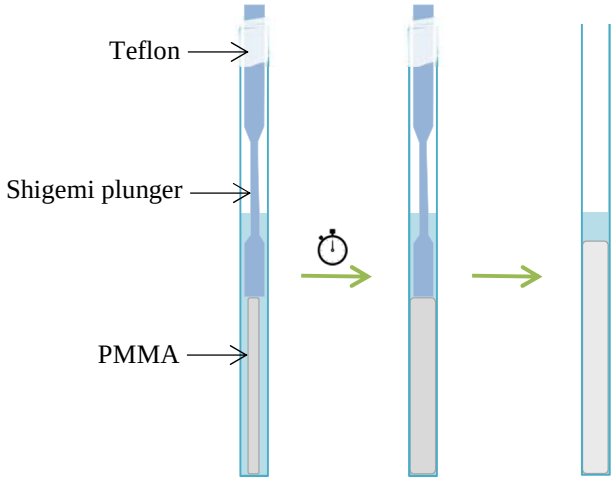

Figure 25: Schematic representation of the swelling process with the use of a Shigemi plunger. The grey square represents the gel stick, dry in the left picture, swollen but still compressed in the middle, and relaxed and fully swollen in the right one.

2. OBJECTIVES

The main objective of this thesis was the exhaustive learning of the theoretical and experimental aspects of modern NMR spectroscopy, with particular emphasis on pulse sequence design and application to the structural elucidation of small molecules. Thus, the study has been focused on research in two general projects:

1.- The development of new NMR experiments for the accurate and efficient measurement of both homo- and heteronuclear coupling constants.

2.- The preparation and study of weak alignment media and the design of novel strategies for the measurement of anisotropic NMR parameters.

These general objectives have been exploited through the work in several areas:

♦ Practical implementation of modern NMR techniques to improve the digital and signal resolution of 2D experiments without compromising the experimental time. In particular, special emphasis will be made on the use of these highly-resolved experiments for the accurate and simultaneous determination of the magnitude and the sign of homonuclear and heteronuclear coupling constants.

♦ Design of improved pulse sequences to achieve the measurement of longer-range heteronuclear connectivities, comparing them with existing NMR methods and evaluating pros and cons.

♦ Implementation of novel NMR approaches to study samples in anisotropic environments, as well as the design of new pulse sequences adapted to the experimental measurement of NMR parameters in these media.

♦ Evaluation of new NMR strategies for efficient structure discrimination using anisotropic NMR parameters.

♦ Application of protocols for the easy automatization and measurement of coupling constants in isotropic and anisotropic media.

3. RESULTS AND DISCUSSION

The experimental results of this thesis are presented as a compendium of 7 publications published in recognized scientific peer-reviewed journals. All these publications are focused on the field of structural elucidation of small molecules through different NMR techniques:

- Detection and application of long-range heteronuclear correlations:

Publication 1:
Extending long-range heteronuclear NMR connectivities by HSQMBC-COSY and HSQMBC-TOCSY experiments
Saurí, J.; Marcó, N.; Williamson, R. T.; Martin, G. E.; Parella, T. J. Magn. Reson. 2015, 258, 25–32.
DOI 10.1016/j.jmr.2015.06.004

- Improvement in signal and digital resolution mainly using spectral-aliased HSQC experiments. Application to the measurement of isotropic and anisotropic NMR parameters:

Publication 2:
Ultra high-resolution HSQC: Application to the efficient and accurate measurement of heteronuclear coupling constants
Marcó, N.; Fredi, A.; Parella, T. Chem. Commun. 2015, 51 (15), 3262–3265.
DOI 10.1039/C4CC10279G

Publication 3:
Isotropic/Anisotropic NMR Editing by Resolution-Enhanced NMR Spectroscopy
Marcó, N.; Gil, R. R.; Parella, T. ChemPhysChem 2018, in press.
DOI: 10.1002/cphc.201800094

- Efficient and accurate measurement of homonuclear and heteronuclear scalar and RDCs in both isotropic and anisotropic media, respectively, along the F1 dimension of novel *J*-resolved HSQC experiments:

Publication 4:

Structural discrimination from in situ measurement of $^{1}D_{CH}$ and $^{2}D_{HH}$ residual dipolar coupling constants

Marcó, N.; Gil, R. R.; Parella, T. Magn. Reson. Chem. 2017, 55 (6), 540–545.
DOI 10.1002/mrc.4575

Publication 5:

Perfect $^{1}J_{CH}$-resolved HSQC: Efficient measurement of one-bond proton-carbon coupling constants along the indirect dimension

Marcó, N.; Souza, A. A.; Nolis, P.; Gil, R. R.; Parella, T. J. Magn. Reson. 2017, 276, 37–42.
DOI: 10.1016/j.jmr.2017.01.002

Publication 6:

$^{1}J_{CH}$ NMR Profile: Identification of key structural features and functionalities by visual observation and direct measurement of one-bond proton-carbon coupling constants

Marcó, N.; Souza, A. A.; Nolis, P.; Cobas, C.; Gil, R. R.; Parella, T. J. Org. Chem. 2017, 82 (4), 2040–2044.
DOI: 10.1021/acs.joc.6b02873

Publication 7:

$^{2}J_{HH}$-resolved HSQC: Exclusive determination of geminal proton-proton coupling constants

Marcó, N.; Nolis, P.; Gil, R. R.; Parella, T. J. Magn. Reson. 2017, 282, 18–26.
DOI: 10.1016/j.jmr.2017.06.014

PUBLICATION 1

Title: Extending long-range heteronuclear NMR connectivities by HSQMBC-COSY and HSQMBC-TOCSY experiments

Authors: Saurí, J.; Marcó, N.; Williamson, R. T.; Martin, G. E.; Parella, T.

Reference: *J. Magn. Reson.* **2015**, *258*, 25–32.

DOI: 10.1016/j.jmr.2015.06.004

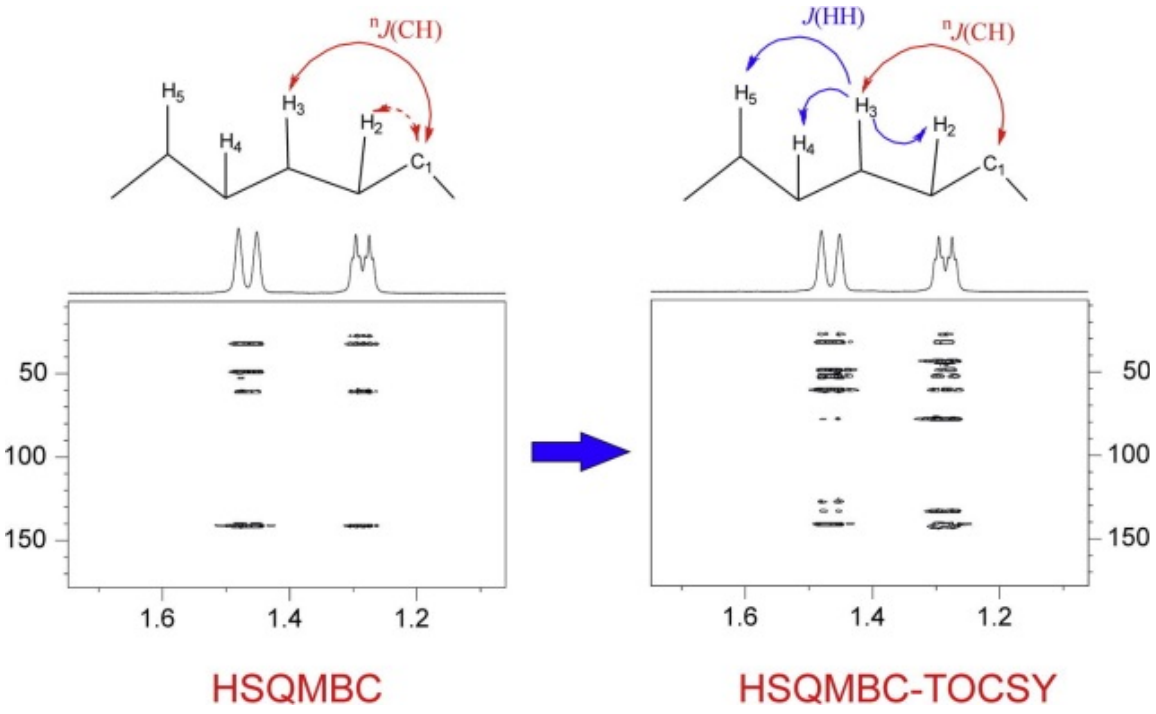

SUMMARY

The detection of heteronuclear long-range proton-carbon ($^{n}J_{CH}$) connectivities is a fundamental step in the structural elucidation of small molecules. Two-bond and three-bond correlations are usually observed in regular HMBC and HSQMBC experiments. Alternatively, the use of additional homonuclear transfers as the propagation of magnetization between remote protons in HSQC pulse sequences (HSQC-COSY and HSQC-TOCSY) has demonstrated to be a valuable tool to detect remote $^{n}J_{CH}$. In this publication, the implementation of COSY and TOCSY transfers into the HSQMBC experiment is evaluated. The newly developed pulse sequences, HSQMBC-COSY and HSQMBC–TOCSY, have been compared with some other popular sequences taking into account the couplings between ^{1}H-^{13}C as well as between ^{1}H-^{15}N. These experiments prove to be very helpful for non-protonated heteronuclei, allowing the observation of missing cross-peaks in conventional experiments or the detection of ultra-long-range correlations (up to five and six bonds away).

Journal of Magnetic Resonance 258 (2015) 25–32

Contents lists available at ScienceDirect

Journal of Magnetic Resonance

journal homepage: www.elsevier.com/locate/jmr

Extending long-range heteronuclear NMR connectivities by HSQMBC-COSY and HSQMBC-TOCSY experiments

Josep Saurí [a,b], Núria Marcó [a], R. Thomas Williamson [b], Gary E. Martin [b], Teodor Parella [a,*]

[a] Servei de Ressonància Magnètica Nuclear, Universitat Autònoma de Barcelona, E-08193 Bellaterra, Barcelona, Spain
[b] NMR Structure Elucidation, Process and Analytical Chemistry, Merck & Co. Inc., 126 E. Lincoln Avenue, Rahway, NJ 07065, USA

ARTICLE INFO

Article history:
Received 20 April 2015
Revised 9 June 2015
Available online 22 June 2015

Keywords:
HSQMBC
HSQC-TOCSY
HSQMBC-COSY
HSQMBC-TOCSY
Long-range correlations
Heteronuclear coupling constants
LR-HSQMBC

ABSTRACT

The detection of long-range heteronuclear correlations presenting *J*(CH) coupling values smaller than 1–2 Hz is a challenge in the structural analysis of small molecules and natural products. HSQMBC-COSY and HSQMBC-TOCSY pulse schemes are evaluated as complementary NMR methods to standard HMBC/HSQMBC experiments. Incorporation of an additional *J*(HH) transfer step in the basic HSQMBC pulse scheme can favor the sensitive observation of traditionally missing or very weak correlations and, in addition, facilitates the detection of a significant number of still longer-range connectivities to both protonated and non-protonated carbons under optimum sensitivity conditions. A comparative $^{1}H–^{13}C$ study is performed using strychnine as a model compound and several examples are also provided including $^{1}H–^{15}N$ applications.

1. Introduction

Tracing long-range homo- and heteronuclear through-bond correlations is a fundamental process in the structure elucidation of small molecules and natural products studied by NMR spectroscopy. Homonuclear TOCSY is a very important NMR experiment for establishing the identity of proton signals belonging to the same spin system [1]. The incorporation of TOCSY transfers in other regular NMR experiments also plays an important role in the propagation of magnetization between remote protons, as recognized for the excellent complementarity between COSY/TOCSY or HSQC/HSQC-TOCSY experiments (Fig. S1 in the SI). The HSQC-TOCSY experiment essentially sorts proton–proton correlations as a function of ^{13}C chemical shift in the second frequency domain using a well defined sequential double stage transfer [2,3]. First, an initial HSQC scheme is used for ^{1}H to ^{13}C magnetization transfer via ^{1}J(CH). Then, the resulting in-phase ^{1}H magnetization is suitable for a subsequent TOCSY transfer, allowing the correlation between protons and protonated carbons belonging to the same *J*(HH) spin subsystem in a single 2D NMR experiment. Numerous modifications of the basic HSQC-TOCSY pulse scheme have been reported including versions designed for the quantitative measurement of the magnitude and the sign of long-range heteronuclear coupling constants (^{n}J(CH); $n > 1$) [4–12]. An equivalent HSQC-COSY experiment provides analogous molecular information but the additional *J*(HH) transfer is often limited to a single neighboring proton step. H2BC has probably become the most popular version of this experiment to trace out two-bond $^{1}H–(^{1}H)–^{13}C$ connectivities, although longer connectivities can also be observed [13]. However, this type of constant-time experiment can impose stringent limitations on the F1 resolution that can be attained. The major limitations of both HSQC-COSY and HSQC-TOCSY experiments is that they only work for protonated carbons and therefore, quaternary carbon information is missing from these spectra.

Non-protonated centers are observed using long-range HMBC [14] and HSQMBC [15] correlation experiments, where the evolution delay (Δ) is optimized to a fixed coupling value (typically between 6 and 10 Hz) for detecting heteronuclear ^{2}J and ^{3}J and, only in favorable cases, ^{4}J correlations. In these experiments, signal intensity depends on $\sin(\pi^{n}J(CH)\Delta)$ and therefore cross-peaks emanating from small ^{n}J(CH) values (<2 Hz) usually present weak intensity or may even be absent. Many different approaches have been proposed to observe such weak/missing cross-peaks such as the use of different delay optimization or the use of the accordion approach combined with constant-time methods [16]. All these HMBC methods have been recently reviewed in depth [17].

A refocused HSQMBC optimized to a very small ^{n}J(CH) value (2–4 Hz), referred to as LR-HSQMBC experiment, has been proposed to efficiently detect correlations corresponding to small

* Corresponding author.
E-mail address: teodor.parella@uab.cat (T. Parella).

http://dx.doi.org/10.1016/j.jmr.2015.06.004
1090-7807/

^{n}J(CH) values [18–20]. It has been demonstrated that the typical range of HMBC data, which usually includes ^{2}J and ^{3}J connections, can be efficiently extended in a similar fashion as an alternative but much less sensitive 1,*n*-ADEQUATE experiment, even in sample-limited situations or in proton-deficient molecules [21]. The LR-HSQMBC method allows the observation of longer-range $>^{3}J$ (^{4}J, ^{5}J, and even ^{6}J) correlations as well as some of the missing $^{2}J/^{3}J$. In the cryptospirolepine example, even ^{6}J and ^{7}J correlations from two N-methyl groups to the carbonyl were observed [22]. As a result, it was concluded that the "short-range" HMBC and the "long-range" LR-HSQMBC are complementary tools to trace out proton/carbon skeletons in natural products of high complexity.

In this work we set out to explore and evaluate two further experimental approaches, broadband HSQMBC-COSY and HSQMBC-TOCSY experiments, as complements to the standard HSQC-TOCSY, HMBC/HSQMBC, LR-HSQMBC, and ADEQUATE experiments to observe either missing or weak short-range ($^{2}J/^{3}J$) as well as long-range ($>^{3}J$) heteronuclear correlations under optimum sensitivity conditions (Scheme 1). The proposed experiments retain the simplicity of their ^{1}H frequency-selective versions (selHSQMBC [23,24], selHSQMBC-COSY [25] and selHSQMBC-TOCSY [26]) which have been recently reported for the quantitative measurement of the magnitude and the sign of ^{n}J(CH) and allow a general and routine application with a minimum set-up.

2. Results and discussion

Fig. 1 presents the three pulse schemes evaluated in the present study to map long-range heteronuclear correlations. The basic pulse scheme of Fig. 1A is a refocused HSQMBC experiment, similar to a conventional HSQC pulse train with the interpulse delay, Δ, optimized to $1/(2 * {}^{n}J(\mathrm{CH}))$ (typically about 50–80 ms). It employs a refocusing INEPT to bring small heteronuclear coupling magnetization back in-phase in order to perform data acquisition using broadband heteronuclear decoupling. The method uses the echo/anti-echo gradient selection protocol and data are phase-sensitive rather than magnitude calculated, the latter being typically employed in the HMBC experiment. The first analog, HSQMBC-COSY, includes a final 90°(y) ^{1}H pulse incorporated in the pulse sequence to generate an additional homonuclear COSY

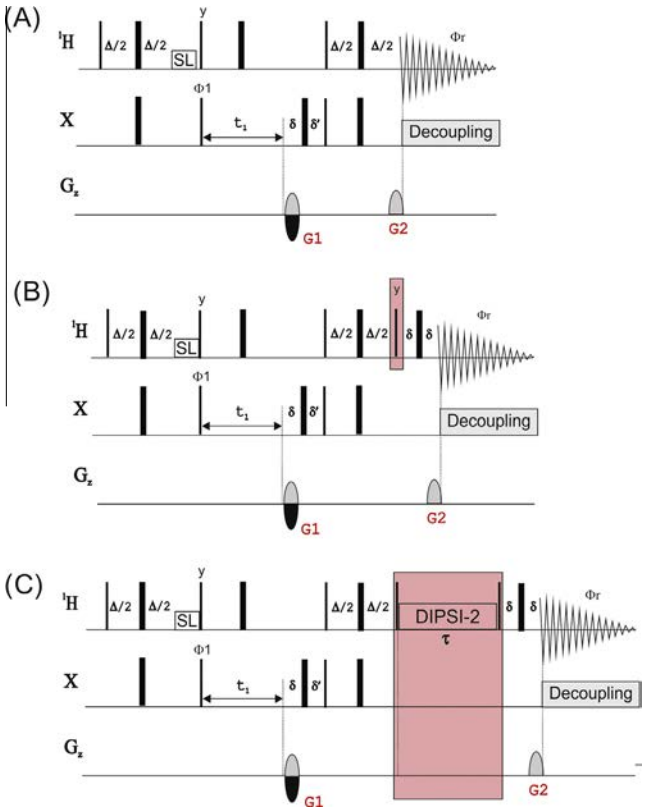

Fig. 1. Pulse schemes for the (A) HSQMBC, (B) HSQMBC-COSY, and (C) HSQMBC-TOCSY heteronuclear correlation experiments. The delay Δ is set to $1/[2 * {}^{n}J(\mathrm{CH})]$ and all ^{13}C 180° pulses were adiabatic CHIRP pulses for broadband inversion and refocusing and broadband heteronuclear decoupling is applied during proton acquisition. The added COSY and TOCSY blocks in B and C are marked with a box. Complete details are found in the experimental section.

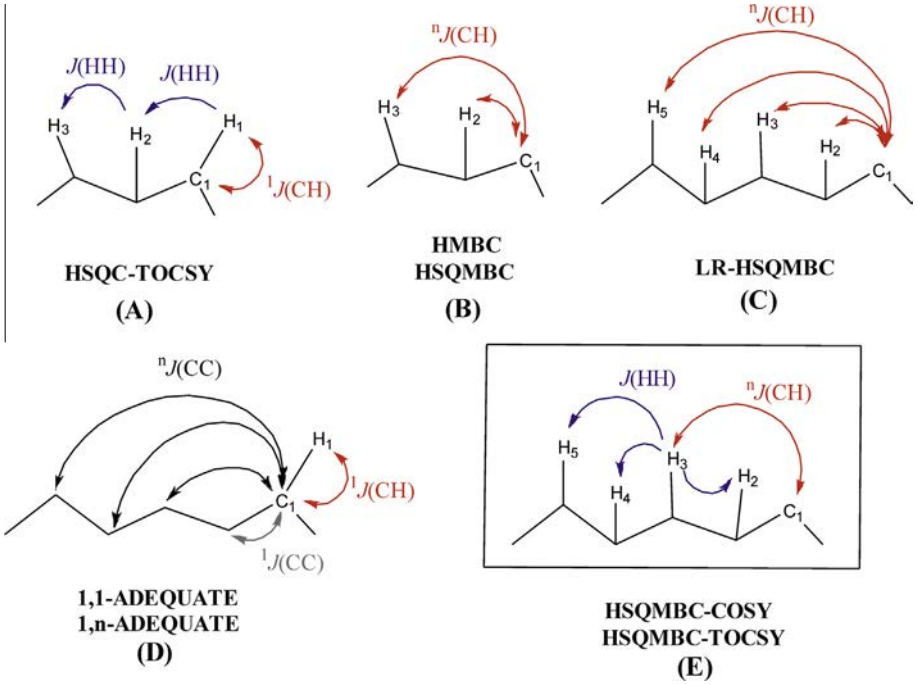

Scheme 1. Magnetization transfer mechanisms involved in different long-range heteronuclear correlation NMR experiments.

transfer (Fig. 1B). This experiment affords a dual step transfer mechanism (^nJ(CH) + J(HH)) since J(HH) couplings also evolve during the INEPT periods. Finally, the HSQMBC-TOCSY pulse scheme (Fig. 1C) incorporates a ^{1}H–^{1}H TOCSY transfer mechanism, being practically the same pulse scheme as the HSQC-TOCSY experiment. The transfer mechanism of the HSQMBC-TOCSY experiment is based on a dual ^nJ(CH) + ΣJ(HH) step where Δ is optimized for ^nJ(CH). In terms of overall pulse sequence length, the HSQMBC-TOCSY sequence is longer than the HSQMBC and HSQMBC-COSY counterparts due to the additional duration of the TOCSY mixing process in the form of a z-filtered DIPSI pulse train. This fact can introduce some sensitivity losses in molecules having shorter T_2 relaxation times but it offers superior performance through modulation of the signal propagation as a function of the TOCSY duration. No attempts have been employed to minimize the presence of direct responses in these experiments by including, for instance, a BIRD element into the initial INEPT period because the last COSY/TOCSY transfer would recover part of these contributions.

All three experiments use the same data acquisition and processing set-up and therefore, it is easy to perform a comparative study in terms of relative sensitivity and the number and nature of the observed cross-peaks from each of the methods. The alkaloid strychnine (1) has been chosen as a target to study the response of long-range correlations as a function of their J(CH) values. This molecule should present 40 ^2J and 68 ^3J heteronuclear connectivities. Taking as a basis the theoretical J(CH) values of strychnine previously calculated by DFT [27], 5 correlations should be expected with ^2J < 1 Hz, 12 with 1 Hz < ^2J < 2 Hz, 11 with ^3J < 1 Hz and 8 with 1 Hz < ^3J < 2 Hz. This means that 42.5% of ^2J and 28% of ^3J connectivities present couplings smaller than 2 Hz and, a priori, they would show a very small intensity or would even be absent in a conventional 8 Hz optimized HSQMBC experiment. Fig. 2 shows the HSQMBC, HSQMBC-COSY and HSQMBC-TOCSY (40 ms mixing time) spectra of strychnine (1) acquired with the pulse sequences described in Fig. 1 and processed identically. It can be quickly observed that a significant number of additional cross-peaks are observed in the two hyphenated experiments. Table 1 summarizes the numbers of correlations obtained in these spectra and compares the results with the data previously reported for the same target molecule using other related NMR experiments such as LR-HSQMBC, decoupled refocused HMBC (D-HMBC) and conventional HMBC, the three experiments were optimized to

Table 1
Comparison of the number and the nature of long-range heteronuclear responses observed in different NMR experiments performed on the alkaloid strychnine.

	^2J	^3J	^4J	^5J	^6J	Total >^3J	Total
2 Hz LR-HSQMBC [a]	33	59	55	11	2	68	160
2 Hz D-HMBC [a]	29	43	34	8	2	44	116
2 Hz HMBC [a]	34	54	43	10	1	54	142
8 Hz HMBC [a]	34	53	36	4	1	41	129
HSQC_TOCSY [b]	23	15	11	2	0	13	51
8 Hz HSQMBC-Refoc [c]	36	58	40	1	0	41	135
8 Hz HSQMBC-COSY [d]	38	58	58	14	2	74	170
8 Hz HSQMBC-TOCSY [e]	38	58	65	18	3	86	182

[a] Taken from [18].
[b] Measured in this work using the pulse sequence of Fig. 1C optimized to 140 Hz.
[c] Measured in this work using pulse sequence of Fig. 1A optimized to 8 Hz.
[d] Measured in this work using the pulse sequence of Fig. 1B optimized to 8 Hz.
[e] Measured in this work using the pulse sequence of Fig. 1C optimized to 8 Hz and using a mixing time of 40 ms.

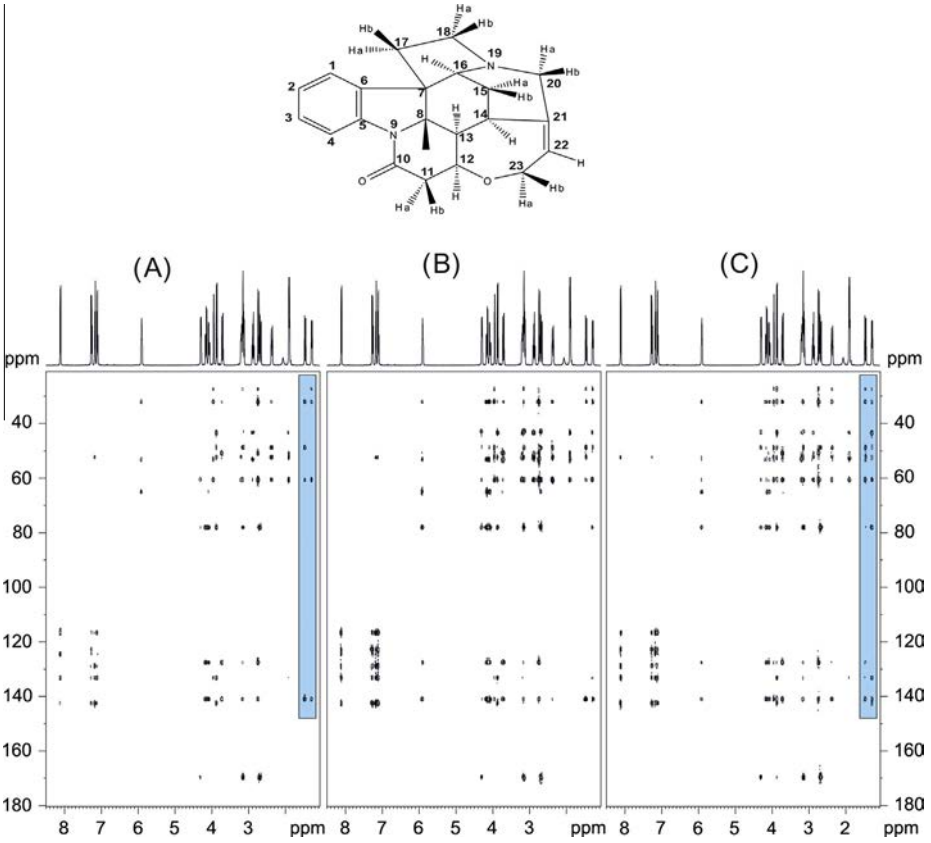

Fig. 2. (A) HSQMBC, (B) HSQMBC-COSY and (C) HSQMBC-TOCSY spectra (8 Hz optimized) of strychnine (**1**). For a detailed comparison, the marked areas are expanded in Fig. 3.

2 Hz, as well as to an HMBC experiment optimized to 8 Hz [18]. In this previous study, it was shown the major number of connectivities were observed in the LR-HSQMBC (68 correlations $>^3J$ and a total of 160 correlations) experiment. Otherwise, the conventional 8 Hz HMBC showed a number of correlations (129) that are in strong agreement with our results obtained with a regular 8 Hz HSQMBC, (135 connectivities). Of particular interest is the excellent and similar behavior of the 8 Hz HSQMBC-COSY vs. 2 Hz LR-HSQMBC, providing a total number of correlations of 162 vs 160, respectively, and 74 $>^3J$ correlations compared to 68. An advantage of the 8 Hz HSQMBC-COSY experiment is that it offers better sensitivity because it avoids the use of long INEPT delays,

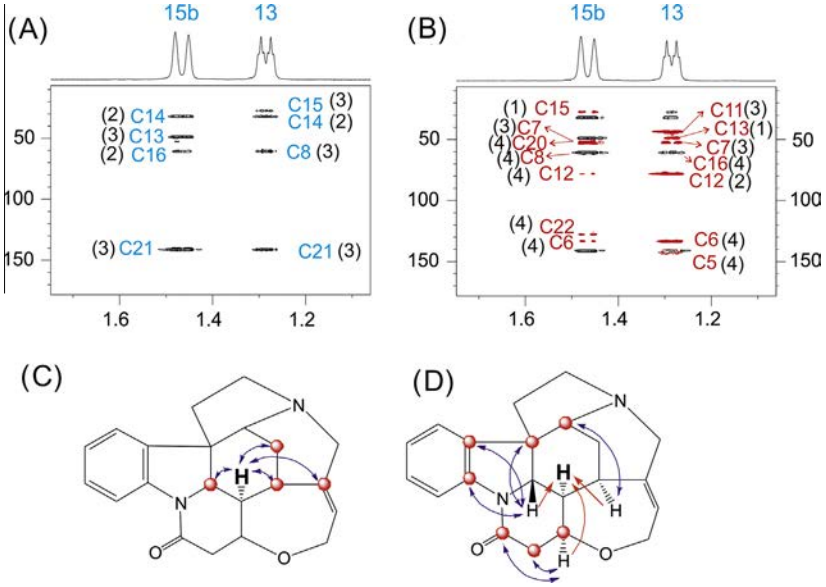

Fig. 3. Expanded areas corresponding to the (A) 8 Hz HSQMBC (see Fig. 2A) and (B) 8 Hz HSQMBC-TOCSY spectra with a 40 ms TOCSY mixing time (see Fig. 2C) of **1**. The number of bonds across which the correlation is observed is shown parenthetically. Schematic illustration showing the (C) direct $^1H–^{13}C$ HSQMBC and (D) relayed HSQMBC-TOCSY correlations observed for the H13 proton.

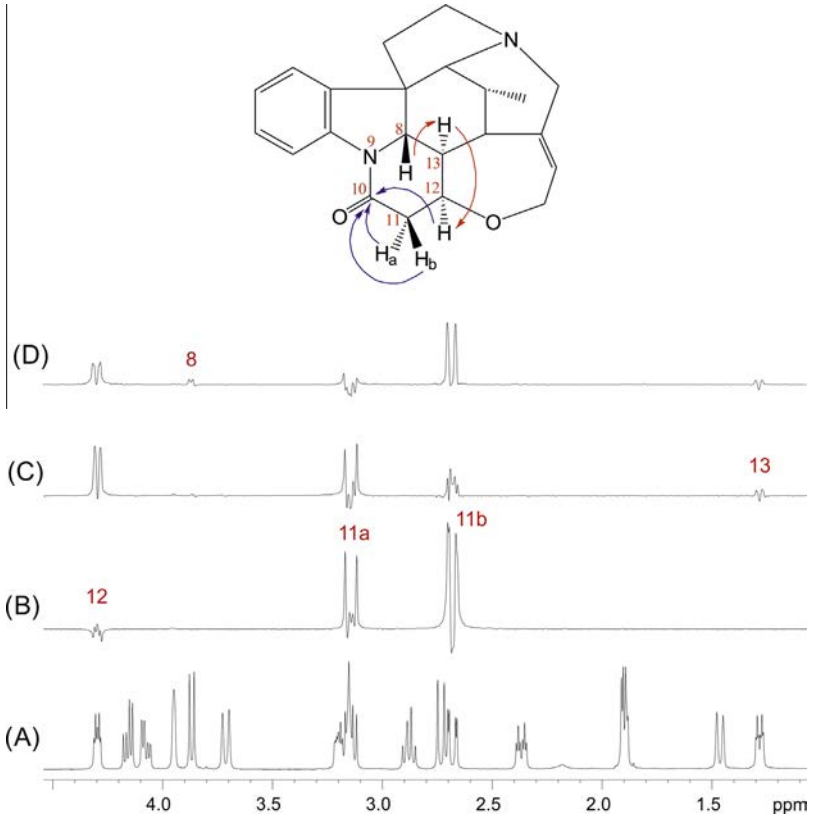

Fig. 4. (A) ^1H Reference spectrum. 1D slices corresponding to the C10 carbon frequencies extracted from the (B) 8 Hz HSQMBC and (C and D) 8 Hz HSQMBC-TOCSY (40 and 60 ms, respectively) spectra of 1. Proton NMR spectrum is shown in (A) for reference. Purple arrows stand for correlations from B whereas the red arrows stand for correlations from C to D). (For interpretation of the references to color in this figure legend, the reader is referred to the web version of this article.)

as found in a 2 Hz optimized LR-HSQMBC experiment (250 ms long), which can become critical in molecules presenting short T_2 relaxation times. The results obtained with the HSQMBC-TOCSY experiment exceed the performance of all other experiments. A total of 182 correlations were observed, 86 of them being of $>^3J$. This represents a 14% increase over the total number of correlations observed in the LR-HSQMBC experiment and a 26% increase in the correlations observed that were $>^3J$ [18]. In order to be confident with data in Table 1 and to compare the relative sensitivity and complementarity between related experiments reported in Ref. [18], we have collected 8 Hz HSQMBC-TOCSY and 2 Hz LR-HSQMBC experiments under the same experimental conditions and overall acquisition times (Figs. S2–S4).

Selected expansions to highlight the complementarity between HSQMBC and HSQMBC-TOCSY spectra are shown in Fig. 3. For instance, H15b and H13 protons each exhibit four intense cross-peaks in the 8 Hz HSQMBC spectrum, corresponding to correlations arising from coupling constants in the range of 3.1–7.6 Hz, all experimentally measured from selHSQMBC experiments [23,24]. In comparison, the number of correlations is increased in the 8 Hz HSQMBC-TOCSY experiment recorded with an additional 40 ms TOCSY transfer (compare Fig. 3A vs B). H15b shows seven additional cross-peaks, including the direct correlation response, a ^3J correlation to the quaternary C7 carbon, and five new ^4J connectivities. As an additional benefit compared to HSQC-TOCSY, long-range correlations can be observed with proton/carbon pairs belonging to different ^{1}H spin systems, such as the four-bond H15b–C22 connectivities through the vicinal J(H15b–H14) = 1.9 Hz coupling, or H15b–C20 through a mixture of both H15b–H14 and J(H15b–H16) = 2.1 Hz transfer mechanisms. On the other hand, H13 shows seven new cross-peaks, including its direct correlation, a ^2J connectivity with C12, two new ^3J correlations to C7 and C11, and three ^4J correlations including the aromatic C5 and C6 non-protonated carbons (Fig. 3C vs D). For instance, the observed correlation of H13 to C5 and C6 arise from an initial ^3J coupling of these carbons to H8 followed by a TOCSY transfer from H8 to H13. It can be concluded that many cross-peaks corresponding to ^nJ(CH) correlations <1 Hz can be detected in a 8 Hz optimized HSQMBC-TOCSY spectrum under optimum sensitivity conditions. The number of connectivities could be increased provided that the use of longer TOCSY allows the J(HH) propagation without serious sensitivity losses by relaxation.

Similar conclusions can be extracted from an equivalent comparative study performed on the alkaloid quinine (see Table S1 and Figs. S5–S7 in the SI). The total number of correlations observed in HSQC-TOCSY, HSQMBC, HSQMBC-COSY and HSQMBC-TOCSY spectra were 98, 112, 127 and 159, respectively. Of these, 31, 32, 44 and 71 cross-peaks correspond to $>^3J$ connectivities, respectively.

The HSQMBC-TOCSY experiment can also benefit from the sequential propagation character associated with the TOCSY transfer. The 8 Hz HSQMBC 1D trace corresponding to the carbonyl C10 carbon exhibits two-bond correlations to the diastereotopic H11a and H11b protons as well as a three-bond correlation to H12 proton (Fig. 4B). These interactions correspond to coupling constant values of −7.9, −6.3, and +2.0 Hz, respectively, as determined from selective HSQMBC-TOCSY-IPAP experiments [26]. It can be shown that the equivalent 8 Hz HSQMBC-TOCSY with a 40 ms DIPSI-2 mixing time affords an additional four-bond connectivity to H13 (Fig. 4C) and the use of a longer mixing time (60 ms) shows a further correlation to the H8 proton (Fig. 4D). Clearly, the H8–C10 peak results from the effective five-bond transfer pathway thanks to the sequential TOCSY transfer via the large J(H8–H13) *trans*

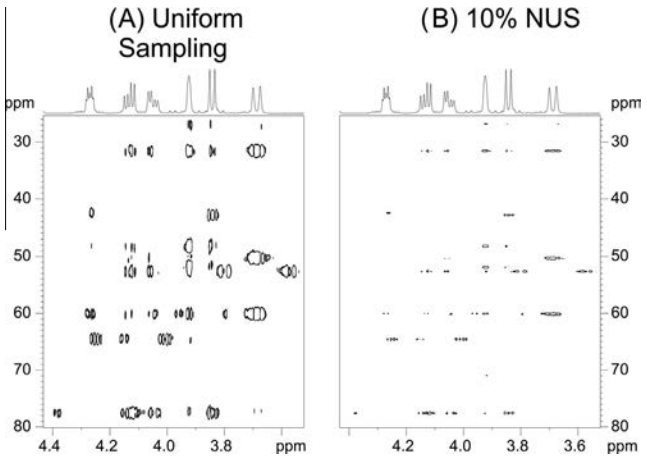

Fig. 6. Comparison of 8 Hz optimized HSQMBC-TOCSY spectra of 1 acquired with (A) uniform sampling (128 t_1 increments) and (B) 10% NUS. Both datasets have been acquired with the same experimental time.

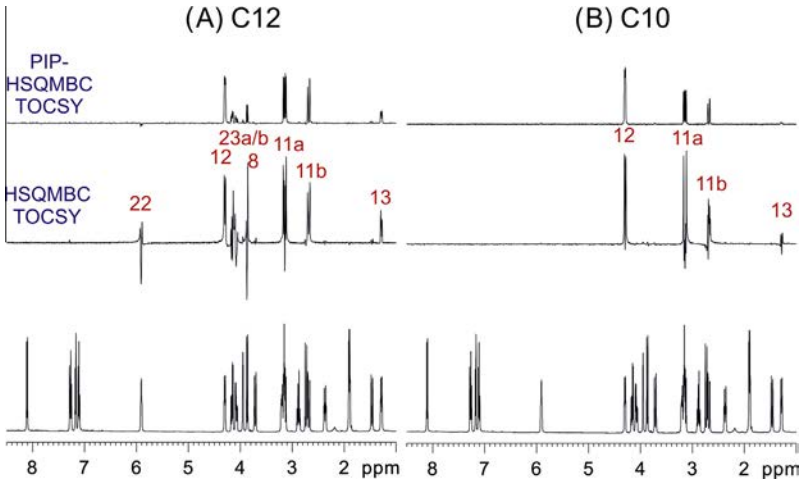

Fig. 5. 1D slices extracted from the (A) C12 and (B) C10 carbon frequencies of the 8 Hz optimized HSQMBC-TOCSY spectrum of strychnine acquired (middle) without and (top) with a ZQF element into the z-filtered DIPSI-2 element (40 ms).

diaxial coupling (10.5 Hz) and not from the direct three-bond correlation through the nitrogen N9 atom. Theoretical calculations afforded H13–C10 and H8–C10 coupling constants of +0.10 and −0.12 Hz, respectively [27].

As shown in Fig. 4C and D and, as was previously reported for other TOCSY-related experiments, signals after the HSQMBC and/or after the DIPSI mixing process can present dispersive anti-phase contributions that lead to distorted cross-peaks. The HSQMBC-TOCSY experiment can be further perfected by incorporating a zero-quantum filter (ZQF) [28] consisting of a simultaneous adiabatic ^{1}H pulse and the gradient G_o applied just after the DIPSI-2 train for a complete removal of any anti-phase contribution (see Fig. S8 in the SI). In this PIP-HSQMBC-TOCSY experiment, pure in-phase (PIP) signals are obtained, as previously reported for related HSQC-TOCSY [10] and PIP-HSQMBC [29] experiments. This can be particularly useful when determining ^{n}J(CH) coupling constants along the detected dimension. In such cases no ^{13}C decoupling is applied during acquisition and the analysis of cross-peaks will exhibit an additional IP splitting due to the active J(CH) value. The price to be paid is a sensitivity loss that in some cases could preclude the observation of some signal(s). For instance, note how the intense H22–C12 or H13-10 cross peaks practically vanishes when a ZQF is applied (Fig. 5). The analysis of pure in-phase multiplets facilitates a more accurate analysis and a reliable extraction of ^{n}J(CH) value. In the case of non-resolved multiplets, ^{n}J(CH) can be extracted comparing linewidths in coupled/decoupled spectra [7]. In contrast to the PIP-HSQMBC experiment [29], a PIP-HSQMBC-TOCSY cross-peak can be the cumulative result of several and different coupling pathway contributions. This would preclude the extraction of ^{n}J(CH) using the IPAP methodology or the determination of the relative sign as reported for selective HSQMBC versions [23–26].

The HSQMBC-TOCSY experiment is amenable for other practical considerations. For instance, the encoding G1 and decoding G2 gradients used for coherence selection are separated by both the long refocusing and the TOCSY periods, which can lengthen the pulse sequence by about 100–120 ms under routine conditions. This prolongation can introduce sensitivity losses due to diffusion effects that can be diminished by a careful setting of the maximum gradient strengths. Conversely, convection effects can also be encountered in routine analysis when working with temperature regulation and common non-viscous solvents. Simply spinning the sample can be a viable means to avoid these problems, thereby maximizing sensitivity. We also have studied the impact of acquiring HSQMBC-TOCSY datasets using conventional vs. non-uniform sampling (NUS) [30]. Important gains in digital resolution along the indirect dimension have been achieved under the same

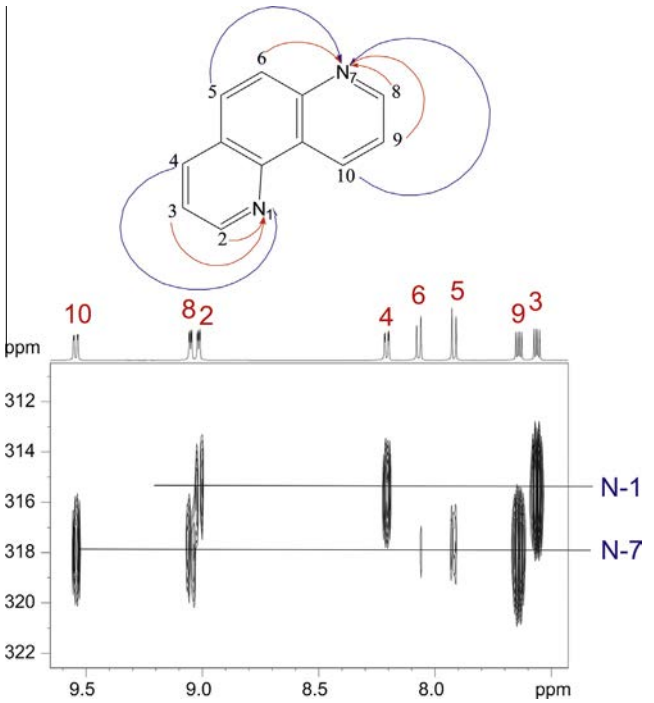

Fig. 8. ^{1}H–^{15}N HSQMBC-TOCSY spectrum (60 ms mixing time) of 1,7-phenantroline optimized to 8 Hz. Red arrows stand for correlations from a conventional HSQMBC whereas the purple arrows stand for additional correlations from this spectrum. (For interpretation of the references to color in this figure legend, the reader is referred to the web version of this article.)

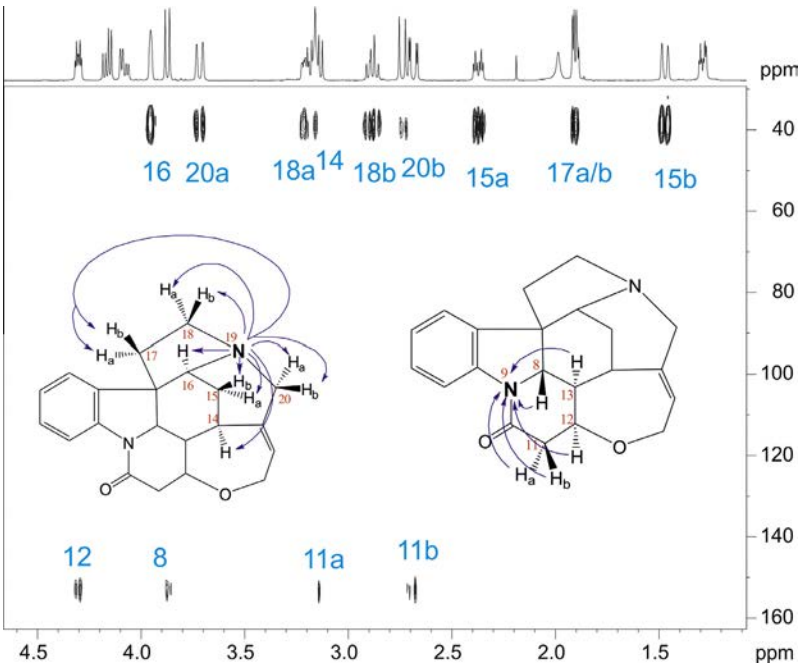

Fig. 7. 8 Hz optimized ^{1}H–^{15}N HSQMBC-TOCSY on strychnine, using a mixing time of 60 ms.

experimental times using 10–25% of NUS data (Fig. 6, Figs. S9 and S10). In the case of PIP-HSQMBC-TOCSY, 25% of NUS keeps the data quality high maintaining the well defined in-phase multiplet structure required for a precise J extraction are maintained; however, sampling the data more sparsely could distort the final multiplets. Although the experimental percentage of applied NUS is a sample-dependent parameter, additional datasets confirming all these predictions are also provided for the cyclic peptide cyclosporine (Figs. S11–S13 in the SI). Alternatively, NUS can also be used to shorten experimental time but spectral quality may be affected if a reduced number of t_1 increments is used.

HSQMBC-TOCSY can be especially interesting when applied to other heteronuclei [31]. Fig. 7 shows the $^{1}H–^{15}N$ counterpart of the HSQMBC-COSY experiment of **1**, which displays all expected ^{2}J, ^{3}J, and ^{4}J proton–nitrogen connectivities for both N9 and N19 centers. There are additional correlations to the aliphatic N19 resonance in the spectrum above that are not observed in either conventional $^{1}H–^{15}N$ HMBC spectra or 2 Hz optimized $^{1}H–^{15}N$ LR-HSQMBC spectra [20]. N19 exhibited correlations to H16, H20a/b, H18a/b, H15a (weak), and H17a/b in the 2-Hz LR-HSQMBC spectrum. In addition, correlations are also observed to H14, H15a (strong peak vs. weak in the LR-HSQMBC spectrum) and to H15b. Another example is shown in Fig. 8. A 10 Hz $^{1}H–^{15}N$ PIP-HSQMBC spectrum of the organic heterocycle 1,7-phenanthroline only shows two intense cross-peaks corresponding to the two-bond N1–H2 and N7–H8 correlations. These couplings are −11.2 and −10.7 Hz, respectively, as measured from their PIP signals (Fig. S14). The additional TOCSY scheme visualizes additional ^{3}J and ^{4}J correlations with excellent sensitivity, despite their very low ^{n}J(NH) values.

3. Conclusions

It has been demonstrated that HSQMBC-COSY and HSQMBC-TOCSY experiments can be valuable and complementary tools to the conventional HSQMBC experiment. As concluded for the LR-HSQMBC experiment, the information density extracted from HSQMBC-COSY and HSQMBC-TOCSY due to the large number of detected ^{n}J correlations is generally too high to be used directly without "filtering" shorter range correlations that would come from HMBC. These experiments can provide additional $^{1}H–^{13}C$ correlations even in the extreme case that the corresponding $^{n}J \sim 0$ Hz. They are useful to confirm regular two- or three-bond correlations that are missing in the conventional HSQMBC experiment, or longer range correlations depending to the duration of the TOCSY mixing time and to the existing ^{1}H spin systems. Naturally, the success of these methods will depend on the molecule and spin systems being studied and on the presence of J(HH).

All of the experiments described use the same acquisition, set-up, and processing protocols as the original HSQMBC experiment and offer better sensitivity than some complementary experiments like the recently proposed LR-HSQMBC that use longer evolution delays or the less sensitive ADEQUATE [32,33] or HCNMBC [34] experiments, which are based on $^{13}C–^{13}C$ and $^{13}C–^{15}N$ transfers at natural abundance, respectively. On the other hand the HSQMBC-TOCSY experiment can be easily tuned for quantitative measurements using the PIP-HSQMBC-TOCSY version which affords pure in-phase multiplets amenable for a direct analysis or for a coupled/decoupled approach. Application to any type of heteronucleus is perfectly suitable, as shown for $^{1}H–^{15}N$ correlation experiments.

4. Methods and materials

NMR experiments were recorded at 298 K on a BRUKER DRX-500 spectrometer equiped with a 3-channel 5-mm cryoprobe incorporating a z-gradient coil. The test sample was 20 mg of strychnine (**1**) in 0.6 ml of $CDCl_3$. The 2D HSQMBC, HSQMBC, and HSQMBC-TOCSY spectra of Fig. 2 were recorded with the pulse sequences shown in Fig. 1A–C, respectively, optimized to 8 Hz ($\Delta = 1/(2 * {}^{n}J(CH)) = 62.5$ ms). The recycle delay was 1 s and 4 scans were collected for each of the 128 t_1 increments accumulated, with 2048 data points in each t_1 increment. Prior to Fourier-transformation, zero-filling to 1024 points in F1 and a squared sine-bell apodization phase-shifted 90° in both dimensions were applied. The total experimental time was about 14 min for each individual experiment. Pulse phases are x unless indicated otherwise and a basic two-step phase cycling scheme is applied: $\Phi_1 = x, -x, \Phi_r = x, -x$. Gradient echo/anti-echo and coherence selection was achieved by switching gradients according to G1/G2 = ±80:20.1. Gradients G1 and G2 with a duration of 1 ms (δ) are used for echo–antiecho coherence selection, δ stands for the ovell duration of the gradient and its recovery delay and $\delta' = \delta + t_1$. TPPI-like incrementation with the echo/anti-echo recording scheme was achieved by simultaneous inversion of ^{13}C pulses applied prior to the variable t_1 period. ^{13}C 180° pulses are applied as CHIRP inversion and refocusing pulses of 500 μs and 2000 μs of duration, respectively. The optional ZQF element in the PIP-HSQMBC-TOCSY experiment (see pulse scheme in Fig. S8) includes a chirped adiabatic 180° ^{1}H pulse of 30 ms of duration applied simultaneously with a purging G0 gradient of 1.6 G cm^{-1} to remove undesired transverse and ZQ contributions.

NUS was applied using the standard protocols incorporated into the TOPSPIN 3.1 software package. Different datasets were recorded with different percentage of data sampling (from 10% to 50%) and processed using the compressed sensing algorithm for reconstructing the final spectra.

$^{1}H–^{15}N$ HSQMBC, HSQMBC-COSY and HSQMBC-TOCSY experiments were recorded on the same sample of strychnine and on a sample of 20 mg of 1,7-phenantroline in $CDCl_3$. These experiments were collected under similar conditions as described for the ^{13}C counterparts, using a G1:G2 gradient strength of ±80:8.1. The interpulse delay was optimized to $\Delta = 1/(2 * {}^{n}J(NH))$ as indicated in each example and the number scans was incremented to 32 per each one of the 32 t_1 increments. Data were processed as described before using a zero-filling to 256 K in the indirect dimension. No NUS were applied in these examples.

Acknowledgments

Financial support for this research provided by MINECO (project CTQ2012-32436) is gratefully acknowledged. We also thank the Servei de Ressonància Magnètica Nuclear, Universitat Autònoma de Barcelona, for allocating instrument time to this project.

Appendix A. Supplementary material

Supplementary data associated with this article can be found, in the online version, at http://dx.doi.org/10.1016/j.jmr.2015.06.004.

References

[1] L. Braunschweiler, R.R. Ernst, Coherence transfer by isotropic mixing: application to proton correlation spectroscopy, J. Magn. Reson. 53 (1983) 521–528, http://dx.doi.org/10.1016/0022-2364(83)90226-3.

[2] L. Lerner, A. Bax, Sensitivity-enhanced two-dimensional heteronuclear relayed coherence transfer NMR spectroscopy, J. Magn. Reson. 69 (1986) 375–380, http://dx.doi.org/10.1016/0022-2364(86)90091-0.

[3] T. Parella, J. Belloc, F. Sánchez-Ferrando, A. Virgili, A general building block to introduce carbon multiplicity information into multi-dimensional HSQC-type experiments, Magn. Reson. Chem. 719 (1998) 715–719, http://dx.doi.org/10.1002/(SICI)1097458X(199810)36:10<715::AID-OMR355>3.0.CO;2-T.

[4] T. Parella, J.F. Espinosa, Long-range proton–carbon coupling constants: NMR methods and applications, Prog. Nucl. Magn. Reson. Spectrosc. 73 (2013) 17–55, http://dx.doi.org/10.1016/j.pnmrs.2013.07.001.
[5] M. Misiak, W. Koźmiński, Determination of heteronuclear coupling constants from 3D HSQC-TOCSY experiment with optimized random sampling of evolution time space, Magn. Reson. Chem. 47 (2009) 205–209, http://dx.doi.org/10.1002/mrc.2362.
[6] W. Koźmiński, Simplified multiplet pattern HSQC-TOCSY experiment for accurate determination of long-range heteronuclear coupling constants, J. Magn. Reson. 137 (1999) 408–412, http://dx.doi.org/10.1006/jmre.1998.1700.
[7] K.E. Kövér, V.J. Hruby, D. Uhrín, Sensitivity- and gradient-enhanced heteronuclear coupled/decoupled HSQC-TOCSY experiments for measuring long-range heteronuclear coupling constants, J. Magn. Reson. 129 (1997) 125–129, http://dx.doi.org/10.1006/jmre.1997.1265.
[8] P. Nolis, T. Parella, Spin-edited 2D HSQC-TOCSY experiments for the measurement of homonuclear and heteronuclear coupling constants: application to carbohydrates and peptides, J. Magn. Reson. 176 (2005) 15–26, http://dx.doi.org/10.1016/j.jmr.2005.05.007.
[9] B.L. Marquez, W.H. Gerwick, R.T. Williamson, Survey of NMR experiments for the determination of nJ(C, H) heteronuclear coupling constants in small molecules, Magn. Reson. Chem. 39 (2001) 499–530, http://dx.doi.org/10.1002/mrc.902.
[10] K. Kobzar, B. Luy, Analyses, extensions and comparison of three experimental schemes for measuring ((n)J(CH) + D(CH))-couplings at natural abundance, J. Magn. Reson. 186 (2007) 131–141, http://dx.doi.org/10.1016/j.jmr.2007.02.005.
[11] P. Nolis, J.F. Espinosa, T. Parella, Optimum spin-state selection for all multiplicities in the acquisition dimension of the HSQC experiment, J. Magn. Reson. 180 (2006) 39–50, http://dx.doi.org/10.1016/j.jmr.2006.01.003.
[12] W. Kozmiński, D. Nanz, Sensitivity improvement and new acquisition scheme of heteronuclear active-coupling-pattern-tilting spectroscopy, J. Magn. Reson. 142 (2000) 294–299, http://dx.doi.org/10.1006/jmre.1999.1939.
[13] N.T. Nyberg, J. Duus, O.W. Sørensen, Heteronuclear two-bond correlation: suppressing heteronuclear three-bond or higher NMR correlations while enhancing two-bond correlations even for vanishing 2JCH, J. Am. Chem. Soc. 127 (2005) 6154–6155, http://dx.doi.org/10.1021/ja050878w.
[14] A. Bax, M.F. Summers, 1H and 13C assignments from sensitivity-enhanced detection of heteronuclear multiple-bond connectivity by 2D multiple quantum NMR, J. Am. Chem. Soc. 108 (1986) 2093–2094, http://dx.doi.org/10.1021/ja00268a061.
[15] R.T. Williamson, B.L. Marquez, W.H. Gerwick, K.E. Kövér, One- and two-dimensional gradient-selected HSQMBC NMR experiments for the efficient analysis of long-range heteronuclear coupling constants, Magn. Reson. Chem. 38 (2000) 265–273, http://dx.doi.org/10.1002/(SICI)1097-458X(200004)38:4<265::AID-MRC637>3.0.CO;2-#.
[16] G.E. Martin, C.E. Hadden, R.C. Crouch, V.V. Krishnamurthy, ACCORD-HMBC: advantages and disadvantages of static versus accordion excitation, Magn. Reson. Chem. 37 (1999) 517–528, http://dx.doi.org/10.1002/(SICI)1097-458X(199908)37:8<517::AID-MRC501>3.0.CO;2-W.
[17] J. Furrer, A comprehensive discussion of HMBC pulse sequences. III. Solving the problem of missing and weakly observed long-range correlations, Concepts Magn. Reson. Part A (2015), http://dx.doi.org/10.1002/cmr.a.21317 (in press).
[18] R.T. Williamson, A.V. Buevich, G.E. Martin, T. Parella, LR-HSQMBC: a sensitive NMR technique to probe very long-range heteronuclear coupling pathways, J. Org. Chem. 79 (2014) 3887–3894, http://dx.doi.org/10.1021/jo500333u.
[19] K.A. Blinov, A.V. Buevich, R.T. Williamson, G.E. Martin, The impact of LR-HSQMBC very long-range heteronuclear correlation data on computer-assisted structure elucidation, Org. Biomol. Chem. 12 (2014) 9505–9509, http://dx.doi.org/10.1039/c4ob01418a.
[20] R.T. Williamson, A.V. Buevich, G.E. Martin, Using LR-HSQMBC to observe long-range $^{1}H–^{15}N$ correlations, Tetrahedron Lett. 55 (2014) 3365–3366, http://dx.doi.org/10.1016/j.tetlet.2014.04.060.
[21] M.M. Senior, R.T. Williamson, G.E. Martin, Using HMBC and ADEQUATE NMR data to define and differentiate long-range coupling pathways: is the Crews rule obsolete?, J Nat. Prod. 76 (2013) 2088–2093, http://dx.doi.org/10.1021/np400562u.
[22] J. Saurí, W. Bermel, A.V. Buevich, E.C. Sherer, L.A. Joyce, M.H.M. Sharam, P.L. Schiff Jr., T. Parella, R.T. Williamson, G.E. Martin, Homodecoupled 1,1- and 1, n-ADEEQUATE: pivotal NMR experiments for the structure revision of cryptospirolepine, Angew. Chem. Intl. Ed. (2015), http://dx.doi.org/10.1002/anie.201502540. in press.
[23] S. Gil, J.F. Espinosa, T. Parella, Accurate measurement of small heteronuclear coupling constants from pure-phase α/β HSQMBC cross-peaks, J. Magn. Reson. 213 (2011) 145–150, http://dx.doi.org/10.1016/j.jmr.2011.09.036.
[24] J. Saurí, T. Parella, J.F. Espinosa, CLIP-HSQMBC: easy measurement of small proton–carbon coupling constants in organic molecules, Org. Biomol. Chem. 11 (2013) 4473–4478, http://dx.doi.org/10.1039/c3ob40675j.
[25] J. Saurí, T. Parella, Efficient measurement of the sign and the magnitude of long-range proton–carbon coupling constants from a spin-state-selective HSQMBC-COSY experiment, Magn. Reson. Chem. 50 (2012) 717–721, http://dx.doi.org/10.1002/mrc.3867.
[26] J. Saurí, J.F. Espinosa, T. Parella, A definitive NMR solution for a simple and accurate measurement of the magnitude and the sign of small heteronuclear coupling constants on protonated and non-protonated carbon atoms, Angew. Chem. Int. Ed. 51 (2012) 3919–3922, http://dx.doi.org/10.1002/anie.201108959.
[27] A.V. Buevich, R.T. Williamson, G.E. Martin, NMR structure elucidation of small organic molecules and natural products: choosing ADEQUATE vs HMBC, J. Nat. Prod. 77 (2014) 1942–1947, http://dx.doi.org/10.1021/np500445s.
[28] M.J. Thrippleton, J. Keeler, Elimination of zero-quantum interference in two-dimensional NMR spectra, Angew. Chem. Int. Ed. 42 (2003) 3938–3941, http://dx.doi.org/10.1002/anie.200351947.
[29] L. Castañar, J. Saurí, R.T. Williamson, A. Virgili, T. Parella, Pure in-phase heteronuclear correlation NMR experiments, Angew. Chem. Int. Ed. Engl. 53 (2014) 8379–8382, http://dx.doi.org/10.1002/anie.201404136.
[30] K. Kazimierczuk, V.Y. Orekhov, Accelerated NMR spectroscopy by using compressed sensing, Angew. Chem. Int. Ed. Engl. 50 (2011) 5556–5559, http://dx.doi.org/10.1002/anie.201100370.
[31] J. Saurí, P. Nolis, T. Parella, Efficient and fast sign-sensitive determination of heteronuclear coupling constants, J. Magn. Reson. 236 (2013) 66–69, http://dx.doi.org/10.1016/j.jmr.2013.08.013.
[32] G.E. Martin, Using 1,1- and 1, n-ADEQUATE 2D NMR Data in Structure Elucidation Protocols, Annu. Rep. NMR Spectrosc. 74 (2011) 215–291, http://dx.doi.org/10.1016/B978-0-08-097072-1.00005-4.
[33] G.E. Martin, M. Reibarkh, A.V. Buevich, K.A. Blinov, R.T. Williamson, Application of 1,*n*-ADEQUATE and modified variants to structure elucidation and spectral assignment problems, eMagRes 3 (2015) 215–234, http://dx.doi.org/10.1002/9780470034590.emrstm1370.
[34] S. Cheatham, P. Gierth, W. Bermel, Ē. Kupče, HCNMBC – a pulse sequence for H–(C)–N multiple bond correlations at natural isotopic abundance, J. Magn. Reson. 247 (2014) 38–41, http://dx.doi.org/10.1016/j.jmr.2014.07.011.

Supporting Information

Extending long-range heteronuclear NMR connectivities by HSQMBC-COSY and HSQMBC-TOCSY experiments

Josep Saurí,[1,2] Núria Marcó,[1] R. Thomas Williamson,[2] Gary E. Martin[2] and Teodor Parella[1,*]

[1]Servei de Ressonància Magnètica Nuclear, Universitat Autònoma de Barcelona, E-08193 Bellaterra, Barcelona, Spain.

[2]NMR Structure Elucidation, Process and Analytical Chemistry, Merck & Co. Inc., 126 E. Lincoln Avenue, Rahway, NJ 07065, USA

Table of contents

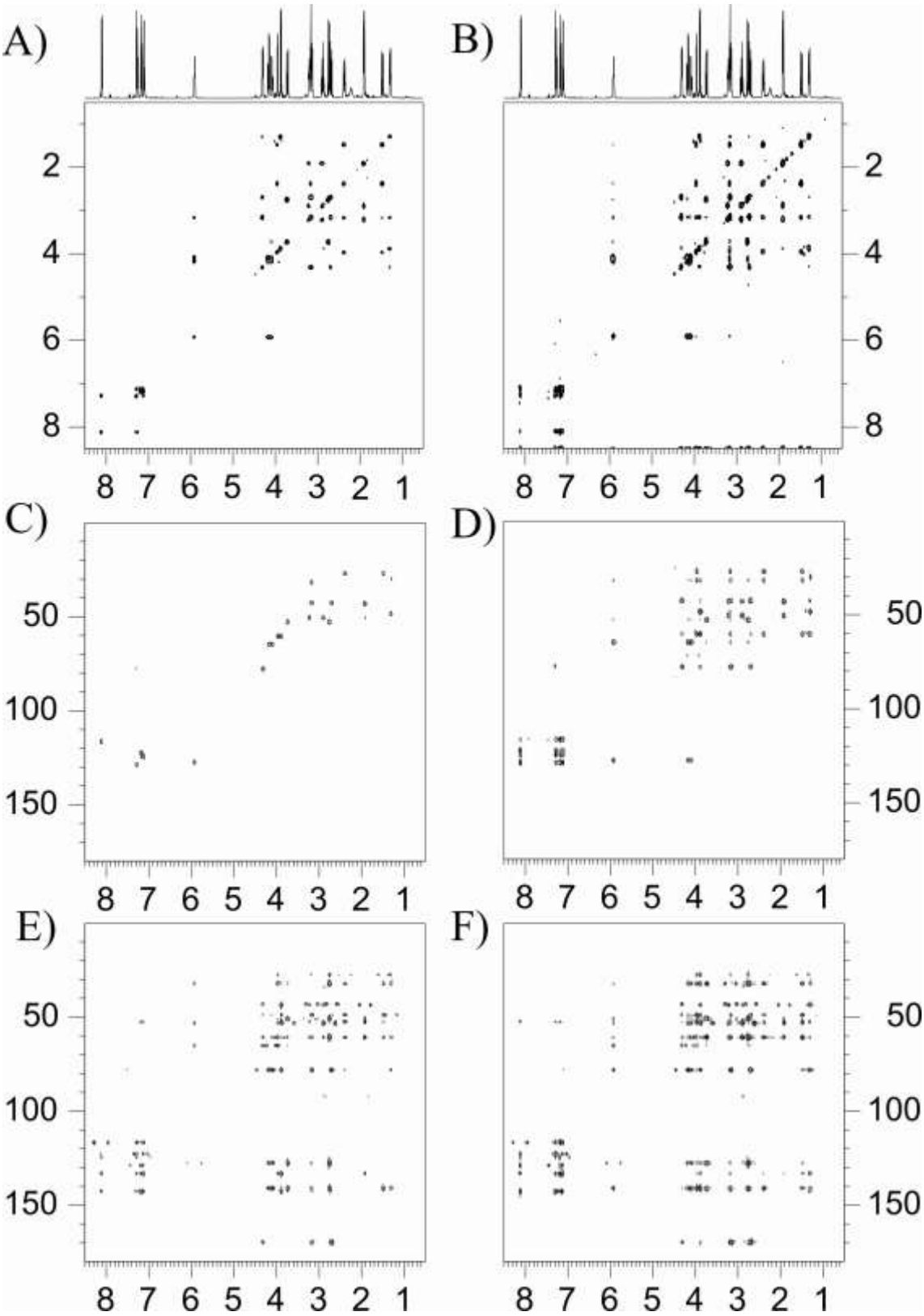

Figure S1: Complementarity between TOCSY-related (60 ms mixing time) versus regular NMR experiments: A) COSY compared to TOCSY; B) HSQC compared to HSQC-TOCSY and C) HSQMBC compared to HSQMBC-TOCSY spectra. The sample is strychnine in $CDCl_3$.

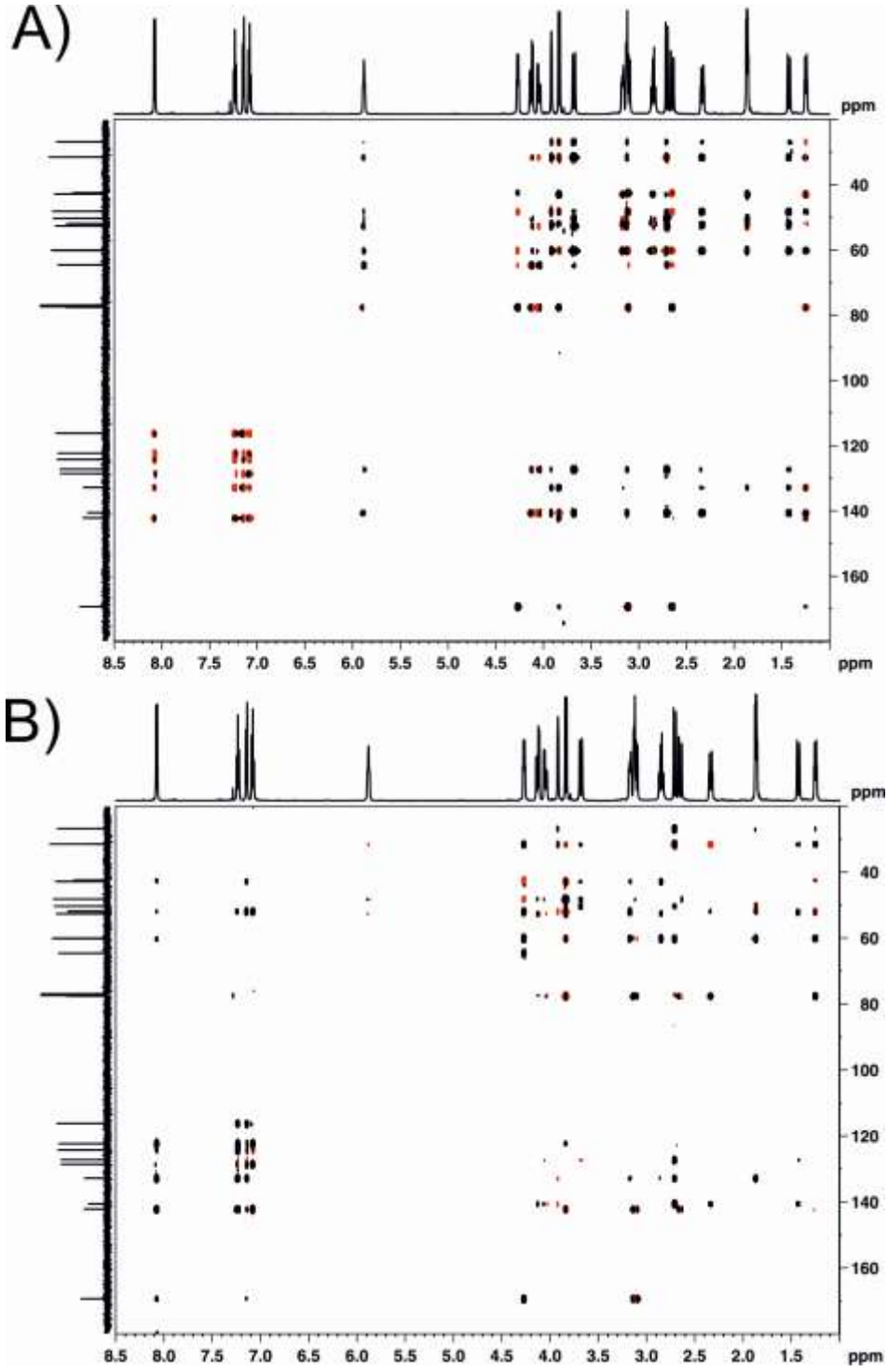

Figure S2: A) HSQMBC-TOCSY and B) LR-HSQMBC spectra of strychnine in $CDCl_3$. For a confidence comparison, both experiments were sequentially recorded in a 1.7mm microcryoprobe using 8 scans per each one of the 128 t_1 increments. The overall acquisition time for each experiment was about 30 minutes.

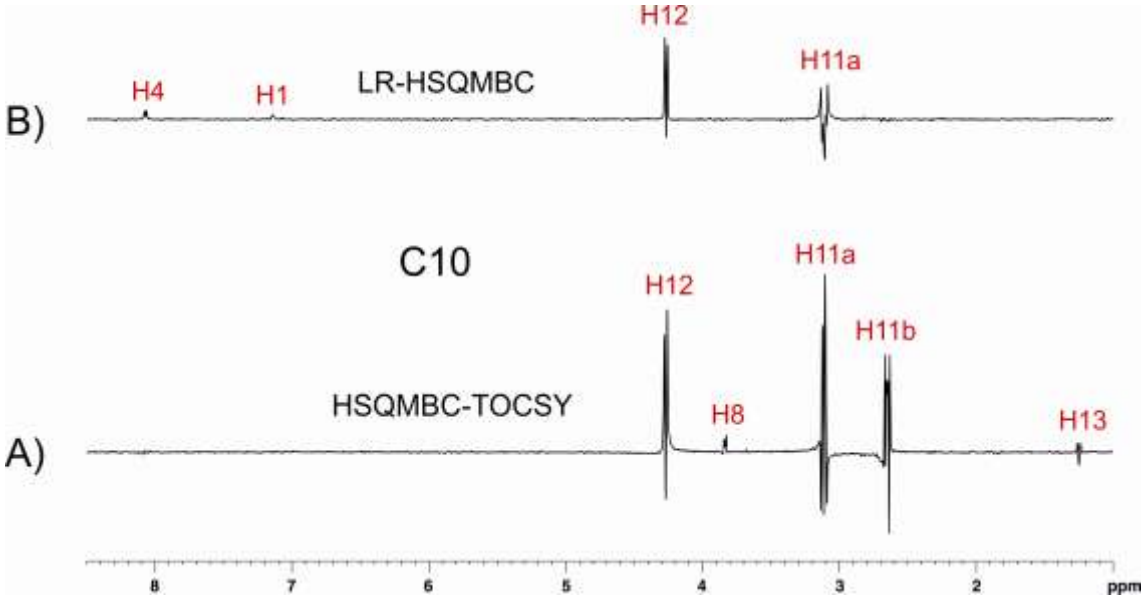

Figure S3: 1D rows extracted at the carbonyl C10 ^{13}C chemical shift from the HSQMBC-TOCSY and LR-HSQMBC spectra of Figure S2. Compare the sensitivity and the complementarity between the two different approaches.

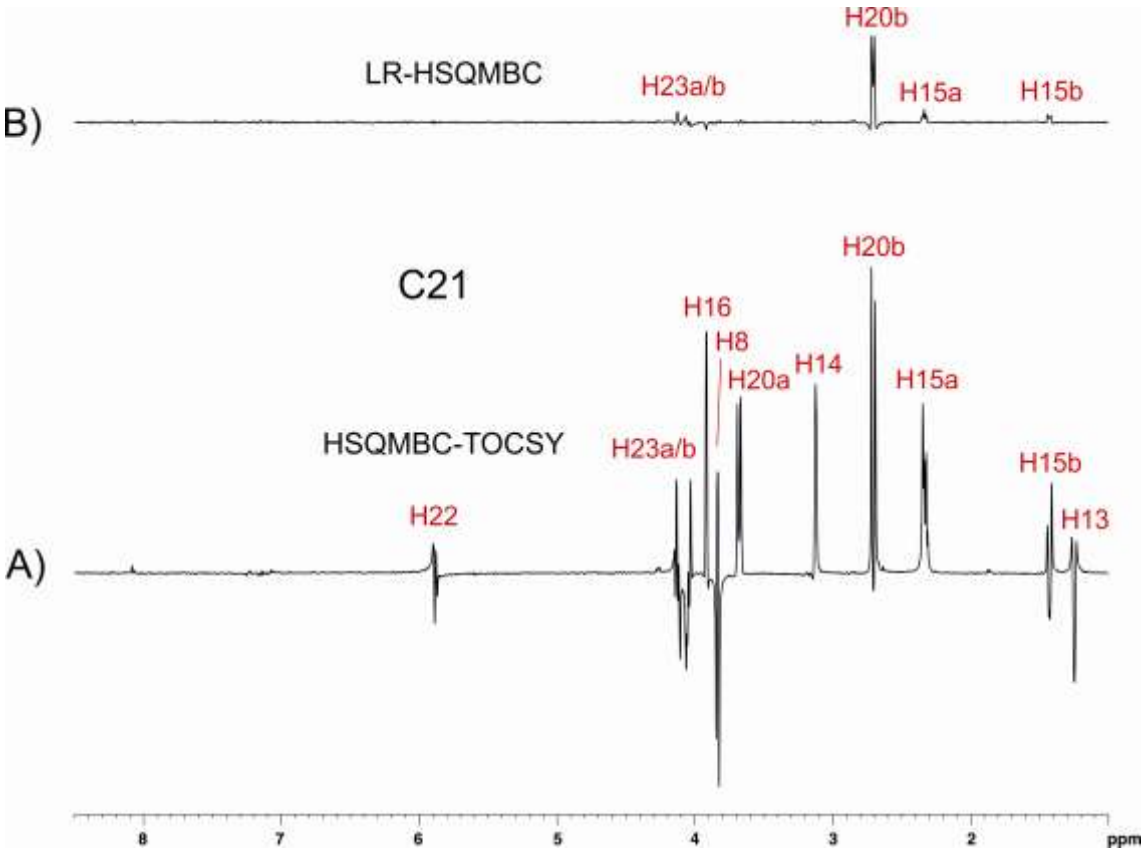

Figure S4: 1D rows extracted at the olefinic C21 ^{13}C chemical shift from the spectra of Figure S2. Compare the sensitivity and the complementarity between the two different approaches.

Table S1: Comparison of long-range heteronuclear responses observed in different NMR experiments performed on quinine, **2**.

	^{2}J	^{3}J	^{4}J	^{5}J	^{6}J	Total $>^{3}J$	Total
HSQC-TOCSY [a]	30	37	30	1	0	31	98
HSQMBC-Refoc [b]	30	50	27	4	1	32	112
HSQMBC-COSY [c]	34	49	37	7	0	44	127
HSQMBC-TOCSY [d]	34	54	49	13	8	71	159

[a] Measured in this work using the pulse sequence of Fig. 1C optimized to 140 Hz and using a mixing time of 60 ms.

[b] Measured in this work using pulse sequence of Fig. 1A optimized to 8 Hz.

[c] Measured in this work using the pulse sequence of Fig. 1B optimized to 8 Hz.

[d] Measured in this work using the pulse sequence of Fig. 1C optimized to 8 Hz and using a mixing time of 60 ms.

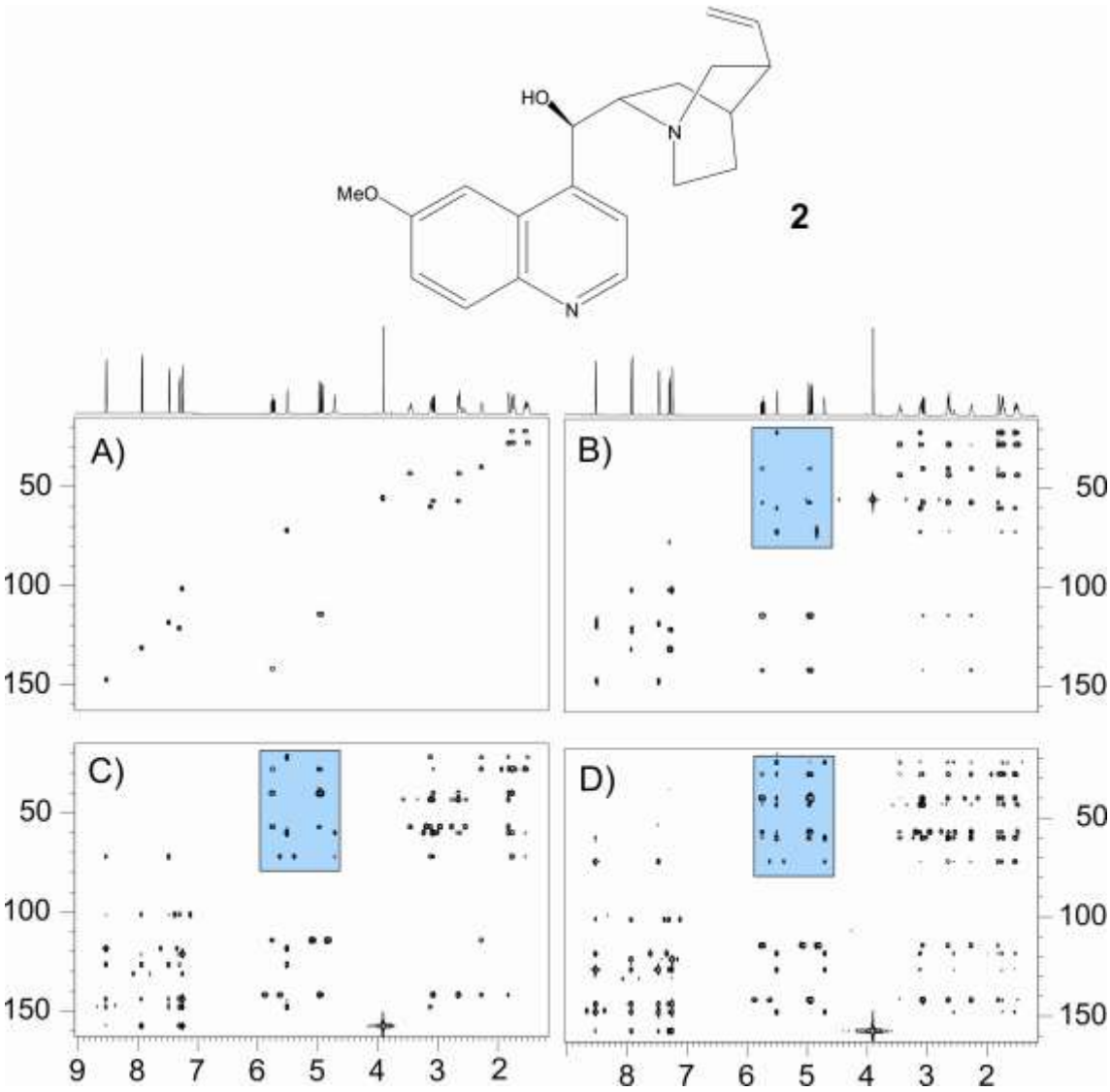

Figure S5: A) HSQC (optimized to 145 Hz), B) HSQC-TOCSY (optimized to 145 Hz and using a mixing time of 60 ms), C) HSQMBC (optimized to 8 Hz) and D) HSQMBC-TOCSY (optimized to 8 Hz and using a mixing time of 60 ms) spectra of quinine (**2**) in $CDCl_3$. See expanded areas in Figure S6.

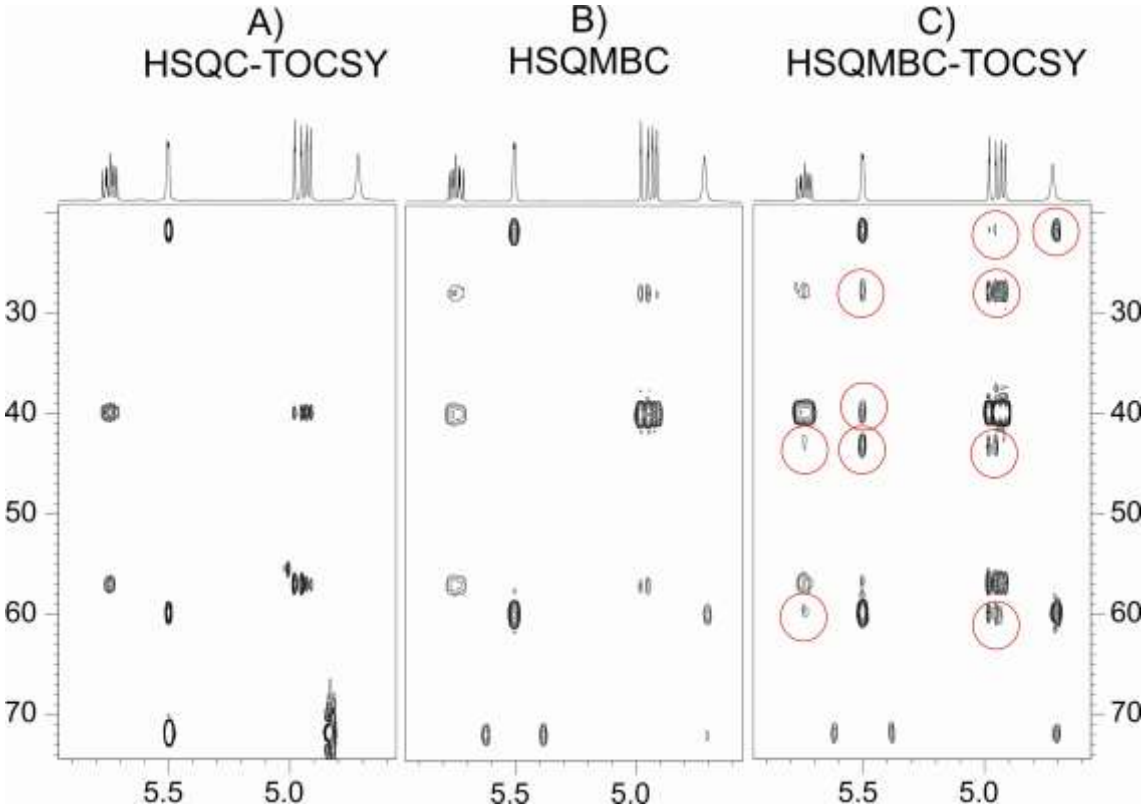

Figure S6: Expanded areas extracted from spectra of Figure S5, corresponding to A) HSQC-TOCSY, B) HSQMBC, and C) HSQMBC-TOCSY experiments of quinine. In C), enhanced cross-peaks are encircled.

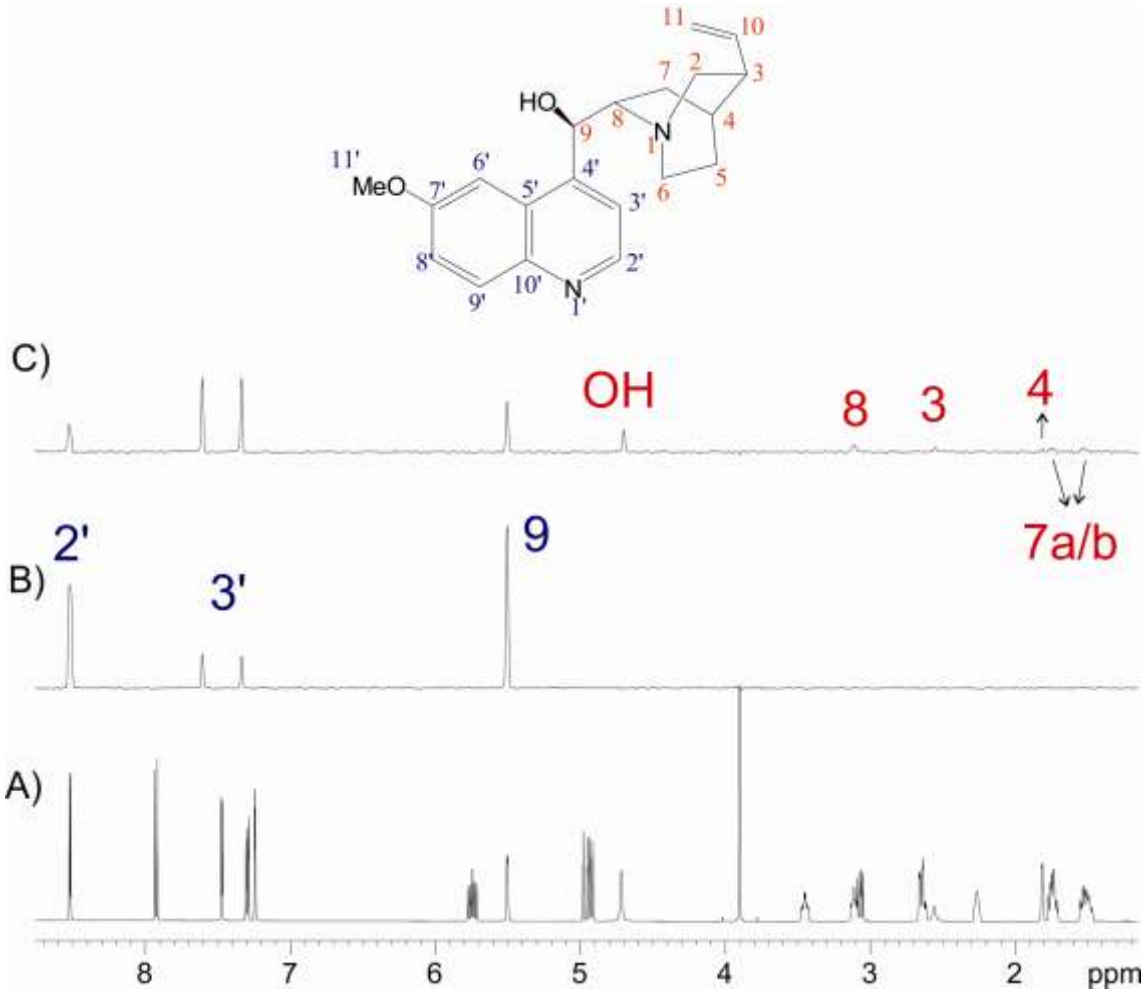

Figure S7: Comparison of 1D slices extracted from the same ^{13}C row at 118.5 ppm (C3') in A) 8 Hz HSQMBC and B) 8 Hz HSQMBC-TOCSY (60 ms) spectra of quinine (as shown in Fig. S5). 16 scans were acquired for each one of the 128 t_1 increments in each experiment. Note that long-range correlations to ^{6}J, ^{7}J and ^{8}J can be observed in C).

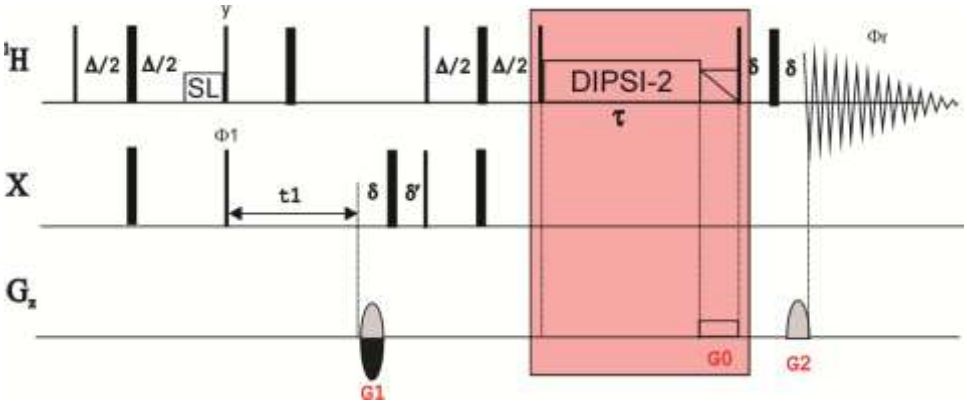

Figure S8: Pulse scheme for the ^{1}H-X PIP-HSQMBC-TOCSY experiment. The delay Δ is set to 1/[2*^{n}J(CH)] and the ZQ-filter after the DIPSI-2 train includes a chirped adiabatic 180° ^{1}H pulse applied simultaneously with a purging G_0 gradient; Broadband heteronuclear decoupling during proton acquisition is optional (not shown).

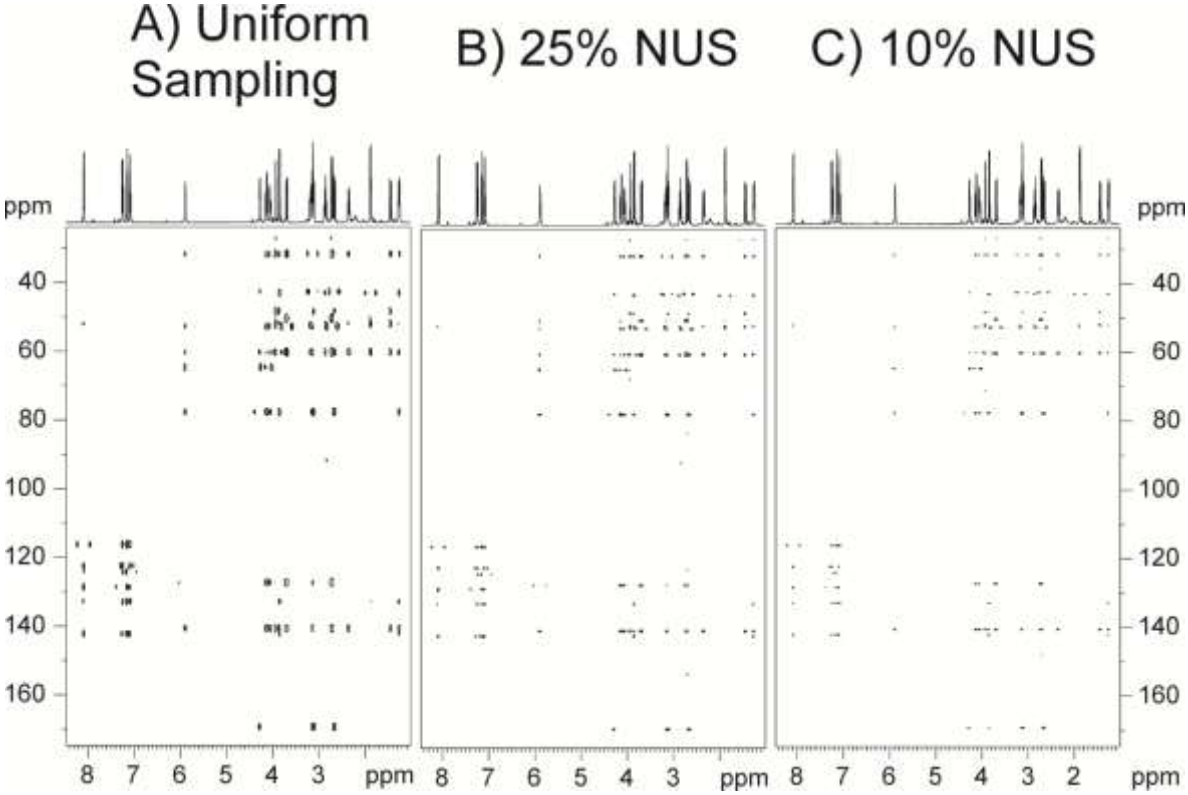

Figure S9: Comparison of 8 Hz optimized HSQMBC-TOCSY spectra of **1** acquired with the same experimental time using A) uniform sampling (128 t_1 increments), B) 25% NUS (512 t_1 increments) and C) 10% NUS (1280 t_1 increments).

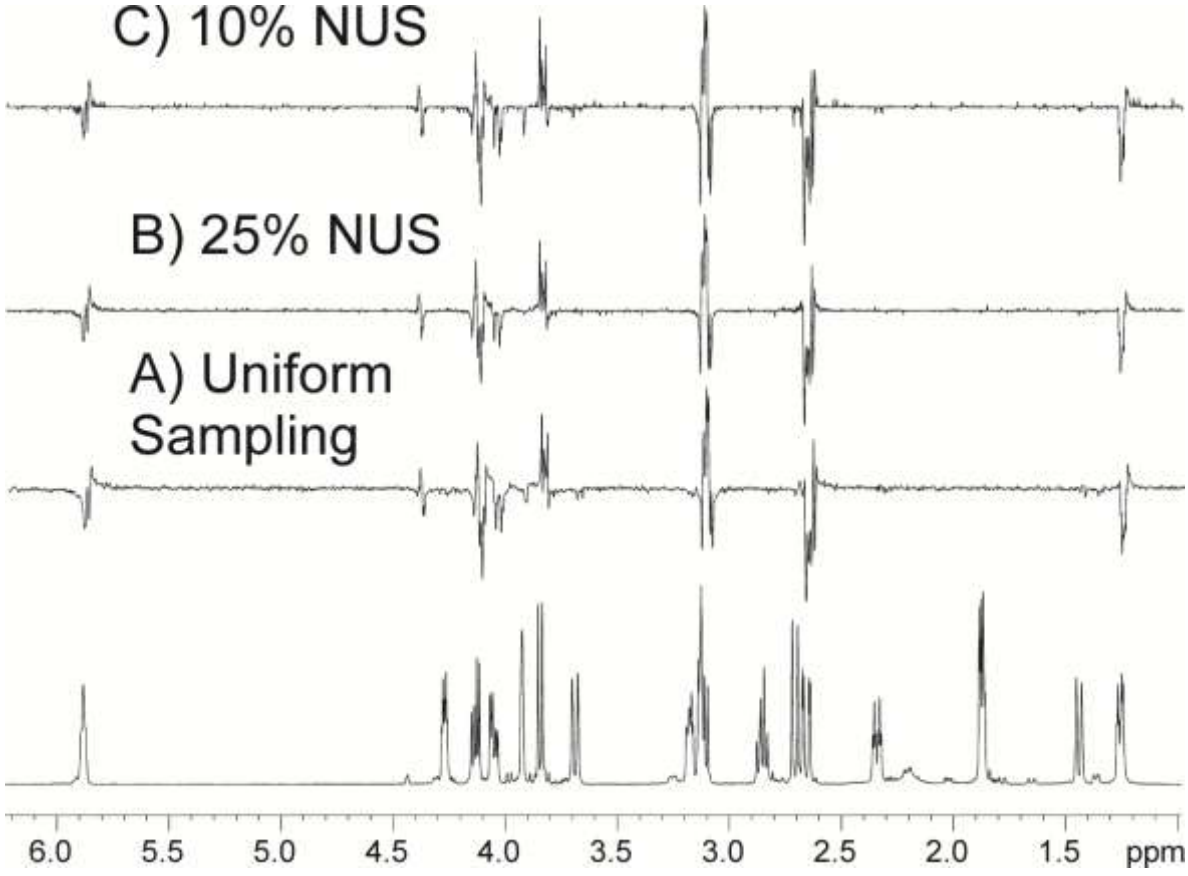

Figure S10: Comparison of 1D slices extracted at the C12 chemical shift from 8 Hz optimized HSQMBC-TOCSY spectra of **1** acquired with B) uniform sampling (128 t_1 increments) and C) 25% NUS and D) 10% NUS (see Figure S9).

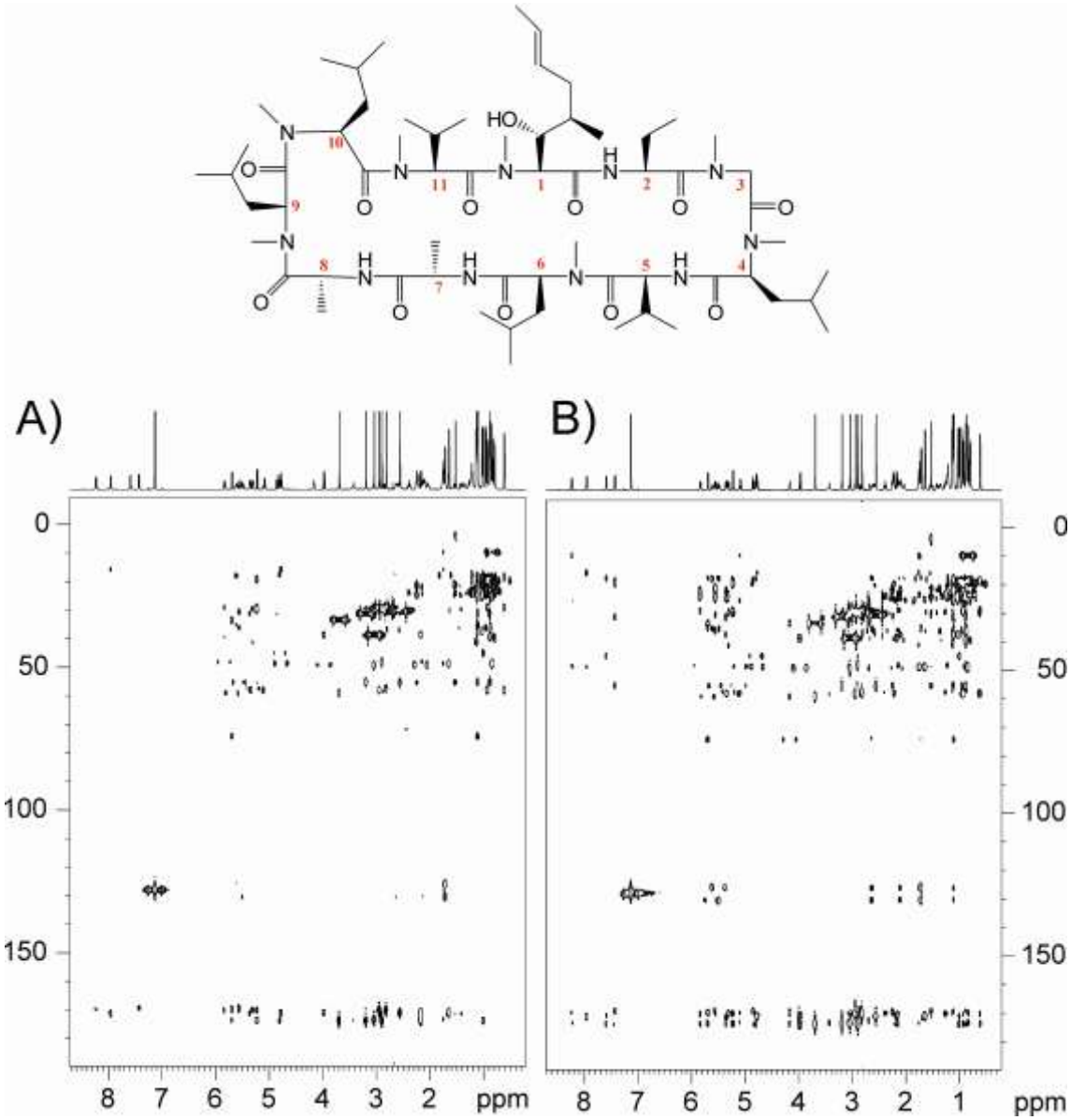

Figure S11: 8 Hz optimized A) HSQMBC and B) HSQMBC-TOCSY (40 ms) spectra of cyclosporine in C_6D_6.

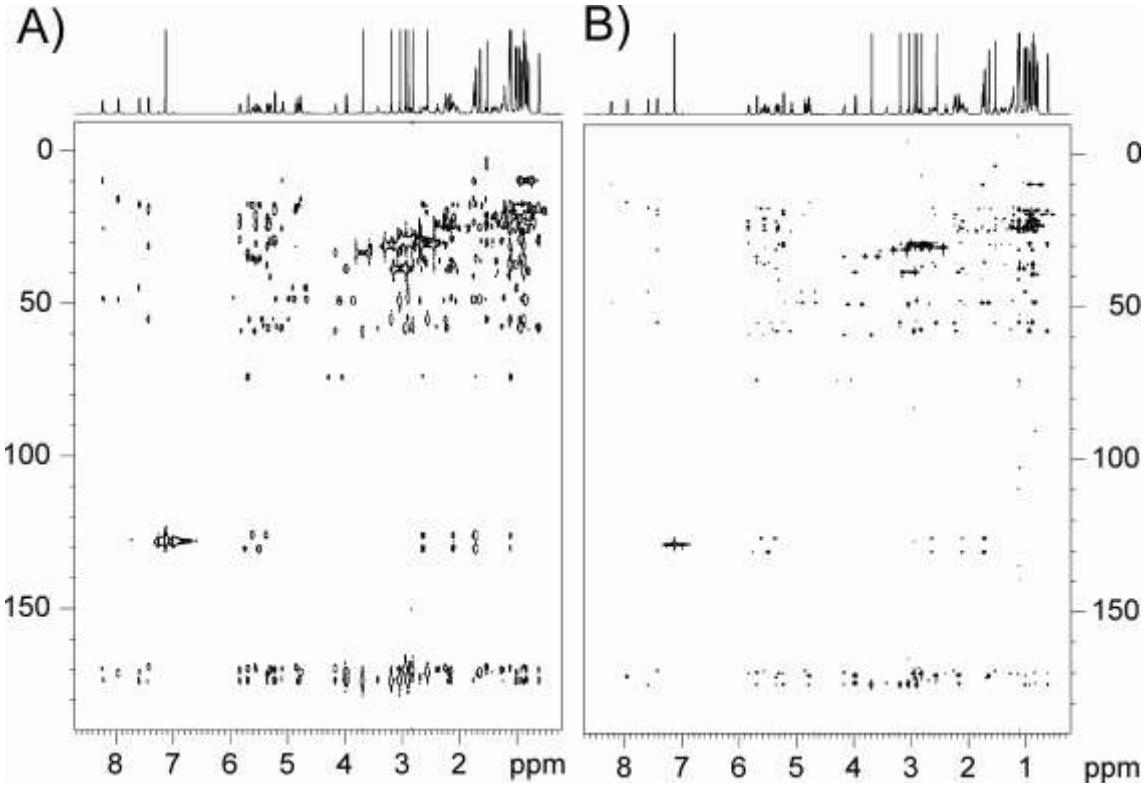

Figure S12: Comparison between a 8 Hz optimized HSQMBC-TOCSY (40 ms) spectra of cyclosporine in C_6D_6 acquired under the same experimental time A) with uniform sampling (128 t_1 increments) and B) with 25% of non-uniform sampling (512 t_1 increments).

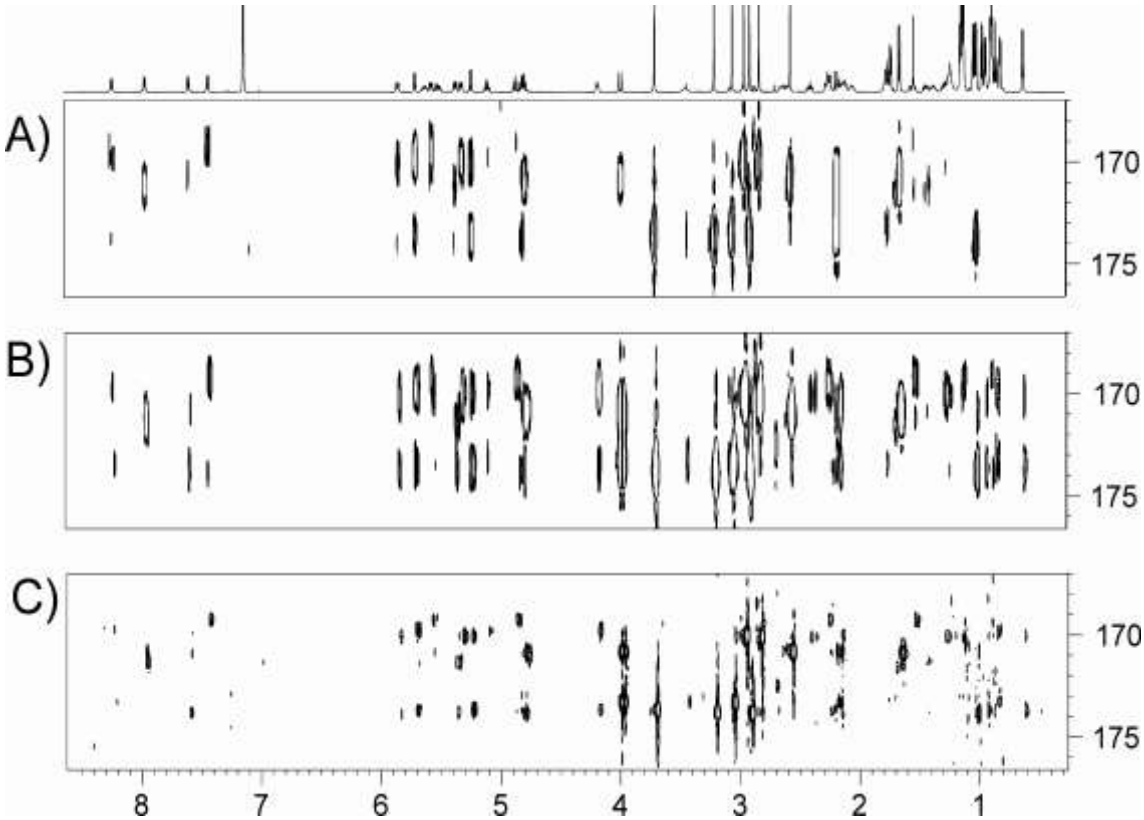

Figure S13: Expansions of the carbonyl region of the 8 Hz optimized A) HSQMBC, B) HSQMBC-TOCSY (40 ms) and C) HSQMBC-TOCSY with 25% NUS spectra of cyclosporine in C_6D_6 acquired with the same experimental times.

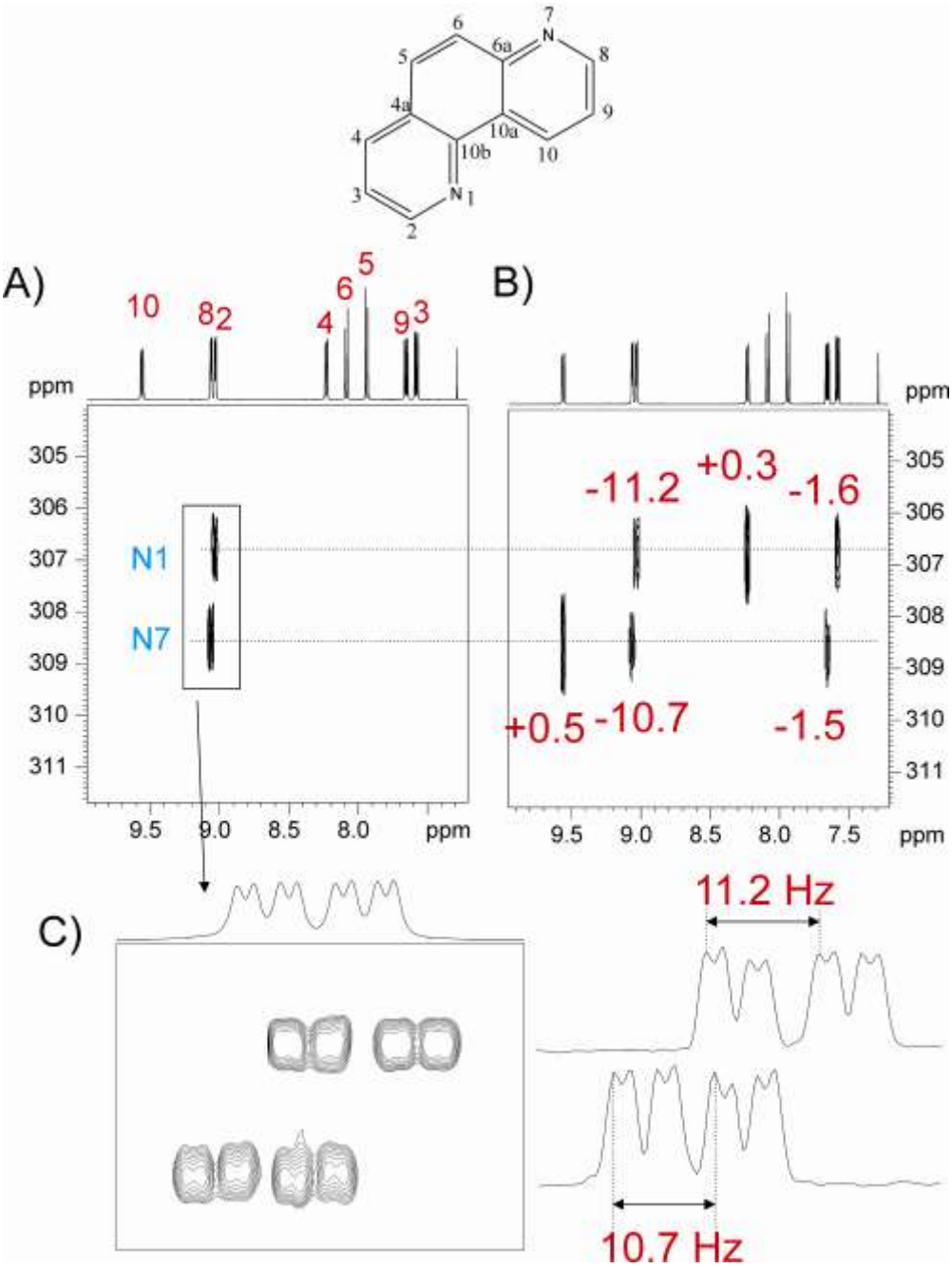

Figure S14: A) PIP-HSQMBC and B) PIP-HSQMBC-TOCSY spectra of 1,7-phenantroline optimized to 12 Hz. Whereas two main cross-peaks corresponding to the ^{2}J(NH) couplings are observed in the standard HSQMBC (see expansion in C)), three- and four-bound NH connectivities are clearly visible in the corresponding HSQMBC-TOCSY spectrum. These long range correlations correspond to coupling values smaller than 1.5 Hz, as confirmed by the IPAP-HSQMBC-TOCSY experiment.

PUBLICATION 2

Title: Ultra high-resolution HSQC: Application to the efficient and accurate measurement of heteronuclear coupling constants

Authors: Marcó, N.; Fredi, A.; Parella, T.

Reference: *Chem. Commun.* **2015**, *51 (15),* 3262–3265.

DOI: 10.1039/C4CC10279G

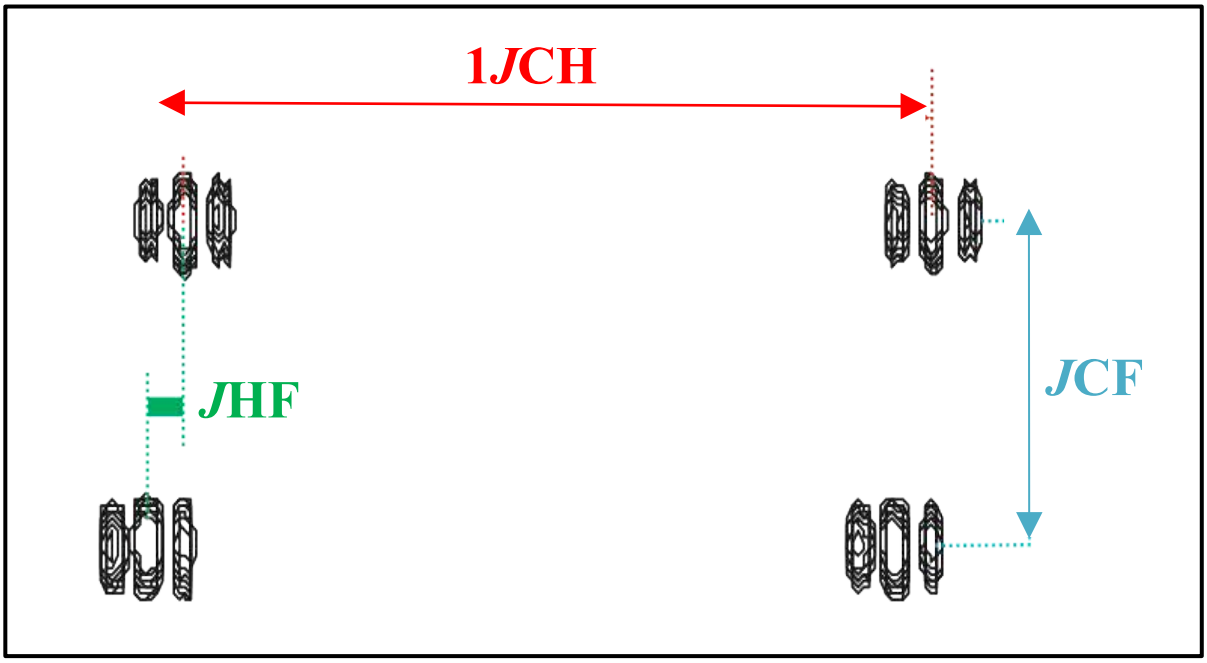

SUMMARY

In the field of NMR, one of the principal aims is obtaining the best available resolution in the least amount of time. Many techniques have been developed over the years to get a desired improved resolution in 2D NMR spectra. Some of the most notorious methods are: i) the reduction of the spectral width to achieve spectral aliasing, ii) the implementation of non-uniform sampling (NUS) to decrease the number of t_1 increments needed for an equal resolution, and iii) the use of broadband homodecoupled or pure-shift techniques in order to simplify multiplet appearance and enhance signal resolution.

Enhanced resolution is fundamental to differentiate hidden signals or to measure couplings with high accuracy. In this publication, it is illustrated how with the simultaneous use of the three resolution-enhanced methods (NUS, spectral aliasing and pure-shift techniques) in a single NMR experiment affords incredible levels of both signal and digital resolution in optimum spectrometer times. It is shown how the resolution achieved allows the measurement, not only of the magnitude, but of the sign of both coupling constants J_{CX} and J_{HX} (being X= ^{19}F, ^{31}P, and ^{2}H) from E.COSY patterns obtained in a fast 2D ultra-high resolved-HSQC spectra. Coupling values smaller than the linewidth can be determined from simplified cross-peaks.

ChemComm

COMMUNICATION

View Article Online
View Journal | View Issue

Cite this: *Chem. Commun.*, 2015, **51**, 3262

Received 23rd December 2014,
Accepted 14th January 2015

DOI: 10.1039/c4cc10279g

www.rsc.org/chemcomm

Ultra high-resolution HSQC: application to the efficient and accurate measurement of heteronuclear coupling constants†

Núria Marcó, André Fredi and Teodor Parella*

A rapid NMR data acquisition strategy in terms of enhanced resolution per time unit for the simple and efficient determination of multiple coupling constants is described. The use of ^{13}C spectral aliasing combined by broadband ^{1}H homodecoupling allows accurate measurements from ultra high resolved 2D HSQC cross-peaks.

Digital resolution and signal resolution are two important concepts in NMR spectroscopy. One of the more critical parameters defining the total acquisition time of a 2D NMR experiment is the number of t_1 evolution times required to achieve a satisfactory digital resolution in its indirect F1 dimension. This is particularly important when analyzing highly congested areas where signal overlap can occur due to the lack of resolution. Many different solutions to improve this limitation have been proposed over the years such as the use of region-selective pulses,[1] spectral-aliasing,[2–8] non-uniform sampling or maximum-entropy reconstruction algorithms,[9] among others. Of these, the use of spectral aliasing plays a particular role for its great simplicity, general application and high efficiency, as demonstrated by the interesting applications reported for kinetic, diffusion and titration NMR studies, in addition to structural characterization of similar compounds or the analysis of highly overlapped spectra and complex mixtures.

In this study, the success in implementing spectral aliasing into routine NMR experiments is expanded by demonstrating its high relevance to the easy measurement of coupling constants from the indirect dimension of 2D HSQC spectra. It also shows its full compatibility with modern pure shift NMR techniques,[10–13] enhancing even more signal dispersion, as recently reported for the determination of small chemical shift differences in enantiodifferentiation studies.[14] The resulting joint effects to combine ^{13}C spectral aliasing in the F1 dimension and broadband ^{1}H homonuclear decoupling in the detected F2 dimension of a 2D HSQC experiment afford ultra high resolved cross-peaks from which the analysis and the extraction of accurate J values become more efficient.

For proof of principle, we illustrate our proposal by measuring the sign and the magnitude of both J(CF) and J(HF) coupling constants in fluorinated compounds from the clean E.COSY pattern obtained in high-resolved HSQC spectra.[15–21] Attempts to measure these couplings from a regular 2D HSQC spectrum frequently encounter the lack of spectral resolution along the F1 dimension. Spectral aliasing is easily achieved by setting a very small ^{13}C spectral width (SW(^{13}C)), and the practical consequence is a tremendous resolution enhancement without any other special requirements such as pulse sequence modification, particular hardware configuration, additional set-up or the need for post-processing tools. For instance, using a conventional SW(^{13}C) of 160 ppm and 128 t_1 increments, a poor digital resolution of 251.5 Hz/Pt is achieved before data processing. Upon reducing SW(^{13}C) to 2 ppm, an improved digital resolution of 3.1 Hz/Pt is automatically achieved which should be equivalent to acquire 10 200 t_1 increments, representing an increased factor in terms of resolution or acquisition time of about 80. As an example, Fig. 1A shows the spectral-aliased HSQC spectrum of 2-fluoropyridine recorded using a 400 MHz spectrometer equipped with a standard broadband probehead. Excellent resolution levels are achieved using SW(^{13}C) of 2 ppm and 128 t_1 increments, within a short experimental time of 7 minutes and without the need for any additional prior calibration or set up. After data processing, the resolution in the F2 and F1 dimensions is 0.5 and 0.2 Hz/Pt, respectively.

Spectral aliasing depends on the quadrature detection mode used in the F1 dimension and, in contrast to the effects associated with spectral folding, the phase properties and the appearance of the E.COSY multiplet structure in the reported HSQC are retained as in the original experiment. Hence, the magnitude and the relative sign between CF and HF couplings can be extracted by a direct and simple analysis of each individual signal. For instance, note the clear splitting and the relative positive/negative slope for all cross-peaks, even for the small couplings of J(C5–F) = +4.4 Hz and J(H5–F) = +2.3 Hz, displayed for the C5–H5 correlation or the small J(H6–F) = −1.1 Hz. All data agree with previously reported results[22] and simple

Servei de Ressonància Magnètica Nuclear, Universitat Autònoma de Barcelona, E-08193 Bellaterra, Barcelona, Spain. E-mail: teodor.parella@uab.cat; Tel: +34 935812291

† Electronic supplementary information (ESI) available: Experimental details and NMR spectra. See DOI: 10.1039/c4cc10279g

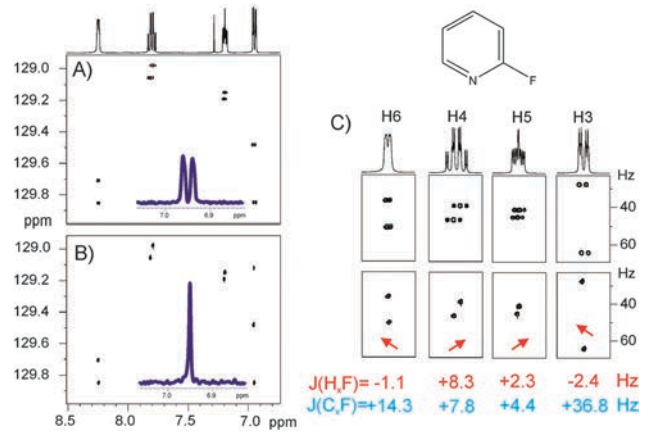

Fig. 1 2D spectral-aliased $^{1}H–^{13}C$ HSQC spectrum of 2-fluoropyridine acquired with a reduced SW(^{13}C) of 2 ppm: (A) without and (B) with broadband ^{1}H homodecoupling in the F2 dimension. (C) Expanded cross-peaks showing the high levels of digitization and signal dispersion achieved for each experiment.

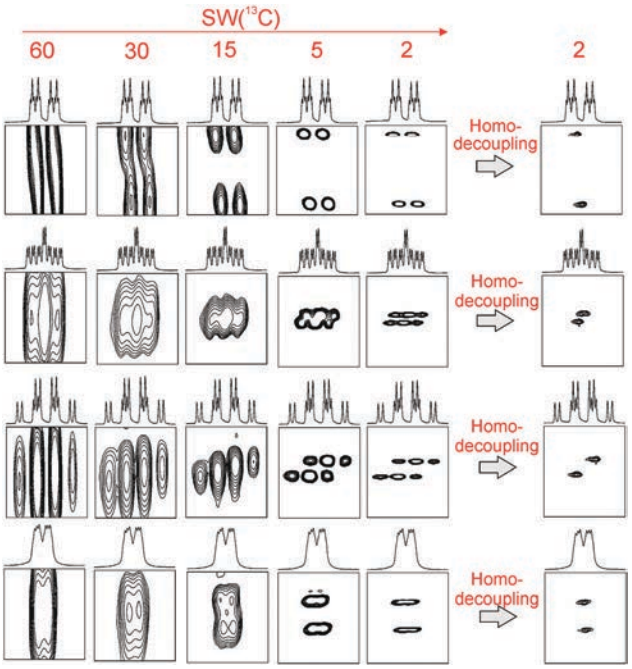

Fig. 2 Experimental effects on signal resolution after reducing SW(^{13}C) in HSQC experiments. In the right column, the additional benefits to add broadband ^{1}H homodeocupling along the detected F2 dimension can be appreciated.

modifications of the basic pulse sequence can offer additional measurements, such as the simultaneous determination of a complete set of magnitudes and signs of ^{1}J(CH), J(FH) and J(FC) coupling constants from a F2-^{13}C-coupled spectral-aliased HSQC spectrum (Fig. S1, ESI†). In these spectra, the observed chemical shift value from signals outside of the active window deviates from its true value due to the extensive signal aliasing. In practice, this is not a problem because the determination of coupling constants is usually performed after a chemical shift assignment process and, therefore, the real chemical shift can be reestablished, if needed, comparing aliased data obtained from a reference HSQC or 1D ^{13}C spectrum,[2] by recording two differently SW(^{13}C)-optimized datasets[2,3,8] or using computer-optimized methods.[4] Anyway, the ambiguity in the incorrect δ(^{13}C) assignment in HSQC spectra is easily resolved because each individual proton yields only a single cross-peak.

Fig. 2 compares the different 2D cross-peak resolutions exclusively as a function of SW(^{13}C), whereas all other experimental parameters remain exactly the same. Clearly, the use of SW(^{13}C) between 2 and 5 ppm resolves most of the coupling patterns. It is also shown how the signal dispersion is further enhanced from the spectral-aliased pure shift HSQC experiment which uses a BIRD-based element for homonuclear decoupling during acquisition[13,14] (see Fig. 1B and the right column in Fig. 2). In addition to the evident simplification of the multiplet structure, a relative sensitivity gain is also achieved by signal collapsing as shown in 1D traces of Fig. 1.

The performance of the experiment has also been verified with albaconazole, a triazole derivative with potent and broad spectrum antifungal activity containing two fluorine atoms in its structure. The advantages of 2D multiplet simplification are visible from the results obtained from the double E.COSY nature of some cross-peaks (Fig. 3). The relative sign and the magnitude of four- and five-bond J(FH) and J(CF) couplings are readily and simultaneously measured. It can be seen how the highly overlapped H-21 and H-23 can be clearly distinguished, allowing the easy measurement of their couplings. In the case of H-23, note the different positive/negative skew observed for their ^{3}J(HF) and ^{5}J(HF) correlations. Note that in the case of the

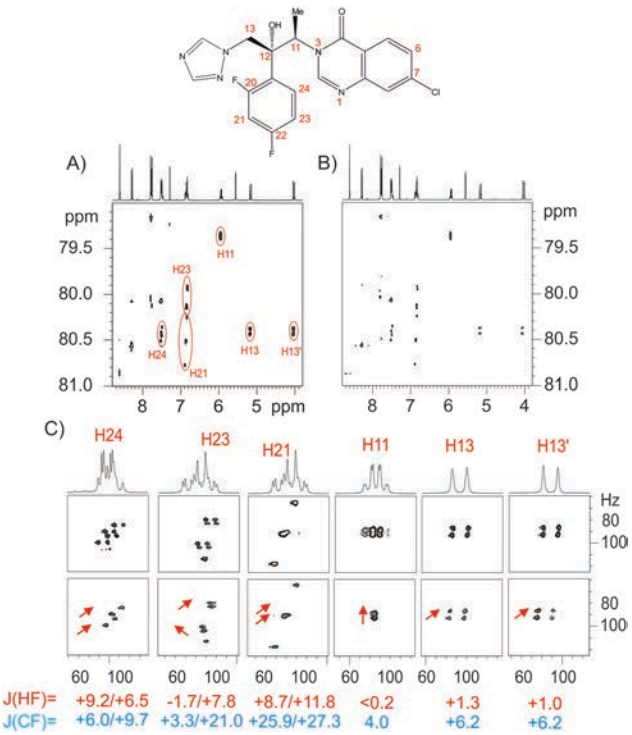

Fig. 3 2D spectral-aliased $^{1}H–^{13}C$ HSQC spectrum of albaconazole acquired with a reduced SW(^{13}C) of 2 ppm: (A) without and (B) with broadband ^{1}H homodecoupling in the detected dimension. (C) Expanded 2D cross-peaks showing the high levels of digitization and signal dispersion for each experiment.

diastereotopic H-13 and H-13′ protons, the geminal ^{2}J(HH) is still observed because BIRD cannot homodecouple these

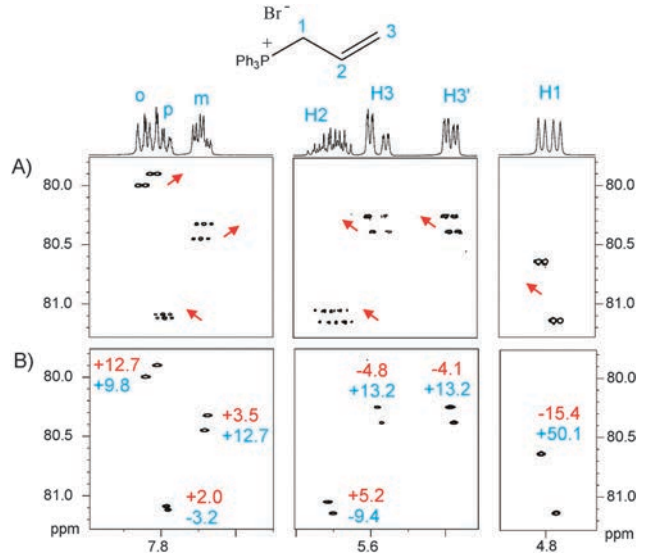

Fig. 4 (A) Spectral-aliased 2D $^{1}H-^{13}C$ HSQC spectrum of allyltriphenylphosphonium bromide acquired with a SW(^{13}C) of 2 ppm. (B) Pure shift version showing ultra simplified cross-peaks. The sign and the magnitude of (top) $J(H_xP)$ and (bottom) $J(C_xP)$ couplings are shown for each cross-peak.

interactions. In these protons, small and positive five-bond ^{5}J(H13–F20) couplings smaller than the line width can be determined, even without being resolved in the conventional ^{1}H multiplet.

A further example involves the measurement of the magnitude and sign of J(CP) and J(HP) in phosphorus-containing molecules (Fig. 4). Previous studies performed these measurements using conventional experiments applying numerous t_1 increments, using scaling J factors along the F1 dimension or by triple resonance $^{1}H/^{13}C/^{31}P$ NMR experiments.[23,24] Note, for instance, the advantageous resolution conditions for the wide and highly complex ^{1}H resonance corresponding to the olefinic H2 proton in allyltriphenylphosphonium bromide, which present an overall multiplet width of 45.9 Hz. The H2–C2 HSQC cross-peak is reduced to an ultra simplified and well resolved two-component E.COSY multiplet pattern with line widths of only 3.5 Hz (Fig. S4, ESI†). It must also be highlighted that ^{4}J(CP) and ^{5}J(PH) are precisely measured. The absolute signs of the involved couplings can be obtained taking a known coupling as a reference cross-peak. In the absence of this reference, a spectral-aliased HSQC-TOCSY experiment can be very helpful because it provides different cross-peaks for the same ^{1}H or ^{13}C peak (Fig. S5, ESI†). Thus, comparison of the skew patterns of all cross-peaks for a determined proton (selected column) or a specific carbon (selected row) can facilitate this determination.

Finally, the method has been applied to a mixture of common deuterated solvents (acetonitrile, acetone, dimethyl sulfoxide, methanol and methylene chloride) for the fast and efficient measurement of J(HD) and J(CD) in residual mono-deuterated isotopomeric derivatives (Fig. 5). The negative slope for all observed cross-peaks confirms the negative sign of the small ^{2}J(HD) couplings, assuming that ^{1}J(CD) is positive. The high precision achieved in the indirect dimension makes these experiments very interesting to obtain H/D and $^{12}C/^{13}C$ isotope effects on both ^{1}H and ^{13}C chemical shifts.

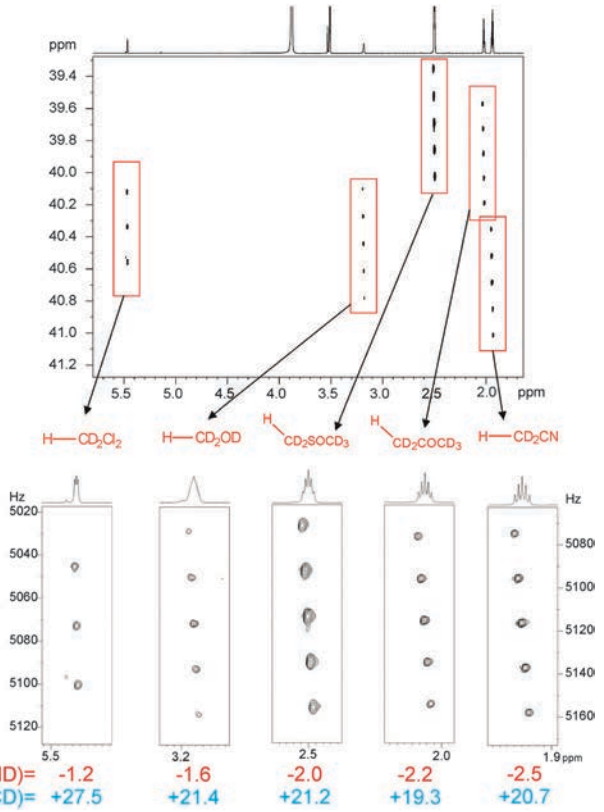

Fig. 5 2D spectral aliased $^{1}H-^{13}C$ HSQC spectrum of a mixture of deuterated solvents acquired with a SW(^{13}C) of 2 ppm. The residual mono-protonated isotopomers are quickly observed in the HSQC spectrum, allowing the fast measurement of ^{2}J(HD) and ^{1}J(CD).

It can be anticipated that spectral aliasing can be extended in a variety of NMR experiments involving J measurement from the F1 dimension of a 2D spectrum. The most obvious applications should be the measurement of the reported J(XH) and J(CX) couplings on non-protonated carbons from spectral aliased HMBC or HSQMBC experiments or the measurement of ^{1}J(CH) along the F1 dimension of F1-coupled HSQC spectra, with particular interest in the measurement of residual dipolar couplings (RDCs) in small molecules dissolved in weakly aligned anisotropic media.[25] Also of interest should be the measurement of long-range proton–carbon coupling constants, as reported for the SJS-HSQC experiment which provide the sign and the magnitude of J(HH) and ^{n}J(CH)[26] (see Fig. S6, ESI†). The feasibility of simplifying multiplet patterns by broadband homodecoupling in this type of experiment is under investigation and will be published elsewhere.

The proposed strategy is far superior to other NMR methods which have been recently introduced to measure the same heteronuclear couplings, some of them require sophisticated pulse sequences with specialized set up, and hardware with special configuration such as triple-resonance hardware capable of performing fluorine detection,[15,16] and others provide only the magnitude of J(HF) couplings[17–20] or/and do not determine the positive/negative sign of the coupling.[19–21] In addition, despite the relative sensitivity losses and the minimum increment of total acquisition time associated with the very narrow SW(^{13}C) and consequently long

evolution times required for the multiple aliasing method (Fig. S2, ESI†), our method offers optimum sensitivity without the important losses associated with other related pure-shift methods. Also, its 2D nature allows it to be used for assignment purposes, avoiding the limitation of signal overlap in 1D NMR methods.

In summary, it has been shown that the superb digital resolution achieved in spectral aliased HSQC experiments allows the easy and simultaneous determination of the magnitude and the sign of J(CX) and J(HX) coupling constants (X = ^{19}F, ^{31}P or ^{2}H). A common feature of spectral aliasing is its general implementation in many routine experiments, even in low field magnets, improving the attainable resolution along the F1 dimension up to two orders of magnitude by a simple change in the ^{13}C spectral width. It has been shown that the gains of introducing aliasing are further improved with the large signal resolution achieved by the collapse of the J(HH) multiplet structure by broadband ^{1}H homodecoupling in the F2 dimension. The resulting 2D cross-peaks exhibit ultra simplified multiplet patterns from which the measurement of the active J values is determined in a straightforward manner. As pointed out already, this general approach introduced in this study can be applicable in many experiments aimed at determining coupling constants with high accuracy. Finally, it should be added that the presented approach is fully compatible with other enhancing methods, such as non-uniform sampling, improving even more the signal resolution obtained per time unit.

Financial support for this research provided by MINECO (project CTQ2012-32436) is gratefully acknowledged. We also thank the Servei de Ressonància Magnètica Nuclear, Universitat Autònoma de Barcelona, for allocating instrument time to this project.

Notes and references

1 W. Willker, U. Flögel and D. Leibfritz, *J. Magn. Reson.*, 1997, **125**, 216–219.
2 D. Jeannerat, *Magn. Reson. Chem.*, 2003, **41**, 3–17.
3 I. Baskyr, T. Brand, M. Findeisen and S. Berger, *Angew. Chem., Int. Ed.*, 2006, **45**, 7821–7824.
4 D. Jeannerat, *J. Magn. Reson.*, 2007, **186**, 112–122.
5 B. Vitorge, S. Bieri, M. Humam, P. Christen, K. Hostettmann, O. Muñoz, S. Loss and D. Jeannerat, *Chem. Commun.*, 2009, 950–952.
6 G. B. B. Njock, D. E. Pegnyem, T. A. Bartholomeusz, P. Christen, B. Vitorge, J.-M. Nuzillard, R. Shivapurkar, M. Foroozandeh and D. Jeannerat, *Chim. Int. J. Chem.*, 2010, **64**, 235–240.
7 A. Cotte, M. Foroozandeh and D. Jeannerat, *Chim. Int. J. Chem.*, 2012, **66**, 764–769.
8 M. Foroozandeh and D. Jeannerat, *ChemPhysChem*, 2010, **11**, 2503–2505.
9 S. G. Hyberts, G. J. Heffron, N. G. Tarragona, K. Solanky, K. A. Edmonds, H. Luithardt, J. Fejzo, M. Chorev, H. Aktas, K. Colson, K. H. Falchuk, J. A. Halperin and G. Wagner, *J. Am. Chem. Soc.*, 2007, **129**, 5108–5116.
10 K. Zangger and H. Sterk, *J. Magn. Reson.*, 1997, **124**, 486–489.
11 J. A. Aguilar, S. Faulkner, M. Nilsson and G. A. Morris, *Angew. Chem., Int. Ed.*, 2010, **49**, 3901–3903.
12 N. H. Meyer and K. Zangger, *ChemPhysChem*, 2014, **15**, 49–55.
13 L. Paudel, R. W. Adams, P. Király, J. A. Aguilar, M. Foroozandeh, M. J. Cliff, M. Nilsson, P. Sándor, J. P. Waltho and G. A. Morris, *Angew. Chem., Int. Ed.*, 2013, **52**, 11616–11619.
14 M. Pérez-Trujillo, L. Castañar, E. Monteagudo, L. T. Kuhn, P. Nolis, A. Virgili, R. T. Williamson and T. Parella, *Chem. Commun.*, 2014, **50**, 10214–10217.
15 K. A. M. Ampt, R. L. E. G. Aspers, P. Dvortsak, R. M. Van Der Werf, S. S. Wijmenga and M. Jaeger, *J. Magn. Reson.*, 2011, **215**, 27–33.
16 R. L. E. G. Aspers, K. A. M. Ampt, P. Dvortsak, M. Jaeger and S. S. Wijmenga, *J. Magn. Reson.*, 2013, **231**, 79–89.
17 J. Saurí, P. Nolis and T. Parella, *J. Magn. Reson.*, 2013, **236**, 66–69.
18 J. F. Espinosa and H. Broughton, *Eur. J. Org. Chem.*, 2013, 6972–6978.
19 S. R. Chaudhari and N. Suryaprakash, *RSC Adv.*, 2014, **4**, 15018–15021.
20 J. A. Aguilar, G. A. Morris and A. M. Kenwright, *RSC Adv.*, 2014, **4**, 8278–8282.
21 M. E. Di Pietro, C. Aroulanda and D. Merlet, *J. Magn. Reson.*, 2013, **234**, 101–105.
22 R. L. Lichter and R. E. Wasylishen, *J. Am. Chem. Soc.*, 1975, **97**, 1808–1813.
23 P. Schmieder, J. H. Ippel, H. van den Elst, G. A. van der Marel, J. H. van Boom, C. Altona and H. Kessler, *Nucleic Acids Res.*, 1992, **20**, 4747–4751.
24 V. V. Krishnamurthy, *J. Magn. Reson., Ser. A*, 1995, **114**, 88–91.
25 C. M. Thiele and W. Bermel, *J. Magn. Reson.*, 2012, **216**, 134–143.
26 P. Trigo-Mouriño, A. Navarro-Vázquez, J. Ying, R. R. Gil and A. Bax, *Angew. Chem., Int. Ed.*, 2011, **50**, 7576–7580.

Supporting Information

Ultra high-resolution HSQC: Application to the efficient and accurate measurement of heteronuclear coupling constants

Núria Marcó, André Fredi, and Teodor Parella*

Table of contents

Experimental Section

NMR experiments were acquired on a Bruker AVANCE spectrometer (Bruker BioSpin, Rheinstetten, Germany) operating at 400.13 MHz proton frequency, equipped with a 5 mm BBOF probe and a z-axis pulsed field gradient accessory (maximum strength of 53.5 G/cm). All spectra were collected on 20 mg of sample (2-fluoropyridine, 2,3-difluoropyridine, albacanazole and allyltriphenylphosphonium bromide) dissolved in 0.6 ml of $CDCl_3$ at a temperature T = 298 K, and processed with the software TOPSPIN 3.1. The sample for measuring J(CD) and J(HD) was prepared mixing 120µl of commercial acetonitrile-d_3 (99.80%), acetone-d_6 (99.80%), DMSO-d_6 (99.80%), methanol-d_4 (99.80%) and CD_2Cl_2 (99.90%).

The non-selective 180º ^1H pulses were of 12.5µs duration. The 2D ^1H-^{13}C HSQC spectra were acquired using the pulse sequence hsqcetgpsi (Bruker's library) and optimized to 140-160 Hz ($\Delta=1/(2*J_{CH})$) depending of the sample (see A+C below). Two scans were collected for each of the 128 t_1 values with 2048 complex points in the corresponding FID. Data were transformed with a shifted sine window function along both the F1 and F2 dimensions and with a zero-filling to 1K in F1. The total experimental time was about 7 minutes for each 2D spectrum. The analog pure-shift HSQC spectra were collected under the same experimental conditions as described in ref. 14 (see A+C below). Broadband homodecoupling during acquisition was achieved applying 130 loops (n) with τ=8-10 ms.

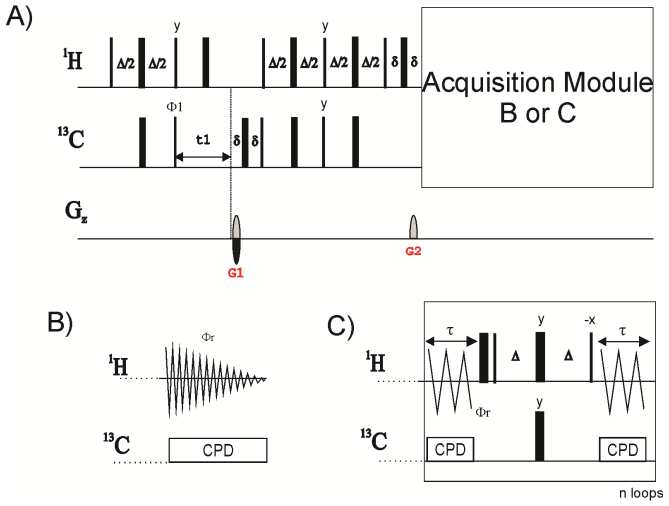

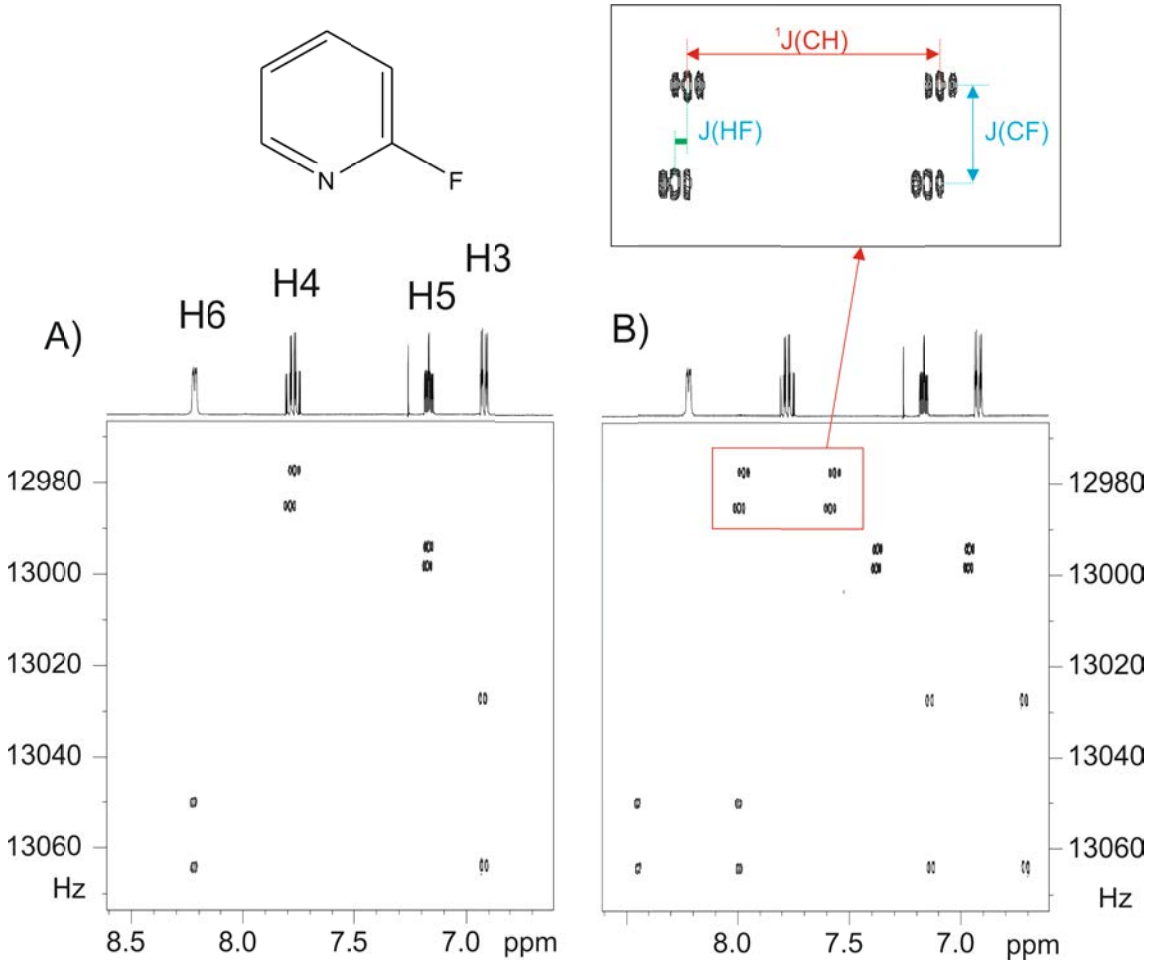

Figure S1: Spectral-aliased HSQC spectrum of 2-fluoropyridine, acquired A) with and B) without broadband ^{13}C heteronuclear decoupling during acquisition. From this latter dataset, a complete set of magnitudes and signs of $^{1}J(CH)$, J(FH) and J(FC) coupling values can be simultaneously measured from each individual high-resolved cross-peak. A SW(^{13}C) of 2 ppm was recorded using 128 t_1 increments, as described in Fig. 2 of the main manuscript.

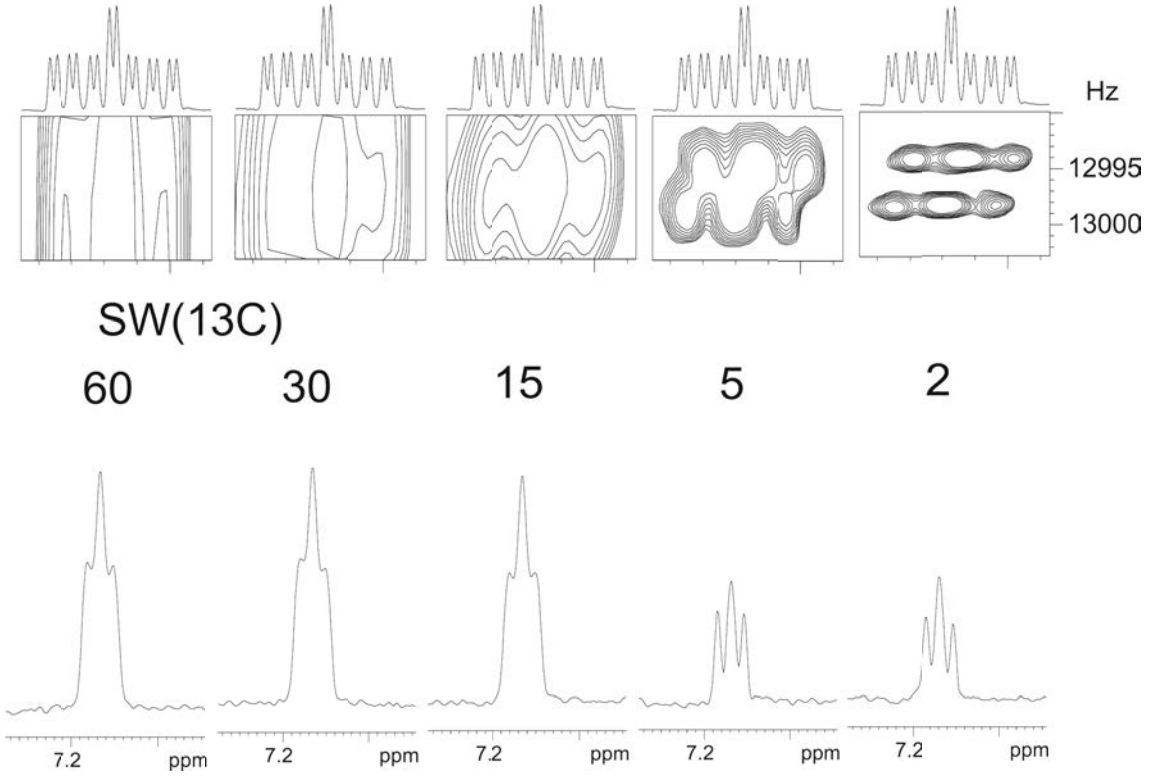

Figure S2: Experimental effects on the 2D signal resolution and sensitivity after reducing the ^{13}C spectral width from 60 to 2 ppm. In the lasts 1D slices (5 and 2 ppm), sensitivity is decreased by a factor of 2 because the corresponding cross-peak are resolved along the F1 dimension in two differentiated components.

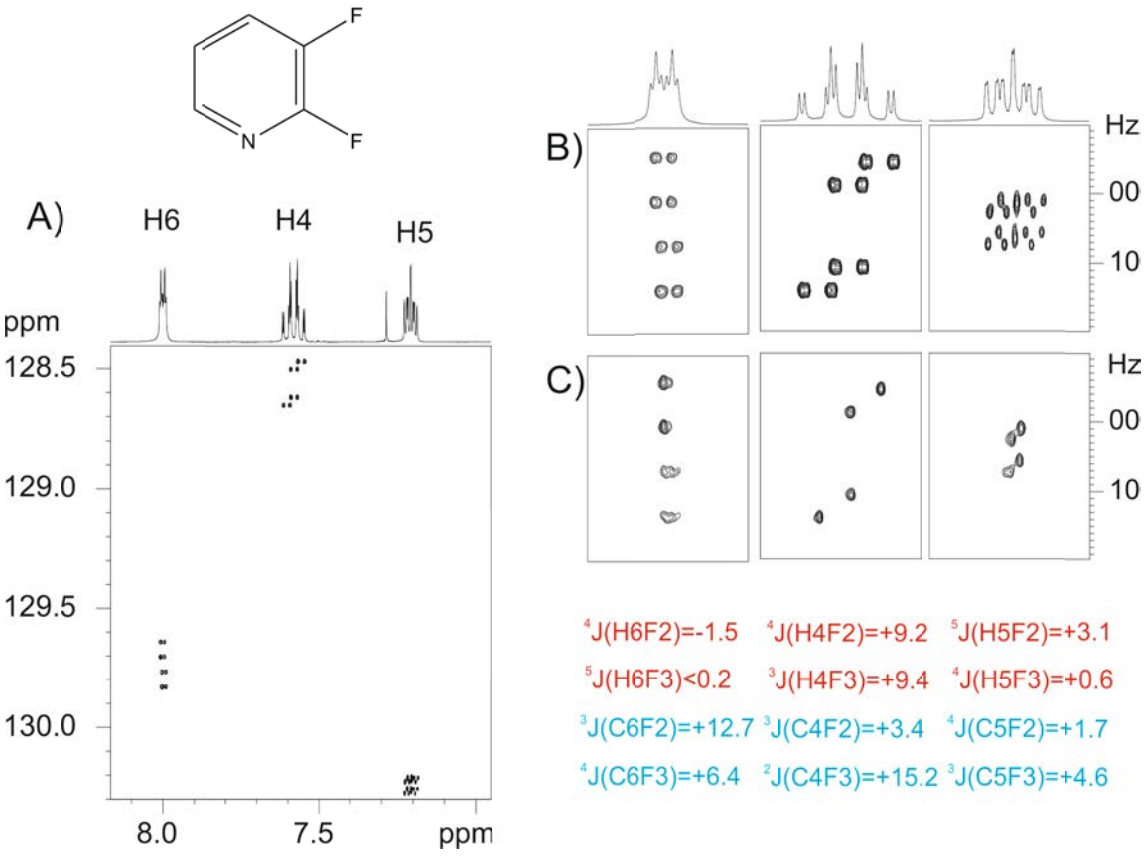

Figure S3: 2D ^{1}H-^{13}C HSQC spectrum of 2,3-difluoropyridine acquired with SW(^{13}C)= 1 ppm and 128 t_1 increments.

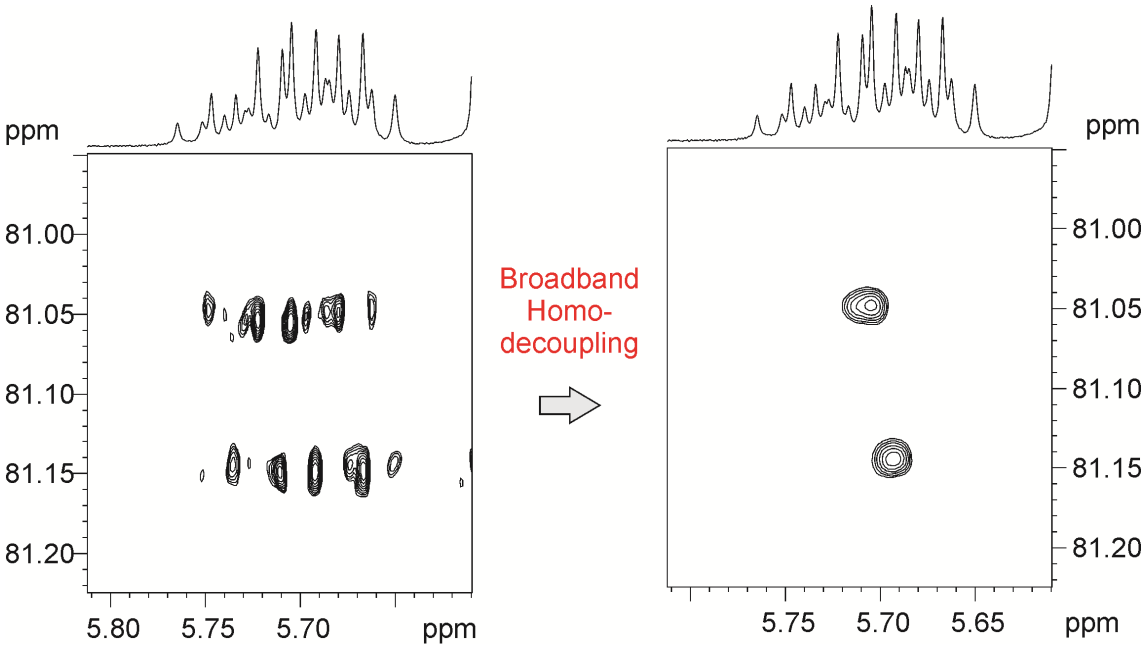

Figure S4: Expansion extracted from spectral aliased spectra of Fig. 4 showing the enhanced signal simplification and dispersion achieved by applying broadband homonuclear decoupling. The cross-peak corresponds to the H2 proton of allyltriphenylphosphonium bromide.

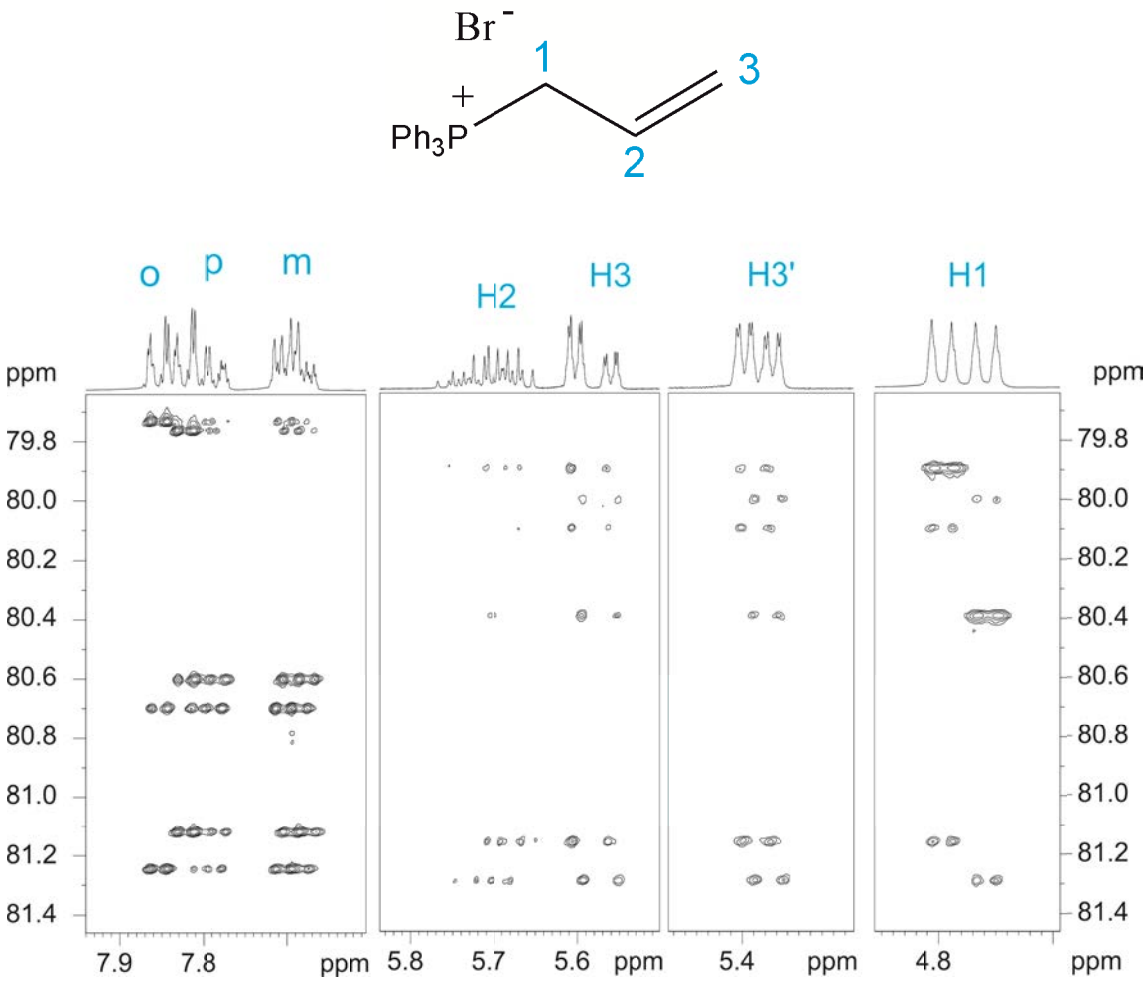

Figure S5: Spectral aliased ^{1}H-^{13}C HSQC-TOCSY of of allyltriphenylphosphonium bromide acquired with a SW(^{13}C) of 2 ppm. Mixing time= 60 ms and number of scans of 16 per t_1 increment. Whereas the analysis of the positive/negative slope of a single cross-peak only provides information about if the involved couplings have the same or opposite sign, the analysis of the positive/negative slope for a set of cross-peaks into the same column (they have the same J(HP) coupling) or the same row (they have the same J(CP)) help in the absolute determination of the positive/negative sign of the involved couplings.

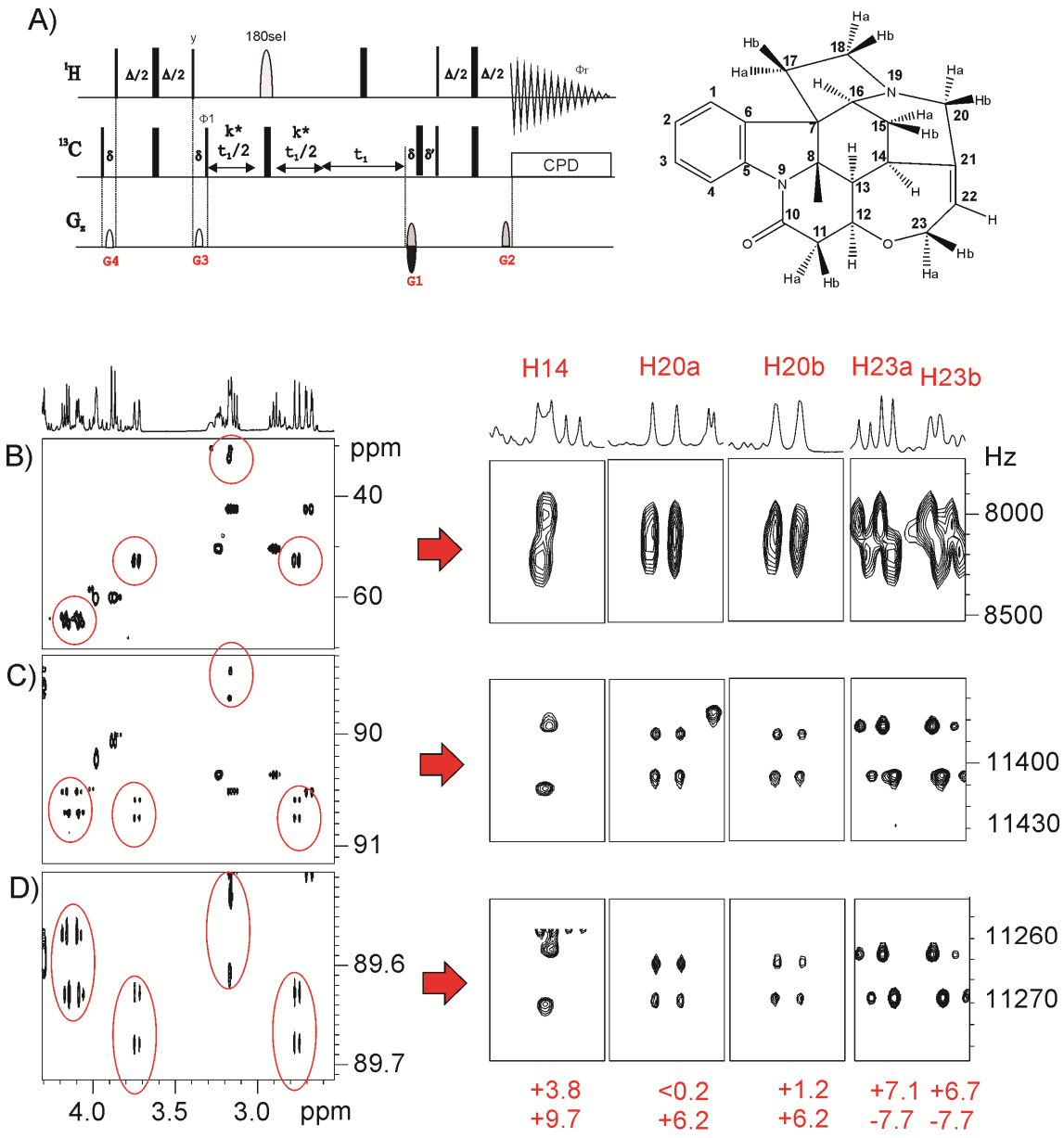

Figure S6: 2D ^{1}H-^{13}C SIS-J-HSQC spectra after selective excitation of the H22 proton (20 ms Gaussian) on a degradated sample of strychnine in CDCl3. A) Standard experiment recorded with SW(^{13}C)=160ppm, TD1=128w and J-scaling=20; B) SW(^{13}C) reduced to 5 ppm and J-scaling=3; C) SW(^{13}C) reduced to 1 ppm and without J-scaling. The E.COSY pattern provides the sign and the magnitude of J(H_x-H22) and ^{n}J(C_x-H22) between the excited proton (passive spin-H22) and the observed CH cross-peak.

PUBLICATION 3

Title: Isotropic/Anisotropic NMR Editing by Resolution-Enhanced NMR Spectroscopy

Authors: Marcó, N.; Gil, R. R.; Parella, T.

Reference: *ChemPhysChem* 2018, in press.

DOI: 10.1002/cphc.201800094

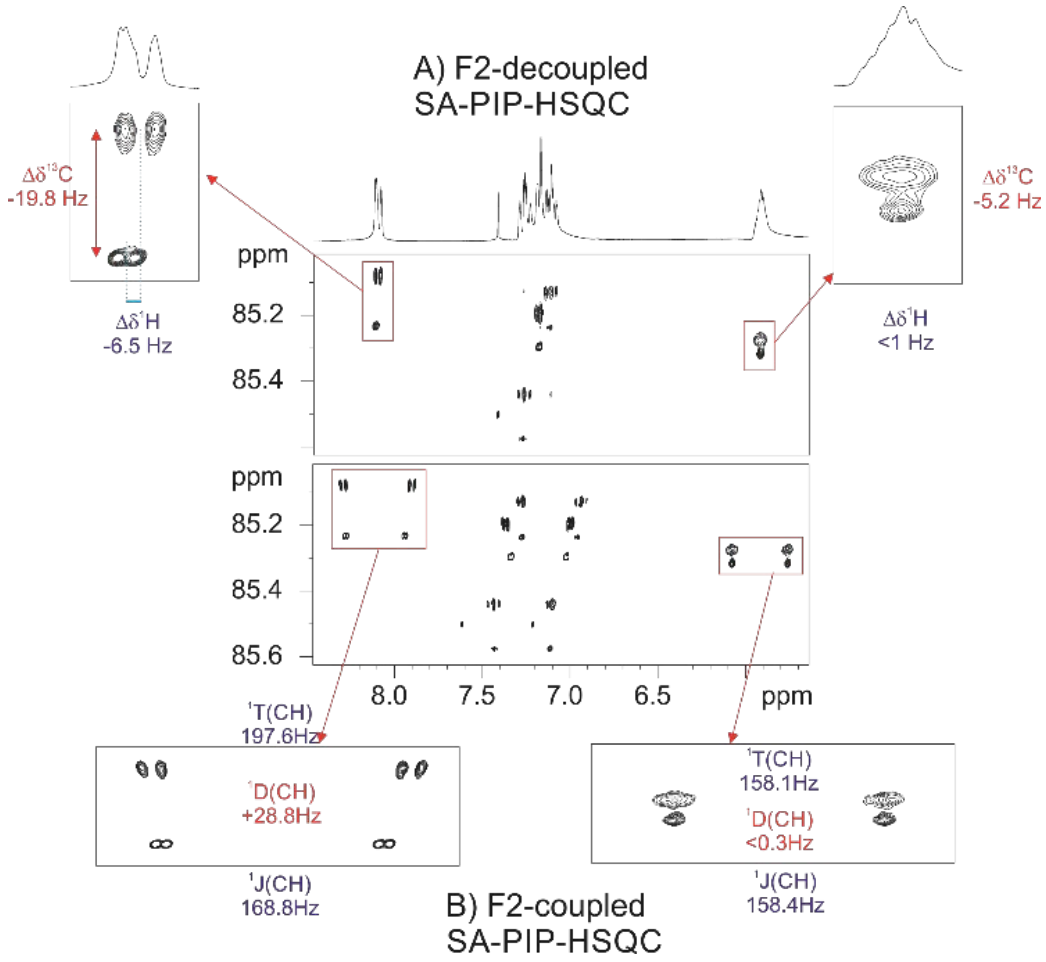

SUMMARY

The two most powerful parameters in the field of the 3D structure determination by weakly alignment NMR spectroscopy are RDCs and RCSAs. In this publication, it is reported the simultaneous measurement of $\Delta\delta(^{1}H)$, $\Delta\delta(^{13}C)$, $^{1}T_{CH}$ and $^{1}J_{CH}$ and consequently RDCs and RCSAs for each available cross-peak. They can be determined in a high-resolved, sign-sensitive, spectral-aliased, pure in-phase HSQC (SA-PIP HSQC) experiment using a PMMA gel as the weakly alignment media. With this implementation, the annoying anti-phase contributions of large ^{1}H-^{1}H coupling constants are avoided guaranteeing the accuracy of the measurement.

As RCSA measurement only needs the variation in the chemical shift, not the chemical shift per se, the loss of the real ^{13}C chemical shift information produced by the spectral aliasing does affect the results.

The high sensitivity of that experiment, similar to the common HSQC, makes it ideal in the case of diluted samples.

ChemPubSoc Europe

DOI: 10.1002/cphc.201800094

CHEMPHYSCHEM Communications

Isotropic/Anisotropic NMR Editing by Resolution-Enhanced NMR Spectroscopy

Núria Marcó,[a] Roberto R. Gil,[b] and Teodor Parella*[a]

Modern resolution-enhanced NMR techniques can monitor the in situ discrimination of co-existing isotropic and anisotropic contributions of small molecules dissolved in weakly aligning PMMA/CDCl3 media. The simultaneous sign-sensitive determination of accurate $\Delta\delta^{iso-aniso}(^1H)$, $\Delta\delta^{iso-aniso}(^{13}C)$ and/or isotropic $^1J_{CH}$ and anisotropic $^1T_{CH}$ coupling constants (and consequently ^1H-^{13}C residual dipolar couplings and $^1H/^{13}C$ residual chemical shift anisotropies) can be performed from spectral-aliased heteronuclear single-quantum correlation spectra.

Anisotropic NMR parameters such as residual dipolar couplings (RDCs), residual chemical shift anisotropies (RCSAs) and residual quadrupolar couplings (RQCs) have proven to provide valuable structural information for small molecules and natural products dissolved in appropriate partially aligning media. One-bond proton-carbon RDCs ($^1D_{CH}$) have become the most effective tools for a reliable one-shot determination of multiple relative configurations.[1–5] On the other hand, the complementary use of other interesting restraints such as geminal proton–proton ($^2D_{HH}$)[6] and long-range proton-carbon ($^nD_{CH}$)[7,8] RDCs as well as ^{13}C RCSAs[9–13] have shown a more limited but not less useful application. Very recently, the benefits to combining computer-assisted structural elucidation (CASE) programs and density functional theory (DFT) calculations in exclusive concert with RDCs and/or RCSAs opens exciting perspectives for the automatic and efficient structural discrimination of challenging molecular structures without the need of the classical scalar *J* couplings or NOEs.[14–16] In contrast to the isotropic (iso) *J* and chemical shifts (δ^{iso}), anisotropic (aniso) RDCs and RCSAs constraints show a strong dependence on the type, nature, and level of molecular alignment of the sample to be analysed, and therefore their accurate determination and reproducibility represent an important, challenging task.

Experimentally, the magnitude and, above all, the sign of RDCs or RCSAs can be determined by comparing two independent measurements in two separate isotropic versus anisotropic samples or at two different alignment conditions. A primary experimental concern is the equivalence between the iso and aniso sample conditions besides to the possible experimental errors induced between the two different measurements. Also, when trying to measure RDCs/RCSAs, sample homogeneity and the absence of isotropic contributions in the anisotropic sample should be minimised to avoid additional errors in the measurement. Thus, the extraction of multiple NMR parameters using a single sample (similar experimental conditions) and from a single measurement should be highly advantageous. Contrary to the general opinion that the presence of the isotropic contribution represents a nuisance, the synchronised determination of both scalar ^1J(CH) and total ^1T(CH) in a single NMR spectrum was initially demonstrated using a DMSO-compatible cross-linked poly(2-hydroxyethyl methacrylate) (poly-HEMA) aligning gel. In such conditions, sizeable ^1H chemical shift dispersions between iso and aniso components ($\Delta\delta = \delta^{iso}$-$\delta^{aniso}$) around 0.1 ppm (≈50 Hz at 500 MHz) could be observed in a *J*SB-HSQC spectrum.[17] These simultaneous *J*/*T* measurements have been further refined in more extreme sample conditions showing smaller magnetic susceptibility differences, such as found in poly(methyl methacrylate) PMMA/$CDCl_3$ media,[3,18] in where more optimal analytical conditions due to the relatively longer T_2 relaxation times and narrower signals are often available.[19–21] In this Communication, a step forward is introduced by extending this optimal, direct recording of ^1H-^{13}C RDCs at the same time that $\Delta\delta(^1H)$ and $\Delta\delta(^{13}C)$ are also detected in molecules dissolved in PMMA/$CDCl_3$ gels. Initially, both isotropic (outside the gel) and anisotropic (inside the gel) contributions are quickly monitored analysing the solvent signal by ^2H NMR. NMR spectra acquired in the fully relaxed media ($\Delta\nu_Q = 0$) can be used as a reference to assign the isotropic contribution to the anisotropic sample. Increasing the compression, the ratio iso/aniso is progressively decreased until that $\Delta\nu_Q$ values about 30–35 Hz prove to give

Table 1. Correlation between NMR experiments and isotropic/anisotropic NMR parameters.

NMR Experiment	Indirect dimension	Detected dimension
1D PSYCHE		$\Delta\delta(^1H)$
1D $^{13}C\{1H\}$		$\Delta\delta(^{13}C)$
2D spectral-aliased PIP-HSQC	$\Delta\delta(^{13}C)$	$\Delta\delta(^1H)$
2D spectral-aliased PIP-HSQC without ^{13}C-decoupling	$\Delta\delta(^{13}C)$	$\Delta\delta(^1H)$ ^1J(CH) ^1T(CH)
2D *J*-resolved HSQC	^{1}J(CH);^{1}T(CH)	$\Delta\delta(^1H)$

[a] *N. Marcó, Dr. T. Parella*
Servei de Ressonància Magnètica Nuclear
Universitat Autònoma de Barcelona
08193, Bellaterra, Catalonia (Spain)
E-mail: teodor.parella@uab.cat

[b] *Prof. Dr. R. R. Gil*
Department of Chemistry
Carnegie Mellon University
Pittsburgh, 15213PA (USA)

Supporting Information and the ORCID identification number(s) for the author(s) of this article can be found under: https://doi.org/10.1002/cphc.201800094.

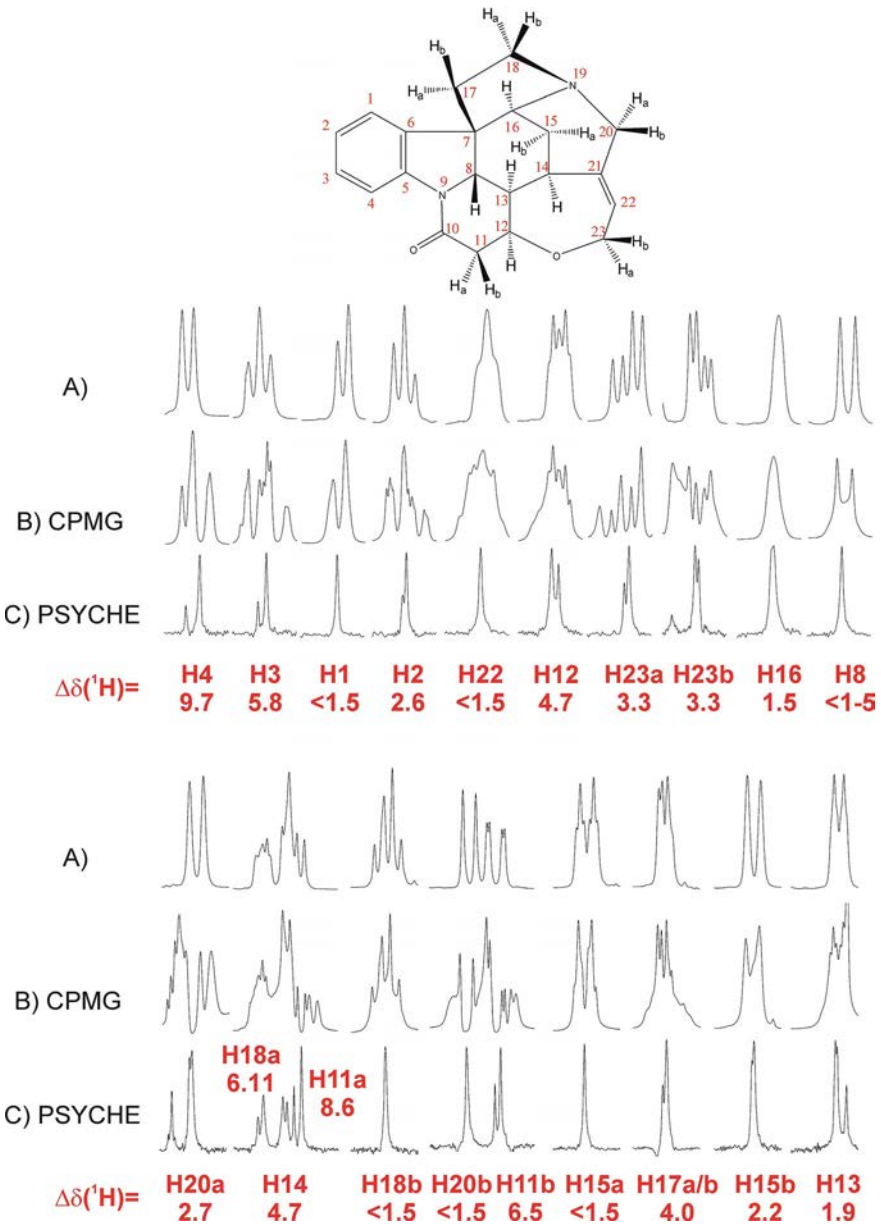

Figure 1. Expanded 1D multiplets corresponding to the 600.13 MHz A) conventional ^{1}H spectrum of an isotropic sample of strychnine (**1**) in $CDCl_3$; and B) CPMG and C) homodecoupled PSYCHE spectra of an anisotropic sample of **1** dissolved in a compressed PMMA/$CDCl_3$ gel (^{2}H $\Delta\nu_Q(CDCl_3) = 33.6$ Hz). Note that $\Delta\delta(^{1}H) > 1.5$ Hz can be determined for those resonances showing differentiated isotropic and anisotropic singlet signals in the homodecoupled spectrum.

satisfactory results for the reliable measurement of RDCs and/or RCSAs. As a reference for subsequent NMR experiments, the signal integration in the ^{2}H spectrum provides the isotropic/anisotropic ratio which also is reflected in the signal intensities of other NMR spectra.

Modern 1D and 2D NMR techniques offer unique features to improve signal overlap and to facilitate assignments. Several NMR approaches are feasible to distinguish between iso and aniso components, depending on the existing differences between $\delta^{iso}/\delta^{aniso}$ and/or $^{1}J_{CH}/^{1}T_{CH}$ coupling values. Table 1 lists some NMR techniques and the corresponding parameters involved in each case.

As a proof of concept, the analysis of the compressed PMMA sample of the target molecule strychnine (**1**) by 1D ^{1}H-CPMG becomes complicated due to the presence of complex multiplets, broad linewidths and high $\delta(^{1}H)$ degeneracy (Figure 1 B). Although it is not apparent, this spectrum contains two sets of indistinguishable signals corresponding to the molecules inside the separate isotropic and anisotropic cavities. Such complexity can be simplified using broadband homodecoupling that efficiently collapse all conventional *J/D* multiplets to singlet patterns. Figure 1 C shows the efficiency of the 1D PSYCHE spectrum[22] in **1** where each set of highly overlapped signals are reduced to two ^{1}H singlets with acceptable linewidths (about 1.8–2.0 Hz) for both iso and aniso signals. Note

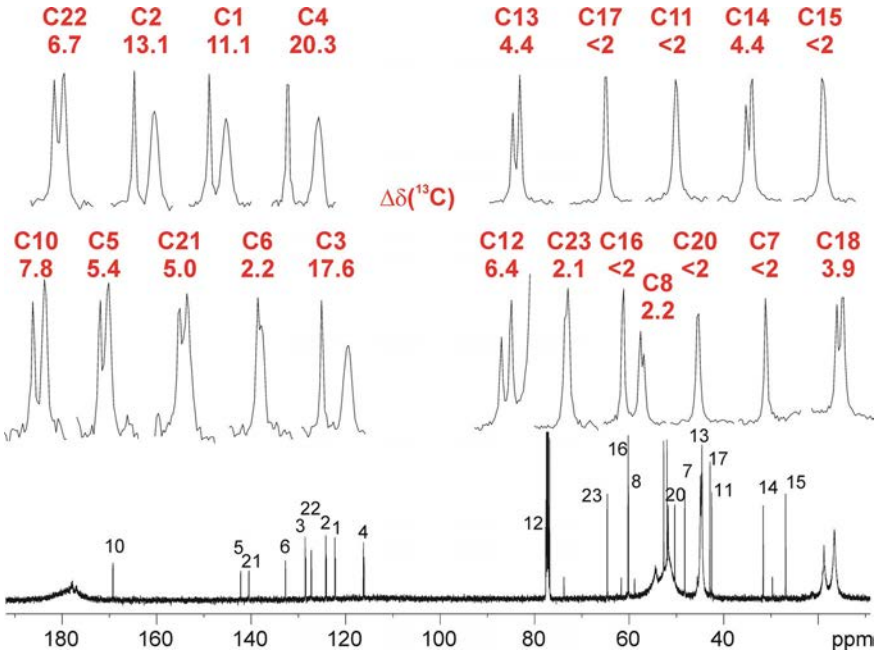

Figure 2. 150.6 MHz 1D $^{13}C\{1H\}$ NMR spectrum of **1** dissolved in a compressed PMMA/CDCl3 gel (^{2}H $\Delta\nu_Q(CDCl_3) = 33.6$ Hz) displaying the individual isotropic and anisotropic contributions. Note that the direct determination of $\Delta\delta(^{13}C) > 2.0$ Hz can be accomplished for most of the resonances.

the distinction of $\Delta\delta(^{1}H)$ below 10 ppb at 600 MHz, being also noteworthy its detection limit up to $\Delta\delta(^{1}H) > 1.5$ Hz and the ambiguity identification of each iso/aniso component and the sign determination.

On the other hand, the simplicity of a regular 1D $^{13}C\{1H\}$ spectrum offers a simple solution to visualise $\Delta\delta(^{13}C)$ with high precision (Figure 2). This is the method of choice to determine ^{13}C RCSAs on both protonated and non-protonated carbons, allowing differentiation of $\Delta\delta(^{13}C) > 2.0$ Hz, which involves separate measurements at two different strong/weak alignment conditions.[11] Obviously, the most pronounced experimental $\Delta\delta(^{13}C)$ effects are observed for the carbonyl, aromatic and olefinic sp^2 carbons (in the range between 20 and 5 Hz), whereas maximum differences up to 4–5 Hz are observed for aliphatic sp^3 carbons. The broader aniso linewidths can be used for assignment purposes and sign determination in favourable cases, and an additional reference fully-relaxed spectrum should be required to extract ^{13}C RCSAs. In this approach, the challenge is to keep equivalent the composition of the solvent, gel, and analyte in all measurements to avoid the introduction of additional changes that would require a further chemical-shift compensated correction.[11]

Herein we propose the use of a spectral aliased (SA), pure in-phase (PIP) HSQC (SA-PIP-HSQC) experiment[23] for the simultaneous monitorization of small $\Delta\delta(^{1}H)$ and $\Delta\delta(^{13}C)$.[24] The obtention of undistorted multiplets, free of *anti*-phase contributions due to the possible existence of large T_{HH} couplings (about 30–40 Hz), is fundamental to ensure the accuracy of the measurement. As a benefit, SA enhances the digital resolution per time unit in the ^{13}C dimension about two orders of magnitude. Because only the determination of $\Delta\delta(^{13}C)$ is the interest, the loss of the right $\delta(^{13}C)$ value along F1 is irrelevant in this case, although it could be quickly recovered from a reference spectrum if required. Also, SA retains the chemical shift sense between peaks in PIP-HSQC, allowing a sign-sensitive determination of both $\Delta\delta(^{13}C)$ and $\Delta\delta(^{1}H)$. Thus, the use of narrow ^{13}C spectral widths ($SW(^{13}C)$) (between 1–4 ppm) and 128–256 t_1 increments offers optimum performance and efficient and direct measurement of both $\Delta\delta(^{1}H)$ and $\Delta\delta(^{13}C)$ along the F2 and F1 dimensions, respectively, up to 1–3 ppb (Figure 3 A). Note that the anisotropic components usually shows broader and complex multiplets that help to the iso/aniso identification. The analysis becomes challenging in the aliphatic region, where $\Delta\delta$ should be smaller (see some challenging cross-peaks corresponding to sp^3 carbons in Figure 4). Under favourable conditions, even some signals that are not differentiated in the high-resolved 1D ^{1}H PSYCHE or $^{13}C\{^{1}H\}$ spectra could be distinguished in the 2D SA-PIP-HSQC spectrum. For instance, it is noteworthy that $\Delta\delta(^{13}C)$ about 2–3 Hz is enough to resolve signals with similar $\delta(^{1}H)$. Also, the broader lineshapes of the aniso signal guarantee the sign determination, as shown for H8 ($\Delta\delta(^{1}H) = -1.8$ Hz). On the other hand, tiny $\Delta\delta(^{13}C)$ differences below 2.0 Hz which cannot be determined from the conventional 1D ^{13}C spectrum, could be measured in signals with different $\delta(^{1}H)$ or multiplet amplitudes, as shown for C11 ($\Delta\delta(^{13}C) = +0.6$ Hz) or C20 (($\Delta\delta(^{13}C) = +0.4$ Hz), or vice-versa.

Similarly, SA can be incorporated in the F2-^{13}C-coupled SA-PIP-HSQC experiment to obtain the characteristic large $^{1}J_{CH}$/$^{1}T_{CH}$ doublets along the F2 dimension. If iso/aniso signal separation is optimum, all four $\Delta\delta(^{1}H)$, $\Delta\delta(^{13}C)$, $^{1}J_{CH}$ and $^{1}T_{CH}$ values can be extracted for each set of CH cross-peaks. Figure 3 B shows the expansions corresponding to the aromatic/olefinic region of the SA-PIP-HSQC spectrum of **1** collected without ^{13}C heterodecoupling. The bonus of this approach is demonstrated by determining the magnitude and sign of $^{1}D_{CH}$ from a single dataset with high accuracy, simplicity and optimum sensitivity.

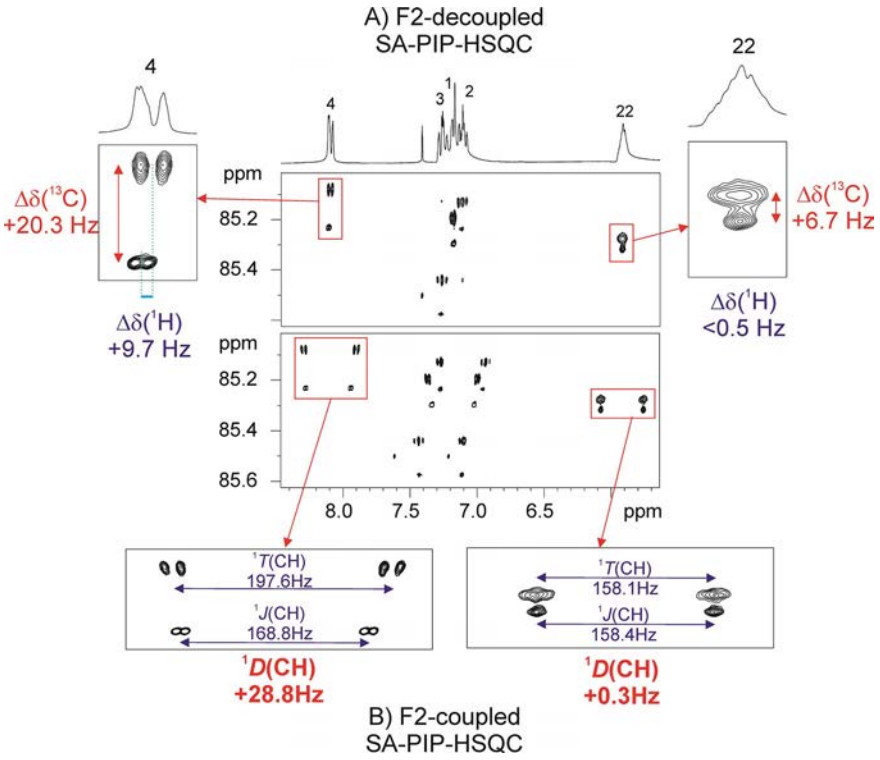

Figure 3. Expansion of the aromatic/olefinic region of the 2D SA-PIP-HSQC spectra of **1** acquired (top) with and (bottom) without broadband heterodecoupling during acquisition, showing how $\Delta\delta(^1H)$, $\Delta\delta(^{13}C)$, $^1J(CH)$ and $^1T(CH)$ (and therefore $^1D(CH)$) (all values in Hz) can be simultaneously determined from well-resolved cross-peaks. Experiments were collected with SW(^{13}C) = 1 ppm (150 Hz), td1 = 256, td2 = 2048, relaxation delay = 1 s, SW(^1H) = 9 ppm. Data were processed with zero-filling to 2048*2048 (QSINE and SSB1 = SSB2 = 2 in both dimensions). FID resolution 4.39 (F2) and 0.98 (F1) Hz/pt. The spectral resolution after processing was of 2.19 (F2) and 0.06 (F1) Hz/pt.

For instance, the large $\Delta\delta(^{13}C)$ of +20.3 Hz obtained for H-4 allows the direct determination of ^1D(C1-H1) of +28.8 Hz. Besides, the determination of the tiny ^1D(CH) of +0.3 Hz in H-22 due to the very similar ^1J(C22-H22) and ^1T(C22-H22) values is only feasible due to its observable $\Delta\delta(^{13}C)$ of +6.7 Hz. As recently reported, $^1J_{CH}$ and $^1T_{CH}$ measurements could also be performed along the indirect F1 dimension of complementary J_{CH}-resolved HSQC (*J*-HSQC) spectra.[19–21,25–27] Figure 5A and 5B compare the SA-PIP-HSQC and *J*-HSQC cross-peaks for the H13 and H15b protons, respectively, of **1**. Note that the observed $\Delta\delta(^{13}C)$ in the SA-PIP-HSQC spectrum is fundamental to distinguish both iso/aniso contributions because the similar values of $\Delta\delta(^1H)$ and $^1J_{CH}$ vs. $^1T_{CH}$ on these signals prevent their precise measurements in the *J*-HSQC spectrum. The measured ^1H-^{13}C RDCs and the magnitude and the sign of the $\Delta\delta(^{13}C)$ and $\Delta\delta(^1H)$ of **1** extracted from these reported PIP-HSQC spectra are in strong agreement with those obtained from the 1D spectra and also with those published in previous reports under similar sample conditions.[11,19–21,23]

In summary, the application of modern resolution-enhanced NMR techniques in compressed PMMA samples allows the fast, in situ and simultaneous determination of a complete set of isotropic and anisotropic parameters from a single NMR dataset. It has been shown that the use of spectral aliasing techniques allows very accurate measures of ^1H-^{13}C RDCs, $\Delta\delta(^{13}C)$ and $\Delta\delta(^1H)$. The sensitivity of the reported NMR experiments is close to the regular HSQC. Therefore, the applicability of the proposed approach is feasible even for dilute samples. These simultaneous measurements could also be made using other alignment media showing more favourable anisotropic conditions, and they could be further improved from the analysis of more simplified multiplets obtained in real-time BIRD-based homodecouped HSQC experiments (see SI).[24,28] Unfortunately, ^{13}C RCSA for non-protonated carbons could be only accessed by 1D $^{13}C\{^1H\}$ or by ultra-high-resolved long-range correlation experiments. Much work is in progress about new NMR methods to measure other anisotropic restraints of those described in this manuscript.

Acknowledgements

Financial support for this research provided by the Spanish MINECO (project CTQ2015-64436-P) is gratefully acknowledged. We also thank the Servei de Ressonància Magnètica Nuclear, Universitat Autònoma de Barcelona, for allocating instrument time to this project. NMR instrumentation at Carnegie Mellon University was partially supported by the NSF (CHE-0130903 and CHE-1039870). RRG gratefully acknowledges support from the NSF (CHE-1111684).

Conflict of interest

The authors declare no conflict of interest.

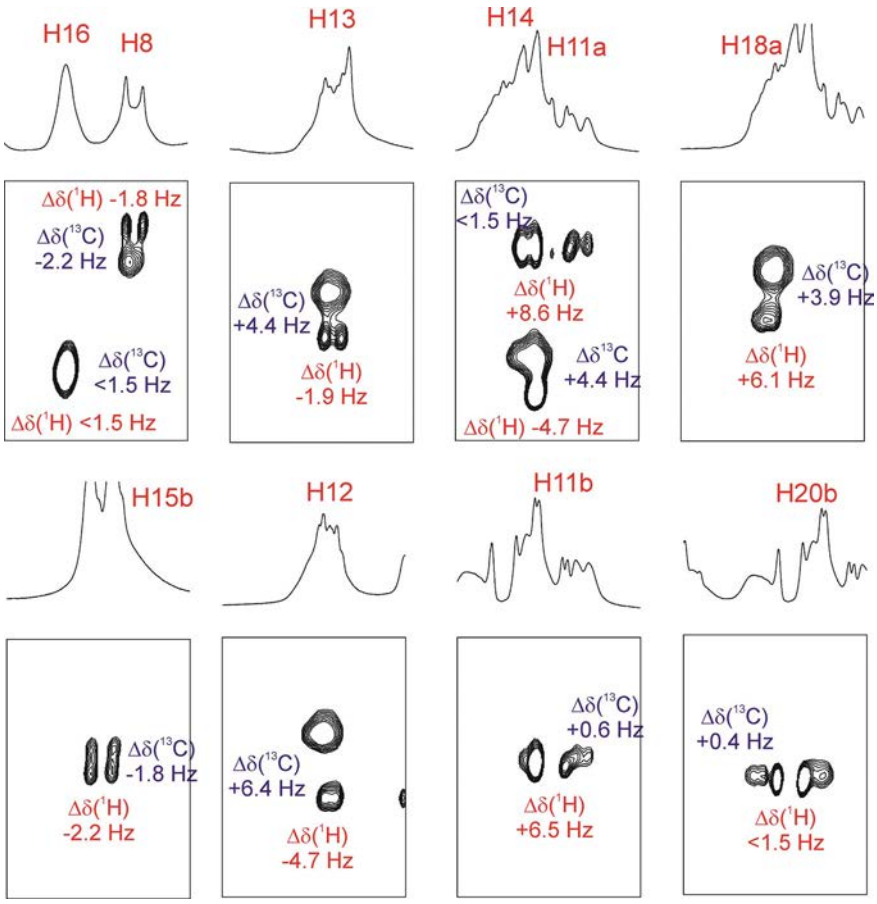

Figure 4. Expansion of some aliphatic cross-peaks in the 2D SA-PIP-HSQC spectrum of **1**, showing how very small $\Delta\delta(^1H)$ and $\Delta\delta(^{13}C)$ values and their signs (in Hz) can be determined from those well-resolved sp^3 signals. Note the broader linewidths for the anisotropic components.

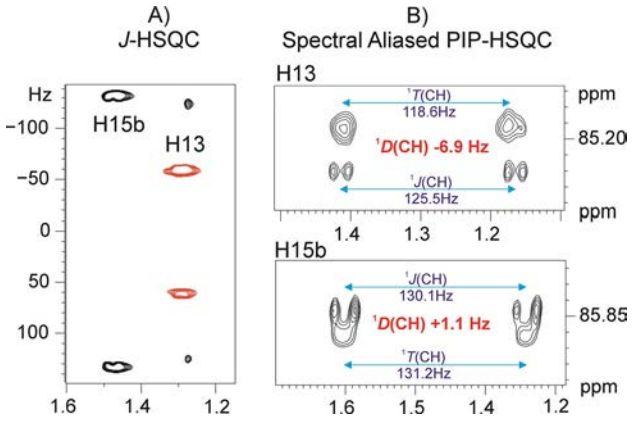

Figure 5. Comparison of some challenging cross-peaks in A) *J*-resolved HSQC and B) SA-PIP-HSQC spectra of **1**. For instance, note how each iso ^1J(CH) and aniso ^1T(CH) splitting of the H13 proton is measured along F2 in B) thanks to its large $\Delta\delta(^{13}C) = +6.9$ Hz, whereas they are not distinguished along F1 in A). Similar reasoning is made for the H15b proton ($\Delta\delta(^{13}C) = -1.8$ Hz).

Keywords: coupling constants · NMR spectroscopy · poly(methyl methacrylate) · small molecules · spectral aliasing

[1] C. M. Thiele, A. Marx, R. Berger, J. Fischer, M. Biel, A. Giannis, *Angew. Chem. Int. Ed.* **2006**, *45*, 4455 – 4460; *Angew. Chem.* **2006**, *118*, 4566 – 4571.
[2] R. R. Gil, *Angew. Chem. Int. Ed.* **2011**, *50*, 7222 – 7224; *Angew. Chem.* **2011**, *123*, 7360 – 7362.
[3] R. R. Gil, C. Gayathri, N. V. Tsarevsky, K. Matyjaszewski, *J. Org. Chem.* **2008**, *73*, 840 – 848.
[4] G. Kummerlöwe, B. Crone, M. Kretschmer, S. F. Kirsch, B. Luy, *Angew. Chem. Int. Ed.* **2011**, *50*, 2643 – 2645; *Angew. Chem.* **2011**, *123*, 2693 – 2696.
[5] M. E. García, S. Pagola, A. Navarro-Vázquez, D. D. Phillips, C. Gayathri, H. Krakauer, P. W. Stephens, V. E. Nicotra, R. R. Gil, *Angew. Chem. Int. Ed.* **2009**, *48*, 5670 – 5674; *Angew. Chem.* **2009**, *121*, 5780 – 5784.
[6] N. Marcó, P. Nolis, R. R. Gil, T. Parella, *J. Magn. Reson.* **2017**, *282*, 18 – 26.
[7] P. Trigo-Mouriño, A. Navarro-Vázquez, J. Ying, R. R. Gil, A. Bax, *Angew. Chem. Int. Ed.* **2011**, *50*, 7576 – 7580; *Angew. Chem.* **2011**, *123*, 7718 – 7722.
[8] N. Nath, E. J. d'Auvergne, C. Griesinger, *Angew. Chem. Int. Ed.* **2015**, *54*, 12706 – 12710; *Angew. Chem.* **2015**, *127*, 12897 – 12901.
[9] F. Hallwass, M. Schmidt, H. Sun, A. Mazur, G. Kummerlöwe, B. Luy, A. Navarro-Vázquez, C. Griesinger, U. M. Reinscheid, *Angew. Chem. Int. Ed.* **2011**, *50*, 9487 – 90; *Angew. Chem.* **2011**, *123*, 9659 – 9662.
[10] G. Kummerlöwe, S. L. Grage, C. M. Thiele, I. Kuprov, A. S. Ulrich, B. Luy, *J. Magn. Reson.* **2011**, *209*, 19 – 30.
[11] N. Nath, M. Schmidt, R. R. Gil, R. T. Williamson, G. E. Martin, A. Navarro-Vázquez, C. Griesinger, Y. Liu, *J. Am. Chem. Soc.* **2016**, *138*, 9548 – 9556.
[12] E. Mevers, J. Saurí, Y. Liu, A. Moser, T. R. Ramadhar, M. Varlan, R. T. Williamson, G. E. Martin, J. Clardy, *J. Am. Chem. Soc.* **2016**, *138*, 12324 – 12327.
[13] D. J. Milanowski, N. Oku, L. K. Cartner, H. R. Bokesch, R. T. Williamson, J. Saurí, Y. Liu, K. A. Blinov, Y. Ding, X. C. Li, D. Ferreira, L. A. Walker, S.

Khan, M. T. Davies-Coleman, J. A. Kelley, J. B. McMahon, G. E. Martin, K. R. Gustafson, *Chem. Sci.* **2018**, *9*, 307 – 314.
[14] Y. Liu, J. Saurí, E. Mevers, M. W. Peczuh, H. Hiemstra, J. Clardy, G. E. Martin, R. T. Williamson, *Science* **2017**, *356*, eaam5349.
[15] E. Troche-Pesqueira, C. Anklin, R. R. Gil, A. Navarro-Vázquez, *Angew. Chem. Int. Ed.* **2017**, *56*, 3660 – 3664; *Angew. Chem.* **2017**, *129*, 3714 – 3718.
[16] A. V. Buevich, M. E. Elyashberg, *Magn. Reson. Chem.* **2018**, https://doi.org/10.1002/mrc.4645.
[17] L. F. Gil-Silva, R. Santamaría-Fernández, A. Navarro-Vázquez, R. R. Gil, *Chemistry* **2016**, *22*, 472 – 476.
[18] C. Gayathri, N. V Tsarevsky, R. R. Gil, *Chemistry* **2010**, *16*, 3622 – 3626.
[19] L. Castañar, M. Garcia, E. Hellemann, P. Nolis, R. R. Gil, T. Parella, *J. Org. Chem.* **2016**, *81*, 11126 – 11131.
[20] N. Marcó, R. R. Gil, T. Parella, *Magn. Reson. Chem.* **2017**, *55*, 540 – 545.
[21] N. Marcó, A. A. Souza, P. Nolis, R. R. Gil, T. Parella, *J. Magn. Reson.* **2017**, *276*, 37 – 42.
[22] M. Foroozandeh, R. W. Adams, N. J. Meharry, D. Jeannerat, M. Nilsson, G. A. Morris, *Angew. Chem. Int. Ed.* **2014**, *53*, 6990 – 6992; *Angew. Chem.* **2014**, *126*, 7110 – 7112.
[23] L. Castañar, J. Saurí, R. T. Williamson, A. Virgili, T. Parella, *Angew. Chem. Int. Ed.* **2014**, *53*, 8379 – 8382; *Angew. Chem.* **2014**, *126*, 8519 – 8522.
[24] M. Pérez-Trujillo, L. Castañar, E. Monteagudo, L. Kuhn, P. Nolis, A. Virgili, R. T. Williamson, T. Parella, *Chem. Commun.* **2014**, *50*, 10214 – 10217.
[25] C. M. Thiele, W. Bermel, *J. Magn. Reson.* **2012**, *216*, 134 – 143.
[26] K. Feher, S. Berger, K. E. Kövér, *J. Magn. Reson.* **2003**, *163*, 340 – 346.
[27] J. D. Snider, E. Troche-Pesqueira, S. R. Woodruff, C. Gayathri, N. V. Tsarevsky, R. R. Gil, *Magn. Reson. Chem.* **2012**, *5*, S86 – S91.
[28] L. Paudel, R. W. Adams, P. Király, J. A. Aguilar, M. Foroozandeh, M. J. Cliff, M. Nilsson, P. Sándor, J. P. Waltho, G. A. Morris, *Angew. Chem. Int. Ed.* **2013**, *52*, 11616 – 11619; *Angew. Chem.* **2013**, *125*, 11830 – 11833.

Manuscript received: January 30, 2018
Accepted manuscript online: February 1, 2018
Version of record online: ■■ ▮▮, 0000

Isotropic/Anisotropic NMR Editing by Resolution-Enhanced NMR Spectroscopy

Núria Marcó,[1] Roberto R. Gil[2] and Teodor Parella[1]

[1]Servei de Ressonància Magnètica Nuclear, Universitat Autònoma de Barcelona, Facultat de Ciències, E-08193 Bellaterra (Barcelona), Catalonia;

[2] Department of Chemistry, Carnegie Mellon University, Pittsburgh, PA, USA;

Experimental Section

All NMR experiments were recorded on a 600 MHz spectrometer equipped with a triple-resonance $^{1}H/^{13}C$/BB inverse probe. The temperature for all measurements was set to 298K. The isotropic sample consisted of 20 mg of **1** dissolved in $CDCl_3$. The anisotropic sample consisted of 20 mg of **1** aligned in a poly(methylmethacrylate*)* (PMMA) gel swollen in $CDCl_3$ using the reversible compression/relaxation method described in ref. 1. The ^{2}H quadrupolar splitting ($\Delta\nu_Q$) for the $CDCl_3$ signal was set to 33.6 Hz.

The 1D ^{1}H-CPMG spectrum shown in Fig. 1B was recorded using the perfect-echo CPMG pulse scheme described in ref. 2. The overall CPMG time was set to 60 ms, using two echo periods of 3.0 ms (10 loops) to allow the elimination of J-modulation effects. The 1D ^{1}H-PSYCHE spectrum shown in Fig. 1C was recorded as described in ref. 3. Data were collected in a 2D acquisition mode, using 32 t_1 increments, SW(F1) = 50 Hz, and a pair of frequency-swept adiabatic chirp pulses of 15ms each one applied with a small flip angle of $\beta = 15^{o}$. Data were processed using the automated *pshift* program.

The 2D SA-PIP-HSQC and *J*-resolved HSQC experiments used in this work are depicted in Figures S1A and S1B, respectively, and they were acquired and processed as described in ref. 4 and 5, respectively. These 2D HSQC spectra were collected using standard parameter sets, with proton 90° pulses of 8.5 μs and carbon 90° pulses of 10.5 μs. SA-PIP-HSQC and $^{1}J_{CH}$-resolved HSQC experiment were acquired with spectral windows of 150 and 500 Hz in F_1, respectively. For broadband carbon inversion and refocusing, 0.5 ms smoothed Chirp pulses sweeping over a frequency band of 60 kHz and a 1:2:1 composite adiabatic pulse with an overall duration of 2 ms duration were used, respectively. The interpulse Δ delays in INEPT were set to 3.5 ms ($\Delta = 1/(2*^{1}J_{CH})$; optimized to $^{1}J_{CH}$ = 145 Hz) and the recycle delay to 1 s. Pulse phases are x unless indicated otherwise (Ψ=y) and a basic two-step phase cycling scheme is applied: Φ_1=x,-x, Φ_r=x,-x. Four scans were collected for each one of the 128 t_1 increments, with 2048 data points in each t_1 increment. Before Fourier-transformation, zero-filling to 2048 points in F1, 4098 points in F2 and a squared sine-bell apodization phase-shifted 90º in both dimensions were applied. Gradient ratios for G1:G2

was set to 80:20.1, measured as a percentage of the absolute gradient strength of 53.5 G/cm. The zero-quantum filter (ZQF) consists of a chirped adiabatic pulse applied simultaneously to a weak rectangular gradient (G0 = 11%) of the same duration (20 ms). Sine bell-shaped gradients had 1 ms of duration and were followed by a recovery delay of 100 μs (δ). All experiments were acquired and processed using the echo/anti-echo protocol where the gradient G1 was inverted for every second FID. Broadband heteronuclear decoupling during proton acquisition is optional, as a function if $^{1}J_{CH}/^{1}T_{CH}$ want to be measured. ^{13}C-heterodecoupoled and ^{13}C-coupled pure shift versions of the SA-PIP-HSQC experiment were recorded under the same acquisition and processed conditions as described previously. Real-time BIRD-based homodecoupling during the ^{1}H acquisition period was implemented as described in ref. 6 and 7, respectively.

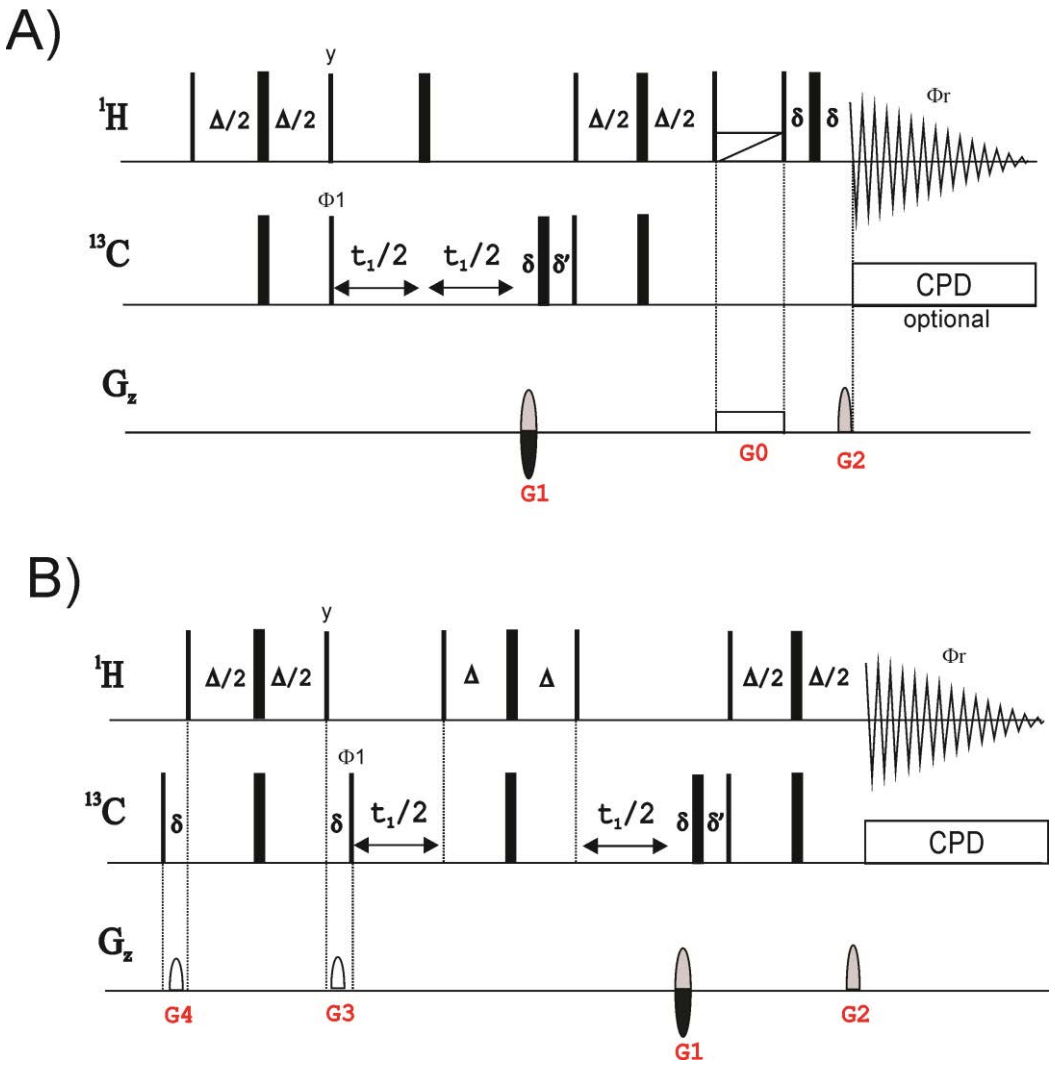

Figure S1. Pulse schemes to record A) spectral-aliased PIP-HSQC and B) *J*-resolved HSQC experiments.

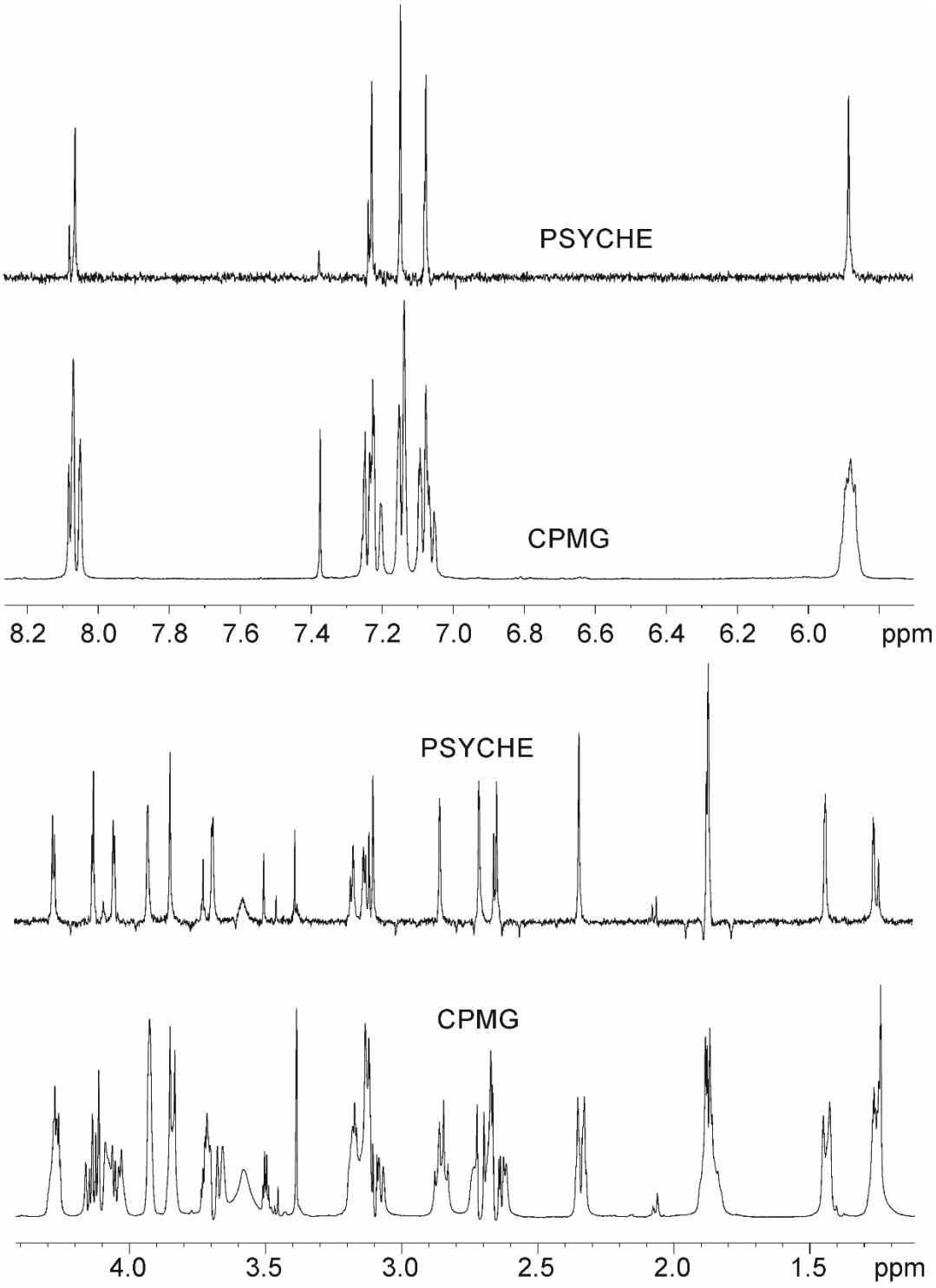

Figure S2. (bottom) 1D ^{1}H CPMG and (top) 1D ^{1}H PSYCHE of an anisotropic sample of **1** dissolved in a compressed PMMA/$CDCl_3$ gel (^{2}H $\Delta\nu_Q(CDCl_3)$ = 33.6 Hz). Expansions are shown in Fig. 2 of the main manuscript.

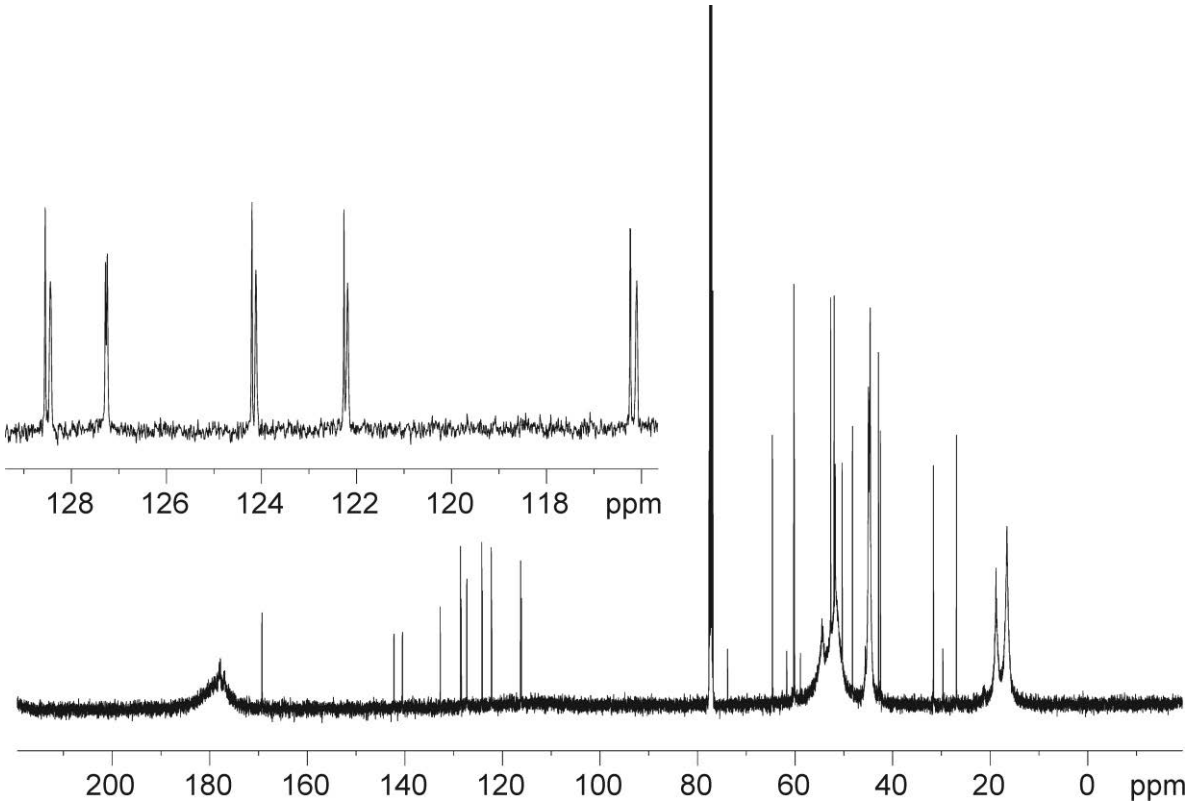

Figure S3. 1D $^{13}C\{^{1}H\}$ spectrum of an anisotropic sample of **1** dissolved in a compressed PMMA/$CDCl_3$ gel (^{2}H $\Delta\nu_Q(CDCl_3)$ = 33.6 Hz). Expansions are shown in Fig. 3 of the main manuscript.

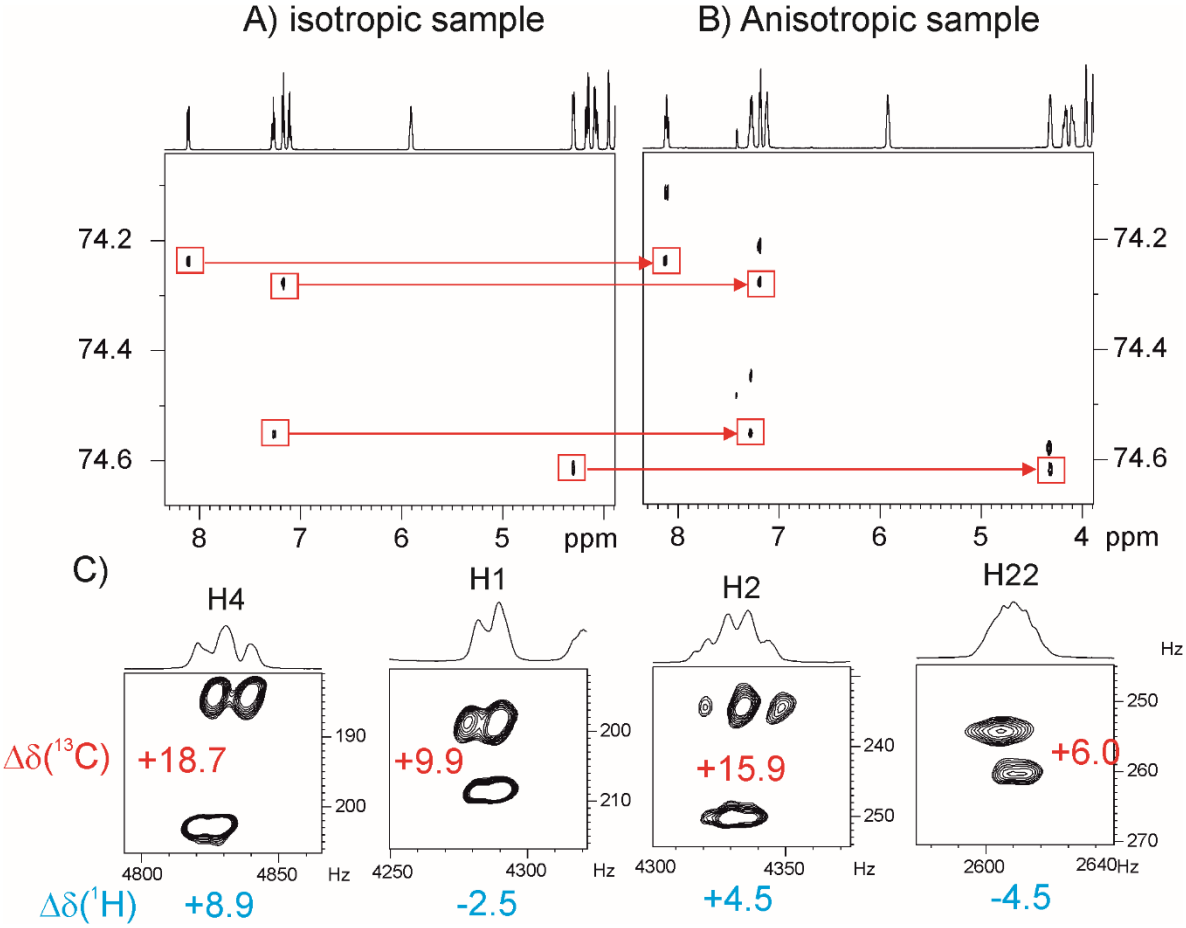

Figure S4. Effects of alignment compression in SA-PIP-HSQC spectra: A) isotropic sample and B) anisotropic sample (^{2}H $\Delta\nu_Q(CDCl_3)$ = 48 Hz) of **1**. Note that isotropic correlations present the same coordinates in both spectra (red boxes). Note that how at this maximum compression, $\Delta\delta(^1H)$ can be measured for the H1 and H22 protons.

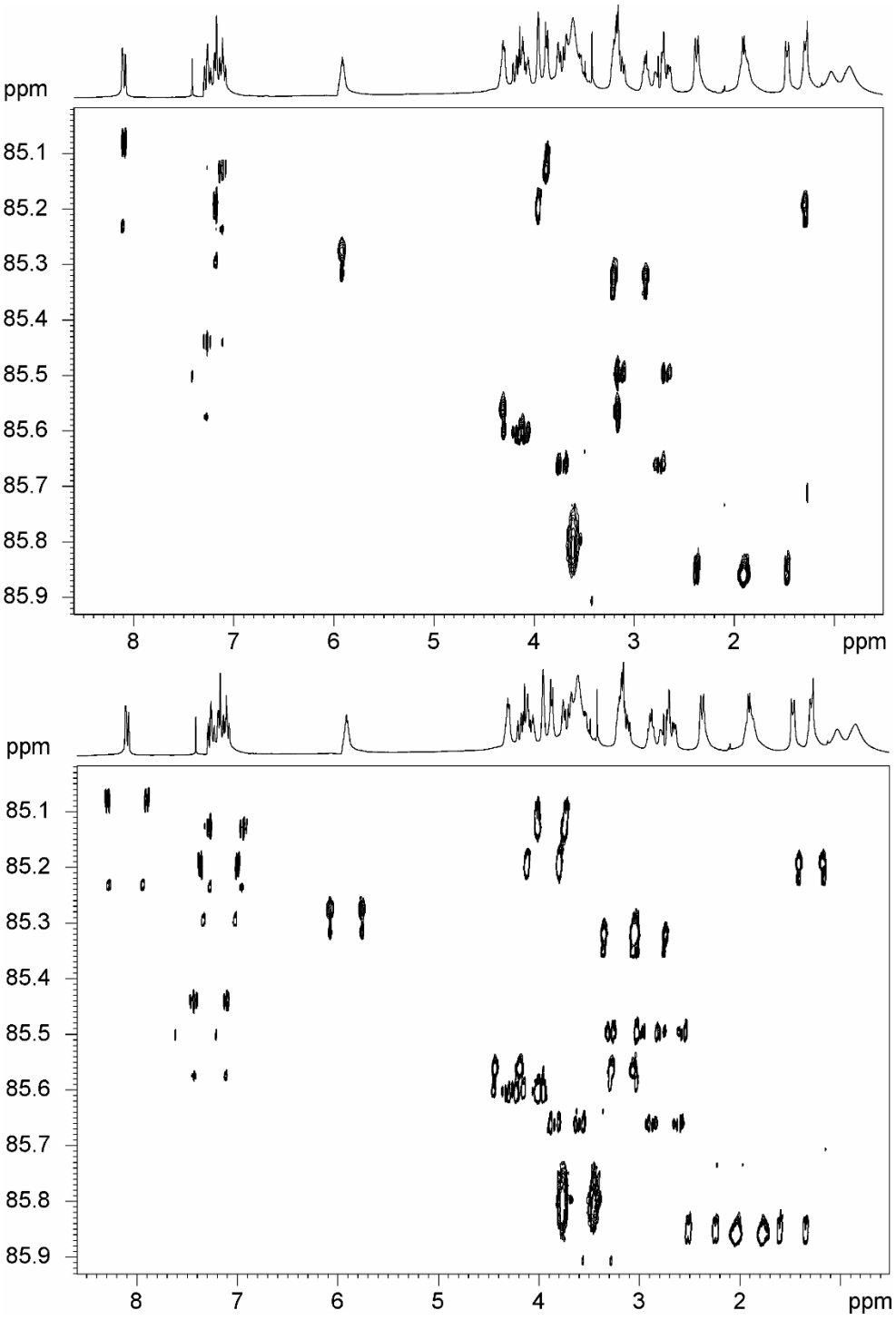

Figure S5: 2D Spectral Aliased PIP-HSQC spectra (top) with and (bottom) of an anisotropic sample of **1** dissolved in a compressed PMMA/$CDCl_3$ gel (^2H $\Delta\nu_Q(CDCl_3)$ = 33.6 Hz), with and without broadband heterodecoupling during acquisition, respectively. Experiments were collected with SW(^{13}C) = 1 ppm and 256 t1 increments.

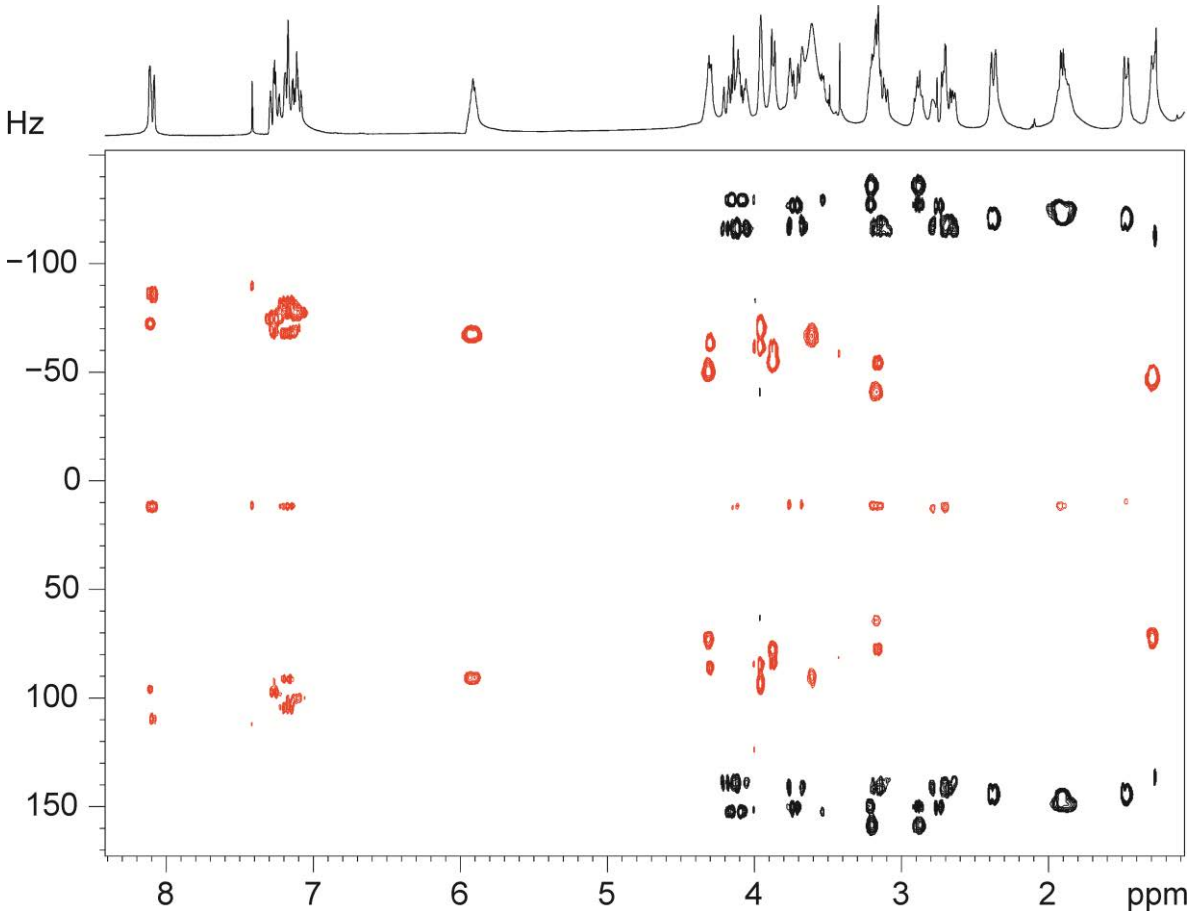

Figure S6: 2D *J*-resolved HSQC of **1** dissolved in a compressed PMMA/$CDCl_3$ gel (^2H $\Delta\nu_Q(CDCl_3)$ = 33.6 Hz),. Note that ^1J and ^1T splittings are not distinguished in some ^1H signals, such as shown for H22, H15a or H13. These separate contributions can be visualised from the corresponding cross-peaks in the SA-PIP-HSQC spectrum. See expansions in Fig. 5 of the main manuscript.

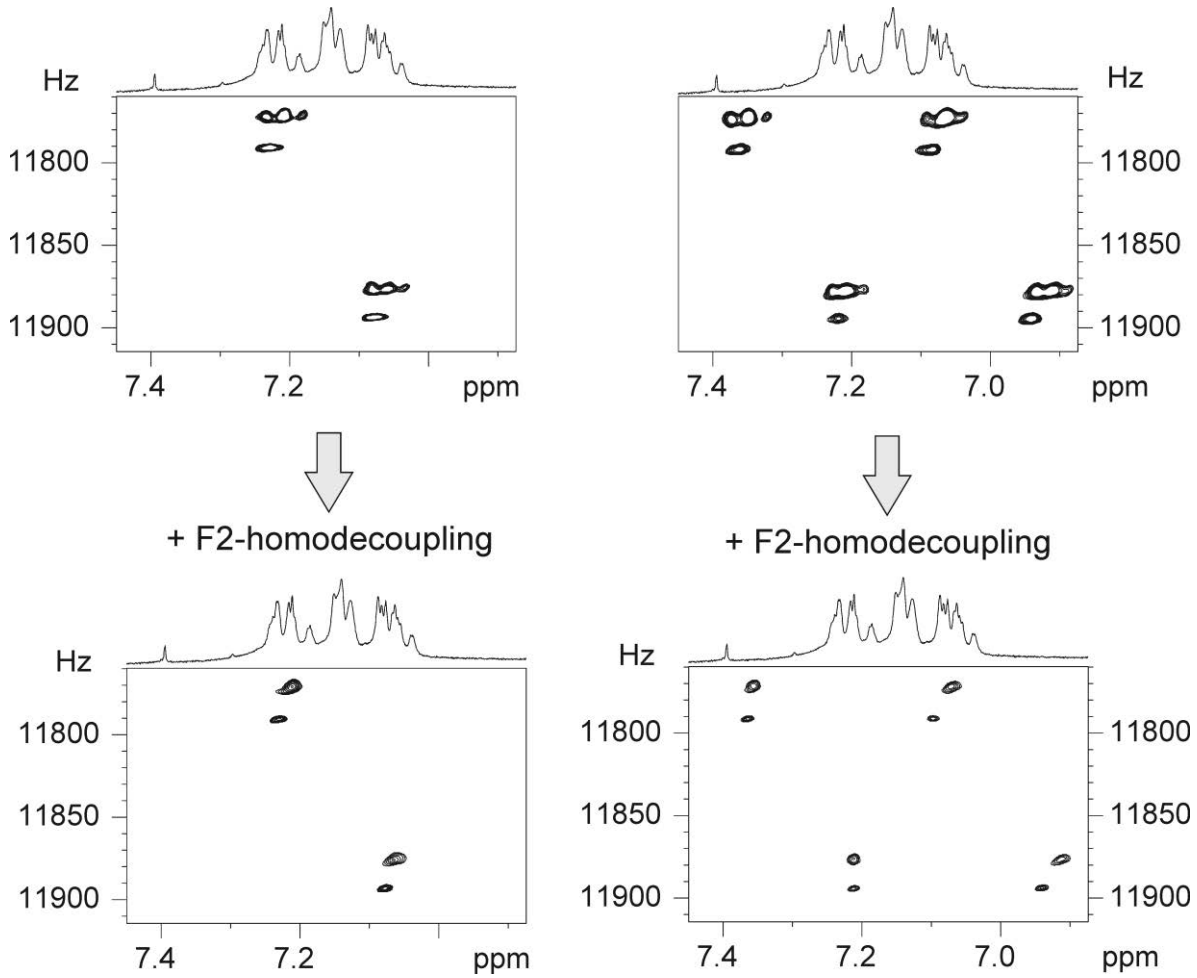

Figure S7: Expansions corresponding to the (top) conventional and (bottom) F2-^{1}H-homodecoupled versions of the SA-PIP-HSQC experiment.

References:

1. C. Gayathri, N. V Tsarevsky, R. R. Gil, *Chemistry* **2010**, *16*, 3622–3626.
2. J. A. Aguilar, M. Nilsson, G. Bodenhausen, G.A. Morris, *Chem. Comm.* **2012**, *48*, 811-813
3. M. Foroozandeh, R. W. Adams, N. J. Meharry, D. Jeannerat, M. Nilsson, G. A. Morris, *Angew. Chem. Int. Ed.* **2014**, *53*, 6990–6992.
4. L. Castañar, J. Saurí, R. T. Williamson, A. Virgili, T. Parella, *Angew. Chem. Int. Ed.* **2014**, *53*, 8379–8382.
5. L. Castañar, M. Garcia, E. Hellemann, P. Nolis, R. R. Gil, T. Parella, *J. Org. Chem.* **2016**, *81*, 11126–11131.
6. L. Paudel, R. W. Adams, P. Kiraly, J. A. Aguilar, M. Foroozandeh, M. J. Cliff, M. Nilsson, P. Sandor, J. P., G. A. Morris, *Angew. Chem. Int. Ed.* **2013**, *52*, 11616-11619.
7. I. Timári, L. Kaltschnee, M. H. Raics, F. Roth, N. G. A. Bell, R. W. Adams, M. Nilsson, D. Uhrín, G. A. Morris, C. M. Thiele, K. E. Kövér, *RSC adv.* **2016**, *6*, 87848-87855.

PUBLICATION 4

Title: Structural discrimination from in situ measurement of $^{1}D_{CH}$ and $^{2}D_{HH}$ residual dipolar coupling constants

Authors: Marcó, N.; Gil, R. R.; Parella, T.

Reference: *Magn. Reson. Chem.* **2017**, *55* (6), 540–545.

DOI: 10.1002/mrc.4575

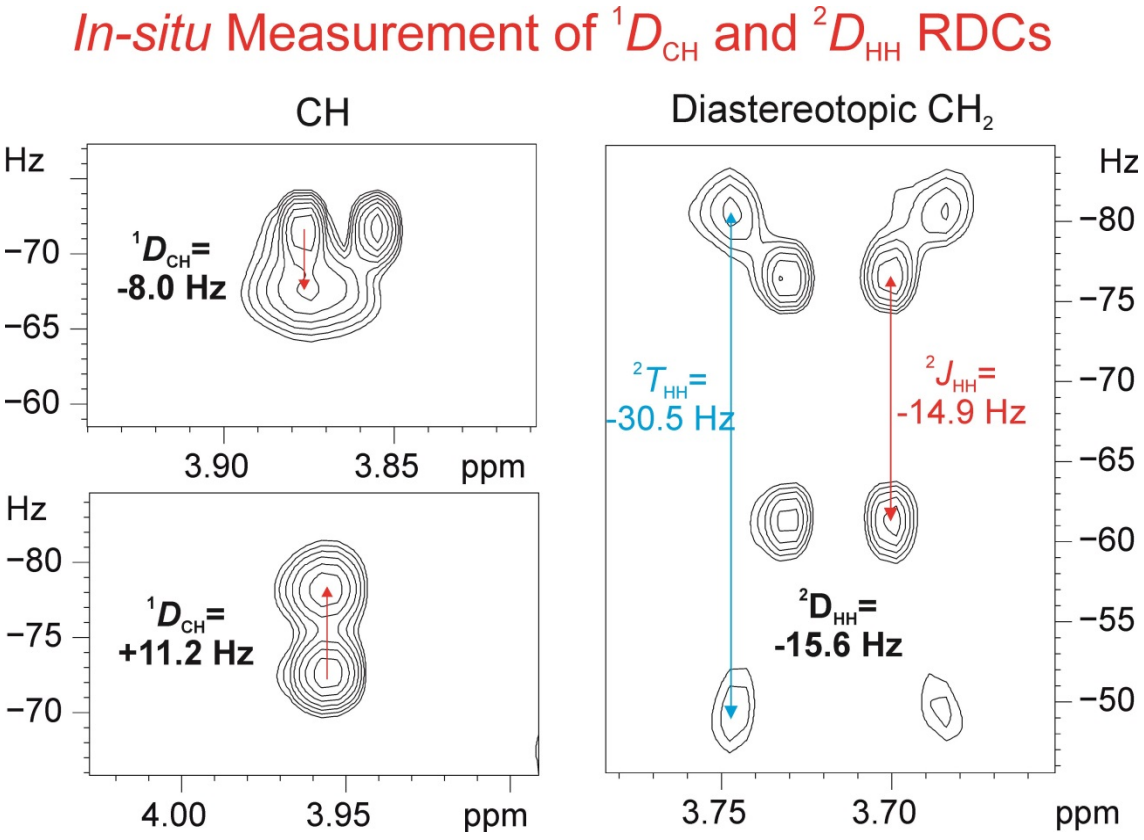

SUMMARY

It is recognized the importance of the non-local character of RDCs in the 3D structural determination of small molecules. Usually, RDCs are measured from the splittings obtained along with the F2 or F1 dimensions of HSQC spectra. The accurate *J* measurement along the direct dimension F2 is challenging due to the extensive line broadening caused for the complex multiplets generated for ^{1}H-^{1}H couplings. As an alternative, the determination of RDCs along F1 can be postulated as a better option. By the use of a novel pulse scheme that combines the ^{13}C editing block, an incremented BIRD^{d,X}-based *J*-resolved element and a final ZQF, the simultaneous measurement of both $^{1}J_{CH}$ and $^{2}J_{HH}$ can be performed from a single dataset.

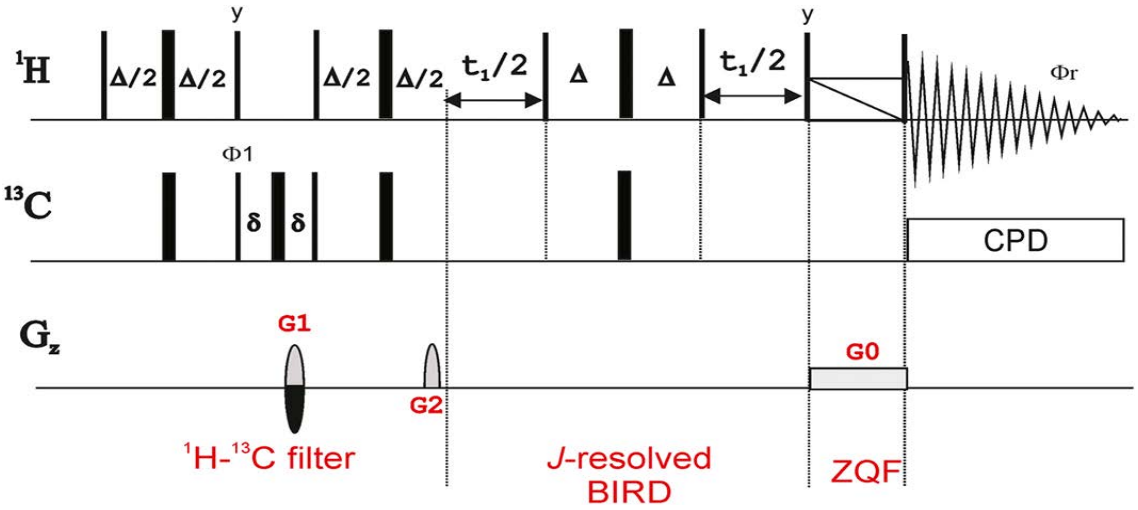

The application of this *J*-resolved HSQC sequence in a sample weakly aligned in PMMA gel allows observing both the isotropic and the anisotropic signals into the same resolution-enhanced spectrum. In this way, $^{1}T_{CH}$ and $^{1}J_{CH}$, as well as $^{2}T_{HH}$ and $^{2}J_{HH}$ can be simultaneously determined along the highly-resolved F1 dimension. A fast and straightforward strategy to assign all diastereotopic protons thanks to the calculation of the alignment tensor is achieved, allowing a robust strategy to determine multiple relative configurations in a fast way.

Research article

MRC

Received: 16 November 2016 Revised: 23 December 2016 Accepted: 29 December 2016 Published online in Wiley Online Library: 8 February 2017

(wileyonlinelibrary.com) DOI 10.1002/mrc.4575

Structural discrimination from *in situ* measurement of $^1D_{CH}$ and $^2D_{HH}$ residual dipolar coupling constants

Núria Marcó,[a] Roberto R. Gil[b] and Teodor Parella[a]*

ABSTRACT: A fast residual dipolar coupling constant-assisted strategy involving the simultaneous determination of scalar and total coupling constants from a single $^1J_{CH}/^2J_{HH}$-resolved NMR spectrum is reported. It is shown that the concerted use of the directly measured $^1D_{CH}$ (for all CH_n multiplicities) and $^2D_{HH}$ residual dipolar couplings allows an on-the-fly assignment of diastereotopic CH_2 protons, as well as of an efficient discrimination between diastereoisomeric structures of strychnine which contains six stereocenters. Copyright © 2017 John Wiley & Sons, Ltd.

Keywords: residual dipolar couplings; NMR; relative configuration; *J*-resolved HSQC; structural discrimination

Introduction

Residual dipolar coupling constants (RDCs) provide structural information of non-local character, permitting the determination of the relative orientation of stereochemical centers regardless of the distance between them. This powerful advantage over conventional isotropic NMR parameters makes RDCs the tool of choice to lift structural ambiguities of small molecules in solution generated by using only scalar coupling constants (*J*) or through-space NOE enhancements.[1] The most valuable RDC restraints are the proton-carbon coupling constants ($^1D_{CH}$) that are usually determined using a two-step NMR measurement approach based on the difference between the scalar coupling constant ($^1J_{CH}$) measured in an isotropic sample and the total coupling constant ($^1T_{CH} = {}^1J_{CH} + {}^1D_{CH}$) measured in a different but, in principle, equivalent anisotropic sample. Many different alignment media have been used to generate such particular anisotropic conditions, basically consisting of strained gels or lyotropic liquid crystals, which produce a restrictive, weak molecular alignment along the main magnetic field.[1] Whereas $^1J_{CH}$ can be accurately determined from many different NMR experiments, the accuracy and simplicity of the $^1T_{CH}$ determination are fundamental for a successful use of RDCs. Thus, the developments on novel NMR techniques to determine $^1D_{CH}$ have been mainly concentrated about the suitability to measure such *J/T* splittings from the direct F2 or the indirect F1 dimension in HSQC-type spectra. At first glance, the measurement from the F2 dimension seems to be more suitable because of its better digital resolution and its ability of measuring the CH couplings for diastereotopic protons, but, in practice, important errors can be introduced because of the wide line broadening, the complex multiplet patterns generated from the interference of large ^1H–^1H dipolar couplings and the existence of strong coupling effects that can produce unsymmetrical and distorted satellite signals.[2] Although some homodecoupled HSQC methods have been proposed to alleviate these drawbacks, their long acquisition times or the undesired J_{CH}-modulation during real-time BIRD-based homodecoupling can limit their routine use.[3] In addition, in some alignment media such as those used in this work, compressed $CDCl_3$-compatible swollen poly(methyl methacrylate) (PMMA) gels, the simultaneous presence of isotropic and anisotropic signals definitively prevents any attempts of success using F2-coupled HSQC experiments.[4] An attractive alternative is to measure *J/T* from the F1 dimension of J_{CH}-resolved experiments, which avoid the strong requirements for a large number of t_1 increments or the use of wide spectral widths needed in δ correlations to achieve high levels of resolution.[4,5] The J_{CH}-resolved HSQC experiment offers excellent sensitivity and simple spectral analysis, but the central lines of the F1-multiplet corresponding to a methylene CH_aH_b group are not observed, and therefore, only the sum $^1J_{CHa} + {}^1J_{CHb}$ can be determined.[6] Although these central lines could be observed from a novel J_{CH}-resolved method, its lower sensitivity and accidental signal overlap limit its performance.[7]

Another controversial subject is the requirement for the accurate measurement of individual $^1D_{CH}$ for each diastereotopic CH_2 proton.[8] It has been shown that the sum $^1D_{CHa} + {}^1D_{CHb}$ can be successfully used in the singular value decomposition (SVD) calculations for effective discrimination of configuration without the need for *a priori* diastereotopic protons assignments in CH_aH_b systems.[4,6,9] Some different methods have been proposed for the simultaneous measurement of both individual $^1D_{CH}$ and $^2D_{HH}$ in methylene systems,[7,10] but most of them were designed for proteins, and a no general approach is available that works in a wide range of sample and spectral conditions. We report here an

* *Correspondence to: Teodor Parella, Servei de Ressonància Magnètica Nuclear, Facultat de Ciéncies, Universitat Autònoma de Barcelona, E-08193 Bellaterra (Barcelona), Catalonia, Spain. E-mail: teodor.parella@uab.cat; rgil@andrew.cmu.edu*

a *Servei de Ressonància Magnètica Nuclear and Departament de Química, Facultat de Ciències, Universitat Autònoma de Barcelona, E-08193 Bellaterra (Barcelona) Catalonia, Spain*

b *Department of Chemistry, Carnegie Mellon University, 4400 Fifth Ave, Pittsburgh, PA, 15213, USA*

improved version of the ^{13}C-edited J_{CH}/J_{HH}-resolved experiment that was previously used to distinguish enantiomers in chiral liquid crystals.[6] The previous method was not suitable for accurate coupling measurements because mixed phases necessitated an undesirable magnitude mode presentation. Our approach affords pure absorption lineshapes, allowing much better accuracy and precision.

Results and Discussion

The novel pulse scheme (Fig. 1) consists of an initial ^{13}C isotope editing block based on the refocused HSQC scheme and an incrementable BIRD-based *J*-resolved t_1 element to allow $^{1}J_{CH}$ evolution while ^{1}H chemical shifts and J_{HH} are refocused. However, the BIRD element also inverts $^{2}J_{HH}$, and therefore, these interactions will be also displayed in the F1 dimension. Finally, the major novelty is the efficiency of the last zero-quantum filter element[11] that completely removes any dispersive signal contribution, as already demonstrated to provide high-quality NMR spectra in other experiments.[12] This new element affords pure in-phase multiplets with perfect absorption lineshapes enabling a suitable phase-sensitive data representation and a feasible quantitative extraction of coupling constant values (Fig. S1). The mismatch between experimental $^{1}J_{CH}$ and delay optimization only affects signal intensity but not the accuracy and/or the precision of the measurement.

Figure 2 shows the experimental $^{1}J_{CH}/^{2}J_{HH}$-resolved spectra of a sample of 20 mg of strychnine in isotropic and anisotropic conditions [^{2}H $\Delta\nu_Q$(CDCl$_3$) = 26 Hz] recorded in only ~6 min for each sample. Note that both $^{1}J_{CH}/^{2}J_{HH}$-resolved spectra provide the typical symmetrical representation along the F1 = 0 axis, with clean doublets due to $^{1}J_{CH}$ for each CH pair, and well-resolved double doublets ($^{1}J_{CHa}$ + $^{2}J_{HaHb}$) for each individual diastereotopic proton in a methylene CH_aH_b group. This symmetry also facilitates a very simple data analysis, and this is particularly important in the direct determination of RDCs thanks to the simultaneous observation of both the isotropic and anisotropic components in the same anisotropic NMR spectrum (Fig. 2B).[13] This is a particular feature of some compressed gels like PMMA that opens a robust approach to determine RDCs in a very quick and single-shot manner, with minimized errors compared to the traditional two-step measurement approach.

The expanded region shown in Fig. 3 outlines the different CH and diastereotopic CH_2 cross-peak patterns obtained in the J_{CH}/J_{HH}-resolved spectrum. The excellent resolution along the indirect dimension allows the perfect distinction between the different isotropic and anisotropic components, and therefore represents a valuable tool for the direct and efficient determination of both $^{1}D_{CH}$ and $^{2}D_{HH}$. For instance, the simple column analysis corresponding to the methine H8 proton allows the precise *in situ* measurement of both $^{1}J_{C8H8}$ (+144.6 Hz) and $^{1}T_{C8H8}$ (+136.6 Hz) yielding a fast and very efficient determination of the corresponding $^{1}D_{C8H8}$ (−8.0 Hz). In a more simple way, this $^{1}D_{C8H8}$ coupling can be measured directly by determining the difference in hertz between the two upfield or downfield components. In the case of methylene CH_aH_b groups, four different $^{1}J_{CHa}/^{1}T_{CHa}$ and $^{2}J_{HaHb}/^{2}T_{HaHb}$ couplings can be extracted for each diastereotopic Ha proton, allowing the direct determination of both $^{1}D_{CHa}$ and $^{2}D_{HaHb}$ provided that enough signal resolution differentiates the iso/aniso components. For instance, assuming that $^{1}J_{CH}$ are positive and $^{2}J_{HH}$ are negative, $^{1}D_{C20aHa}$ = −8.2 Hz and $^{2}D_{H2aH20b}$ = −15.6 Hz can be directly obtained from the peak separation along the F1 dimension (Fig. 3B).

Most of the $^{1}D_{CH}$ and $^{2}D_{HH}$ RDCs in **1** have been extracted from a single J_{CH}/J_{HH}-resolved dataset, and the major challenges were only found for the mentioned H18a/H18b and the degenerate H17a/H17b protons, which were excluded from further calculations. In case of doubts, the reference $^{1}J_{CH}/^{2}J_{HH}$-resolved spectrum in isotropic conditions can assist the identification and assignment of the isotropic signals in the anisotropic sample (Fig. S1). For **1**, most of the anisotropic components have been distinguished from their broader lineshapes and wider multiplicities. In some cases, the co-existence of both iso/aniso signals can produce some accidental signal overlap and therefore can make the *J*/*T* extraction difficult. On the other hand, the J_{CH}/J_{HH}-resolved experiment does not provide the sign neither $^{1}J/T_{CH}$ nor $^{2}J/T_{HH}$, but assuming that $^{1}J_{CH}$ are positive and $^{2}J_{HH}$ are large and negative, obtaining the absolute sign of $^{1}D_{CH}$ and $^{2}D_{HH}$ is usually an easy task. An exception is found for H18a and H18b protons where the isotropic $^{2}J_{H18aH18b}$ is easily determined to be −9.5 Hz but the corresponding $^{2}T_{H18aH18b}$ splitting is not well resolved along F1, deducing that it corresponds to

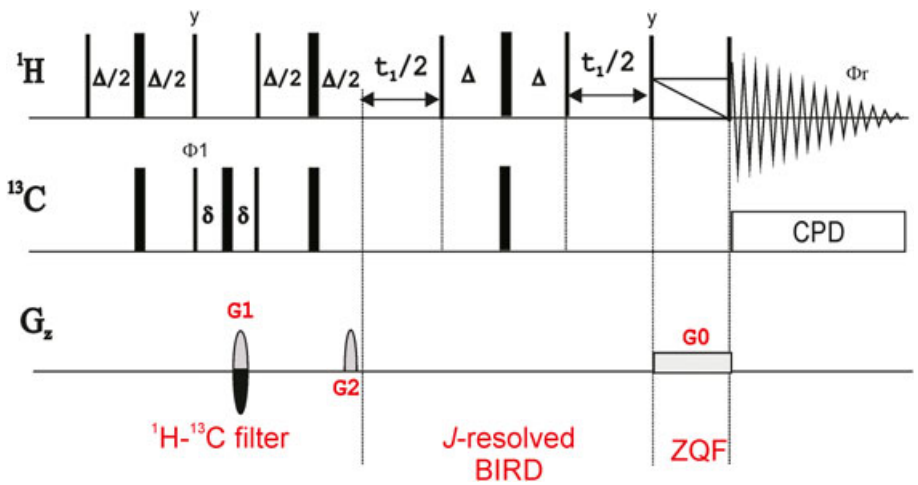

Figure 1. Zero quantum-filtered $^{1}J_{CH}/^{2}J_{HH}$-resolved pulse scheme to measure $^{1}J_{CH}/^{1}T_{CH}$ and $^{2}J_{HH}/^{2}T_{HH}$ in small molecules at natural abundance. Narrow-filled and wide-filled bars correspond to 90 and 180 ° pulses, respectively, with phase *x* unless indicated otherwise. The interpulse delay in INEPT and BIRD elements is set to $\Delta = 1/(2^{*}{}^{1}J_{CH})$. Coherence order selection and echo/anti-echo phase-sensitive detection are achieved with gradient pulses G1 and G2 in the ratio of 80 : 20.1. A basic two-step phase cycle is used: $\phi_1 = x,-x$ and $\phi_r = x,-x$.

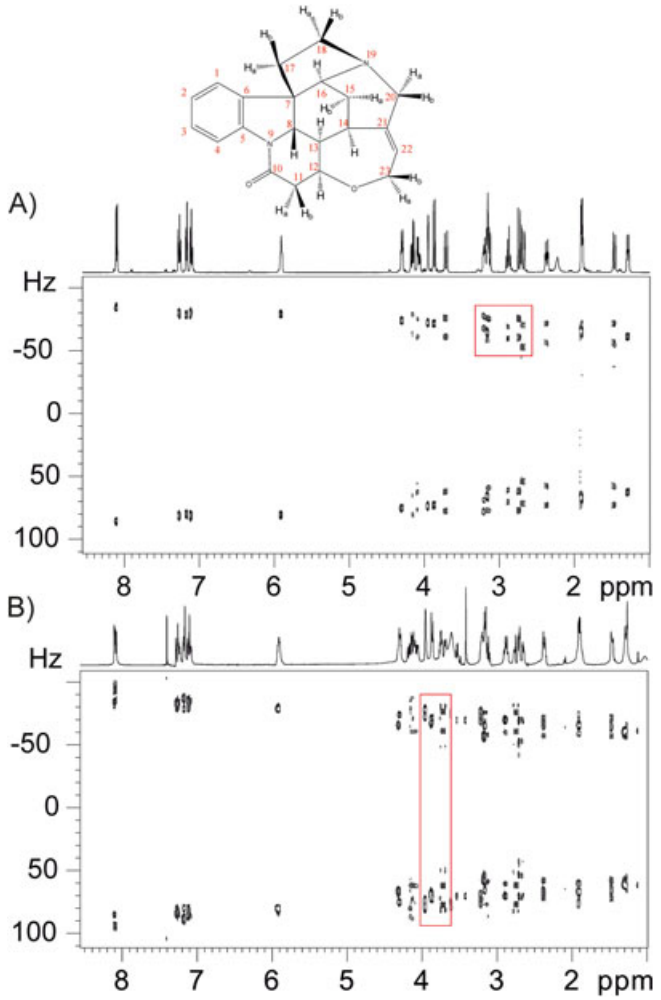

Figure 2. 500.13 MHz $^{1}J_{CH}/^{2}J_{HH}$-resolved spectra of strychnine (**1**) in (A) isotropic $CDCl_3$ and (B) anisotropic poly(methyl methacrylate)–$CDCl_3$ [^{2}H $\nu_Q(CDCl_3)$ = 26 Hz] conditions. The projections along the F2 dimension are the conventional ^{1}H spectrum in isotropic conditions and the ^{1}H–CPMG spectrum in anisotropic conditions, respectively. Marked red boxes are expanded in Figs 3 and S1. Experimental conditions: 2 K(F2) * 128(F1), pre-scan delay = 1 s, Δ = 3.6 ms, *ns* = 2, SW(F2) = 10 ppm, SW(F1) = 250 Hz, FID resolution = 4.88(F2) * 3.90(F1) Hz and acquisition time = 6 min for each spectrum. Data were processed with 2 K(F2) * 2 K(F2), WDW1 = WDW2 = QSINE and SSB = 2, giving a spectral resolution of 2.44(F2) * 0.12(F1) Hz.

a small absolute value (<±2 Hz). This makes difficult to accurately determine both the magnitude and sign of $^{2}D_{H18aH18b}$ (in the range about +7/+11 Hz), and also limiting the accurate measurement of $^{1}D_{C18H18a}$ (tentatively about 0 Hz). It is important to note that a *D* value of 0 Hz also provides structural information, indicating that this particular internuclear vector is oriented in the magic angle of the alignment tensor.

We have evaluated the robustness of the J_{CH}/J_{HH}-resolved experiment by SVD fitting of 10 $^{1}D_{CH}$ for methines, 10 individual $^{1}D_{CH}$ for methylene protons and 4 $^{2}D_{HH}$ RDC data to the structures of eight possible diastereoisomers of strychnine generated from MM-based geometries using MSpin,[14] as used in Snider *et al.*[4] Six different calculations have been performed with a special emphasis on the inclusion of individual $^{1}D_{CH}$ for each methylene proton, the homonuclear $^{2}D_{HH}$ values or the use of sums of $^{1}D_{CHa}$ + $^{1}D_{CHb}$ in CH_2 systems (Table S1).[4] Three selected $^{1}D_{CH}$ datasets (with and without $^{2}D_{HH}$) have been chosen: (i) only incorporating CH groups, (ii) including all individual $^{1}D_{CH}$ for both CH and CH_2 spin systems and (iii) using the individual $^{1}D_{CH}$ for CH and the overall sum $^{1}D_{CHa}$ + $^{1}D_{CHb}$ for methylenes (SVD calculation without prior diastereotopic ^{1}H assignment). Definitive conclusions can be extracted from the analysis of the *Q* factors obtained for each isomer and calculation (Table 1 and Fig. 4).

First of all, the six calculations provide a solid discrimination of the correct configuration [isomer 6; *Q*(6) = 7*R*,8*S*,12*S*,13*R*,14*R*,16*S*] *versus* the second lowest value [isomer 5 that corresponds to the C12 epimer; *Q*(5) = 7*R*,8*S*,12*R*,13*R*,14*R*,16*S*] that is in accordance with related works.[4,15,16] As a general trend, it is observed that *Q*(6) has a narrow range in all calculations (0.094–0.116), whereas *Q*(5) shows the largest dispersion (0.134–0.262). The *Q* factor by itself is not very indicative because it depends on the experimental RDCs to be used and also on the quality of the geometry of the computer-generated structures to be fit. For quantifying an objective level of efficient discrimination, a *Q* ratio (Q_r) factor comparing the two lowest *Q* structures and a *Q* global (Q_g) factor, defined as Q_r/Q_{avg}, where Q_{avg} is the average *Q* factor for all involved stereoisomers, to get more insight on the overall discrimination quality over the whole set of possible isomers are introduced (Tables 1, S1 and S2 and Fig. S2).

In 2012, a new strategy to assign diastereotopic CH_2 protons by calculating the alignment tensor and performing the selection of configuration without previous assignment the CH_2 proton was reported.[4] Once the alignment tensor was known, a new input file in MSpin was created, and the individual couplings for $^{1}D_{CHa}$ and $^{1}D_{CHb}$ were back predicted. The reason why the tensor has to be used is that if the SVD fitting is performed using the sums $^{1}D_{CHa}$ + $^{1}D_{CHb}$ for CH_2 groups, the program back calculates only the sums. In this previous work, the sums were collected using the F1 ^{1}H-coupled *J*-scaled BIRD HSQC, which fails to provide the individual values for $^{1}D_{CHa}$ and $^{1}D_{CHb}$ separately. Hence, in order to compare the back calculated individual couplings, we measured them using the *J*-scaled BIRD HMQC-HSQC experiment, which suffers from serious distortions ('banana-shaped' peaks), and both the *J* and *T* splittings could not be measured accurately. In the current work, we can measure simultaneously each individual CH_2 splitting together with the $^{2}J_{HH}/^{2}D_{HH}$, and we can exploit a very useful feature implemented in MSpin. If we perform SVD fittings of RDC data to structures using an input file that only contains the $^{1}D_{CH}$ values for CH groups and the $^{2}D_{HH}$ values for CH_2 groups, leaving blank the fields for the $^{1}D_{CH}$ values for CH_2 groups, the program back calculates all the values including those that were left blank. To score the quality of the fitting, the *Q* factor is calculated using only the experimental values that were fed into the program comparing the experimental with the back-calculated RDCs. Selection of configuration is performed using only these experimental values without the need of *a priori* assignment of the diastereotopic protons. For instance, the calculation with the exclusive use of $^{1}D_{CH}$ only for CH distinguishes the correct structure of strychnine (with five CH stereocenters) but with modest Q_r (0.73) and Q_g (2.77) values. The inclusion of $^{2}D_{HH}$ in this calculation generates a significant divergence in the incorrect structure, improving Q_r up to 0.50, although Q_g remains moderate (1.71). This same tendency on the improved discrimination quality is generally observed when adding $^{2}D_{HH}$ in any calculation. At this moment, each diastereotopic proton was straightforwardly assigned by comparison of the back-calculated RDCs with the experimental ones, and the corresponding experimental $^{1}D_{CH}$ values are added to the input table for a new SVD fitting (Table S3). Clearly, the best degree of discrimination

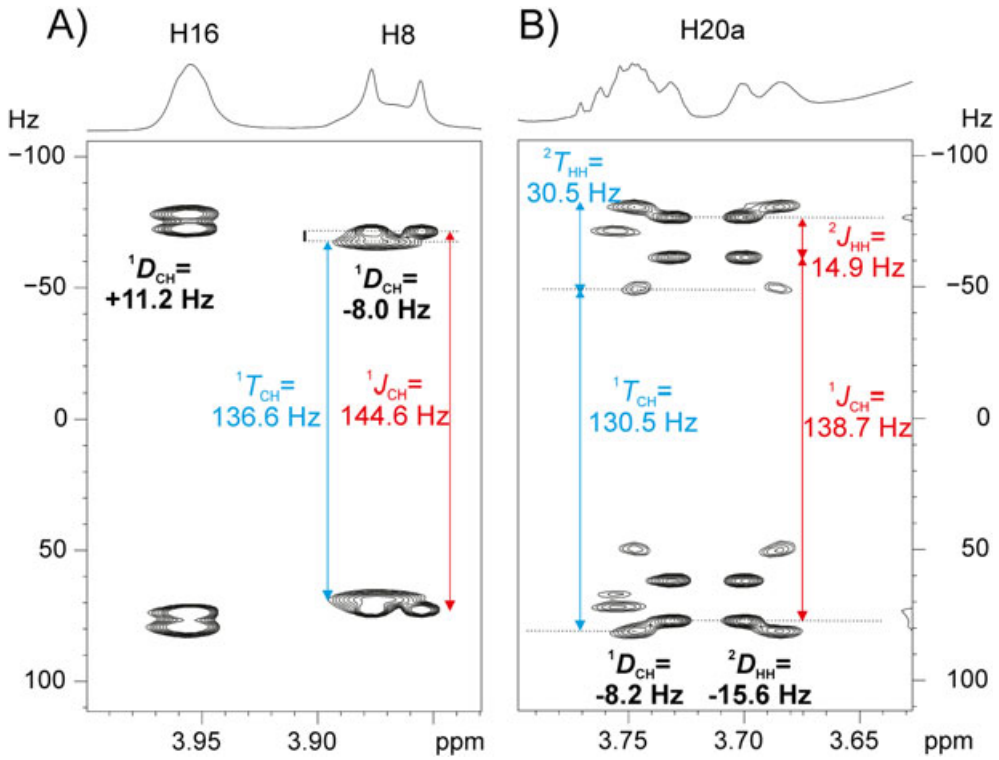

Figure 3. Coupling patterns for individual signals in the $^{1}J_{CH}/^{2}J_{HH}$-resolved spectrum of strychnine in poly(methyl methacrylate)-$CDCl_3$ gel: (A) the C16–H16 and C8–H8 methine protons and (B) the diastereotopic H20 proton belonging to the CH20a–H20b group. Signals corresponding to the isotropic component are distinguished from their sharper line widths.

Table 1. Summary of the individual quality (*Q*), *Q* ratio (Q_r) and *Q* global (Q_g) factors obtained from several fittings of residual dipolar coupling constant data applied to (**1**)

	Q factors			
NMR restraints	7*R*,8*S*,12*S*,13*R*,14*R*,16*S*	7*R*,8*S*,12*R*,13*R*,14*R*,16*S*	*Q* ratio	*Q* global
$^{1}D_{CH}$ only for CH	0.098	0.134	0.73	2.77
$^{1}D_{CH}$ only for CH + $^{2}D_{HH}$	0.094	0.188	0.50	1.71
$^{1}D_{CH}$ for all CH/CH_2	0.116	0.247	0.47	0.93
$^{1}D_{CH}$ for all CH/CH_2 + $^{2}D_{HH}$	0.112	0.262	0.43	0.87
$^{1}D_{CH}$ for CH and sum for CH_2	0.105	0.156	0.67	2.34
$^{1}D_{CH}$ for CH and sum for CH_2 + $^{2}D_{HH}$	0.098	0.198	0.49	1.69

is achieved using individual $^{1}D_{CH}$ for each CH and CH_2 protons with lowest Q_r and Q_g factors of 0.43 and 0.87, respectively. These Q_r factors are in strong agreement with previously reported results for strychnine/PMMA-$CDCl_3$, using other NMR experiments ($Q_r = 0.39$)[4] or adding other NMR restraints such as long-range CH couplings (Q_r = 0.45 with $^{1}D_{CH}$; Q_r = 0.76 with $^{n}D_{CH}$; and Q_r = 0.48 with $^{1}D_{CH}$ + $^{n}D_{CH}$)[15] or ^{13}C residual chemical shift anisotropy (RCSA) ($Q_r = 0.43$ with $^{1}D_{CH}$ + ^{13}C RCSA and $Q_r = 0.49$ with only ^{13}C RCSA)[16] (Table S4). Very similar results are also obtained with RDC data collected at a different compression (^{2}H $\nu_Q(CDCl_3)$ = 49 Hz) (Fig. S3 and Tables S3 and S5).

Conclusions

In summary, it has been shown a general strategy for the fast and efficient discrimination of the correct configuration of strychnine against all its possible stereoisomers using both $^{1}D_{CH}$ and $^{2}D_{HH}$ RDCs. The advantages of such an approach are based on several combined facts: (i) an efficient NMR experiment that provides reliable values of $^{1}J_{CH}/^{1}T_{CH}$ for both CH and diastereotopic CH_2 protons as well as of the geminal $^{2}J_{HH}/^{2}T_{HH}$ couplings in a sensitive and straightforward way, (ii) the use of a particular sample condition (PMMA gel) that allows to visualize directly in a single spectrum both isotropic (*J* couplings) and anisotropic (*T* couplings) components, (iii) the direct determination of the corresponding $^{1}D_{CH}$ and $^{2}D_{HH}$ RDCs from a single NMR dataset, (iv) a fast and straightforward strategy to assign all pairs of diastereotopic protons on-the-fly as the discrimination of the correct structure is performed and (v) the improved structural discrimination quality when all these RDCs data are jointly used in the calculation. It has been shown that this better discrimination is not based on an improvement of the *Q* factor in the correct structure, but considerably poor fitting results for the rest of

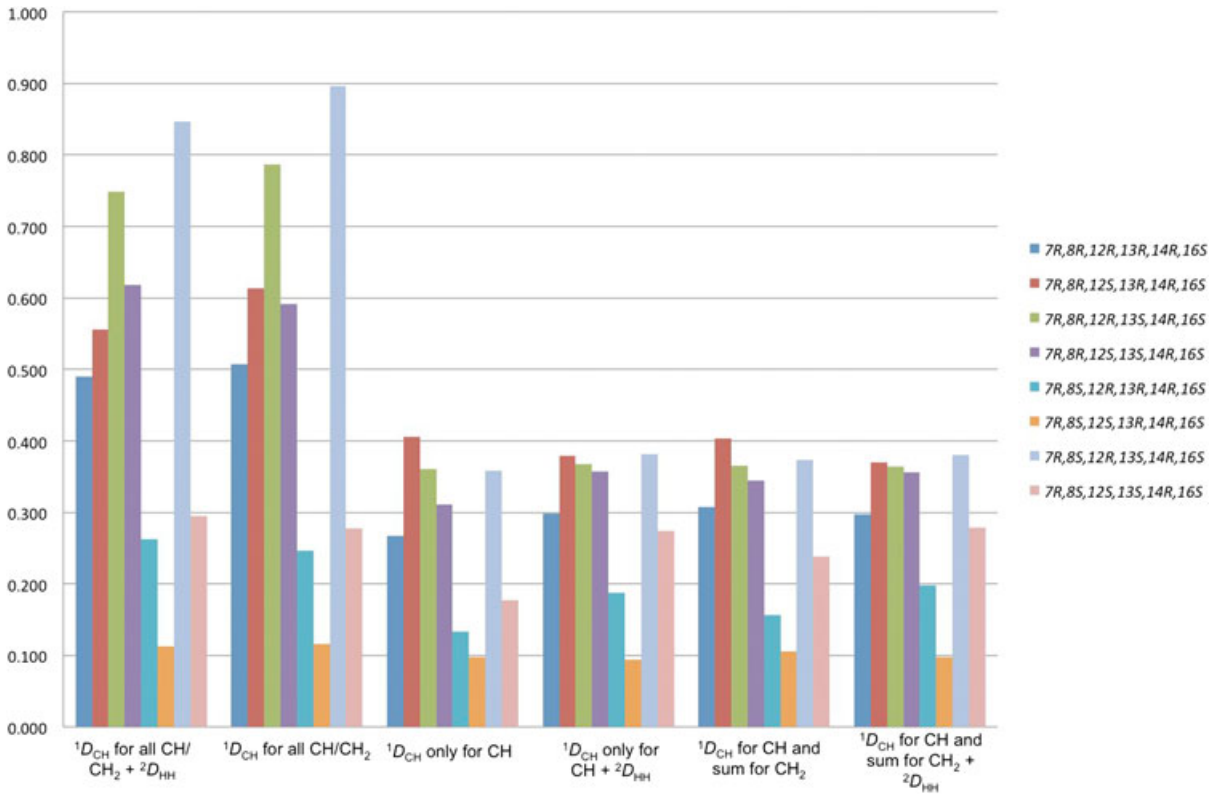

Figure 4. *Q* factors (*y*-axis) obtained for eight possible structures of strychnine using six different sets of $^1D_{CH}$ and/or $^2D_{HH}$ residual dipolar coupling constants determined from a single J_{CH}/J_{HH}-resolved spectrum. Note that (i) all calculations determine the correct structure (lowest *Q* factor) with configuration 7*R*,8*S*,12*S*,13*R*,14*R*,16*S* and (ii) the major overall discrimination is achieved using individual $^1D_{CH}$ for all CH and CH$_2$ protons (with and without $^2D_{HH}$).

the incorrect structures. Using the novel Q_r and Q_g quality factors, a fast view about the overall quality of discrimination between the possible candidate structures and the complete set of structures, respectively, can be realized. This strategy should also be compatible for molecules involving CH_3 groups or for other samples with different alignment properties or dissolved in other alignment media.

Methods and Materials

All NMR experiments were recorded on a Bruker Avance 500 spectrometer (Bruker Corporation, Rheinstetten, Germany) equipped with a cryoprobe at 298 K. The sample consisted of 20 mg of strychnine (**1**) aligned in a PMMA gel swollen in $CDCl_3$ using the reversible compression/relaxation method.[4] Two different measurements were performed using compressions with ^{2}H quadrupolar splitting ($\Delta\nu_Q$) for the $CDCl_3$ of 26 and 49 Hz.

Two-dimensional $^1J_{CH}/^2J_{HH}$-resolved spectra were recorded with proton 90 ° pulses of 6.0 μs and carbon 90 ° pulses of 14.0 μs. For broadband carbon inversion and refocusing, 0.5-ms-smoothed Chirp pulses and a four-Chirp composite pulse of 2 ms duration were used, respectively. The interpulse Δ delays in INEPT and BIRD elements were set to 3.5 ms ($\Delta = 1/(2\times {}^1J_{CH})$) and the recycle delay to 1 s. Two scans were accumulated for each one of the 128 t_1 increments, and the number of complex data points in t_2 was set to 2048. Spectra were acquired with an spectral window of 5000 Hz (in ω_2) and 250 Hz (in ω_1) giving an FID resolution of 4.9 (F2) and 3.90 (F1) Hz, respectively. Prior to Fourier transformation of each data, zero filling to 2048 in ω_1 and a π/2-shifted-squared cosine window function (QSINE, SSB: 2) in both dimensions were applied. After applying zero filling, the digital resolution was 2.44 (F2) and 0.12 (F1) Hz, respectively. Gradient ratios for G1 : G2 were set to 80 : 20.1 measured as percentage of the absolute gradient strength of 53.5 G/cm. Sine bell-shaped gradients had 1 ms of duration and were followed by a recovery delay of 100 μs (δ). All experiments were acquired and processed using the echo/anti-echo protocol where the gradient G1 was inverted for every second FID.

The 3D structures of all compounds were generated using the MacroModel Suite from Shrödinger (https://www.schrodinger.com/MacroModel/). The diastereomers were automatically generated using the LigPrep module in MacroModel and further energy minimized using the molecular mechanics force field (MMFF). AM1 and density functional theory (DFT) (B3LYP/6-31G*) calculations were performed in Gaussian 09 (http://www.gaussian.com). As performed in Snider *et al.*,[4] because of ring tension limitations, eight geometrically possible 3D diastereomeric structures of strychnine (**1**) were generated, which has six chiral carbons (7, 8, 12, 13, 14 and 16). Maintaining the absolute configuration of C7 as *R* and keeping the configurations of C14 and C16 as *R* and *S*, respectively (due to geometrical restrictions), there are three remaining chiral carbons to vary in order to generate a pool of $2^3 = 8$ possible configurations: (i) 7*R*,8*R*,12*R*,13*R*,14*R*,16*S*; (ii) 7*R*,8*R*,12*S*,13*R*,14*R*,16*S*; (iii) 7*R*,8*R*,12*R*,13*S*,14*R*,16*S*; (iv) 7*R*,8*R*,12*S*,13*S*,14*R*,16*S*; (v) 7*R*,8*S*,12*R*,13*R*,14*R*,16*S*; (vi) 7*R*,8*S*,12*S*,13*R*,14*R*,16*S*; (vii) 7*R*,8*S*,12*R*,13*S*,14*R*,16*S*; and (viii) 7*R*,8*S*,12*S*,13*S*,14*R*,16*S*. Calculations have also been performed on the basis of 13 diastereoisomeric structures calculated at a DFT level (Table S6 and Fig. S4), obtaining similar results and general trends as using the MM-based eight stereoisomers database.

Fitting of RDC data to structures was performed using the MSpin software package (Mestrelab Research SL, Santiago de Compostela, Spain; http://www.mestrelab.com).

Acknowledgements

Financial support for this research provided by Spanish MINECO (project CTQ2015-64436-P) is gratefully acknowledged. We also thank to the Servei de Ressonància Magnètica Nuclear, Universitat Autònoma de Barcelona, for allocating instrument time to this project. NMR instrumentation at Carnegie Mellon University was partially supported by the US National Science Foundation (NSF) (CHE-0130903 and CHE-1039870). R. R. G. gratefully acknowledges support from the NSF (CHE-1111684).

References

[1] a) C. M. Thiele. *Concepts Magn. Reson. Part A* **2007**, *30A*, 65–80; b) C. M. Thiele. *European J. Org. Chem.* **2008**, *34*, 5673–5685; c) G. Kummerlöwe, B. Luy. *Ann. Rep. NMR Spectroscopy* **2009**, *68*, 193–232; d) R. R. Gil. *Angew. Chem. Int. Ed. Engl.* **2011**, *50*, 7222–7224; e) R. R. Gil, C. Griesinger, A. Navarro-Vázquez, H. Sun. *Structure Elucidation in Organic Chemistry*, Wiley-VCH Verlag GmbH & Co. KGaA, **2015**, pp. 279–324; f) R. R. Gil. *Reference Module in Chemistry, Molecular Sciences and Chemical Engineering*, Encyclopedia of Spectroscopy and Spectrometry, Elsevier Inc., **2017**, 946–955.

[2] A. Enthart, J. C. Freudenberger, J. Furrer, H. Kessler, B. Luy. *J. Magn. Reson.* **2008**, *192*, 314–322.

[3] a) I. Timári, L. Kaltschnee, A. Kolmer, R. W. Adams, M. Nilsson, C. M. Thiele, G. A. Morris, K. E. Kövér. *J. Magn. Reson.* **2014**, *239*, 130–138; b) T. Reinsperger, B. Luy. *J. Magn. Reson.* **2014**, *239*, 110–120; c) L. Kaltschnee, A. Kolmer, I. Timari, V. Schmidts, R. W. Adams, M. Nilsson, K. E. Kövér, G. A. Morris, C. M. Thiele. *Chem. Commun.* **2014**, *50*, 2512–2514; d) I. Timári, L. Kaltschnee, M. H. Raics, F. Roth, N. G. A. Bell, R. W. Adams, M. Nilsson, D. Uhrín, G. A. Morris, C. M. Thiele, K. E. Kövér. *RSC Advances* **2016**, *6*, 87848–87855.

[4] a) R. R. Gil, C. Gayathri, N. V. Tsarevsky, K. Matyjaszewski. *J. Org. Chem.* **2008**, *73*, 840–848; b) C. Gayathri, N. V. Tsarevsky, R. R. Gil. *Chem. A Eur. J.* **2010**, *16*, 3622–3626; c) J. D. Snider, E. Troche-Pesqueira, S. R. Woodruff, C. Gayathri, N. V. Tsarevsky, R. R. Gil. *Magn. Reson. Chem.* **2012**, *5*, S86–S91.

[5] a) K. Feher, S. Berger, K. E. Kövér. *J. Magn. Reson.* **2003**, *163*, 340–346; b) C. M. Thiele, W. Bermel. *J. Magn. Reson.* **2012**, *216*, 134–143; c) K. E. Kövér, K. Feher. *J. Magn. Reson.* **2004**, *168*, 307–313.

[6] a) M. L. Liu, R. D. Farrant, J. M. Gillam, J. K. Nicholson, J. C. Lindon. *J. Magn. Reson. Ser. B* **1995**, *109*, 275–283; b) L. Ziani, J. Courtieu, D. Merlet. *J. Magn. Reson.* **2006**, *183*, 60–67; c) U. R. Prabhu, S. R. Chaudhari, N. Suryaprakash. *Chem. Phys. Lett.* **2010**, *500*, 334–341; d) L. Castañar, M. García, E. Hellemann, P. Nolis, R. R. Gil, T. Parella. *J. Org. Chem.* **2016**, *81*, 11126–11131.

[7] J. Saurí, L. Castañar, P. Nolis, A. Virgili, T. Parella. *J. Magn. Reson.* **2014**, *242*, 33–40.

[8] a) C. M. Thiele, S. Berger. *Org. Lett.* **2003**, *5*, 705–708; b) C. M. Thiele. *J. Org. Chem.* **2004**, *69*, 7403–7413; c) R. R. Gil, C. Gayathri, N. V. Tsarevsky, K. Matyjaszewski. *J. Org. Chem.* **2008**, *73*, 840–848.

[9] a) M. Ottiger, F. Delaglio, J. L. Marquardt, N. Tjandra, A. Bax. *J. Magn. Reson.* **1998**, *134*, 365–369; b) J. A. Losonczi, M. Andrec, M. W. Fischer, J. H. Prestegard. *J. Magn. Reson.* **1999**, *138*, 334–342.

[10] a) P. Tzvetkova, S. Simova, B. Luy. *J. Magn. Reson.* **2007**, *186*, 193–200; b) J. Furrer, M. John, H. Kessler, B. Luy. *J. Biomol. NMR* **2007**, *37*, 231–243; c) E. Miclet, D. C. Williams Jr., G. M. Clore, D. L. Bryce, J. Boisbouvier, A. Bax. *J. Am. Chem. Soc.* **2004**, *126*, 10560–10570; d) T. Carlomagno, W. Peti, C. Griesinger. *J. Biomol. NMR* **2000**, *17*, 99–109.

[11] M. J. Thrippleton, J. Keeler. *Angew. Chem. Intl. Ed.* **2003**, *42*, 3938–3941.

[12] a) B. Luy. *J. Magn. Reson.* **2009**, *201*, 18–24; b) L. Castañar, J. Saurí, R. T. Williamson, A. Virgili, T. Parella. *Angew. Chem. Intl. Ed.* **2014**, *53*, 8379–8382; c) N. Giraud, L. Béguin, J. Courtieu, D. Merlet. *Angew. Chem. Intl. Ed.* **2010**, *20*, 3481–3484.

[13] L. F. Gil-Silva, R. Santamaría-Fernández, A. Navarro-Vázquez, R. R. Gil. *Chem. A Eur. J.* **2016**, *22*, 472–476.

[14] A. Navarro-Vázquez. *Magn. Reson. Chem.* **2012**, *50*, S73–S79.

[15] N. Nath, E. J. d'Auvergne, C. Griesinger. *Angew. Chem. Intl. Ed.* **2015**, *54*, 12706–12710.

[16] N. Nath, M. Schmidt, R. R. Gil, R. T. Williamson, G. E. Martin, A. Navarro-Vázquez, C. Griesinger, Y. Liu. *J. Am. Chem. Soc.* **2016**, *138*, 9548–9556.

Supporting information

Additional supporting information may be found in the online version of this article at the publisher's web site.

Structural discrimination from *in-situ* measurement of $^{1}D_{CH}$ and $^{2}D_{HH}$ residual dipolar coupling constants

Núria Marcó,[1] Roberto R. Gil[2,*] and Teodor Parella[1,*]

[1]Servei de Ressonància Magnètica Nuclear, Universitat Autònoma de Barcelona, Facultat de Ciències, E-08193 Bellaterra (Barcelona), Catalonia, Spain.

[2] Department of Chemistry, Carnegie Mellon University, Pittsburgh, PA, United States

Table of Contents

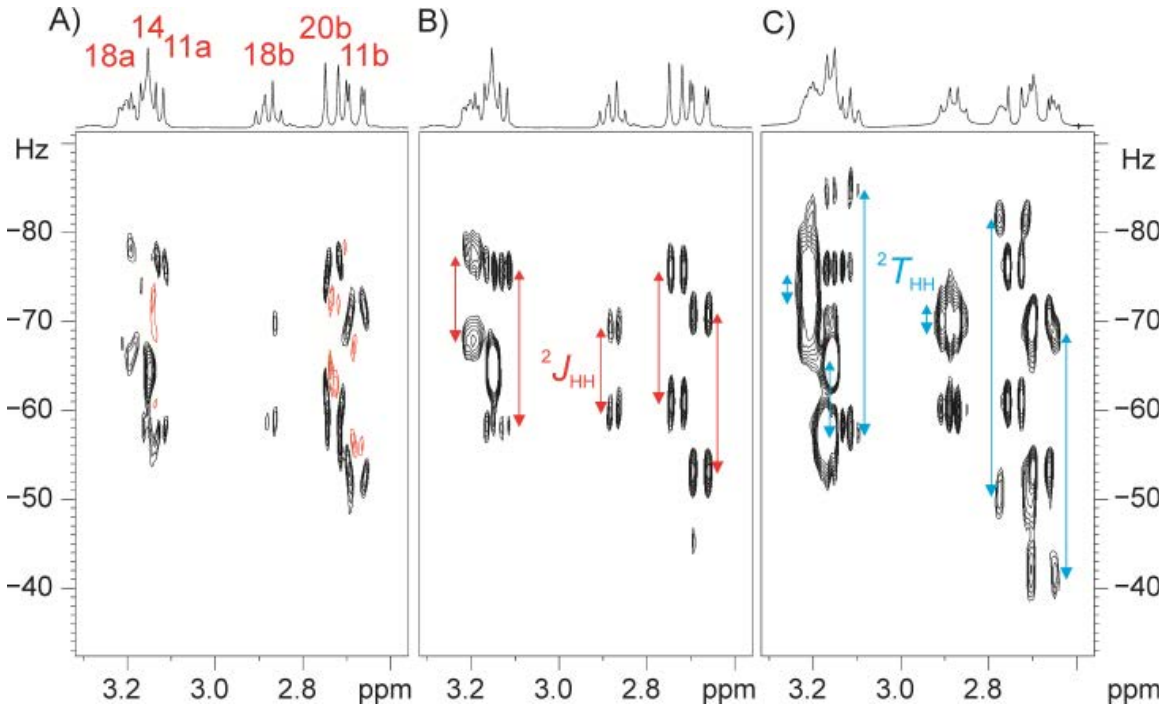

Figure S1. Expanded region of the 2D J_{CH}/J_{HH}-resolved spectra of **1** in A-B) isotropic ($CDCl_3$) and C) anisotropic ($CDCl_3$-PMMA) sample conditions. Effect on the spectral quality achieved A) without and B) with application of the ZQF element (30 ms adiabatic CHIRP pulse applied simultaneously with a weak (3%) rectangular gradient of the same duration). B-C) Isotropic *vs.* anisotropic spectra showing that the isotropic component in the anisotropic sample can be used as an internal reference to determine directly $^1D_{CH}$ and $^2D_{HH}$ by peak distance measurement in spectrum C. Vertical red and blue arrows indicate $^2J_{HH}$ and $^2T_{HH}$, respectively.

Table S1: *Q* factors obtained for eight possible structures of strychnine using different set of RDCs $\Delta\nu_Q$ ($CDCl_3$) = 26 Hz). They were calculated using 10 $^1D_{CH}$ for CH, 8 $^1D_{CH}$ for CH_2 and 4 $^2D_{HH}$ (H17 and H18 protons were excluded).

Isomer	$^1D_{CH}$ for all CH/CH_2 + $^2D_{HH}$	$^1D_{CH}$ for all CH/CH_2	$^1D_{CH}$ only for CH	$^1D_{CH}$ only for CH + $^2D_{HH}$	$^1D_{CH}$ for CH and $\Sigma(^1D_{CHa}+^1D_{CHb})$ for CH_2	$^1D_{CH}$ for CH and $\Sigma(^1D_{CHa}+^1D_{CHb})$ for CH_2 + $^2D_{HH}$
7R,8R,12R,13R,14R,16S	0,489	0,507	0,267	0,298	0,308	0,297
7R,8R,12S,13R,14R,16S	0,555	0,613	0,406	0,379	0,403	0,370
7R,8R,12R,13S,14R,16S	0,749	0,787	0,361	0,368	0,365	0,364
7R,8R,12S,13S,14R,16S	0,619	0,592	0,311	0,357	0,345	0,356
7R,8S,12R,13R,14R,16S	0,262	0,247	0,134	0,188	0,156	0,198
7R,8S,12S,13R,14R,16S	**0,112**	**0,116**	**0,098**	**0,094**	**0,105**	**0,098**
7R,8S,12R,13S,14R,16S	0,847	0,897	0,359	0,382	0,374	0,380
7R,8S,12S,13S,14R,16S	0,295	0,278	0,177	0,274	0,238	0,278
Q_{ratio}	0,43	0,47	0,73	0,50	0,67	0,49
$Q_{average}$	0,491	0,504	0,264	0,292	0,287	0,293
Q_{global}	0,871	0,933	2,783	1,712	2,354	1,689

The *Q* factors obtained from the same RDCs datasets using a DFT structure of the correct isomer *7R,8S,12S,13R,14R,16* are:

	DFT	MM
$^1D_{CH}$ for all CH/CH_2 + $^2D_{HH}$	0,082	0,112
$^1D_{CH}$ for all CH/CH_2	0,088	0,116
$^1D_{CH}$ only for CH	0,080	0,098
$^1D_{CH}$ only for CH + $^2D_{HH}$	0,072	0,094

The effect to exclude the smallest RDCs (highest errors) of the calculation ($^1D_{CH}$ for all CH/CH_2 + $^2D_{HH}$) is summarized in the following table:

	Q factors (26 Hz) *7R,8S,12S,13R, 14R,16S*	*7R,8S,12R,13 R,14R,16S*	Q_{ratio}	Q_{global}
Calc 1: Excluding H17a/b & H18a/b	0,111	0,257	0,43	0,879
Calc 2: calc 1 + Excluding H13	0,1	0,252	0,40	0,829
Calc 3: Calc 2 + Excluding H15aH15b	0,09	0,253	0,36	0,749
calc 3 using the DFT structure	0,061			

Table S2: Comparison of several *Q* factors for different calculations and datasets performed at $\Delta\nu_Q$ ($CDCl_3$) = 26 and 49 Hz.

	Q factors (26 Hz)			
	7R,8S,12S,13R ,14R,16S	*7R,8S,12R,13R ,14R,16S*	*Q*ratio	*Q*global
$^1D_{CH}$ only for CH	0,098	0,134	0,73	2,770
$^1D_{CH}$ only for CH + $^2D_{HH}$	0,094	0,188	0,50	1,712
$^1D_{CH}$ for all CH/CH2	0,116	0,247	0,47	0,932
$^1D_{CH}$ for all CH/CH2 + $^2D_{HH}$	0,112	0,262	0,43	0,871
$^1D_{CH}$ for CH and the sum $^1D_{CHa}$+$^1D_{CHb}$ for CH_2	0,105	0,156	0,67	2,345
$^1D_{CH}$ for CH and sum$^1D_{CHa}$+$^1D_{CHb}$ for CH_2 + $^2D_{HH}$	0,098	0,198	0,49	1,689
	Q factors (49 Hz)			
	7R,8S,12S,13R ,14R,16S	*7R,8S,12R,13R ,14R,16S*	*Q*ratio	*Q*global
$^1D_{CH}$ only for CH	0,055	0,106	0,52	2,109
$^1D_{CH}$ only for CH + $^2D_{HH}$	0,078	0,178	0,44	1,485
$^1D_{CH}$ for all CH/CH2	0,101	0,247	0,41	0,802
$^1D_{CH}$ for all CH/CH2 + $^2D_{HH}$	0,11	0,27	0,41	0,812
$^1D_{CH}$ for CH and the sum $^1D_{CHa}$+$^1D_{CHb}$ for CH_2	0,064	0,129	0,50	1,798
$^1D_{CH}$ for CH and the sum $^1D_{CHa}$+$^1D_{CHb}$ for CH_2 + $^2D_{HH}$	0,082	0,189	0,43	1,461

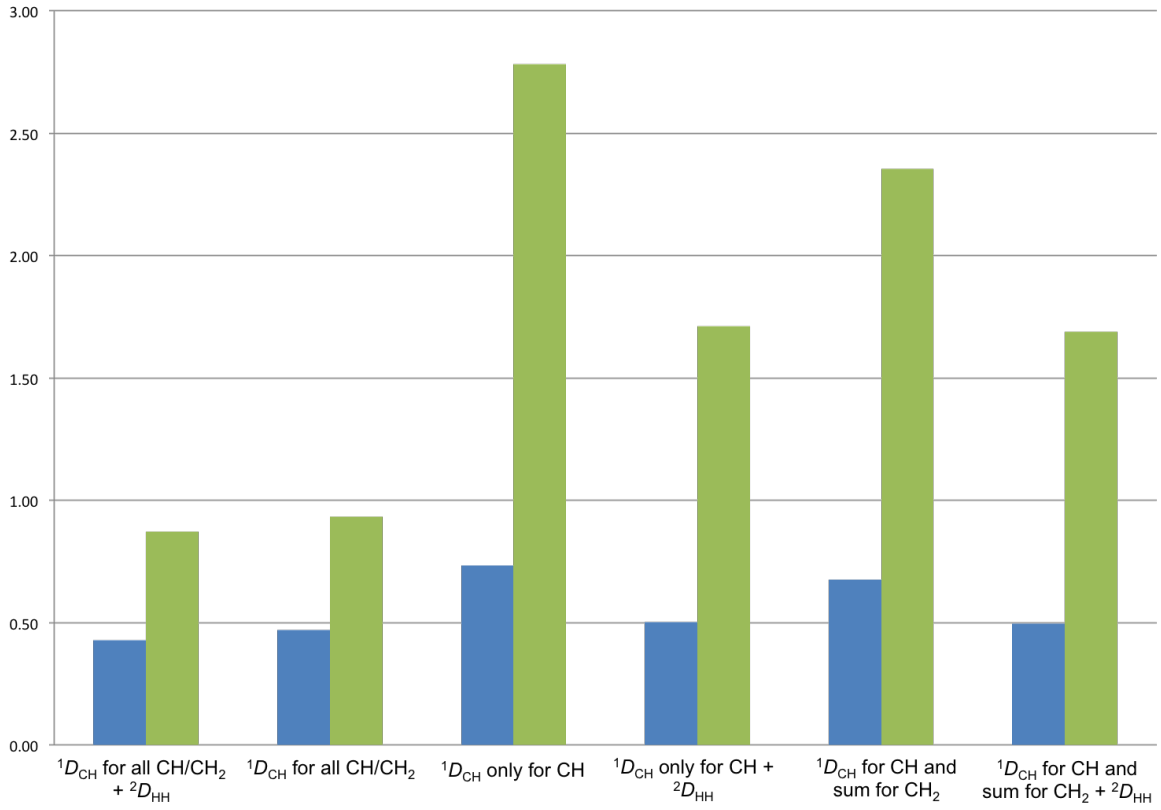

Figure S2. Q_r (blue) and Q_g (green) quality factors obtained for six different sets of $^1D_{CH}$ and/or $^2D_{HH}$ RDCs determined from a single J_{CH}/J_{HH}-resolved spectrum ($\Delta\nu_Q$ ($CDCl_3$) = 26 Hz) (see table S1A). The lowest Qr and Qg determines the best quality factors for discriminating the correct configuration of strychnine between the two lowest and all possible stereoisomers, respectively.

Table S3: Scalar, total and residual dipolar coupling constants of strychnine measured in $CDCl_3$-PMMA gel at $\Delta\nu_Q$ ($CDCl_3$) = 26 and 49 Hz.

	($\Delta\nu_Q$ ($CDCl_3$) = 36 Hz)[a]		This work ($\Delta\nu_Q$ ($CDCl_3$) = 26 Hz)			This work ($\Delta\nu_Q$ ($CDCl_3$) = 49 Hz)		
	J	*D*	*J*	*T*	*D*	*J*	*T*	*D*
C1H1	158.38	20.97	159.1	176.5	17.4	159.1	193.2	34.1
C2H2	161.70	12.29	161.2	170.6	9.4	161.2	181	19.8
C3H3	160.19	10.04	161.9	169.1	7.2	161.9	176.,1	14,2
C4H4	168.35	21.58	170.7	188.3	17.6	170.7	205.5	34.8
C8H8	144.91	-9,75	144.6	136.6	-8.0	144.6	128.7	-15.9
C12H12	149.03	-20,59	149.1	132.1	-17	149.1	114.9	-34,2
C13H13	124.88	-4,87	123.7	122.4	-1.3	123.7	119.4	-4.3
C14H14	131.03	-20,66	130.9	116.1	-14.8	130.9	95.9	-35
C16H16	146.55	14,04	146.7	157.9	11.2	146.7	170.7	24
C22H22	158.91	-1,06	159.5	159.5	0	159.5	159.5	0
C11H11a	260.84	-3.46	134.8	143.4	8.6	134.8	150	15.2
C11H11b			124.8	111.2	-13.6	124.8	97.8	-27
C15H15a	260.66	2.54	129.2	131.4	2.2	129.2	137.8	8.6
C15H15b			130.3	134.5	4.2	130.3	130.7	0.4
C17H17a	265.92	1.38	133,1			133.1	133.1	
C17H17b			133.1			133.1	133.1	
C18H18a	276.20	6.89	146	145.5	-0.5	146	145	-1
C18H18b			130.5	140.5	10	130.5	153.3	22.8
C20H20a	276.56	-7.39	138.7	130.5	-8.2	138.7	123.1	-15.6
C20H20b			137.7	132.9	-4.8	137.7	128.9	-8.8
C23H23a	282.42	-10.3	144.8	149.4	4.6	144.8	159.9	15.1
C23H23b			137.9	116.5	-21.4	137.9	93.3	-44.6
H11aH11b			-17.7	-27.5	-9.8	-17.7	-36.7	-19

H15aH15b			-14.8	-3.2	11.6	-14.8	7.2	22
H17ah17b				0			0	
H18aH18b			-9.5	2	11.5	-9.5	11.5	21
H20aH20b			-14.9	-30.5	-15.6	-14.9	-44.9	-30
H23ah23b			-14.4	-26.4	-12	-14.4	-35.4	-21

[a] Data extracted from: J. D. Snider, E. Troche-Pesqueira, S. R. Woodruff, C. Gayathri, N. V. Tsarevsky and R. R. Gil, *Magn. Reson. Chem.*, **2012**, *5*, S86-S91.

Table S4: Comparison of all quality factors obtained in this work with those calculated from other related works.

	Q factors				
NMR Restraints	*7R,8S,12S,13R, 14R,16S*	*7R,8S,12R,13R, 14R,16S*	***Q* ratio**	***Q* global**	
$^1D_{CH}$ only for CH	0,098	0,134	**0,73**	**2,770**	This work
$^1D_{CH}$ only for CH + $^2D_{HH}$	0,094	0,188	**0,50**	**1,712**	This work
$^1D_{CH}$ for all CH/CH_2	0,116	0,247	**0,47**	**0,932**	This work
$^1D_{CH}$ for all CH/CH_2 + $^2D_{HH}$	0,112	0,262	**0,43**	**0,871**	This work
$^1D_{CH}$ for CH and the sum $^1D_{CHa}$+$^1D_{CHb}$ for CH_2	0,105	0,156	**0,67**	**2,345**	This work
$^1D_{CH}$ for CH and the sum $^1D_{CHa}$+$^1D_{CHb}$ + $^2D_{HH}$	0,098	0,198	**0,49**	**1,689**	This work
$^1D_{CH}$ for CH and the sum $^1D_{CHa}$+$^1D_{CHb}$ for CH_2	0,045	0,115	**0,391**		With JSB-HSQC[a]
$^1D_{CH}$ for CH and $^1D_{CHa}$+$^1D_{CHb}$ for CH_2	0,054	0,115	**0,470**		[b]
$^1D_{CH}$ + ^{13}C RCSA	0,05	0,1	**0,500**		stretching[c]
Only ^{13}C RCSA	0,071	0,129	**0,550**		stretching[c]

$^1D_{CH}$ + ^{13}C RCSA	0,174	0,399	**0,436**		compression [c]
Only ^{13}C RCSA	0,19	0,389	**0,488**		compression [c]
$^1D_{CH}$	0,086	0,189	**0,455**		[d]
only $^nD_{CH}$	0,17	0,223	**0,762**		[d]
$^1D_{CH}$ + $^nD_{CH}$	0,09	0,186	**0,484**		[d]

[a] J. D. Snider, E. Troche-Pesqueira, S. R. Woodruff, C. Gayathri, N. V. Tsarevsky and R. R. Gil, *Magn. Reson. Chem.*, **2012**, *5*, S86-S91.
[b] With our DFT-based structure
[c] N. Nath, M. Schmidt, R.R. Gil, R.T. Williamson, G.E. Martin, A. Navarro-Vázquez, C. Griesinger and Y. Liu, *J. Am. Chem. Soc.*, **2016**, *138*, 9548-9556.
[d] N. Nath, E. J. d'Auvergne and C. Griesinger, *Angew. Chem. Intl. Ed.,* **2015**, *54*, 12706-12710.

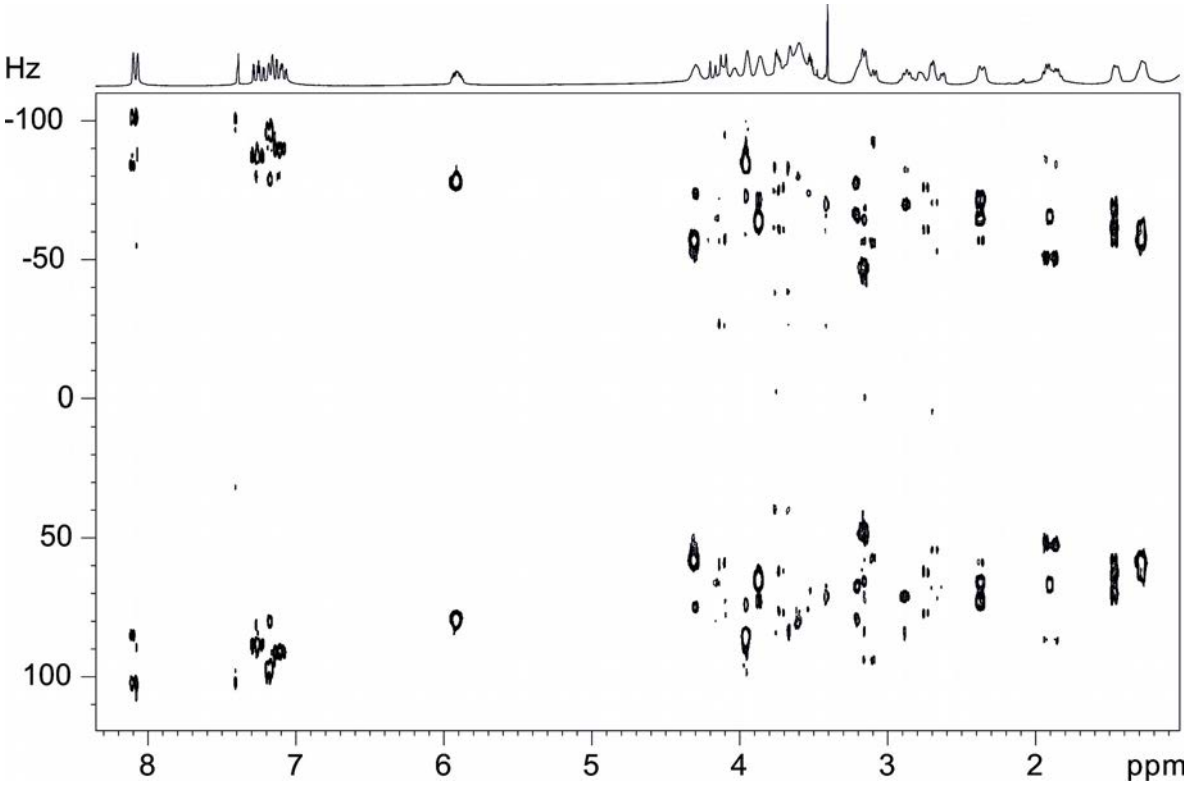

Figure S3: $^1J_{CH}/^2J_{HH}$-Resolved spectrum of strychnine in $CDCl_3$/PMMA gel ($\Delta\nu_Q$ = 49Hz).

Table S5: Experimental and calculated RDCs (at two different compressions) obtained for the DFT-based structure of the correct structure of strychnine:

	Q = 0,085 $\Delta\nu_Q$ =26 Hz		Q = 0,090 $\Delta\nu_Q$ = 49 Hz	
	Exp	Calc	Exp	Calc
C1H1	17.4	16.85	34.1	32.49
C2H2	9.4	9,66	19.8	22.37
C3H3	7.2	7.85	14.22	16.27
C4H4	17.6	17.09	34.8	32.95
C8H8	-8.04	7.76	-15.9	-12.89
C12H12	-17	-16.69	-34.2	-34.99
C13H13	-1.3	-3.87	-4.3	-5.7
C14H14	-14.8	-16.79	-35	-35.41
C16H16	11.2	10.69	24	24.01
C22H22	0	0.27	0	1.87
C11H11a	8.6	8.92	15.2	17.03
C11H11b	-13.6	-15.17	-27	-29.14
C15H15a	2.2	1.86	8.6	5.31
C15H15b	4.2	3.11	0.4	3.83
C17H17a	-	-4.78	-	-11
C17H17b	-	9.54	-	20.69
C18H18a	-0.5	0.78	-1	0.75
C18H18b	10	10.17	22.8	23.08
C20H20a	-8.2	-7.21	-15.6	-15.95
C20H20b	-4.8	-3.43	-8.8	-5.05
C23H23a	4.6	4.22	15.1	12.15
C23H23b	-21.4	-20.96	-44.6	-43.2
H11aH11	-9.8	-10.25	-19	-20.84

b H15aH15				
b	11.6	11.06	22	20.98
H17ah17b	-	10.27	-	21,72
H18aH18				
b	11.5	10.96	21	22.03
H20aH20				
b	-15.6	.14.47	-30	-27.87
H23ah23b	-12	-12.05	-21	-22.45

Table S6: *Q* factors obtained for 13 possible DFT generated diastereomeric structures of strychinine using different set of RDCs at 2H RQC of 26 Hz. They were calculated using 10 $^{1}D_{CH}$ for CH, 8 $^{1}D_{CH}$ for CH_2 and 4 $^{2}D_{HH}$ (H17 and H18 protons were excluded)

	$^{1}D_{CH}$ for all CH/CH_2 + $^{2}D_{HH}$	$^{1}D_{CH}$ for all CH/CH_2	$^{1}D_{CH}$ only for CH	$^{1}D_{CH}$ only for CH + $^{2}D_{HH}$	$^{1}D_{CH}$ for CH and sums $^{1}D_{CHa}$ +$^{1}D_{CHb}$ for CH_2	$^{1}D_{CH}$ for CH and sums $^{1}D_{CHa}$ +$^{1}D_{CHb}$ for CH_2 + $^{2}D_{HH}$
*RSSRRS*_Strychnine	0,087	0,093	0,080	0,073	0,091	0,080

RSRSRS	0,864	0,917	0,394	0,419	0,420	0,414
RSRSSS	0,727	0,727	0,417	0,629	0,530	0,627
RSRRRS	0,497	0,541	0,105	0,187	0,147	0,198
RSSSRS	0,312	0,306	0,165	0,282	0,265	0,291
RSRRSS	0,768	0,762	0,546	0,700	0,595	0,689
RSSSRS	0,725	0,692	0,550	0,657	0,557	0,644
RSSRSS	0,772	0,786	0,679	0,738	0,694	0,726
SSRSSR	0,547	0,587	0,425	0,393	0,413	0,383
SSSSSR	0,416	0,420	0,233	0,325	0,294	0,328
SSRRSR	0,842	0,876	0,305	0,374	0,351	0,374
SSSRSR	0,431	0,484	0,345	0,373	0,355	0,369
RSRSSR	0,721	0,723	0,345	0,552	0,507	0,567
*Q*ratio	0,28	0,30	0,76	0,39	0,62	0,40
*Q*average	0,59	0,61	0,35	0,44	0,40	0,44
*Q*global	0,47	0,50	2,14	0,89	1,55	0,92

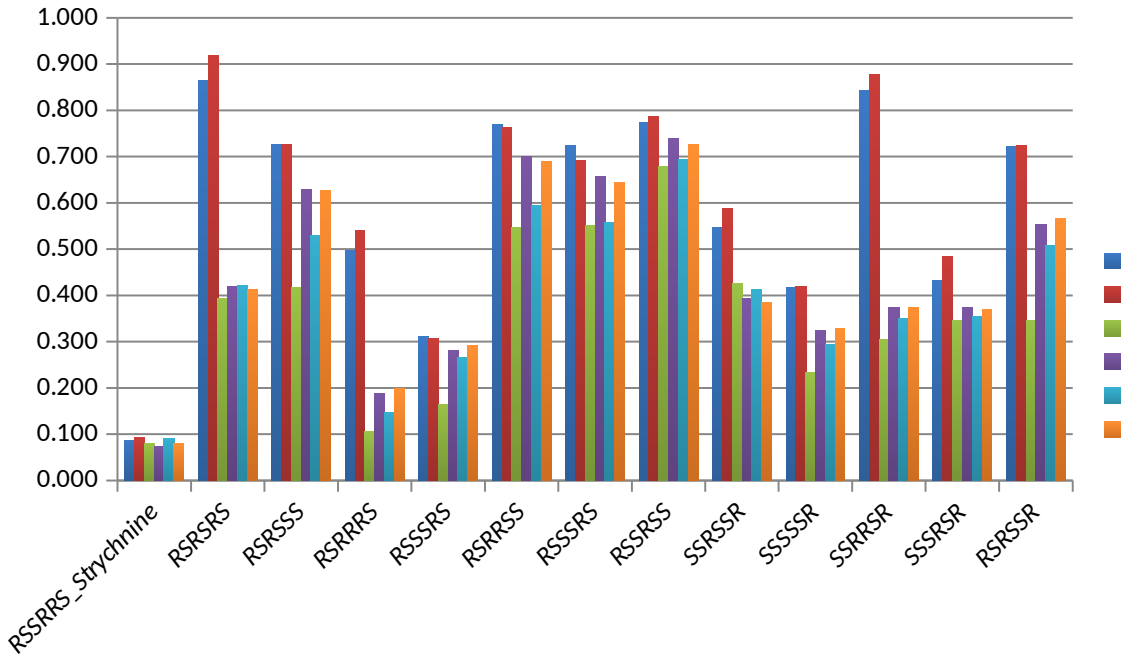

Figure S4. *Q* factors (y-axis) obtained for thirteen possible DFT-based structures of strychnine using six different set of $^{1}D_{CH}$ and/or $^{2}D_{HH}$ RDCs determined from a single J_{CH}/J_{HH}-resolved spectrum (see table S6). Note that i) all calculations determine the correct structure (lowest *Q* factor) with configuration 7*R*,8*S*,12*S*,13*R*,14*R*,16*S*, and ii) the major overall discrimination is achieved using individual $^{1}D_{CH}$ for all CH and CH_2 protons (with and without $^{2}D_{HH}$).

Pulse Program fro BRUKER spectrometers

```
;teo_hsqc_jres
;JCH/JHH-resolved experiment
;for AVANCE spectrometers  (checked TSv3.2)
;with optional BIRD-based homodecoupling (cnst15)
;or 2JHH-resolved format (cnst14)

#include <Avance.incl>
#include <Grad.incl>
#include <Delay.incl>
#include <De.incl>

"p2=p1*2"
"d0=3u"
"d2=1s/(cnst2*2)"
"d4=1s/(cnst2*4)"

"in0=inf1/2"

"DELTA=p16+d16+p2+d13*2-4u"
"DELTA2=d4-p14/2-4u"
"DELTA4=d4-p14/2-4u-p16-d16"
"DELTA5=d2-larger(p2,p14)/2"

if "cnst15==1"
  {
dwellmode explicit
"d22=aq/2*l2"
}

"acqt0=0"
baseopt_echo


1 ze
2 d1 do:f2
  d12 pl1:f1
3 (p1 ph1)
  DELTA2 pl0:f2
  4u
  (center (p2 ph1) (p14:sp3 ph6):f2 )
  4u
  DELTA2 pl2:f2 UNBLKGRAD
  (center (p1 ph2) (p3 ph3):f2 )
  d13
  (p2 ph1)
  d13
  p16:gp1*EA
  d16 pl0:f2
  (p24:sp7 ph4):f2
```

```
 4u
 DELTA pl2:f2
 (center (p1 ph1) (p3 ph4):f2 )
 DELTA2 pl0:f2
 4u
 (center (p2 ph1) (p14:sp3 ph1):f2 )
 4u
 DELTA4
 p16:gp2
 d16

 d0
 (p1 ph1)
 DELTA5 pl0:f2
 (center (p2 ph1) (p14:sp3 ph1):f2 )
 DELTA5 pl2:f2
 (p1 ph1)

 if "cnst14==1"
  {
 (p4 ph1):f2   ;OPTIONAL for specific 2JHH-J-resolved spectrum
}

 d0

 p1 ph2
 d12 pl0:f1
 300u gron0
 p32:sp29:f1 ph1
 100u groff
 d16 BLKGRAD
 d12 pl1:f1
 d12 pl12:f2
 p1 ph1

if "cnst15==1"
  {
   ACQ_START(ph30,ph31)
   0.05u DWL_CLK_ON cpd2:f2
   0.1u REC_UNBLK
   d22
   0.05u DWL_CLK_OFF
   0.1u REC_BLK do:f2


;bird y
5 (p1 ph15)
  DELTA5 pl0:f2
  (center (p2 ph16) (p14:sp3 ph16):f2 )
  DELTA5 pl12:f2
  (p1 ph17)
```

```
;chem. shift refoc.
  20u
  (p2 ph15):f1
  20u

   0.05u DWL_CLK_ON cpd2:f2
   0.1u REC_UNBLK
   d22
   0.05u DWL_CLK_OFF
   0.1u REC_BLK  do:f2

;bird -x
 (p1 ph25)
  DELTA5 pl0:f2
  (center (p2 ph26) (p14:sp3 ph26):f2 )
  DELTA5 pl12:f2
  (p1 ph27)

;chem. shift refoc.
  20u
  (p2 ph25):f1
  20u

   0.05u DWL_CLK_ON  cpd2:f2
   0.1u REC_UNBLK
   d22
   0.05u DWL_CLK_OFF
   0.1u REC_BLK do:f2

 lo to 5 times l2

10 rcyc=2
 }
 else
 {
 go=2 ph31 cpd2:f2
 }

  d1 do:f2 mc #0 to 2
     F1EA(calgrad(EA), caldel(d0, +in0))
exit

ph1=0
ph2=1
ph3=0 2
ph4=0
ph6=0

ph15=1
ph16=2
```

```
ph17=3
ph25=2
ph26=3
ph27=0

ph30=0
ph31=0 2

;pl0 : 120dB
;pl1 : f1 channel - power level for pulse (default)
;pl2 : f2 channel - power level for pulse (default)
;pl10: f1 channel - power level for TOCSY-spinlock
;sp3: f2 channel - shaped pulse 180 degree
;spnam3: Crp60,0.5,20.1
;sp7: f2 channel - shaped pulse (180degree refocussing)
;spnam7: Crp60comp.4
;p1 : f1 channel -  90 degree high power pulse
;p2 : f1 channel - 180 degree high power pulse
;p3 : f2 channel -  90 degree high power pulse
;p14: f2 channel - 180 degree shaped pulse for inversion
;     = 500usec for Crp60,0.5,20.1
;p16: homospoil/gradient pulse                      [1 msec]
;p24: f2 channel - 180 degree shaped pulse for refocussing
;     = 2msec for Crp60comp.4
;d0 : incremented delay (2D)                        [3 usec]
;d1 : relaxation delay; 1-5 * T1
;d2 : 1/(2J(XH))
;d4 : 1/(4J(XH))
;d16: delay for homospoil/gradient recovery
;cnst2: = J(XH)
;cnst15: = conventional(0)/pure shift(1)
;cnst14: = conventional(0)/2JHH-resolved(1)
;cnst17: = -0.5 for Crp60comp.4
;in0: 1/(2 * SW(X)) = DW(X)
;nd0: 2
;NS: 2 * n
;DS: >= 16
;td1: number of experiments
;FnMODE: echo-antiecho

;use gradient ratio:         gp 1 : gp 2 : gp 0
;                              80 : 20.1 :   11   for C-13

;for z-only gradients:
;gpz1: 80%
;gpz2: 20.1% for C-13
;gpz0: 11%

;use gradient files:
;gpnam1: SINE.100
;gpnam2: SINE.100
```

Tutorial explaining how to perform structure discrimination and stereochemical assignments for diastereotopic CH_2 protons using MSpin.

Step 1: Calculation using 10 $^1D_{CH}$ only belonging to methine (CH) groups. This is the MSpin file defining all couplings:

```
rdc_data {
#H-2
4		31		9.4
#H-3
5		32		7.2
#H-1
3		30		17.4
#H-4
6		33		17.6
#H-22
19		38		0
#H-17ab
27		44
27		45
#H-18ab
28		46
28		47
#H-23ab
18		36
18		37
#H-15ab
25		41
25		42
#H-11ab
12		34
12		35
#H-20ab
21		39
21		40
#H-14
22		24		-14.8
#H-12
13		16		-17
#H-16
26		43		11.2
#H-13
15		23		-1.3
#H-8
11		14		-8
#
#Two-Bond HH RDCs
#
#H11a-H11b
34		35
#H15a-H15b
41		42
#H17a-H17b
44		45
#H18a-H18b
46		47
#H20a-H20b
39		40
#H23a-H23b
36		37

}
grid {
256
}
```

Step 2: Calculated *Q* factors: The program discriminates isomer 6 (correct structure) from the incorrect ones (isomer 5 has the second lowest *Q* value). The discrimination is considered moderate (*Q*r=0,098 vs 0,134)

Quality factors for all conformers in solution 1

Conformer	<*Q*>	Highest *Q*	Lowest *Q*
1	0.268626	1.7226e-281	1.69773e-313
2	0.409294	1.7226e-281	1.69773e-313
3	0.36354	1.7226e-281	1.69773e-313
4	0.315734	1.7226e-281	1.69773e-313
5	0.133802	1.7226e-281	1.69773e-313
6	0.0975169	1.7226e-281	1.69773e-313
7	0.359907	1.7226e-281	1.69773e-313
8	0.182503	1.7226e-281	1.69773e-313

Step 3: Experimental *vs.* calculated RDCs for isomer 6.

Once the alignment tensor is calculated and all *Q* factors are obtained for all structures, the program affords the calculated $^{1}D_{CH}$ and $^{2}D_{HH}$ for all pairs of each isomer. Below is the list of experimental *vs*. calculated values for the selected isomer 6.

All $^{1}D_{CH}$ and $^{2}D_{HH}$ (marked with ***) not included as input in the calculation are shown in red.

In blue, experimental values not included in the calculation.

In green, the calculated $^{2}D_{HH}$ that can be used to check the accuracy of the corresponding experimental values.

The comparison between red and blue/green values allows the on-the-fly stereoassignment of individual diastereotopic protons in CH_2 groups and also can be used for to validate experimental data

	Exp Hz	Comp Hz
C4,H31	9.40	9.34
C5,H32	7.20	7.32
C3,H30	17.40	17.16
C6,H33	17.60	17.11
C19,H38	0.00	0.59
C22,H24	-14.80	-17.26
C13,H16	-17.00	-15.03
C26,H43	11.20	10.88
C15,H23	-1.30	-3.01
C11,H14	-8.00	-7.55

C27,H44	***	-5.77	*
C27,H45	***	9.15	*
C28,H46	***	9.73	10
C28,H47	***	2.76	-0.5
C18,H36	***	-20.54	-21.4
C18,H37	***	4.42	4.6
C25,H41	***	2.82	2.2
C25,H42	***	0.88	4.2
C12,H34	***	6.59	8.6
C12,H35	***	-13.06	-13.6
C21,H39	***	-8.76	-8.2
C21,H40	***	-2.04	-4.8
H34,H35	***	-11.47	-9.8
H41,H42	***	10.40	11.6**
H44,H45	***	10.26	11.5**
H46,H47	***	11.99	*
H39,H40	***	-14.60	-15.6
H36,H37	***	-10.63	-12

Step 4: Repeat the calculation as step 1 but including the new assigned RDCs: 5 $^2D_{HH}$ (protons H17 out): Discrimination of 6 vs 5 is much better!!!!

Isomer	<*Q*>	Highest *Q*	Lowest *Q*
1	0.321709	1.7226e-281	1.69773e-313
2	0.389786	1.7226e-281	1.69773e-313
3	0.36024	1.7226e-281	1.69773e-313
4	0.351856	1.7226e-281	1.69773e-313
5	0.184424	1.7226e-281	1.69773e-313
6	0.0924997	1.7226e-281	1.69773e-313
7	0.373441	1.7226e-281	1.69773e-313
8	0.270089	1.7226e-281	1.69773e-313

Step 5: Repeat the calculation as step 4 but including now the new stereoassigned 10 $^2D_{HH}$ belonging to CH_2. This is the new input file:

```
rdc_data {
```

```
#H-2
4	31	9.4
#H-3
5	32	7.2
#H-1
3	30	17.4
#H-4
6	33	17.6
#H-22
19	38	0
#H-17ab
27	44
27	45
#H-18ab
28	46	10
28	47	-0.5
#H-23ab
18	36	-21.4
18	37	4.6
#H-15ab
25	41	4.2
25	42	2.2
#H-11ab
12	34	8.6
12	35	-13.6
#H-20ab
21	39	-8.2
21	40	-4.8
#H-14
22	24	-14.8
#H-12
13	16	-17
#H-16
26	43	11.2
#H-13
15	23	-1.3
#H-8
11	14	-8
#
#Two-Bond HH RDCs
#
#H11a-H11b
34	35	-9.8
#H15a-H15b
41	42	11.6
#H17a-H17b
44	45
#H18a-H18b
46	47	11.5
#H20a-H20b
39	40	-15.6
#H23a-H23b
36	37	-12

}
grid {
256
}
```

Step 6: *Q* factors: *Q*(6) is worst tan other calculations probably because more experimental data have been used. However, note that although *Q*(6)) is higher the discrimination of 6 vs 5 (Qr) and 6 vs the rest (Qg) is much better!!!!

Quality factors for all conformers in solution 1

Conformer<*Q*>	Highest *Q*	Lowest *Q*

1	0.538493	1.7226e-281	1.69773e-313
2	0.552556	1.7226e-281	1.69773e-313
3	0.744113	1.7226e-281	1.69773e-313
4	0.672611	1.7226e-281	1.69773e-313
5	0.258365	1.7226e-281	1.69773e-313
6	0.118295	1.7226e-281	1.69773e-313
7	0.831805	1.7226e-281	1.69773e-313
8	0.284022	1.7226e-281	1.69773e-313

Table S7: Coordinate files of the 8 different diastereoisomers of strychnine used in the calculations

47
1- RRR 7R8R12R13R14R16S
C -0.115023 -7.307554 3.099094
C 1.024920 -6.454184 3.009393
C 2.273359 -6.893322 3.405307
C 2.374640 -8.204651 3.881160
C 1.249604 -9.055336 3.931062
C -0.013932 -8.611834 3.527591
C 0.623399 -5.185338 2.264910
N -1.252117 -6.579195 2.699924
C -2.504472 -7.011458 2.328535
O -2.894652 -8.174914 2.409900
C -0.830674 -5.193872 2.769768
C -3.422445 -5.913032 1.771026
C -2.617220 -4.767689 1.134937
H -0.806697 -4.997130 3.859583
C -1.768348 -4.147160 2.231889
H -2.029083 -5.215656 0.327915
O -3.438730 -3.729337 0.609622
C -2.882317 -3.114968 -0.561137
C -1.407567 -2.767462 -0.525863
C -0.568308 -2.678013 0.527863
C 0.922234 -2.433454 0.367359
C -1.025650 -2.823872 1.959071
H -2.466710 -3.896672 3.048302
H -1.694281 -1.983138 2.188225
C 0.195973 -2.735390 2.913999
C 1.246516 -3.774353 2.458436
C 0.855537 -5.507994 0.769480
C 2.020975 -4.619120 0.395119
N 1.784284 -3.371669 1.123349
H 3.154298 -6.266111 3.317178
H 3.343622 -8.587468 4.196903
H 1.368316 -10.075025 4.292445
H -0.877922 -9.264637 3.581025
H -4.071208 -5.549558 2.576113
H -4.077046 -6.357437 1.012355
H -3.056148 -3.802887 -1.397289
H -3.460885 -2.208594 -0.766626
H -0.990347 -2.611246 -1.521132
H 1.139593 -1.416304 0.719514
H 1.213558 -2.423348 -0.690767

H	-0.107059	-2.914723	3.952938
H	0.623560	-1.723988	2.911912
H	2.074299	-3.809435	3.175343
H	-0.002718	-5.265981	0.145116
H	1.101726	-6.555577	0.557584
H	2.117601	-4.487346	-0.687875
H	2.961860	-5.061722	0.744886

47

2- RRS 7R8R12S13R14R16S

C	-0.034560	2.990209	4.703806
C	0.434874	1.714823	4.281741
C	1.130054	0.889347	5.144986
C	1.342605	1.350176	6.447893
C	0.844402	2.600038	6.871315
C	0.139026	3.433098	5.996638
C	-0.133632	1.431873	2.895492
N	-0.625788	3.641943	3.601207
C	-1.425620	4.749341	3.568614
O	-1.752151	5.401654	4.560849
C	-0.161624	2.905952	2.447021
C	-1.859502	5.197626	2.178730
C	-1.936691	4.109955	1.091839
H	0.900799	3.222318	2.393198
C	-0.664678	3.269572	1.058849
H	-2.019945	4.651060	0.138843
O	-3.128273	3.354684	1.263973
C	-3.542415	2.689169	0.070658
C	-2.951882	1.322870	0.045673
C	-1.639702	1.027580	0.106946
C	-1.186271	-0.405737	0.306391
C	-0.517812	2.052917	0.106287
H	0.083078	3.988718	0.679114
H	-0.402568	2.424056	-0.920577
C	0.803659	1.328426	0.509678
C	0.547495	0.543221	1.820461
C	-1.495459	0.760944	3.171274
C	-1.269981	-0.669095	2.725262
N	-0.398597	-0.582198	1.546792
H	1.466764	-0.097201	4.844103
H	1.880734	0.724566	7.157746
H	1.014362	2.922392	7.896700
H	-0.227637	4.399522	6.323709
H	-1.142080	5.967741	1.868789
H	-2.842515	5.672517	2.284135
H	-3.316703	3.256255	-0.839366
H	-4.632473	2.597137	0.127053
H	-3.679467	0.513528	0.072944

H	-0.575139	-0.709628	-0.553292
H	-2.031018	-1.106708	0.295974
H	1.622310	2.047408	0.639895
H	1.145323	0.656359	-0.288490
H	1.489003	0.126327	2.194694
H	-2.307557	1.232340	2.618361
H	-1.811234	0.770040	4.222149
H	-2.208951	-1.202781	2.542269
H	-0.741274	-1.226403	3.508618

47

3- RSR 7R8R12R13S14R16S

C	0.695560	3.897166	0.950553
C	1.053187	2.558023	0.585611
C	2.358008	2.241668	0.258046
C	3.305887	3.269427	0.304041
C	2.948511	4.581256	0.681448
C	1.628799	4.908523	1.008036
C	-0.138601	1.637067	0.777831
N	-0.702076	3.978375	1.090700
C	-1.551567	5.060008	1.234695
O	-1.201640	6.186795	1.576982
C	-1.177506	2.760557	0.536505
C	-3.018758	4.758835	0.819210
C	-3.516142	3.384347	1.297223
H	-1.216614	3.032005	-0.533548
C	-2.520110	2.304195	0.938969
H	-3.603794	3.455968	2.391031
O	-4.800993	2.998122	0.781723
C	-5.399610	1.846643	1.434246
C	-4.673518	0.494907	1.350343
C	-3.544867	0.218774	0.659576
C	-2.622829	-0.983289	0.823493
C	-2.942485	1.302373	-0.167303
H	-2.401466	1.808832	1.908914
H	-3.662563	1.721267	-0.879724
C	-1.752910	0.733942	-1.001433
C	-0.621553	0.379331	-0.022295
C	0.009693	1.074777	2.209746
C	-0.845578	-0.177235	2.316787
N	-1.178322	-0.610095	0.961478
H	2.652022	1.228295	0.004765
H	4.344057	3.052500	0.058301
H	3.713757	5.354661	0.708931
H	1.354567	5.924778	1.268428
H	-3.088712	4.832519	-0.272778
H	-3.667238	5.542038	1.228208
H	-6.392689	1.721854	0.989793

H	-5.547632	2.101644	2.490116
H	-5.080086	-0.270176	2.009667
H	-2.729164	-1.636135	-0.051710
H	-2.928961	-1.595429	1.681168
H	-1.407483	1.453740	-1.752951
H	-2.065689	-0.141496	-1.586116
H	0.219987	-0.081255	-0.550701
H	-0.259700	1.805019	2.982184
H	1.051500	0.781667	2.400268
H	-1.729715	0.029179	2.931249
H	-0.295729	-0.971943	2.833451

47

4- RSS 7R8R12S13S14R16S

C	-8.769460	-8.390325	-2.555028
C	-7.356744	-8.571309	-2.691261
C	-6.759854	-9.768011	-2.345151
C	-7.588256	-10.790223	-1.870418
C	-8.984401	-10.613818	-1.765117
C	-9.591495	-9.403069	-2.113698
C	-6.764828	-7.358483	-3.386624
N	-9.090967	-7.057173	-2.879346
C	-10.289716	-6.389673	-2.923183
O	-11.379224	-6.908237	-2.679966
C	-7.833246	-6.383213	-2.826131
C	-10.217111	-4.937185	-3.438681
C	-8.908772	-4.146064	-3.217033
H	-7.706117	-6.241897	-1.737050
C	-7.720822	-5.049839	-3.444375
H	-8.909921	-3.713353	-2.209571
O	-8.850700	-3.076083	-4.198283
C	-7.686524	-2.225002	-4.169512
C	-6.443429	-2.869260	-4.776189
C	-5.793901	-3.900112	-4.190699
C	-4.686696	-4.764883	-4.767325
C	-6.381414	-4.450465	-2.930551
H	-7.719286	-5.204272	-4.531021
H	-6.535907	-3.664956	-2.181466
C	-5.413742	-5.489911	-2.303535
C	-5.360361	-6.701794	-3.240693
C	-6.819520	-7.680139	-4.896945
C	-5.868793	-6.734227	-5.603284
N	-4.934461	-6.227038	-4.600017
H	-5.694037	-9.930337	-2.467230
H	-7.152466	-11.748931	-1.594419
H	-9.599029	-11.434799	-1.400849
H	-10.662283	-9.267164	-2.011438
H	-10.434439	-4.983469	-4.514291

H -11.044106 -4.375608 -2.987102
H -7.508927 -1.858762 -3.152231
H -7.933423 -1.345861 -4.775033
H -6.122597 -2.499173 -5.745953
H -3.744238 -4.515525 -4.264109
H -4.521267 -4.533219 -5.827052
H -5.742587 -5.786903 -1.300583
H -4.415590 -5.056825 -2.155324
H -4.631290 -7.435866 -2.881028
H -6.471552 -8.706334 -5.080468
H -7.829895 -7.606761 -5.316098
H -5.319963 -7.257889 -6.393905
H -6.439071 -5.941163 -6.100361
47
5- SRR 7R8S12R13R14R16S
C -9.831863 -1.612148 -2.120234
C -9.012863 -2.702488 -1.765902
C -9.576002 -3.891913 -1.325634
C -10.967842 -3.977854 -1.240060
C -11.777803 -2.886817 -1.594077
C -11.209992 -1.688333 -2.034951
C -7.556197 -2.392192 -1.996577
N -9.041810 -0.500933 -2.448762
C -9.442570 0.818063 -2.630352
O -10.585655 1.159113 -2.937205
C -7.639238 -0.872893 -2.272278
C -8.377847 1.905578 -2.304565
C -6.968811 1.373718 -1.985945
H -7.151388 -0.666606 -3.234200
C -7.149870 0.078772 -1.194320
H -6.487357 1.213344 -2.961354
O -6.136467 2.249459 -1.232804
C -4.739452 2.097641 -1.568702
C -4.194190 0.677209 -1.672302
C -4.735116 -0.460321 -1.186065
C -4.175972 -1.849890 -1.406659
C -5.985302 -0.414601 -0.358670
H -7.943734 0.251718 -0.447371
H -5.824271 0.256886 0.495524
C -6.363805 -1.789391 0.198739
C -6.472845 -2.768219 -0.963332
C -7.031546 -3.143532 -3.231433
C -5.529732 -2.902303 -3.169863
N -5.204298 -2.850276 -1.740432
H -8.960115 -4.747265 -1.064648
H -11.431843 -4.901641 -0.900467
H -12.859608 -2.973681 -1.519404

H -11.845221 -0.847448 -2.291645
H -8.326666 2.602860 -3.148484
H -8.752954 2.476590 -1.446098
H -4.160299 2.650585 -0.822152
H -4.586040 2.599115 -2.531811
H -3.264507 0.606613 -2.236049
H -3.679586 -2.169088 -0.481072
H -3.387898 -1.846519 -2.170218
H -7.313908 -1.738963 0.745174
H -5.611681 -2.131817 0.921316
H -6.674500 -3.768976 -0.561023
H -7.465137 -2.792628 -4.174631
H -7.238179 -4.219381 -3.153505
H -5.287891 -1.962929 -3.681598
H -4.976875 -3.704467 -3.668704
47
6- SRS 7R8S12S13R14R16S Strychnine
C -0.928284 5.983882 0.490736
C 0.110585 5.108392 0.149970
C 1.341893 5.601766 -0.263658
C 1.517960 6.985191 -0.337306
C 0.473800 7.856475 0.005015
C -0.763062 7.356645 0.421349
C -0.298609 3.672306 0.363661
N -2.085258 5.259401 0.808598
C -3.360632 5.753674 0.988521
O -3.642066 6.935511 1.183579
C -1.832875 3.825718 0.609897
C -4.466830 4.701935 0.929557
C -4.210062 3.456849 0.039511
H -2.129255 3.307950 1.531970
C -2.777028 3.441148 -0.536023
H -4.933565 3.469556 -0.786073
O -4.508529 2.327047 0.872216
C -4.607433 1.087240 0.182308
C -3.261459 0.446783 0.190081
C -2.198262 0.947793 -0.463118
C -0.820321 0.338048 -0.348552
C -2.296218 2.204336 -1.305517
H -2.769322 4.256648 -1.279194
H -2.967626 2.016881 -2.153335
C -0.909288 2.558937 -1.866284
C 0.079837 2.626475 -0.703037
C 0.410815 3.107434 1.601667
C 0.184788 1.612301 1.474793
N 0.186260 1.336425 0.030683
H 2.163434 4.936509 -0.512171

H	2.475058	7.392510	-0.656153
H	0.626777	8.931620	-0.056475
H	-1.564495	8.042518	0.673736
H	-5.366126	5.206930	0.554175
H	-4.682050	4.409559	1.965079
H	-5.019262	1.200505	-0.826792
H	-5.302201	0.455748	0.745939
H	-3.155661	-0.444103	0.804185
H	-0.543995	-0.100013	-1.316106
H	-0.803502	-0.501581	0.358198
H	-0.933556	3.516173	-2.402116
H	-0.587689	1.812182	-2.603994
H	1.075863	2.841483	-1.109183
H	0.022537	3.504160	2.546330
H	1.488150	3.318830	1.573673
H	-0.767832	1.349948	1.950826
H	0.973168	1.045039	1.979663

47

7- SSR 7R8S12R13S14R16S

C	-1.266340	3.980945	3.975095
C	-0.583877	2.854289	3.476342
C	0.801788	2.850158	3.392493
C	1.498217	3.985980	3.812211
C	0.811045	5.110970	4.294123
C	-0.584380	5.116940	4.372039
C	-1.554722	1.792792	3.005000
N	-2.652047	3.750018	3.957692
C	-3.670367	4.631939	4.248241
O	-3.499250	5.752532	4.732237
C	-2.847671	2.329793	3.705738
C	-5.080340	4.220997	3.808102
C	-5.344105	2.741179	3.516970
H	-2.939957	1.881946	4.707838
C	-4.110746	2.075207	2.948902
H	-5.653708	2.244668	4.445199
O	-6.426857	2.631193	2.556975
C	-6.754638	1.312128	2.072451
C	-5.734936	0.610807	1.164386
C	-4.478998	1.031738	0.884851
C	-3.346380	0.174893	0.346551
C	-4.026400	2.354185	1.433988
H	-4.284572	1.007788	3.146471
H	-4.698646	3.149828	1.090487
C	-2.644675	2.727446	0.918855
C	-1.671558	1.700318	1.457204
C	-1.231976	0.342938	3.363922
C	-2.043948	-0.483311	2.363976

N	-2.092801	0.310688	1.132180
H	1.343229	1.997544	2.993961
H	2.584586	4.005466	3.754199
H	1.370695	5.989372	4.608215
H	-1.101311	5.993926	4.745979
H	-5.304996	4.815711	2.912674
H	-5.785416	4.559092	4.577522
H	-7.683756	1.418626	1.502562
H	-6.971931	0.670608	2.934065
H	-6.035067	-0.385666	0.844703
H	-3.140080	0.477122	-0.687689
H	-3.638287	-0.881195	0.297353
H	-2.371222	3.740636	1.232755
H	-2.629016	2.743503	-0.178930
H	-0.689096	1.857229	0.994220
H	-1.479000	0.088499	4.399723
H	-0.165265	0.130566	3.220427
H	-3.038737	-0.686384	2.772880
H	-1.566912	-1.451496	2.179880

47

8- SSS 7R8S12S13S14R16S

C	-4.849512	5.056517	2.558395
C	-5.384618	3.982639	3.299621
C	-5.672899	4.137949	4.648155
C	-5.419537	5.375609	5.245593
C	-4.881227	6.437371	4.500185
C	-4.590369	6.282217	3.142384
C	-5.526803	2.735668	2.455078
N	-4.660256	4.677021	1.227077
C	-4.208570	5.410203	0.138445
O	-3.855346	6.586070	0.170005
C	-5.190423	3.342293	1.058959
C	-4.204637	4.609303	-1.177979
C	-3.554583	3.245411	-0.939641
H	-6.130203	3.501755	0.505499
C	-4.271357	2.527842	0.192521
H	-2.497947	3.441944	-0.715327
O	-3.609196	2.351682	-2.077940
C	-2.878084	1.099883	-1.920183
C	-3.488648	0.080060	-0.939958
C	-3.634784	0.303990	0.390680
C	-4.424917	-0.504195	1.403219
C	-3.220370	1.653729	0.894039
H	-5.024101	1.902217	-0.316008
H	-2.189972	1.856167	0.576712
C	-3.206482	1.741320	2.404471
C	-4.624495	1.547928	2.877662

C	-6.891309	2.041578	2.451606
C	-6.585296	0.673773	1.830999
N	-5.250569	0.317659	2.323701
H	-6.078545	3.321055	5.237606
H	-5.637391	5.519354	6.302002
H	-4.690211	7.392165	4.985316
H	-4.179309	7.109361	2.573613
H	-3.642450	5.162736	-1.938097
H	-5.230219	4.509137	-1.550638
H	-1.832700	1.313150	-1.669113
H	-2.870205	0.635422	-2.912560
H	-3.868877	-0.838664	-1.379186
H	-3.709848	-1.068658	2.014749
H	-5.051857	-1.252994	0.904416
H	-2.808538	2.709374	2.730042
H	-2.545307	0.976213	2.831717
H	-4.625553	1.448473	3.970746
H	-7.658957	2.585006	1.891216
H	-7.265479	1.907970	3.474873
H	-6.616166	0.748652	0.738748
H	-7.326737	-0.071669	2.135176

PUBLICATION 5

Title: Perfect $^{1}J_{CH}$-resolved HSQC: Efficient measurement of one-bond proton-carbon coupling constants along the indirect dimension

Authors: Marcó, N.; Souza, A. A.; Nolis, P.; Gil, R. R.; Parella, T.

Reference: *J. Magn. Reson*. **2017**, *276*, 37–42.

DOI: 10.1016/j.jmr.2017.01.002

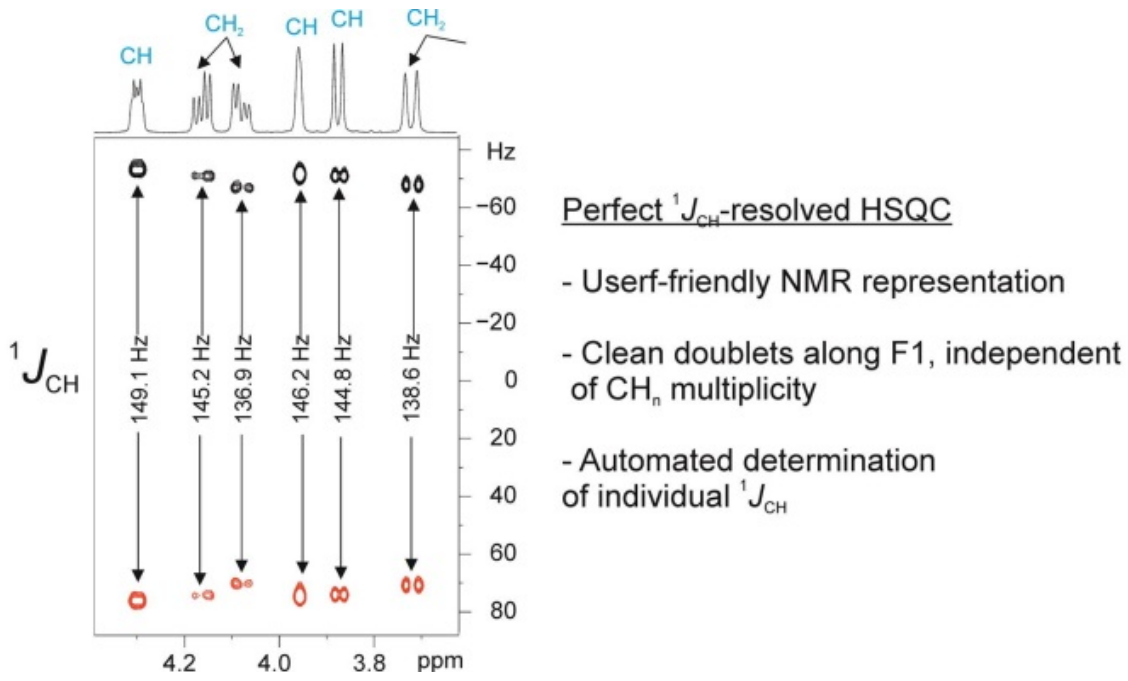

SUMMARY

The efficient and accurate determination of the scalar $^{1}J_{CH}$ coupling constants can become a fundamental step for correct structural elucidation task. The measurement of $^{1}J_{CH}$ along the F1 or F2 dimension of HSQC experiments has been explored with different approaches. Herein it is described the successful implementation of a PerfectBIRD block into a *J*-resolved HSQC sequence for the accurate and automated measurement of $^{1}J_{CH}$ for all ^{13}C multiplicities along the indirect F1 dimension. In particular, this element cleans contributions arising from $^{2}J_{HaHb}$ modulation and allows the individual $^{1}J_{CHa}$ and $^{1}J_{CHb}$ determination in prochiral CH_2 spin systems.

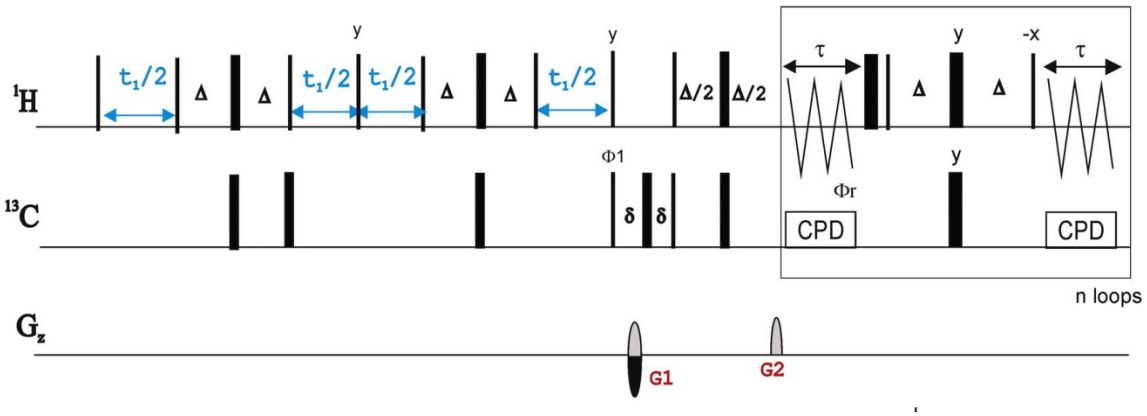

This new sequence has been proved for the correct and accurate measurement of $^{1}D_{CH}$ which have been applied to determine the full stereochemistry of a multiple-stereocenters containing molecule. Related versions including *J*-scaling factors, real-time broadband homodecoupling and NUS techniques have been redesign to avoid problems due to signal overlapping.

Journal of Magnetic Resonance 276 (2017) 37–42

Contents lists available at ScienceDirect

Journal of Magnetic Resonance

journal homepage: www.elsevier.com/locate/jmr

Perfect $^1J_{CH}$-resolved HSQC: Efficient measurement of one-bond proton-carbon coupling constants along the indirect dimension

N. Marcó [a], A.A. Souza [a,b], P. Nolis [a], R.R. Gil [c], T. Parella [a,*]

[a] Servei de Ressonància Magnètica Nuclear, Universitat Autònoma de Barcelona, E-08193 Bellaterra (Barcelona), Catalonia, Spain
[b] Departamento de Química, Universidade Federal do Piauí, 64049-550 Teresina, PI, Brazil
[c] Department of Chemistry, Carnegie Mellon University, Pittsburgh, PA, USA

ARTICLE INFO

Article history:
Received 24 November 2016
Revised 30 December 2016
Accepted 1 January 2017
Available online 3 January 2017

Keywords:
BIRD
Perfect-BIRD
J-resolved
J-resolved HSQC
One-bond proton-carbon coupling constants
Residual dipolar coupling constants

ABSTRACT

A versatile $^1J_{CH}$-resolved HSQC pulse scheme for the speedy, accurate and automated determination of one-bond proton-carbon coupling constants is reported. The implementation of a perfectBIRD element allows a straightforward measurement from the clean doublets obtained along the highly resolved F1 dimension, even for each individual $^1J_{CHa}$ and $^1J_{CHb}$ in diastereotopic H_aCH_b methylene groups. Real-time homodecoupling during acquisition and other alternatives to minimize accidental signal overlapping in overcrowded spectra are also discussed.

1. Introduction

One-bond proton-carbon coupling constants (the scalar $^1J_{CH}$ coupling in isotropic media or the total $^1T_{CH}$ coupling in anisotropic media) are fundamental NMR restraints in the structural determination of small molecules. In particular, residual dipolar couplings (RDCs) have become very powerful to solve challenging structural questions in molecules dissolved in weakly aligned media. Their success relies on the determination of relative orientations of specific chemical bonds with respect to a molecular alignment tensor. For instance, it is possible to unravel the relative configuration of multiple stereochemical centers without a previous knowledge of scalar *J* coupling constants and NOE enhancements [1]. One-bond proton-carbon RDCs ($^1D_{CH} = {}^1T_{CH} - {}^1J_{CH}$) are the most efficient parameters for unequivocal structural discrimination, whereas two-bond geminal proton-proton coupling constants ($^2J_{HH}$ in isotropic media and $^2T_{HH}$ in anisotropic media) have also shown an excellent complementarity for this purpose [2]. New strategies involving long-range proton-carbon RDCs ($^nD_{CH}$) [3] or residual ^{13}C chemical shift anisotropy (RCSA) [4] promise to be of great help in proton-deficient molecules with a prominent lack of protonated carbons. From the NMR methodological point of view, the interest has been extensively focused on the suitability of measuring $^1J_{CH}$ from the direct (F2) or the indirect (F1) dimension of HSQC spectra. In particular, the extraction of individual $^1J_{CH}$ values in diastereotopic protons H_aCH_b of methylene systems has always been a challenging task and obtaining clean *J* patterns for these protons has not been easy (Fig. 1). Probably, the easiest way to measure these couplings would be the F2-heterocoupled CLIP-HSQC experiment [5] where each ^1H signal appears as a large doublet along F2 due to $^1J_{CH}$ (Fig. 1A). Recently, two improved solutions (perfectHSQC [6] and PIP-HSQC [7] experiments) have been proposed to remove the interference of undesired J_{HH} modulation during the INEPT periods in HSQC experiments. Both approaches afford pure in-phase multiplets with respect to $^1J_{CH}$ and J_{HH}, allowing a much accurate measurement of $^1J_{CH}$ especially when large J_{HH} values are present, as it can happen when measuring RDCs. The major drawbacks to measure accurately $^1J_{CH}$ from the F2 dimension are due to the presence of complex J_{HH} multiplets, the broader linewidths commonly observed in anisotropic conditions and the significant signal distortions which may appear due to strong coupling effects. To alleviate some of these problems, several interferogram-based broadband homodecoupled versions of the CLIP-HSQC have been reported (Fig. 1B and C) [8], although all of them require time-consuming 3D acquisition modes that greatly hamper its routine use. Very recently, an optimized BIRD-based real-time homode-

* Corresponding author.
E-mail address: teodor.parella@uab.cat (T. Parella).

http://dx.doi.org/10.1016/j.jmr.2017.01.002
1090-7807/

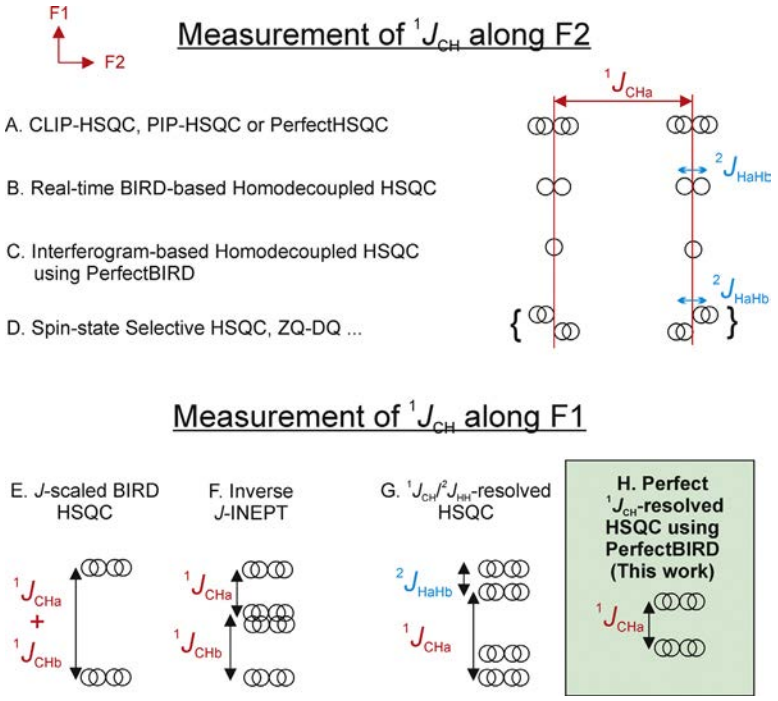

Fig. 1. Schematic *J* coupling patterns for one of the diastereotopic protons' (H_a) cross-peak (with an arbitrary multiplicity along F2) belonging to a H_aCH_b methylene group in several implementations of (A–D) F2-and (E–H) F1-heterocoupled HSQC experiments. All patterns E–H could be further simplified along the horizontal F2 dimension by homodecoupling, similarly as shown in B.

coupled HSQC experiment has been developed to obtain simplified ^{1}H multiplet patterns in F2 without sacrificing sensitivity. However, diastereotopic CH_2 protons appear distorted and partially homodecoupled because the $^2J_{HH}$ splitting is not removed by the BIRD effect (Fig. 1B) and, in addition, $^1J_{CH}$ and J_{HH} modulations during the homodecoupling block could induce unexpected effects and non-accurate measurements [8d].

The measurement of $^1J_{CH}/^1T_{CH}$ along the F1 dimension of HSQC spectra has been another alternative approach largely explored (Fig. 1E–G) [9]. All these methods work very well for CH systems where a clean doublet is obtained, but the major criticisms come from the fact that only the sum of $^1J_{CHa} + {}^1J_{CHb}$ is obtained for H_a-CH_b groups, as reported in the *J*-scaled BIRD-HSQC (JSB-HSQC) experiment (Fig. 1E) [9d–9g]. Some alternatives have been reported to measure individual $^1J_{CH}$ values in CH_2 but they all suffer from some important practical drawbacks. Here we offer a solution to this problem by proposing a novel perfect $^1J_{CH}$-resolved HSQC experiment that allows an accurate determination of $^1J_{CH}$ along F1 for any ^{1}H multiplicity and with excellent levels of resolution.

2. Results and discussion

The proposed pulse sequence of Fig. 2A has been derived from three early ideas: (i) previous schemes where the initial fixed INEPT element in the HSQC pulse sequence was made variable to allow the modulation of $^1J_{CH}$ during the indirect dimension [10], (ii) the perfectHSQC experiment [6] that uses a perfectINEPT element [11d] to avoid J_{HH} modulation during the INEPT periods, and (iii) the use of a new perfectBIRD element, previously implemented in an interferogram-based version of the broadband homodecoupled HSQC experiment [8a], to efficiently remove the $^2J_{HaHb}$ modulation in methylene H_aCH_b signals generated by a $BIRD^{d,X}$ module [12]. This classical $BIRD^{d,X}$ element consists of a 90°(^{1}H)-Δ-180°(^{1}H,X)-Δ-90°(^{1}H) cluster (Δ = 1/($2 * {}^1J_{CH}$)) that inverts both $^1J_{CHa}$ and $^2J_{HaHb}$. A simple modification referred to as $BIRD^d$ [13], employing the 90°(^{1}H)-Δ-180°(^{1}H,X)-Δ-90°(^{1}H),180°(^{13}C) element, adds a last 180°(^{13}C) pulse that re-inverts again ^{13}C magnetization and therefore only $^2J_{HaHb}$ remains inverted. In our proposal, the initial INEPT period in a conventional HSQC scheme is replaced by an incrementing perfectBIRD element (from point a to d in Fig. 1A) which is based on the perfect-echo concept successfully implemented in many interesting applications [11]. It consists of a double echo building block, τ-$BIRD^d$-τ-90$_y$(^{1}H)-τ-$BIRD^{d,X}$-τ-, in order to let $^2J_{HaHb}$ evolve during both echoes (from point a to b and c to d in Fig. 1A) while $^1J_{CHa}$ only evolves during the second one (from point c to d in Fig. 1A). Thus, $^2J_{HaHb}$ is fully refocused at the end of the perfectBIRD and the signal will be only modulated by $^1J_{CHa}$ (Fig. 1H). The perfect $^1J_{CH}$-resolved HSQC experiment is originally designed to allow independent $^1J_{CH}$ (*J*-scale factor κ) and/or δ(^{13}C) (δ-scale factor κ′) evolution during two different variable t_1 periods. However, we have concentrated our study in a classical J_{CH}-resolved presentation (κ = 1 and κ′ = 0) because the spectral symmetry around the F1 = 0 axis affords a user-friendly fingerprinting visualization, with a clear and quick $^1J_{CH}$ profiling for all ^{1}H signals that is suitable for a reliable automated extraction of $^1J_{CH}$ values (Fig. 2B). In addition, the use of a very reduced spectral width in F1 (sw(F1) = 250 Hz) ensures high levels of digitization and accurate measurements. This approach is highly recommendable for small molecules where the probability of signal overlap is low. In cases of accidental signal overlap due to the presence of ^{1}H signals with similar $^1J_{CH}$ and δ(^{1}H), a δ-correlation presentation offering better signal dispersion along F1 may be advisable. Thus, the possibility to use independent κ and κ′ scaling factors retains good levels of digital resolution by using reduced sw(F1). Fig. 2C shows the corresponding *J*-upscaled/δ-downscaled perfect $^1J_{CH}$-resolved HSQC spectrum of strychnine (**1**) acquired with κ = 5, κ′ = 0.1 and sw(F1) = 3000 Hz. The use of large κ values would decrease the overall

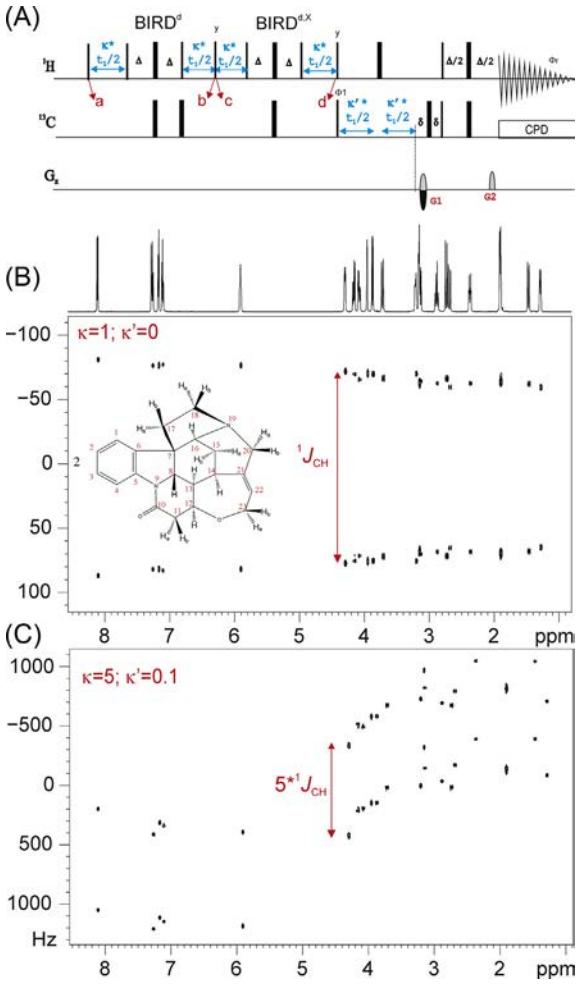

Fig. 2. (A) General pulse scheme of the perfect J_{CH}-resolved HSQC experiment. Thin and thick rectangles represent 90° and 180° rectangular pulses, respectively, applied along the x-axis unless indicated differently. Inversion and refocusing 180° ^{13}C pulses can be applied as adiabatic pulses. The perfectBIRD element consists of two incrementing BIRD^d (from point a to b) and BIRD^{d,X} (from point c to d) pulse clusters, in order to let $^2J_{HaHb}$ evolve during both echoes while $^1J_{CHa}$ only evolves during the second one. The inter-pulse delays in INEPT and BIRD elements are optimized according to $\Delta = 1/(2 * {}^1J_{CH})$. The factors κ and κ′ are used to scale up or scale down the independent $^1J_{CH}$ (J-scale κ factor) and/or δ(^{13}C) (δ-scale κ′ factor) evolution during the two different variable t_1 periods. The echo/anti-echo encoding in F1 was achieved by changing the sign of G1 between successive t_1 increments. The duration of a pulsed-field gradient and of the subsequent recovery delay amounts to δ and the ratio between G1:G2 were 80:20.1. A basic two-step phase cycling is applied: $\phi_1 = x, -x$; $\phi_{rec} = x, -x$. (B and C) 2D perfect $^1J_{CH}$-resolved HSQC spectra of strychnine (**1**) in $CDCl_3$ recorded at 600 MHz proton frequency with (B) κ = 1, κ′ = 0 and sw(F1) = 250 Hz and (C) κ = 5, κ′ = 0.1 and sw(F1) = 3000 Hz, respectively. Other experimental conditions are the same for both spectra: 2048 complex data points in F2, 256 t_1 increments, 2 scans per t_1, 1 s of pre-scan delay and Δ optimized to 140 Hz. FID resolution before processing was 1.9 Hz/pt. The experimental time for each 2D spectrum was of 14 m 30 s.

sensitivity of the experiment but digital resolution could be properly optimized (i) acquiring a major number of t_1 increments, (ii) setting a major κ/κ′ scaling proportionality that allows the use of more reduced sw(F1), or (iii) using non-uniform sampling (NUS) schemes [9d].

Each ^1H signal in the perfect $^1J_{CH}$-resolved HSQC spectrum displays a clean anti-phase doublet along F1 corresponding to its $^1J_{CH}$ value (Figs. 3 and S1). The mismatch between $^1J_{CH}$ and the BIRD delay setting is not critical and it can only generate some residual signals at F1 = 0 that do not interfere with the measurement. Interestingly, note that different $^1J_{CH}$ values for each CH and all diastereotopic CH_2 protons are quickly visualized and precisely measured,

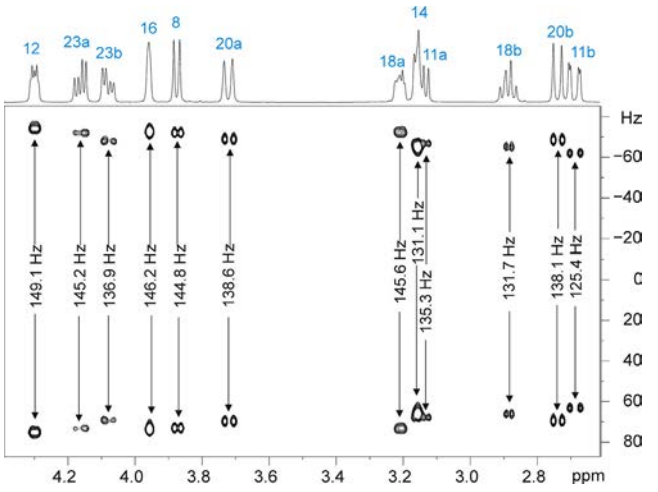

Fig. 3. Expansion of the aliphatic area of the spectrum in Fig. 2B clearly showing the magnitudes of $^1J_{CH}$ for all CH protons and also each different diastereotopic methylene protons. Spectral resolution in F1 is 0.24 Hz/pt.

as performed for H18a (145.6 Hz) and H18b (131.7 Hz) or H23a (145.2 Hz) and H23b (136.9 Hz). In other cases, it is also possible to differentiate similar values, as found for H20a (138.6 Hz) and H20b (138.2 Hz). All these measurements can be performed automatically because of the symmetry of cross-peaks with respect to the F1 = 0 axis (Table S1). $^1J_{CH}$ mainly depends on the *s* character of the CH bond and the electronegativity effects of substituents and neighbours nuclei. Thus, such observed differences of $^1J_{CH}$ in CH_2 can give an insight about their equatorial and axial positions and therefore can be helpful in their stereoselective assignments. It is also interesting to compare the accuracy of the measurement along F1 or F2 dimensions in terms of digital and signal resolution. Using sw(F1) of 250 Hz and 256 complex t_1 increments, the FID digital resolution in the perfect $^1J_{CH}$-resolved HSQC is about 1.9 Hz/Pt. In contrast, in F2 measurements from the F2 using a ^1H spectral width of 10 ppm (6000 Hz in a 600 MHz spectrometer) and 4 k data points, the FID digital resolution is about 1.5 Hz/Pt. On the other hand, signal resolution also takes into account the overall multiplet width and therefore the accuracy in perfect $^1J_{CH}$-resolved HSQC should be better than a conventional PIP-HSQC or perfectHSQC experiment because of the absence of J_{HH} splittings. These high levels of both digital and signal resolution should be only attainable in the recent real-time homodecoupled HSQC experiment [8d].

The perfect $^1J_{CH}$-resolved HSQC experiment retains the basic pulse train of the regular HSQC experiment and therefore its performance can be further improved by adding complementary features, such as solvent suppression schemes, multiplicity editing, NUS enhancement or BIRD-based real-time homodecoupling along the F2 dimension [14]. As an example, Fig. 4A shows the homodecoupled version of the perfect $^1J_{CH}$-resolved HSQC experiment. It works well for isotropic samples, with an excellent simplification of J_{HH} coupling patterns to singlets and without a considerable increase of linewidths. Fig. 4C shows the corresponding spectrum acquired combining homodecoupling and 50% NUS, demonstrating that cross-peak simplification, improved sensitivity (averaged 70% for CH and 28% for CH_2), and equivalent resolution and measurement accuracy can be simultaneously achieved with shorter acquisition times (compare internal F2 projection in 4B *vs.* 4C). Unfortunately, homodecoupling remains partial in diastereotopic CH_2 protons because $^2J_{HH}$ is also inverted by the BIRD element and a doublet due to an apparent $^2J_{HH}$ is still observed.

The outstanding features of perfect $^1J_{CH}$-resolved HSQC are finally demonstrated in the challenging determination of both

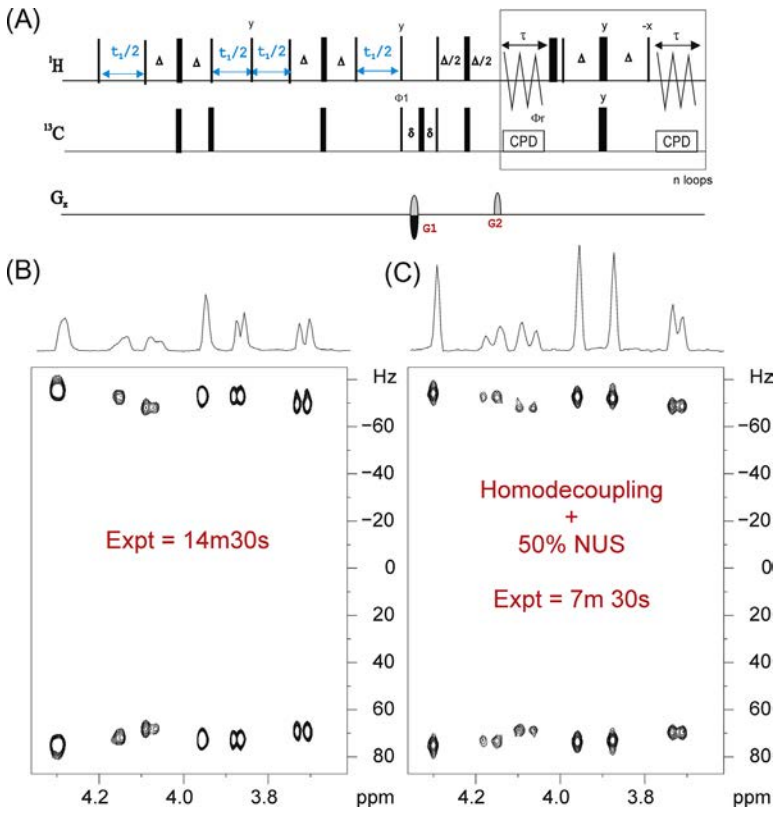

Fig. 4. (A) Pulse sequence of the real-time BIRD-based homodecoupled perfect $^1J_{CH}$-resolved HSQC experiment. (B and C) Comparison between the (B) conventional and (C) homodecoupled perfect $^1J_{CH}$-resolved HSQC spectra of **1** recorded under the same experimental conditions as described in Fig. 2B. The only differences are the use of 50% NUS and the homodecoupled acquisition in spectrum C, saving 50% of spectrometer time. From the internal F2 projections at the top of 2D spectra, also note the improved cross-peak simplification and sensitivity enhancements achieved by signal collapsing for all CH and CH_2 protons in the homodecoupled spectrum *vs.* the conventional one.

the magnitude and the sign of all individual $^1D_{CH}$ RDCs of **1** weakly aligned in a $CDCl_3$-compatible poly(methyl methacrylate) (PMMA) gel from a single NMR spectrum [15] (Fig. 5). Despite the small δ (^1H) differences between the isotropic and anisotropic cross-peaks, $^1D_{CH}$ RDCs can be directly determined from this single NMR spectrum. It is observed how the relative orientation of each diastereotopic CH_2 proton is correlated with their different $^1D_{CH}$ values. For instance, +3.8 Hz and −24.0 Hz are measured for H23a and H23b, respectively, or +7.7 Hz and −17.4 Hz for H11a and H11b, respectively. The obtained RDC data agree with those published in related works (Table S2) [9f,10]. In this type of samples, the simultaneous measurement of $^1J_{CH}$ and $^1T_{CH}$ (and consequently $^1D_{CH}$) along F1 is strongly advantageous because there is no interference of $^2J_{HH}/^2D_{HH}$ and it is performed independent of ^1H multiplet complexities and lineshapes. In such anisotropic conditions, the full collapsing of multiplets by homodecoupling should not be so advantageous because linewidths are broader and also because the presence of larger T_{HH} couplings (30–40 Hz) can difficult their efficient decoupling. The direct measurement of $^1D_{CH}$ RDCs in the equivalent *J*-upscaled/δ-downscaled perfect $^1J_{CH}$-resolved HSQC spectrum acquired with $\kappa' = 0.1$ could be also problematic depending on the ^1H and ^{13}C RCSA. For the same reasons, the attempts to perform these measurements along the F2 dimension in regular PIP-HSQC or perfectHSQC fails due to the lack of F1 resolution. The option to use highly resolved F2-spectral-aliased HSQC spectra only works for carbons having a large ^{13}C RCSA (olefinic and aromatics) but fails for most of the aliphatic carbons. The experiment would partially work for methyl protons in very strong alignment conditions because the perfectBIRD module only inverts two protons attached on the same carbon [8d].

3. Conclusions

In summary, we have reported a robust and fast approach for the accurate and automated extraction of $^1J_{CH}$ for all carbon multiplicities. The novelty relies on the selectivity of the perfectBIRD element to differentiate the evolution of $^1J_{CH}$ *vs.* $^2J_{HH}$ in diastereotopic CH_2 protons. The measurement is accurately performed along the indirect F1 dimension and therefore it is irrespective of ^1H multiplet complexity along F2. The experiment can be easily tuned to avoid signal overlapping by monitoring a *J*-upscaling/δ-downscaling scaling factors proportionality, can incorporate real-time homodecoupling during acquisition to afford multiplet simplification and enhanced sensitivity, and NUS can also be applied to economize spectrometer time. The experiment does not need any calibration and therefore is ideal for routine applications. The potential of the method has been demonstrated by measuring $^1D_{CH}$ RDCs in challenging sample conditions.

4. Experimental section

NMR experiments were recorded on a 600 MHz spectrometer equipped with a triple-resonance $^1H/^{13}C/^{15}N$ inverse probe. The temperature for all measurements was set to 298 K. The isotropic sample was prepared by dissolving 20 mg of strychnine (**1**) in $CDCl_3$. The anisotropic sample was prepared as described in Ref. [11b] of the manuscript. They consisted of 20 mg of **1** aligned in a PMMA gel swollen in $CDCl_3$ using the reversible compression/relaxation method [15b]. The alignment was monitored from the ^2H quadrupolar splitting ($\Delta\nu_Q$) of the $CDCl_3$ signal that was set to 37 Hz.

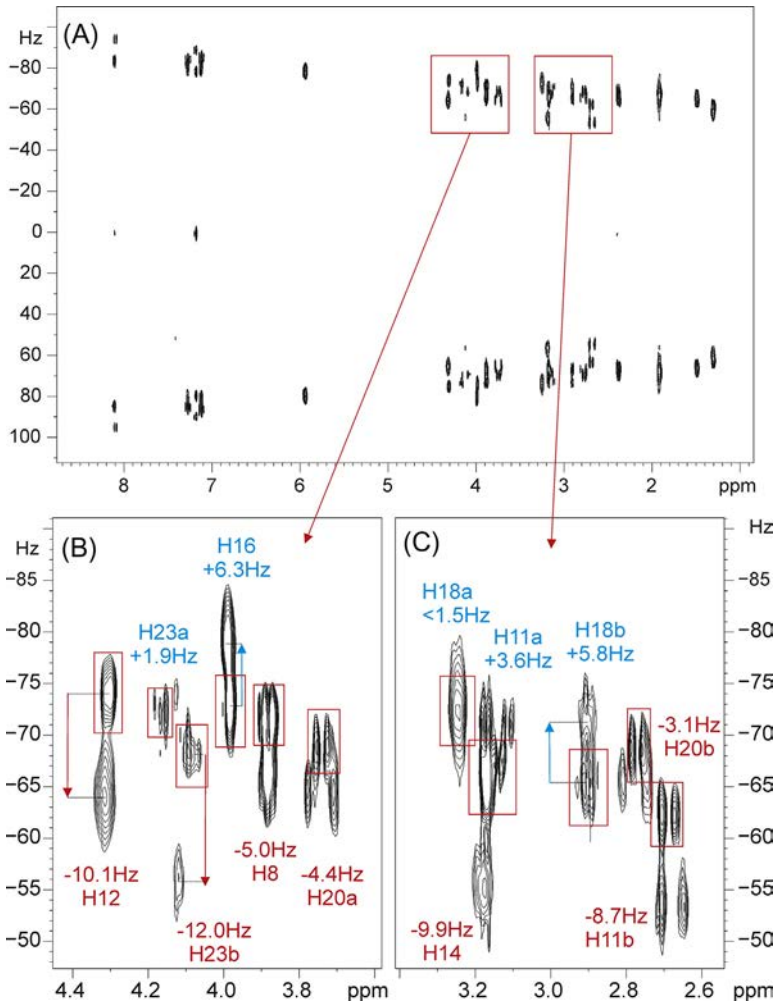

Fig. 5. (A) Perfect $^{1}J_{CH}$-resolved HSQC spectrum of **1** in compressed PMMA/$CDCl_3$ (^{2}H quadrupolar coupling ($CDCl_3$) = 37 Hz), acquired using the pulse sequence of Fig. 1A with κ = 1, κ′ = 0 and sw(F1) = 250 Hz. (B and C) Expanded regions corresponding to the insets marked in A showing how $^{1}D_{CH}/2$ can be directly extracted for each resolved ^{1}H signal. The experimental conditions were the same as described in Fig. 2B. Red boxes in B and C correspond to the isotropic components (see Fig. S2 in the supporting information). Also note how the anisotropic components present a broader lineshapes. (For interpretation of the references to color in this figure legend, the reader is referred to the web version of this article.)

NMR spectra were recorded with proton 90° pulses of 8.5 μs and carbon 90° pulses of 10.5 μs. For broadband carbon inversion and refocusing, 0.5 ms smoothed Chirp pulses sweeping over a frequency band of 60 kHz and a four-Chirp composite pulse of 2 ms duration were used, respectively. The interpulse Δ delays in INEPT and BIRD elements were set to 3.57 ms ($\Delta = 1/(2 * {}^{1}J_{CH})$; optimized to $^{1}J_{CH}$ = 140 Hz) and the recycle delay to 1 s. 2 scans were accumulated for each one of the 256 t_1 increments and the number of complex data points in t_2 was set to 2048. Spectra were acquired with an spectral window of 6010 Hz (in F_2) and 250 Hz (in F_1) giving a FID resolution of 5.86 (F2) and 1.95 (F1) Hz, respectively. Prior to Fourier-transformation of each data, zero filling to 1024 in F1 and a π/2-shifted squared cosine window function (QSINE, SSB: 2) in both dimensions were applied. After applying zero filling, the digital resolution was 2.93 (F2) and 0.24 (F1) Hz, respectively. Linear prediction was not applied. An error of ±0.5 Hz in the determination of $^{1}J_{CH}$ is assumed as a conservative estimate. Gradient ratios for G1:G2 were set to 80:20.1, measured as percentage of the absolute gradient strength of 53.5 G/cm. Sine bell shaped gradients had 1 ms of duration and were followed by a recovery delay of 100 μs (δ). All experiments were acquired and processed using the echo/anti-echo protocol where the gradient G1 was inverted for every second FID. Real-time BIRD-based homodecoupling was performed using 10.3 ms chunk length and 8 loops (2048 complex points in F2).

The java applet jmeasurement.jar described at the end of the SI for extracting $^{1}J_{CH}$ automatically is available on request.

Fitting of RDC data to structures was performed using the MSpin software package (Mestrelab Research SL, Santiago de Compostela, Spain); [16]. The 3D structures of all compounds were initially generated using the MacroModel Suite from Shrödinger (https://www.schrodinger.com/MacroModel/). The diastereomers were automatically generated using the LigPrep module in MacroModel and further energy minimized using the MMFFs molecular mechanics force field. AM1 and DFT (B3LYP/6-31G*) calculations were performed in Gaussian 09 (http://www.gaussian.com).

Acknowledgments

Financial support for this research provided by Spanish MINECO (project CTQ2015-64436-P) is gratefully acknowledged. We also thank to the Servei de Ressonància Magnètica Nuclear, Universitat Autònoma de Barcelona, for allocating instrument time to this project. AAS gratefully acknowledges support from the Brazilian agency CAPES (BEX 5382/15-7). NMR instrumentation at Carnegie Mellon University was partially supported by the NSF (CHE-

0130903 and CHE-1039870). RRG gratefully acknowledges support from the NSF (CHE-1111684).

Appendix A. Supplementary material

Supplementary data associated with this article can be found, in the online version, at http://dx.doi.org/10.1016/j.jmr.2017.01.002.

References

[1] (a) C.M. Thiele, Concepts Magn. Reson. Part A 30A (2007) 65–80;
(b) C.M. Thiele, Eur. J. Org. Chem. (2008) 5673–5685;
(c) G. Kummerlöwe, B. Luy, Annu. Rep. NMR Spectrosc. 68 (2009) 193–232;
(d) A. Schuetz, J. Junker, A. Leonov, O.F. Lange, T.F. Molinski, C. Griesinger, J. Am. Chem. Soc. 129 (2007) 15114–15115.
[2] (a) C.M. Thiele, J. Org. Chem. 69 (2004) 7403–7413;
(b) P. Tzvetkova, S. Simova, B. Luy, J. Magn. Reson. 186 (2007) 193–200;
(c) J. Saurí, L. Castañar, P. Nolis, A. Virgili, T. Parella, J. Magn. Reson. 242 (2014) 33–40.
[3] (a) L. Verdier, P. Sakhaii, M. Zweckstetter, C. Griesinger, J. Magn. Reson. 163 (2003) 353–359;
(b) C.M. Thiele, A. Marx, R. Berger, J. Fisher, M. Biel, Angew. Chem., Int. Ed. 45 (2006) 4455–4460;
(c) P. Trigo-Mouriño, A. Navarro-Vázquez, J. Ying, R.R. Gil, A. Bax, Angew. Chem., Int. Ed. 50 (2011) 7576–7580;
(d) N. Nath, E.J. d'Auvergne, C. Griesinger, Angew. Chem., Int. Ed. 54 (2015) 12706–12710.
[4] (a) F. Hallwass, M. Schmidt, H. Sun, A. Mazur, G. Kummerlowe, B. Luy, A. Navarro-Vázquez, C. Griesinger, U.M. Reinscheid, Angew. Chem., Int. Ed. 50 (2011) 9487–9490;
(b) G. Kummerlowe, S.L. Grage, C.M. Thiele, I. Kuprov, A.S. Ulrich, B. Luy, J. Magn. Reson. 209 (2011) 19–30;
(c) N. Nath, M. Schmidt, R.R. Gil, R.T. Williamson, G.E. Martin, A. Navarro-Vázquez, C. Griesinger, Y. Liu, J. Am. Chem. Soc. 138 (2016) 9548–9556.
[5] A. Enthart, J.C. Freudenberger, J. Furrer, H. Kessler, B. Luy, J. Magn. Reson. 192 (2008) 314–322.
[6] J. Saurí, E. Sistaré, R.T. Williamson, G.E. Martin, T. Parella, J. Magn. Reson. 252 (2015) 170–175.
[7] L. Castañar, J. Saurí, R.T. Williamson, A. Virgili, T. Parella, Angew. Chem., Int. Ed. 53 (2014) 8379–8382.
[8] (a) I. Timári, L. Kaltschnee, A. Kolmer, R.W. Adams, M. Nilsson, C.M. Thiele, G.A. Morris, K.E. Kövér, J. Magn. Reson. 239 (2014) 130–138;
(b) T. Reinsperger, B. Luy, J. Magn. Reson. 239 (2014) 110–120;
(c) L. Kaltschnee, A. Kolmer, I. Timári, V. Schmidts, R.W. Adams, M. Nilsson, K. E. Köver, G.A. Morris, C.M. Thiele, Chem. Commun. 50 (2014) 2512–2514;
(d) I. Timári, L. Kaltschnee, M.H. Raics, F. Roth, N.G.A. Bell, R.W. Adams, M. Nilsson, D. Uhrín, G.A. Morris, C.M. Thiele, K.E. Kövér, RSC Adv. 6 (2016) 87848–87855;
(e) A. Lupulescu, G.L. Olsen, L. Frydman, J. Magn. Reson. 218 (2012) 141–146.
[9] (a) M. Liu, R.D. Farrant, J.M. Gillam, J.K. Nicholson, J.C. Lindon, J. Magn. Reson. B 109 (1995) 275–283;
(b) K. Fehér, S. Berger, K.E. Kövér, J. Magn. Reson. 163 (2003) 340–346;
(c) K.E. Kövér, K. Fehér, J. Magn. Reson. 168 (2004) 307–313;
(d) C.M. Thiele, W. Bermel, J. Magn. Reson. 216 (2012) 134–143;
(e) J. Saurí, L. Castañar, P. Nolis, A. Virgili, T. Parella, J. Magn. Reson. 216 (2014) 33–40;
(f) J.D. Snider, E. Troche-Pesqueira, S.R. Woodruff, C. Gayathri, N.V. Tsarevsky, R.R. Gil, Magn. Reson. Chem. 5 (2012) S86–S91;
(g) L. Castañar, M. García, E. Hellemann, P. Nolis, R.R. Gil, T. Parella, J. Org. Chem. 81 (2016) 11126–11131;
(h) N. Cramer, S. Helbig, A. Baro, S. Laschat, R. Diestel, F. Sasse, D. Mathieu, C. Richter, G. Kummerlöwe, B. Luy, H. Schwalbe, ChemBioChem 9 (2008) 2474–2486.
[10] (a) G.P. Kelly, F.W. Muskett, D. Whitford, J. Magn. Reson. B 113 (1996) 88–90;
(b) C. Lendel, P. Damberg, J. Biomol. NMR 44 (2009) 35–42;
(c) J. Furrer, M. John, H. Kessler, B. Luy, J. Biomol. NMR 37 (2007) 231–243.
[11] (a) K. Takegoshi, K. Ogura, K. Hikichi, J. Magn. Reson. 84 (1989) 611–615;
(b) J.A. Aguilar, M. Nilsson, G. Bodenhausen, G.A. Morris, Chem. Commun. 48 (2012) 811–813;
(c) R.W. Adams, C.M. Holroyd, J.A. Aguilar, M. Nilsson, G.A. Morris, Chem. Commun. 49 (2013) 358–360;
(d) B. Baishya, C.L. Khetrapal, J. Magn. Reson. 242 (2014) 143–154;
(e) B. Baishya, C.L. Khetrapal, K.K. Dey, J. Magn. Reson. 234 (2013) 67–74.
[12] J.R. Garbow, D.P. Weitekamp, A. Pines, Chem. Phys. Lett. 93 (1982) 504–509.
[13] D. Uhrín, T. Liptaj, K.E. Kövér, J. Magn. Reson. A 101 (1993) 41–46.
[14] L. Paudel, R.W. Adams, P. Királi, J.A. Aguilar, M. Foroozandeh, M.J. Cliff, M. Nilsson, P. Sándor, J.P. Waltho, G.A. Morris, Angew. Chem., Int. Ed. 52 (2013) 11616–11619.
[15] (a) R.R. Gil, C. Gayathri, N.V. Tsarevsky, K. Matyjaszewski, J. Org. Chem. 73 (2008) 840–848;
(b) C. Gayathri, N.V. Tsarevsky, R.R. Gil, Chem. Eur. J. 16 (2010) 3622–3626;
(c) L.F. Gil-Silva, R. Santamaría-Fernández, A. Navarro-Vázquez, R.R. Gil, Chem. Eur. J. 22 (2016) 472–476;
(d) E. Hellemann, R.R. Teles, H. Hallwass, W. Barros Jr., A. Navarro-Vázquez, R. R. Gil, Chem. Eur. J. 22 (2016) 16632–16635.
[16] A. Navarro-Vázquez, Magn. Reson. Chem. 50 (2012) S73–S79.

Supporting Information

Perfect $^{1}J_{CH}$-resolved HSQC: Efficient measurement of one-bond proton-carbon coupling constants along the indirect dimension.

N. Marcó,[a] A. A. Souza,[a,b] P. Nolis,[a] R. R. Gil[c] and T. Parella*[a]

[a]Servei de Ressonància Magnètica Nuclear, Universitat Autònoma ed Barcelona, E-08193 Bellaterra (Barcelona), Catalonia, Spain.

[b]Departamento de Química, Universidade Federal do Piauí, 64049-550, Teresina, PI, Brazil.

[c]Department of Chemistry, Carnegie Mellon University, Pittsburgh, PA, USA.

Table of contents:

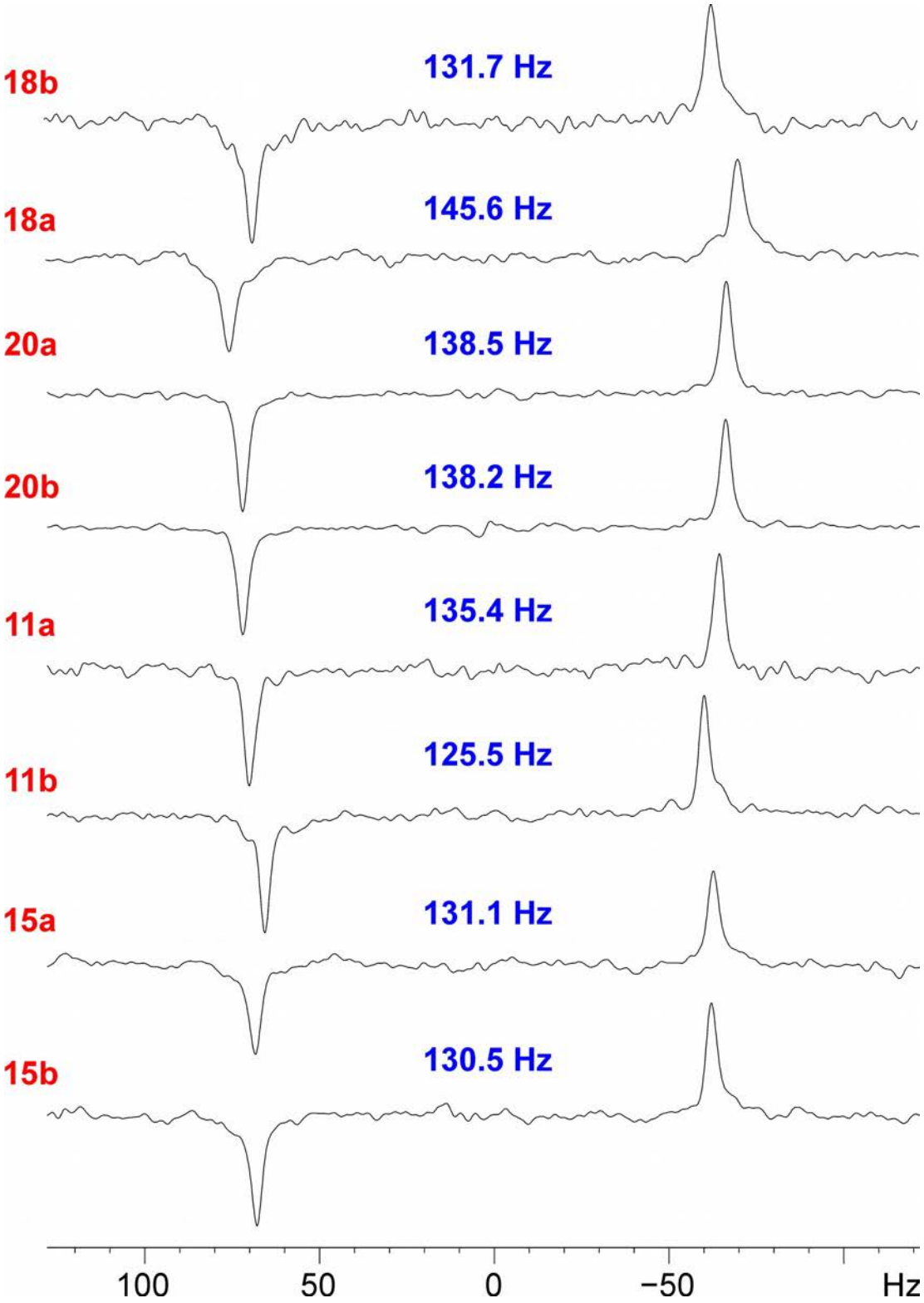

Figure S1: F1 slices taken at some selected CH_2 protons. Linewidths are ~3.4 Hz, FID resolution is 1.95 Hz and spectral resolution is 0.24 Hz after processing.

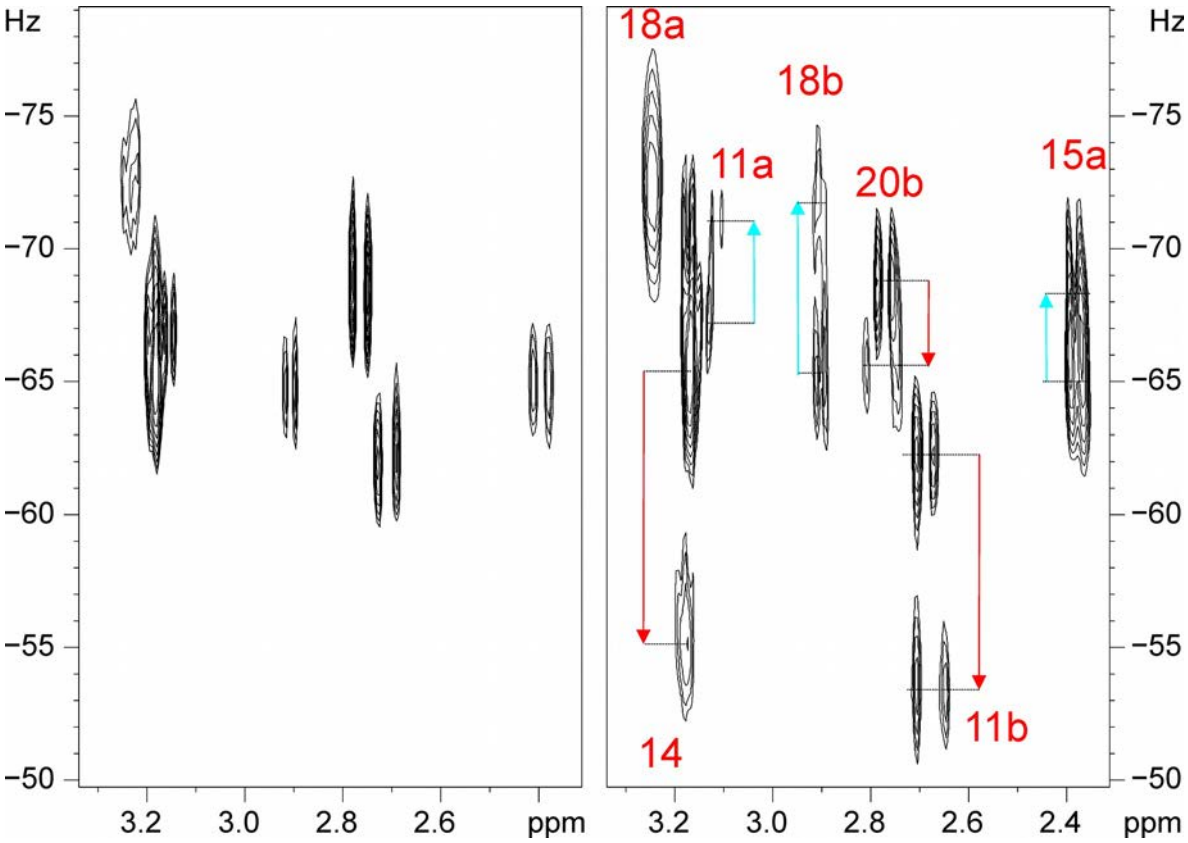

Figure S2: Comparison between 2D perfect $^{1}J_{CH}$-resolved HSQC spectra of strychnine in (left) isotropic and (right) anisotropic conditions.

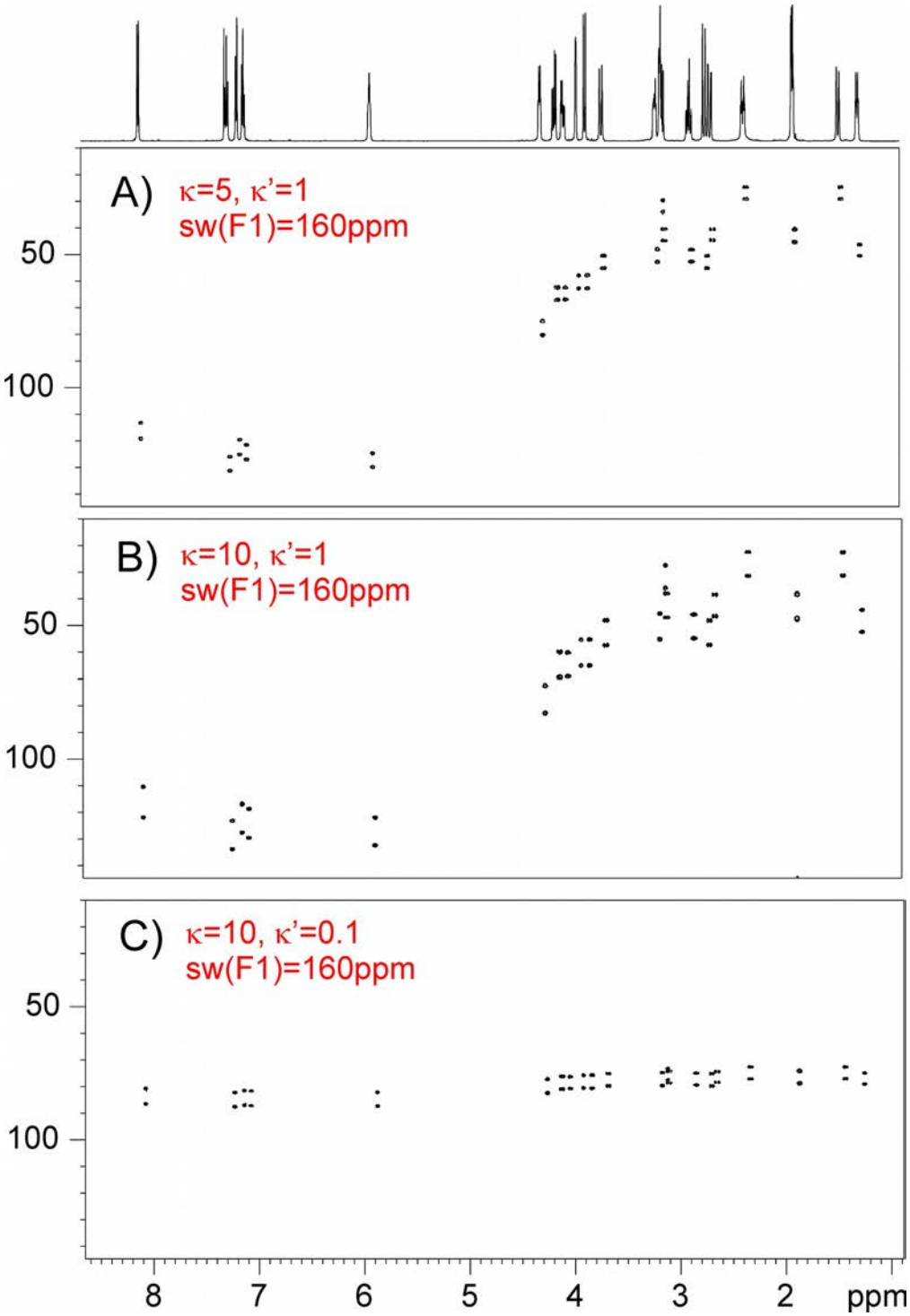

Figure S3: 2D $^{1}J_{CH}$-scaled and δ^{13}C-scaled perfect $^{1}J_{CH}$-resolved HSQC spectra of strychnine acquired using the pulse scheme of Fig. 2A with A) κ = 5 , κ' = 1 and SW(F1) = 160 ppm; B) κ = 10 , κ' = 1 and SW(F1) = 160 ppm; and C) κ= 10 , κ' = 0.1 and SW(F1) = 160ppm;. All other parameters as described in Figure 2.

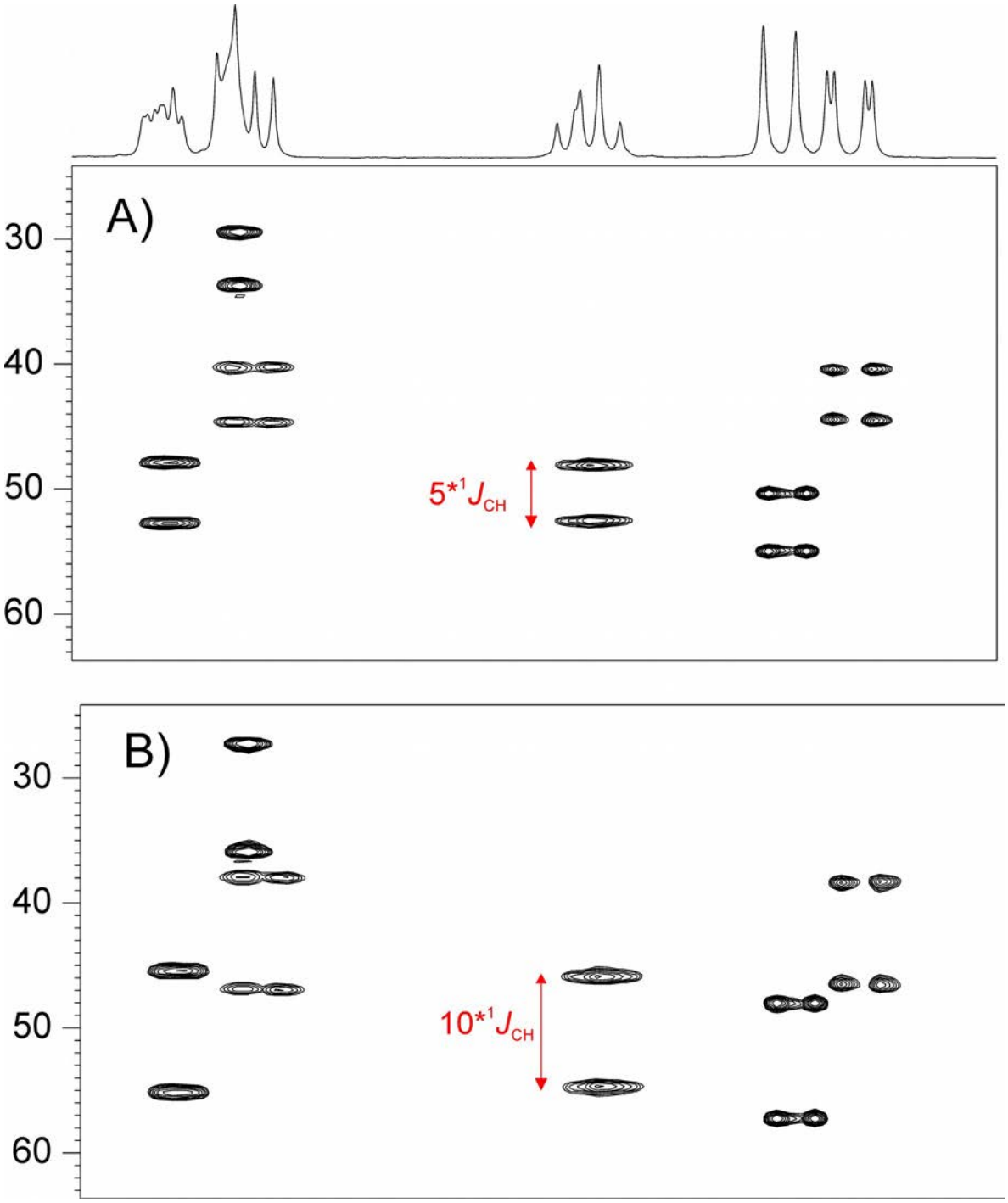

Figure S4: Expansions corresponding to the spectra of Fig. S3A and S3B, respectively.

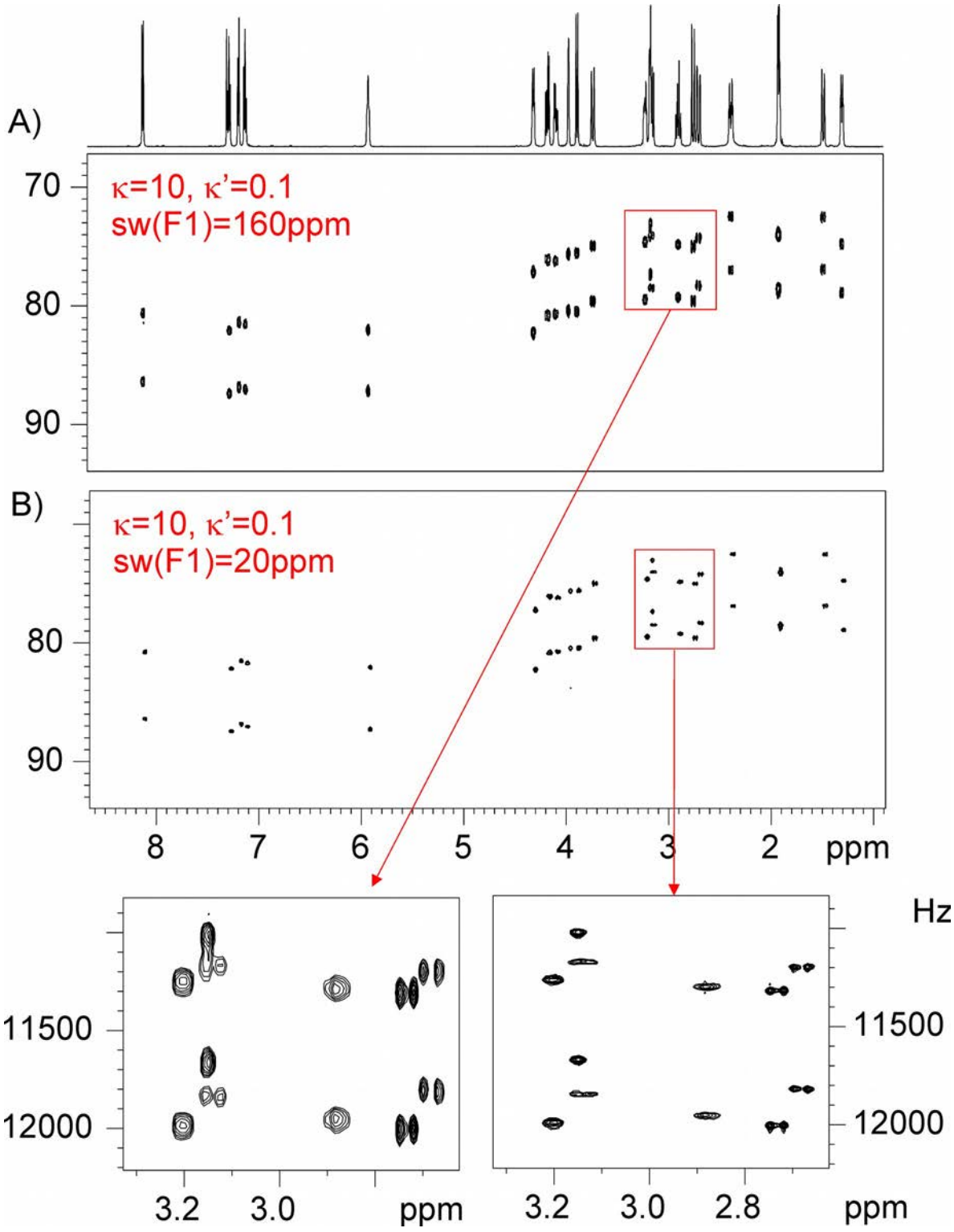

Figure S5: Effect to reduce sw(F1) in δ^{13}C-downscaled perfect $^{1}J_{CH}$-resolved HSQC spectra.

Table S1: One-bond proton-carbon coupling constants of strychnine measured with different NMR methods.

		Ref. 2a	PIP-HSQC (Ref. 7)	κ = 1, κ' = 0 sw(F1) = 1.66 ppm	κ = 5, κ' = 1 sw(F1) = 160 ppm	κ = 10, κ' = 1 sw(F1) = 160 ppm	κ = 5, κ' = 0.1 sw(F1) = 20 ppm
	ppm	F2 coupled	F2 coupled	FID Res.: 2 Hz F1 coupled[a]	FID Res.:188 Hz F1 coupled[a]	FID Res.: 188 Hz F1 coupled[a]	FID Res.: 23 Hz F1 coupled[a]
H13	1.29	124.38	124.80	124.49	127.38	125.02	125.08
H15b	1.47	130.36	129.90	130.49	132.10	132.10	130.64
H17a/b	1.90	132.93	133.20	133.03	136.81	134.45	134.74
H15a	2.37	129.93	130.90	131.07	132.10	132.10	131.52
H11b	2.69	126.08	125.50	125.41	122.66	123.84	125.37
H20b	2.74	138.91	138.70	138.15	139.17	139.17	137.96
H18b	2.88	131.20	131.70	131.67	132.09	132.10	131.22
H11a	3.14	135.06	135.40	135.34	134.45	136.96	135.33
H14	3.15	130.36	131.30	131.07	132.09	129.75	130.05
H18a	3.21	146.17	146.30	145.63	146.93	146.25	145.87
H20a	3.72	138.91	138.80	138.62	141.53	140.35	138.55
H8	3.87	144.89	144.90	144.83	148.61	146.25	144.99
H16	3.96	146.60	146.70	146.18	146.25	143.89	146.45
H23b	4.08	137.20	137.20	136.91	136.81	141.61	136.50
H23a	4.16	145.74	145.50	145.21	146.25	139.17	144.70
H12	4.30	149.17	150.00	149.10	150.97	150.97	149.38
H22	5.91	159.43	158.80	158.60	155.68	158.04	158.76
H2	7.11	161.56	160.80	160.06	165.12	162.76	160.52
H1	7.17	159.00	158.30	158.11	160.40	160.40	158.76
H3	7.27	159.85	159.20	158.35	160.40	158.04	158.76
H4	8.11	168.40	168.40	168.10	174.55	172.20	168.72

[a] Measured automatically using the java applet

Table S2: One-bond proton-carbon coupling constants (in Hz) of strychnine measured in PMMA/$CDCl_3$ gel.

	($\Delta\nu_Q$ ($CDCl_3$) = 36Hz) (ref 9f)		**Perfect Bird (this work)**[a] **($\Delta\nu_Q$ ($CDCl_3$) = 37 Hz)**		
	J_{CH}	D_{CH}	J_{CH}	T_{CH}	D_{CH}
C1H1	158.38	20.97	158.1	178.5	20.4
C2H2	161.70	12.29	160.1	171.4	11.3
C3H3	160.19	10.04	158.3	169.4	11.1
C4H4	168.35	21.58	168.1	189.4	21.3
C8H8	144.91	-9,75	144.8	133.8	-10.0
C12H12	149.03	-20,59	149.1	129.0	-20.1
C13H13	124.88	-4,87	124.5	119.5	-5.0
C14H14	131.03	-20,66	131.1	111.3	-19.8
C16H16	146.55	14,04	146.2	158.8	12.6
C22H22	158.91	-1,06	158.6[b]	158.6[b]	< 3
C11H11a	260.84	-3,46	135.3	143.0	7.7
C11H11b			125.4	108.0	-17.4
C15H15a	260.66	2,54	131.1[b]	131.1[b]	< 3
C15H15b			130.5[b]	130.5[b]	< 3
C17H17a	265,92	1,38	133.1[b]	133.1[b]	< 3
C17H17b			133.1[b]	133.1[b]	< 3
C18H18a	276.20	6,89	145.6[b]	145.6[b]	< 3
C18H18b			131.7	143.3	11.6
C20H20a	276.56	-7,39	138.6	129.8	-8.8
C20H20b			138.1	131.8	-6.3
C23H23a	282.42	-10,3	145.2	149.0	3.8
C23H23b			136.9	112.9	-24.0

[a] Measured manually

[b] Not measured.

Table S3: *Q* factors obtained for eight possible structures of strychnine using RDCs of Table S2 ($\Delta\nu_Q$ ($CDCl_3$) = 37 Hz). Isomer 6 corresponds to the correct structure of strychnine, as evidence with the lowest Q factor.

Quality factors for all conformers in solution 1

Conformer<Q>	Highest Q	Lowest Q	
1: *7R,8R,12R,13R,14R,16S*	0.536091	1.0774e-244	1.69184e-306
2: *7R,8R,12S,13R,14R,16S*	0.579169	1.0774e-244	1.69184e-306
3: *7R,8R,12R,13S,14R,16S*	0.758604	1.0774e-244	1.69184e-306
4: *7R,8R,12S,13S,14R,16S*	0.676194	1.0774e-244	1.69184e-306
5: *7R,8S,12R,13R,14R,16S*	0.204568	1.0774e-244	1.69184e-306
6: *7R,8S,12S,13R,14R,16S*	0.0735346	1.0774e-244	1.69184e-306
7: *7R,8S,12R,13S,14R,16S*	0.869824	1.0774e-244	1.69184e-306
8: *7R,8S,12S,13S,14R,16S*	0.255259	1.0774e-244	1.69184e-306

Automated extraction of $^{1}J_{CH}$ coupling values

Herein is presented a java applet that successfully performs the automated $^{1}J_{CH}$ spectral analysis from the $^{1}J_{CH}$ resolved perfect HSQC NMR experiment. Below is detailed a tutorial with the necessary steps to run the applet. Special emphasis is given in the generation of the input .csv file which is the key point for the applet to work properly. Furthermore, the applet algorithms behind the automation measurement will be explained.

User Tutorial

When the .jar java applet file is executed a Graphical User Interface (GUI) is launched. Applet GUI is very simple and intuitive and the procedure steps to follow are as well.

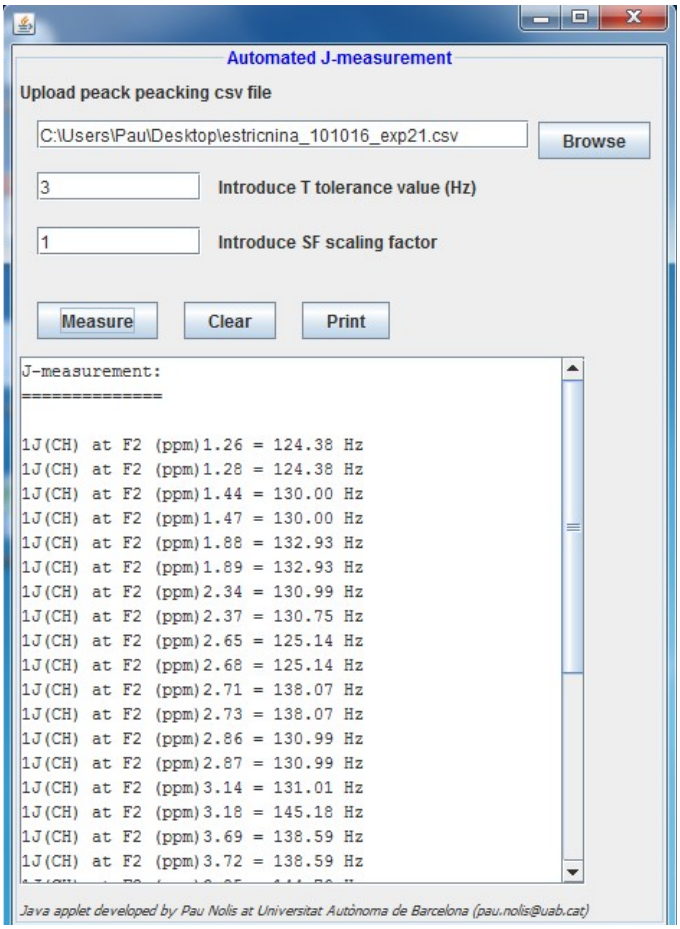

Step 1: Browse in your computer a .csv file extracted from peak picking analysis in Bruker software. Details on how to generate properly this input file are explained below.

Step 2: Set tolerance to missalignment (3 Hz is a recommended value). Set the SF *J*-scaling factor used in the $^{1}J_{CH}$ resolved perfect HSQC NMR experiment. If any scaling factor is applied, set 1 in the text area.

Step 3: Click Measure button and the result will be displayed in the text area. Obtained results are listed in terms of cross-peaks coordinate (1H chemical shift in ppm) and the corresponding coupling $^{1}J_{CH}$ in Hz. Optionally Print button can be used to create a PDF file report. Clear button cleans text area and procedure can be executed again with another CSV file.

Note: *In order to launch the java applet Jmeasurement.jar is a requirement to have previosuly installed in your system the JRE (Java Runtime Environtment). Any further questions/suggestions to pau.nolis@uab.cat.*

Input file generation

The applet is designed to read .csv file generated from Topspin 2.x (Bruker Software) that should be created as explained next. Very similar procedure can be done in Topspin 3.x. although not details are provided for this version.

1) Select Peak Picking from Analysis menu

2) Because the presented experiment presents F1-coupled antiphase signals it is important select All in the Pick peaks of sign in order to select both positive and negative peaks.

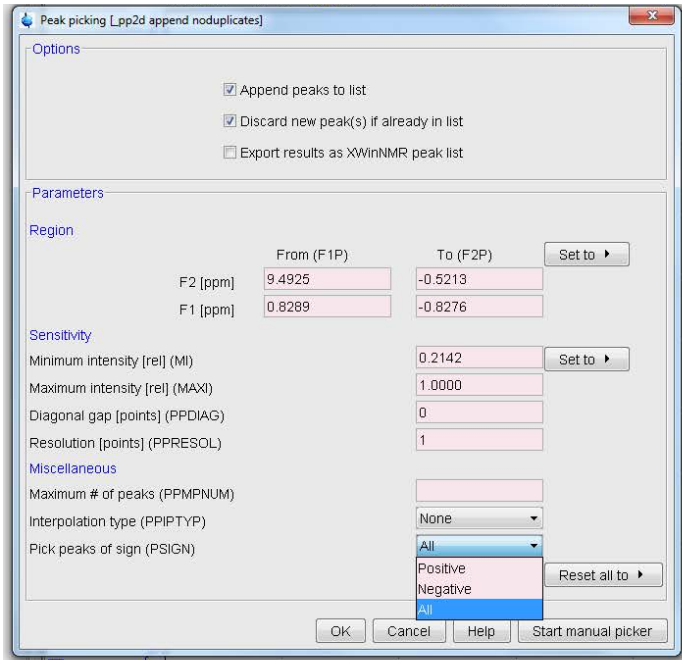

3) Once the peak picking is done the Peaks label should be selected in order to prepare the peak table to be exported as .csv

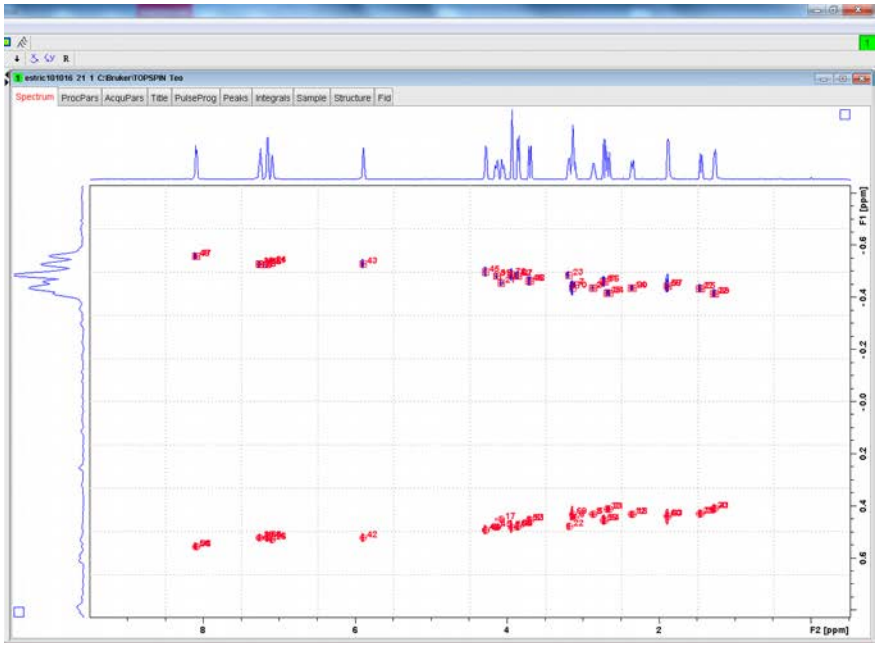

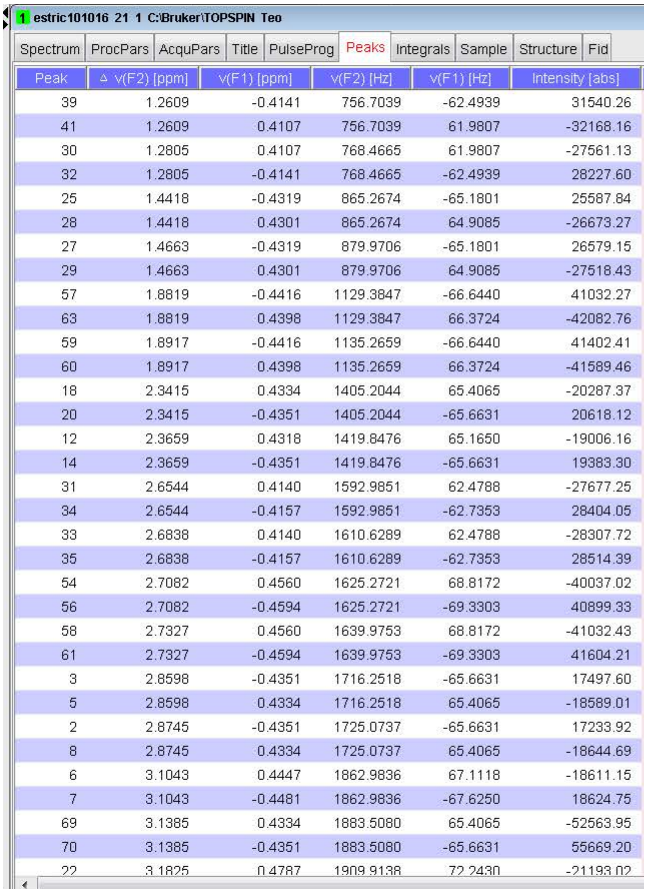

Peak	ν(F2) [ppm]	ν(F1) [ppm]	ν(F2) [Hz]	ν(F1) [Hz]	Intensity [abs]
39	1.2609	-0.4141	756.7039	-62.4939	31540.26
41	1.2609	0.4107	756.7039	61.9807	-32168.16
30	1.2805	0.4107	768.4665	61.9807	-27561.13
32	1.2805	-0.4141	768.4665	-62.4939	28227.60
25	1.4418	-0.4319	865.2674	-65.1801	25587.84
28	1.4418	0.4301	865.2674	64.9085	-26673.27
27	1.4663	-0.4319	879.9706	-65.1801	26579.15
29	1.4663	0.4301	879.9706	64.9085	-27518.43
57	1.8819	-0.4416	1129.3847	-66.6440	41032.27
63	1.8819	0.4398	1129.3847	66.3724	-42082.76
59	1.8917	-0.4416	1135.2659	-66.6440	41402.41
60	1.8917	0.4398	1135.2659	66.3724	-41589.46
18	2.3415	0.4334	1405.2044	65.4065	-20287.37
20	2.3415	-0.4351	1405.2044	-65.6631	20618.12
12	2.3659	0.4318	1419.8476	65.1650	-19006.16
14	2.3659	-0.4351	1419.8476	-65.6631	19383.30
31	2.6544	0.4140	1592.9851	62.4788	-27677.25
34	2.6544	-0.4157	1592.9851	-62.7353	28404.05
33	2.6838	0.4140	1610.6289	62.4788	-28307.72
35	2.6838	-0.4157	1610.6289	-62.7353	28514.39
54	2.7082	0.4560	1625.2721	68.8172	-40037.02
56	2.7082	-0.4594	1625.2721	-69.3303	40899.33
58	2.7327	0.4560	1639.9753	68.8172	-41032.43
61	2.7327	-0.4594	1639.9753	-69.3303	41604.21
3	2.8598	-0.4351	1716.2518	-65.6631	17497.60
5	2.8598	0.4334	1716.2518	65.4065	-18589.01
2	2.8745	-0.4351	1725.0737	-65.6631	17233.92
8	2.8745	0.4334	1725.0737	65.4065	-18644.69
6	3.1043	0.4447	1862.9836	67.1118	-18611.15
7	3.1043	-0.4481	1862.9836	-67.6250	18624.75
69	3.1385	0.4334	1883.5080	65.4065	-52563.95
70	3.1385	-0.4351	1883.5080	-65.6631	55669.20
22	3.1825	0.4787	1909.9138	72.2430	-21193.02

Peak table should contain 6 columns displayed in the following order: Peak, F2[ppm], F1[ppm], F2[Hz], F1[Hz] and Intensity(abs). To do so pressing the right mouse button a Table Properties submenu is displayed when you can prepare the table as explained.

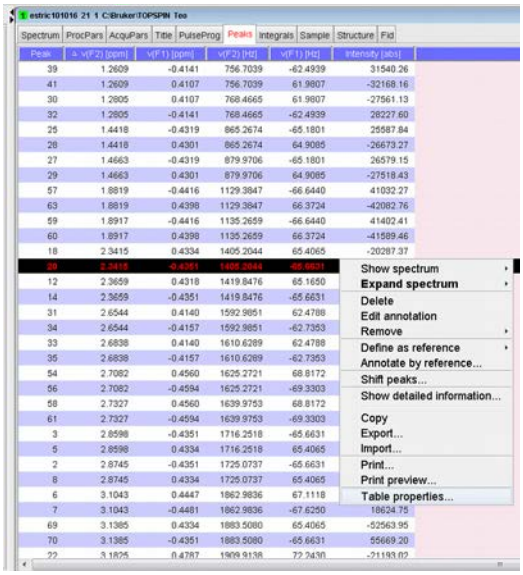

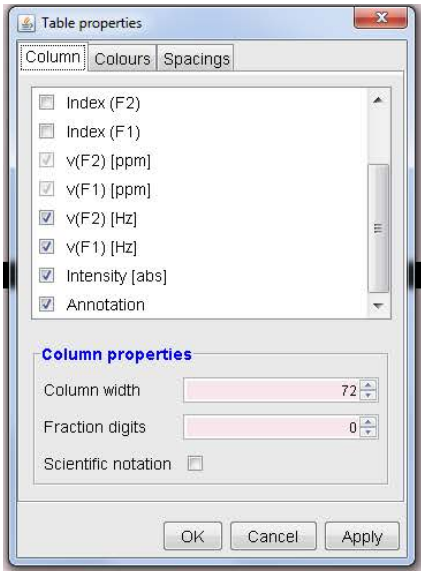

Ordering F2[ppm] in ascendant order will generate an ordered output file by the applet which is recommended but not mandatory.

4) With peak table prepared properly just export table in .csv format and that's it you can enjoy the java applet.

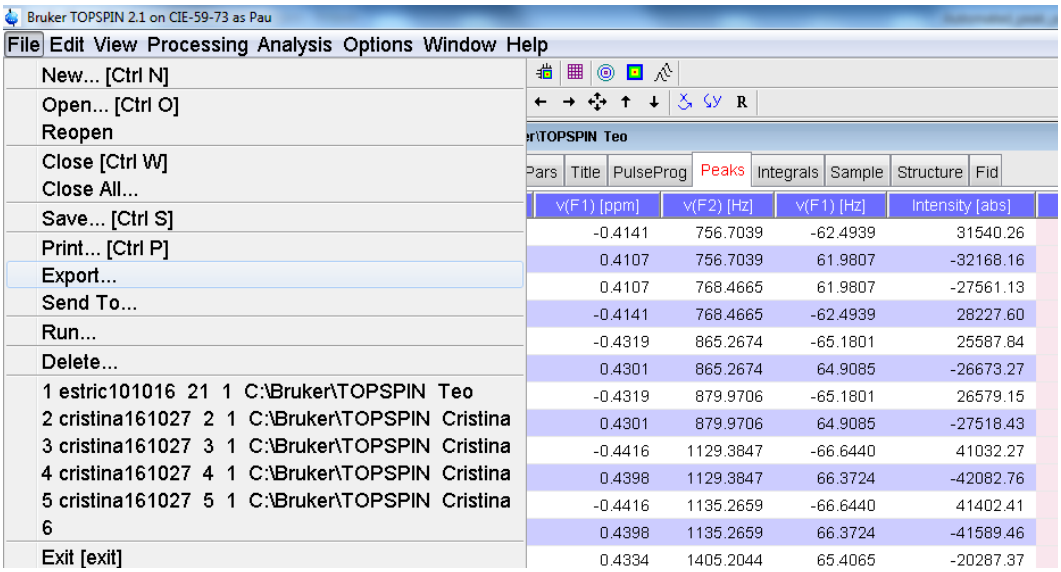

Java applet algorithms

Basically, two different algorithms run when using the applet depending on the scaling factor SF. Details are explained below.

SF = 1 algorithm

When SF is set to 1 (no *J*-scaling is applied), the implemented algorithm search two aligned peaks in the acquisition dimension (F2 in Bruker format). Because the alignment is almost never perfect a degree of tolerance T for peak misalignment is allowed. A recommended value is 3 Hz.

F2 restriction: Absolute_mode(peak1_F2frequency – peak2_F2frequency) < Tolerance (Hz)

Once a peak pair is found, the algorithm checks that those peaks present an equidistant displacement respect de the indirect dimension spectrum center (zero). Again, because experimentally the equidistance is experimentally never perfect a certain tolerance is allowed by the algorithm and specified by the user.

F1 restriction: *Absolute_mode (Absolute_mode(peak1_F1frequency) – Absolute_mode(peak2_F1frequency)) < Tolerance (Hz)*

It is noticeable that this *F1 restriction* permits distinction of different J couplings when having F2-overlapped peaks. However, if the difference between involved couplings is less than the user specified tolerance, for instance 3 Hz, the applet will calculate four couplings instead of the expected two (see scheme below). Therefore a visual inspection is required to decide the correct peak pairs couples. See scheme below.

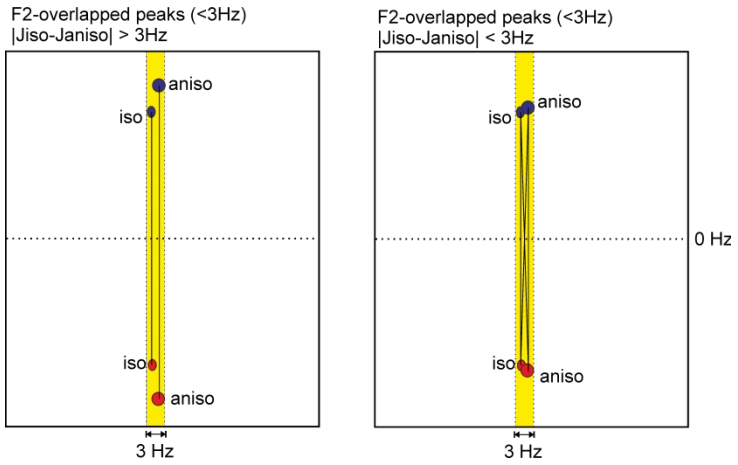

SF > 1 algorithm

In that case F2-restriction is maintained as for SF=1 above explained algorithm. However, because chemical shift evolution implies that Jres representation is lost, *F1 restriction* is redefined because spectral F1-symmetry no longer exists. In that case instead of a symmetry restriction, we introduce a restriction concerning the antiphase coupling pattern and the expected *J* values between 110 and 190 Hz taking into account we will work in weakly oriented media.

F1 restriction:

*peak1_intensity*peak2_intensity < 0 and coupling > 110Hz and coupling < 190Hz*

With this F1 restriction we are able to discern between couplings of F2-overlapped signals A and B when |δa-δb| >> lower(^1J_A,^1J_B) but the applet will fail and calculate cross couplings when |δa-δb| << lower(^1J_A,^1J_B). See scheme below.

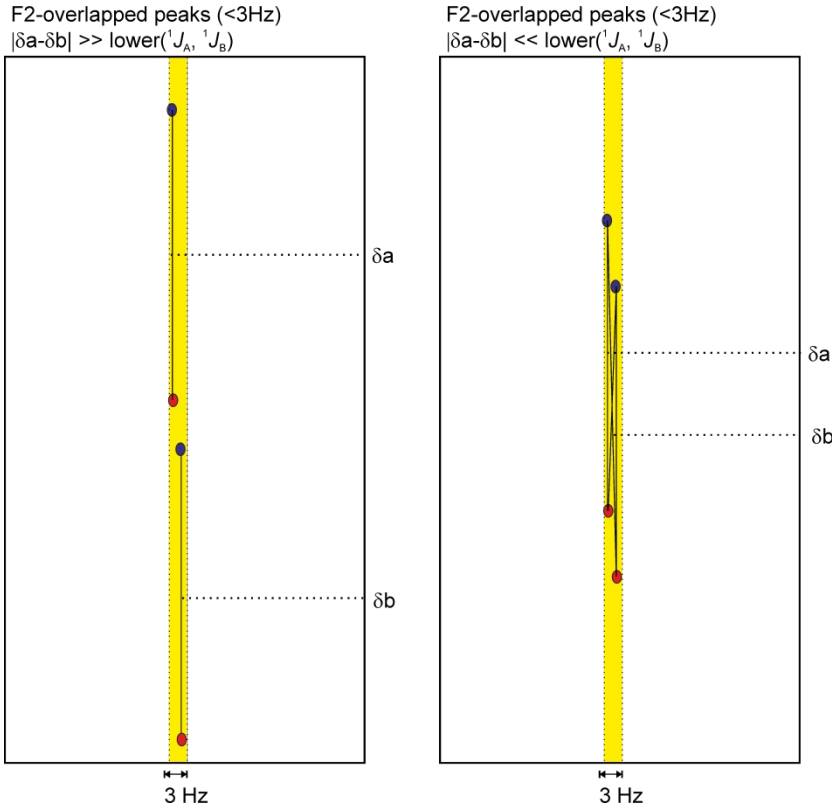

Therefore, spectroscopist should pay attention to this special case and check which two of the four automatically calculated couplings are correct.

Bruker pulse program of the Perfect 1JCH-HSQC experiment

```
;Perfect-1JCH-HSQC
;Tested in TS3.1

#include <Avance.incl>
#include <Grad.incl>
#include <Delay.incl>
#include <De.incl>

;deactive ps if not homodecoupling during acquisition is performed
#define ps
define loopcounter count

"d19=dw*l12"
"DELTA7=d19/2"
"d20=d2-larger(p2,p14)/2"

"p2=p1*2"
"d0=3u"
"d2=1s/(cnst2*2)"
"d4=1s/(cnst2*4)"

"in0=inf1/2"

"DELTA=p16+d16+p2+d13*2-4u"
"DELTA2=d4-p14/2-4u"
"DELTA4=d4-p14/2-4u-p16-d16"
"DELTA5=d2-larger(p2,p14)/2"

"count=(aq/d19)-1"
"acqt0=0"
baseopt_echo

dwellmode explicit


1 ze
2 d1 do:f2
  d12 pl1:f1
3 (p1 ph1)

  d0
  p1 ph1
  DELTA5 pl0:f2
  (center (p2 ph1) (p14:sp3 ph6):f2 )
  DELTA5 pl2:f2
  p1 ph1
  (p4 ph1):f2
  d0
  p1 ph2
  d0
  p1 ph1
  DELTA5 pl0:f2
```

```
  (center (p2 ph1) (p14:sp3 ph6):f2 )
  DELTA5 pl2:f2
  p1 ph1
  d0

  (center (p1 ph2) (p3 ph3):f2 )
  d13 UNBLKGRAD
  (p2 ph1)
  d13
  p16:gp1*EA
  d16 pl0:f2
  (p24:sp7 ph4):f2
  4u
  DELTA pl2:f2
  (center (p1 ph1) (p3 ph4):f2 )
  DELTA2 pl0:f2
  4u
  (center (p2 ph1) (p14:sp3 ph1):f2 )
  4u
  DELTA4
  p16:gp2
  d16 pl12:f2
  d12 BLKGRAD

#ifdef ps
4 ACQ_START(ph30,ph31) ;takes de

;initial half chunk
  10u pl12:f2
   10u cpd2:f2
  0.05u DWL_CLK_ON
  0.1u REC_UNBLK
  DELTA7
  0.1u REC_BLK
  0.05u DWL_CLK_OFF
   10u do:f2
   10u

(p1 ph1)
d20 pl0:f2
(center (p2 ph2) (p14:sp3 ph1):f2 )
d20 pl2:f2
(p1 ph7)
160u
(p2 ph1)

;looped chunks
5  10u pl12:f2
   10u cpd2:f2

    0.05u DWL_CLK_ON
  0.1u REC_UNBLK
  d19
  0.1u REC_BLK
```

```
  0.05u DWL_CLK_OFF
   10u do:f2
   10u

(p1 ph1)
d20 pl0:f2
(center (p2 ph2) (p14:sp3 ph1):f2 )
d20 pl1:f1 pl2:f2
(p1 ph7)
160u
(p2 ph1)
lo to 5 times count

  10u pl12:f2
   10u cpd2:f2

    0.05u DWL_CLK_ON
  0.1u REC_UNBLK
  DELTA7
  0.1u REC_BLK
  0.05u DWL_CLK_OFF
   10u do:f2
   10u
50u
    rcyc=2

#else
d12 pl12:f2
go=2 ph31 cpd2:f2
#endif

  d1 do:f2 mc #0 to 2
     F1EA(calgrad(EA), caldel(d0, +in0))
exit

ph1=0
ph2=1
ph3=0 2
ph4=0
ph6=0
ph7=2

ph15=1
ph16=2
ph17=3

ph25=2
ph26=3
ph27=0

ph30=0
ph31=0 2
```

```
;pl0 : 120dB
;pl1 : f1 channel - power level for pulse (default)
;pl2 : f2 channel - power level for pulse (default)
;sp3: f2 channel - shaped pulse 180 degree
;spnam3: Crp60,0.5,20.1
;sp7: f2 channel - shaped pulse (180degree refocusing)
;spnam7: Crp60comp.4
;p1 : f1 channel -  90 degree high power pulse
;p2 : f1 channel - 180 degree high power pulse
;p3 : f2 channel -  90 degree high power pulse
;p14: f2 channel - 180 degree shaped pulse for inversion
;     = 500usec for Crp60,0.5,20.1
;p16: homospoil/gradient pulse                          [1 msec]
;p24: f2 channel - 180 degree shaped pulse for refocusing
;     = 2msec for Crp60comp.4
;d0 : incremented delay (2D)                            [3 usec]
;d1 : relaxation delay; 1-5 * T1
;d2 : 1/(2J(XH))
;d4 : 1/(4J(XH))
;d16: delay for homospoil/gradient recovery
;cnst2: = J(XH)
;cnst17: = -0.5 for Crp60comp.4
;in0: 1/(2 * SW(X)) = DW(X)
;nd0: 2
;NS: 2 * n
;DS: >= 4
;td1: number of experiments
;FnMODE: echo-antiecho

;use gradient ratio:   gp 1 : gp 2
;                  80 : 20.1   for C-13

;for z-only gradients:
;gpz1: 80%
;gpz2: 20.1% for C-13

;use gradient files:
;gpnam1: SINE.100
;gpnam2: SINE.100
```

PUBLICATION 6

Title: $^{1}J_{CH}$ NMR Profile: Identification of key structural features and functionalities by visual observation and direct measurement of one-bond proton-carbon coupling constants

Authors: Marcó, N.; Souza, A. A.; Nolis, P.; Cobas, C.; Gil, R. R.; Parella, T.

Reference: *J. Org. Chem.* **2017**, *82* (4), 2040–2044.

DOI: 10.1021/acs.joc.6b02873

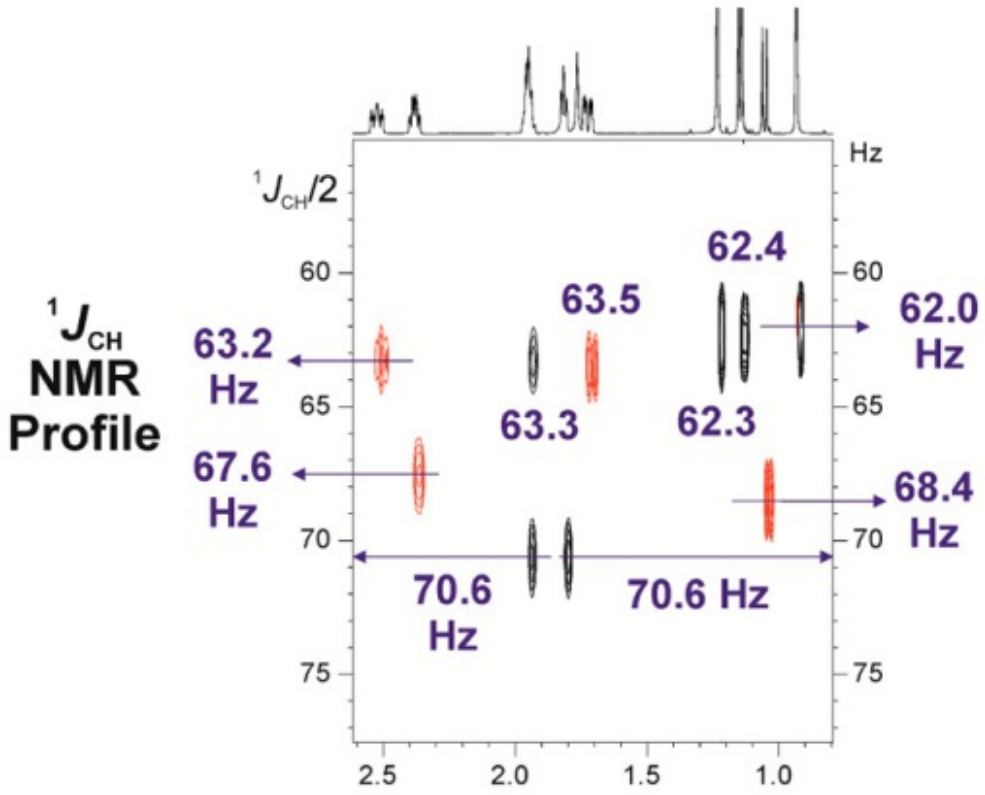

SUMMARY

This publication describes the development and application of a new 2D graphical interface for the fast and accurate determination of the $^{1}J_{CH}$ coupling constant in small molecules. This intuitive $^{1}J_{CH}$ NMR profile is generated from a novel *J*-resolved-HSQC experiment that correlates $\delta(^{1}H)$ in F2 directly with $^{1}J_{CH}$ in F1. This pulse sequence contains an initial multiplicity editing HSQC element, followed by a perfect BIRD *J*-resolved block that refocuses J_{HH} modulation and a ZQF to provide PIP signals in F1. Thanks to the ME block, protons belonging to CH/CH_3 vs CH_2 are quickly differentiated, facilitating signal assignment.

The symmetrical $^{1}J_{CH}$ data representation allows an easy *J* measurement manually or by automatic peak picking. With the assignment of the ^{1}H and the ^{13}C, the interpretation of the results obtained with this profile is easy and fast.

JOC The Journal of Organic Chemistry

Article

pubs.acs.org/joc

$^1J_{CH}$ NMR Profile: Identification of Key Structural Features and Functionalities by Visual Observation and Direct Measurement of One-Bond Proton-Carbon Coupling Constants

Núria Marcó,[†] Alexandre A. Souza,[†,∥] Pau Nolis,[†] Carlos Cobas,[‡] Roberto R. Gil,[§] and Teodor Parella*[,†]

[†]Servei de Ressonància Magnètica Nuclear, Universitat Autònoma de Barcelona, E-08193 Bellaterra (Barcelona) Catalonia, Spain

[‡]Mestrelab Research, Santiago de Compostela, E-15706 A Coruña, Spain

[§]Department of Chemistry, Carnegie Mellon University, Pittsburgh, Pennsylvania 15213, United States

[∥]Departamento de Química, Universidade Federal do Piauí, Teresina, PI 64049-550, Brazil

Supporting Information

ABSTRACT: A user-friendly NMR interface for the visual and accurate determination of experimental one-bond proton-carbon coupling constants ($^1J_{CH}$) in small molecules is presented. This intuitive $^1J_{CH}$ profile correlates directly to $\delta(^1H)$, and $^1J_{CH}$ facilitates the rapid identification and assignment of ^1H signals belonging to key structural elements and functional groups. Illustrative examples are provided for some target molecules, including terminal alkynes, strained rings, electronegative substituents, or lone-pair-bearing heteronuclei.

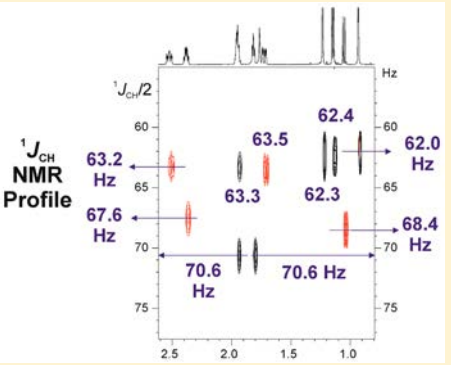

INTRODUCTION

Heteronuclear one-bond proton-carbon coupling constants ($^1J_{CH}$) offer a wealth of structural, stereochemical, and conformational information in small synthetic and natural products in solution.[1] As a general trend, $^1J_{CH}$ values range from 120 to 250 Hz, typically 120−140 Hz for aliphatic, 140−170 Hz for olefinic or aromatic, 170−200 Hz in characteristic aromatic heterocycles, and around 250 Hz in terminal alkynes. The magnitude of $^1J_{CH}$ is directly related to the *s* character of the CH bond and also is strongly influenced by the nature of substituents on the carbon center and on its surroundings. Within the last four decades, a large number of scientific publications demonstrating the success of these couplings to identify key structural features and functional groups have been extensively reported. For instance, characteristic $^1J_{CH}$ couplings are fundamental to determine the anomeric α/β configuration in hexopyranoses, to assign sp triple bond protons, to characterize aromatic heterocycles, and to confirm the presence of electronegative nuclei (oxygen, chlorine or bromine, etc.) or of strained ring systems such as cyclopropanes, epoxides, cyclobutanes, or fused bicycle systems (norbornanes, pinanes, etc.).[1]

$^1J_{CH}$ values are currently determined from well-defined doublets along the direct F_2[2,3] or the indirect F_1[4] dimensions in modern HSQC experiments. These measurements are usually performed by determining the distance in hertz between the two separated components of each individual cross-peak, although more sophisiticated approaches involving simulations and *J* modulations have also been proposed.[5] In general, most of these studies have concentrated on the accuracy, general applicability, and the simplicity of such measurements. We propose here a completely new and complementary approach to visualize, analyze, and even determine directly and precisely $^1J_{CH}$ values in a very straightforward way. Our method is based on the generation of a helpful $^1J_{CH}$ NMR profile that allows the observation of the complete range of $^1J_{CH}$ existing in a given molecule at a glance. This 2D $^1J_{CH}$ profile correlates directly $\delta(^1H)$ and $^1J_{CH}$, and it can be interpreted like an NMR chromatography, where ^1H signals at the detected F_2 dimension are dispersed by their $^1J_{CH}$ in F_1, resembling the popular DOSY representation, where ^1H signals are dispersed as a function of their diffusion coefficients.[6]

RESULTS AND DISCUSSION

For this purpose, we have designed a novel *J*-resolved HSQC (HSQC-$^1J_{CH}$) pulse scheme that contains three sequential steps (Figure 1): (i) an initial 1D ^{13}C isotope filter based on the multiplicity-edited (ME) HSQC pulse timing to select ^1H directly attached to ^{13}C;[7] (ii) a *J*-resolved block based on the

Received: December 1, 2016
Published: January 9, 2017

DOI: 10.1021/acs.joc.6b02873
J. Org. Chem. 2017, 82, 2040−2044

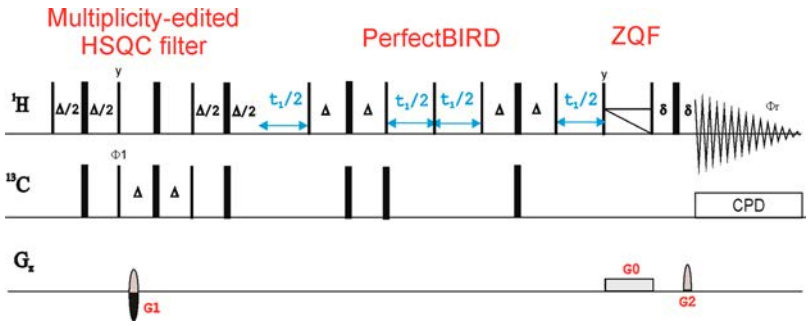

Figure 1. General pulse scheme to record two-dimensional HSQC-$^1J_{CH}$ experiments. Thin and thick rectangles represent 90 and 180° rectangular pulses, respectively, applied along the *x* axis unless indicated differently. A basic two-step phase cycling is applied: $\phi_1 = x,-x$; $\phi_{rec} = x,-x$. Inversion and refocusing 180° ^{13}C pulses can be applied as adiabatic pulses. The interpulse delays in INEPT and BIRD elements are optimized according to $\Delta = 1/(2*^1J_{CH})$. The ratio between gradients G1/G2 was 80:20.1, and the final ZQF consists of a chirped adiabatic pulse applied simultaneously to a rectangular gradient (G0). The echo/antiecho encoding in F1 was achieved by changing the sign of G1 between successive t_1 increments. More details can be found in the Supporting Information.

perfectBIRD element[3c] to allow the exclusive evolution of $^1J_{CH}$, whereas $^2J_{HH}$ values are efficiently refocused; and (iii) a final zero-quantum filter (ZQF)[8] prior to acquisition to remove any unwanted dispersive contribution to the line shapes.

This experiment initially produces a symmetrical spectrum with respect to $F_1 = 0$, where, in an unprecedented way, all ^1H signals show a clean doublet along the F_1 dimension due to $^1J_{CH}$, irrespective of their methine, methylene, or methyl nature. As a proof of concept, Figure 2A shows the superb features of the 140 Hz optimized HSQC-$^1J_{CH}$ spectrum of the alkaloid strychnine (**1**), where signals present a pure in-phase character in F_1 with respect to $^1J_{CH}$, whereas their relative positive/negative phase generated by the ME block allows a quick distinction between CH/CH_3 (up) and CH_2 (down) protons. In order to further facilitate the qualitative and quantitative analysis of this simple spectrum, the alternative visualization and analysis of only one part of the spectrum, the so-called $^1J_{CH}$ NMR profile, is proposed (Figure 2B). Taking advantage of its symmetry, we reconstructed half of the spectrum by a simple spectral self-combination postprocessing (an automated algorithm is available for Mnova software package). The $^1J_{CH}$ profile affords a very useful interface to quickly identify characteristic $^1J_{CH}$ values that can confirm the existence of particular structural features and/or functional groups in an unknown structure. Assuming that HSQC-$^1J_{CH}$ experiments will be recorded once the assignment of both ^1H and ^{13}C chemical shifts would already been established by traditional NMR methods, the interpretation of the $^1J_{CH}$ NMR profile becomes obvious, easy, and fast. Each ^1H signal appears just to the coordinate $^1J_{CH}/2$ along F_1, allowing a direct determination of $^1J_{CH}$ and an overall visualization of the full range of existing $^1J_{CH}$ values in the molecule. For instance, a complete set of experimental $^1J_{CH}$ ranging from 124.2 to 168.2 Hz is observed in **1** that can be related to several functionalities and structural features present in the molecular structure. First, the large difference of 15.7 Hz observed for the diastereotopic H18a (145.9 Hz) and H18b (130.2 Hz) protons can be attributed to the Perlin effect, which correlates $^1J_{CH}$ to the lone-pair orientation of the neighboring N19 amine nitrogen. In this case, $^1J_{CH}$ is larger when the respective CH bond is *cis* to the nitrogen lone pair than when it is in a *trans* rearrangement.[9] Similar effects are observed for the aliphatic H16 (146.4 Hz) and H8 (144.9 Hz) methine protons and for H12 (149.1 Hz), which is adjacent to an oxygen nucleus. Also the relative orientation of H11a and H11b protons with respect to the

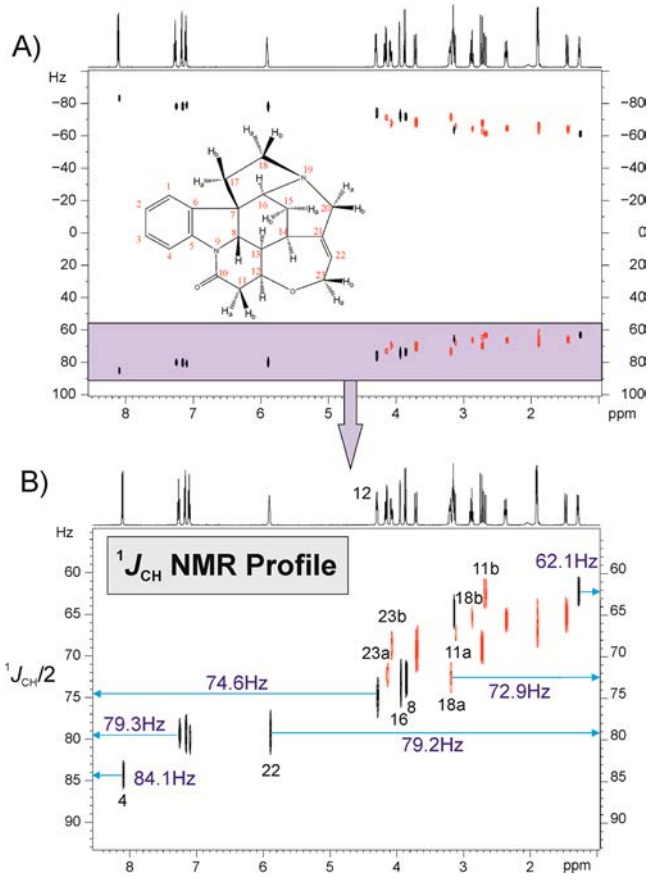

Figure 2. (A) 600.13 MHz 2D HSQC-$^1J_{CH}$ spectrum of strychnine (**1**) in $CDCl_3$ from which $^1J_{CH}$ could be extracted from the clean doublet in F_1 for each individual ^1H signal. (B) Graphical and more intuitive $^1J_{CH}$ NMR profile from which the magnitude of $^1J_{CH}/2$ (in Hz) can be directly obtained from the F_1 coordinate of each cross-peak. Illustrative $^1J_{CH}$ values are given in hertz for some selected peaks. Positive black peaks correspond to CH/CH_3, and negative red peaks are CH_2. See more detailed expanded areas in Figure S1.

carbonyl C10 can be established by the large difference of their $^1J_{CH}$ (134.2 vs 124.7, respectively) and the larger $^1J_{CH}$ of H4 (about 10 Hz) compared to that of the other aromatic protons, which is attributed to the presence of the N9 amide group in its *ortho* position. Finally, the H23a/b protons (144.4 and 136.3 Hz, respectively) are a good example showing how $^1J_{CH}$ values

DOI: 10.1021/acs.joc.6b02873
J. Org. Chem. 2017, 82, 2040−2044

The Journal of Organic Chemistry Article

smaller than expected are the result of the opposite effect between Perlin and hyperconjugative (C−H) → π* interactions.[1b]

The $^1J_{CH}$ data extracted from the profile manually or from an automated peak picking correlate very well with those determined by measuring individually each doublet along F_1 from the spectrum of Figure 2A and also agree with experimental data measured from other NMR methods in previous works.[10] In the past years, the potential prediction of theoretical $^1J_{CH}$ values for accurate structure elucidation and validation has been revisited by several authors.[11] We have compared our experimental results with those calculated by DFT,[11a] and a good correlation can be traced for all protons, although a general and systematic overestimation of the theoretical values by 2−3% exists (see Figure 3 and Table S1).

Figure 3. Correlation between experimental (blue; measured in this work) and theoretical (red; DFT calculations from ref 11a) $^1J_{CH}$ values (in Hz) in **1**. Note the systematic 2−3% overestimation of the theoretical values.

Figure 4 shows the $^1J_{CH}$ NMR profile of (+)-isopinocampheol (**2**) as an example of a molecule containing a strained bicyclo[3.1.1] skeleton. It is a good example demonstrating that $^1J_{CH}$ does not correlate with chemical shifts. As a quick view, all ^{1}H involved in the characteristic strained bridge shows $^1J_{CH}$ larger than usual [H1 (141.2 Hz), H5 (141.2 Hz), H7s (135.2 Hz), and H7a (136.8 Hz)], whereas all other aliphatic signals

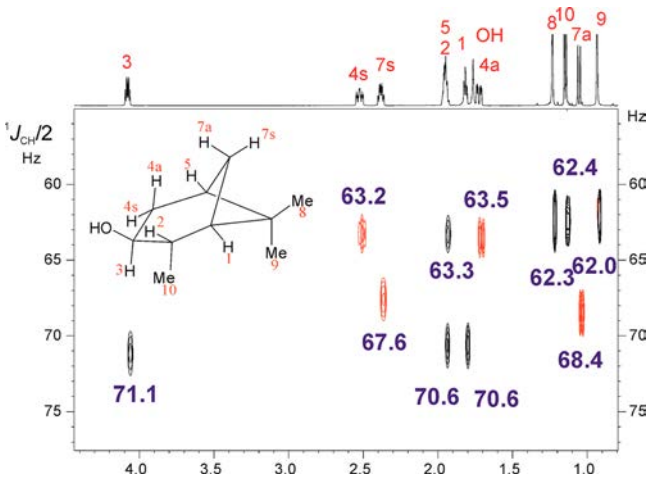

Figure 4. $^1J_{CH}$ NMR profile of (+)-isopinocampheol (**2**) in $CDCl_3$. The magnitude of $^1J_{CH}/2$ (in Hz) is extracted directly from the F_1 coordinate of each individual cross-peak.

present typical magnitudes in the range between 124 and 127 Hz. Also note the large $^1J_{CH}$ of H3 (142.2 Hz) due to the presence of the hydroxyl group and the efficient distinction between the fully overlapped H2 and H5 signals. Similarly, Figure 5 shows the $^1J_{CH}$ NMR profile of 2-exobromonorbor-

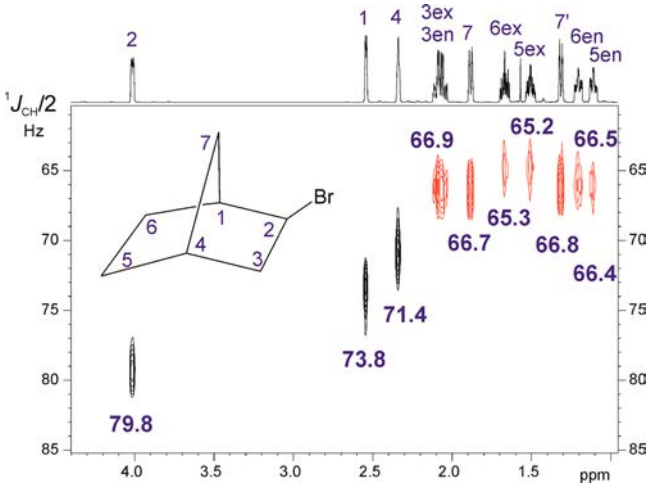

Figure 5. $^1J_{CH}$ NMR profile of 2-exobromonorbornane (**3**) in $CDCl_3$. The magnitude of $^1J_{CH}/2$ (in Hz) is extracted directly from the F_1 coordinate of each individual cross-peak.

nane (**3**), which contains a strained bicyclo[2.2.1] skeleton and an electronegative bromine substituent. At first sight, all CH_2 protons do not seem to show relevant $^1J_{CH}$ differences (between 130.4 and 133.6 Hz), but exo protons clearly present values (about 130.5 Hz) smaller than that of their endo pairs (about 133 Hz), demonstrating the excellent level of resolution achieved in F_1. On the other hand, the two bridged H1 and H4 protons have $^1J_{CH}$ values of 147.6 and 142.8 Hz, respectively, and the presence of Br is experimentally evidenced by the large $^1J_{CH}$ of H2 (159.6 Hz).

Even in the case where signal overlap precludes an accurate extraction of $^1J_{CH}$ due to the presence of similar $^1J_{CH}$ and $\delta(^1H)$, the analysis of the $^1J_{CH}$ profile can be used as a positive indicator for the absence of specific functionalities and differential structural elements. For instance, leaving aside its olefinic H4 proton (159.5 Hz), the steroid progesterone shows a characteristic fingerprinting with a large number of aliphatic ^{1}H resonances without a clear distinction of individual $^1J_{CH}$ (ranging from 124 to 130 Hz) (Figure S5). In a similar way, the $^1J_{CH}$ NMR profile of the carbohydrate sucrose shows a uniform and narrow range of $^1J_{CH}$ between 144.4 and 146.0 Hz, except for the H5 of the fructose ring (149.2 Hz) and the anomeric H1 proton (169.4 Hz) that confirms the α configuration in the glucose ring (Figure S6). These values completely agree with those reported previously.[5]

The HSQC-$^1J_{CH}$ can be recorded with a standard setup to monitor a wide range of $^1J_{CH}$ values. Because the key indirect dimension only displays doublets due to $^1J_{CH}$, these experiments can also be successfully recorded in the lowest magnetic fields, as shown for the antimalarial drug quinine at 400 MHz (Figure S7), where the accidental ^{1}H signal overlap in F_2 is the only potential drawback. Signal intensities in HSQC-$^1J_{CH}$ depend on several factors but mainly of the Δ delay optimization. Thus, a reoptimization of Δ can be required to observe very large $^1J_{CH}$ values, as found for the tryine derivative **4**,[12] which contains two terminal alkyne protons with $^1J_{CH}$

DOI: 10.1021/acs.joc.6b02873
J. Org. Chem. 2017, 82, 2040−2044

values around 251 Hz (Figure 6). In that particular case, a non-edited version of the HSQC-$^1J_{CH}$ pulse scheme (Figure S4)

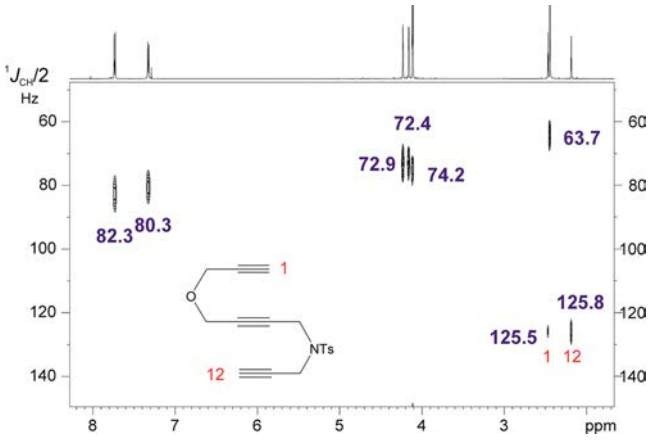

Figure 6. $^1J_{CH}$ NMR profile of the tryine derivative (**4**) in $CDCl_3$ obtained from a non-edited version of the pulse scheme of Figure 1 (optimized to 180 Hz). The magnitude of $^1J_{CH}/2$ (in Hz) is extracted directly from the *y* coordinate of each individual cross-peak.

optimized to 180 Hz has been used. In addition, broadband homodecoupling can be implemented in the F_2 dimension (Figure S8) to afford simplified *J* multiplet patterns, making it very easy to automate peak-picking (Figure S9).

CONCLUSIONS

In short, a new graphical interface to visualize and determine accurately the magnitude of $^1J_{CH}$ for all the protons of a molecule is now available. The advantage for using this intuitive $^1J_{CH}$ NMR profile is that the typical *J* measurement on doublets is avoided, minimizing common drawbacks associated with limited ^1H signal resolution and dispersion, multiplet complexity and distortions, or general applicability to any CH_n multiplicity, particularly when it comes to diastereotopic CH_2 protons. It has been shown that the simple determination of the F_1 coordinate in the $^1J_{CH}$ profile directly affords $^1J_{CH}/2$. In addition, this spectral representation provides a general and quick overview of all experimental $^1J_{CH}$, identifying key structural features, getting experimental evidence to the presence of representative functional groups, and facilitating stereochemical assignments. Without a doubt, further developments in complementary theoretical predictions of $^1J_{CH}$ will help in the use of these parameters in computer-assisted structure elucidation (CASE) and verification (ASV) programs.

EXPERIMENTAL SECTION

NMR experiments were recorded on a 600 MHz spectrometer equipped with a triple-resonance $^1H/^{13}C/^{15}N$ inverse probe. The temperature for all measurements was set to 298 K. All samples were prepared by dissolving 20 mg of the target molecule in the corresponding deuterated solvent. All products **1**, **2**, and **3** in the main text and **5**, **6**, and **7** in the Supporting Information were commercially available. The triene **4** was a loan from Prof. A. Roglans and Dr. A. Pla-Quintana from Universitat de Girona.

NMR spectra were recorded with proton 90° pulses of 8.5 μs and carbon 90° pulses of 10.5 μs. For broadband carbon inversion and refocusing, 0.5 ms smoothed chirp pulses (shape name: Crp60,0.5,20.1) and a four-chirp composite pulse of 2 ms duration (shape name: Crp60comp.4) were used, respectively, sweeping over a frequency band of 60 kHz. For the multiplicity editing block, the CRISIS (compensation of refocusing inefficiency with synchronized inversion sweep) approach was applied using two 1.73 ms refocusing pulses (shape name: Crp60_xfilt.2) as described in ref 7. Adiabatic ^{13}C decoupling (with 1.5 ms chirped pulses; shape name: Crp42,1.5,20.2) was applied during ^1H acquisition. The interpulse Δ delays in INEPT and BIRD elements were set to 3.57 ms ($\Delta = 1/(2*^1J_{CH})$; optimized to $^1J_{CH}$ = 140 Hz), and the recycle delay was set to 1 s. Two scans were accumulated for each one of the 256 t_1 increments, and the number of complex data points in t_2 was set to 2048. A basic two-step phase cycling is applied: $\phi_1 = x,-x$; $\phi_{rec} = x,-x$. Spectra were acquired with a spectral window of 6010 Hz (in F_2) and 250 Hz (in F_1), giving a FID resolution of 5.86 (F_2) and 1.95 (F_1) Hz, respectively. All experiments were acquired and processed using the echo/antiecho protocol where the gradient G1 was inverted for every second FID. Prior to Fourier transformation of the data, zero filling to 1024 in F_1 and a $\pi/2$-shifted squared cosine window function (QSINE, SSB: 2) in both dimensions were applied. Zero filling of the digital resolution was applied at 2.93 (F_2) and 0.24 (F_1) Hz, respectively. Gradient ratios for G1/G2 were set to 80:20.1 and measured as a percentage of the absolute gradient strength of 53.5 G/cm. Sine-bell-shaped gradients had 1 ms of duration and were followed by a recovery delay of 100 μs (δ). The final ZQF consists of a 30 ms chirped adiabatic pulse applied simultaneously to a rectangular gradient (G0 = 11%).

A java applet (jmeasurement.jar) for extracting $^1J_{CH}$ automatically from the HSQC-$^1J_{CH}$ spectrum is available on request. A script to automatically process the HSQC-$^1J_{CH}$ spectrum to afford the $^1J_{CH}$ NMR profile is available in the Mnova software package.

ASSOCIATED CONTENT

Supporting Information

The Supporting Information is available free of charge on the ACS Publications website at DOI: 10.1021/acs.joc.6b02873.

Experimental section, details of NMR spectra, and pulse program (PDF)

AUTHOR INFORMATION

Corresponding Author

*Tel: +34 935812291. E-mail: teodor.parella@uab.cat.

ORCID

Pau Nolis: 0000-0003-2360-1709

Teodor Parella: 0000-0002-1914-2709

Notes

The authors declare no competing financial interest.

ACKNOWLEDGMENTS

Financial support for this research provided by Spanish MINECO (Project CTQ2015-64436-P) is gratefully acknowledged. A.A.S. gratefully acknowledges support from the Brazilian agency CAPES (BEX 5382/15-7). We also thank to the Servei de Ressonància Magnètica Nuclear, Universitat Autònoma de Barcelona, for allocating instrument time to this project. NMR instrumentation at Carnegie Mellon University was partially supported by the NSF (CHE-0130903 and CHE-1039870). R.R.G. gratefully acknowledges support from the NSF (CHE-1111684).

REFERENCES

(1) (a) Hansen, P. E. *Prog. Nucl. Magn. Reson. Spectrosc.* **1981**, *14*, 175−295. (b) Contreras, R. H.; Peralta, J. E. *Prog. Nucl. Magn. Reson. Spectrosc.* **2000**, *37*, 321−345.

(2) (a) Enthart, A.; Freudenberger, J. C.; Furrer, J.; Kessler, H.; Luy, B. *J. Magn. Reson.* **2008**, *192*, 314−322. (b) Castañar, L.; Sistaré, E.; Virgili, A.; Williamson, R. T.; Parella, T. *Magn. Reson. Chem.* **2015**, *53*, 115−119. (c) Castañar, L.; Saurí, J.; Williamson, R. T.; Virgili, A.; Parella, T. *Angew. Chem., Int. Ed.* **2014**, *53*, 8379−8382.

DOI: 10.1021/acs.joc.6b02873
J. Org. Chem. 2017, 82, 2040−2044

(3) (a) Timári, I.; Kaltschnee, L.; Kolmer, A.; Adams, R. W.; Nilsson, M.; Thiele, C. M.; Morris, G. A.; Kövér, K. E. *J. Magn. Reson.* **2014**, *239*, 130−138. (b) Reinsperger, T.; Luy, B. *J. Magn. Reson.* **2014**, *239*, 110−120. (c) Kaltschnee, L.; Kolmer, A.; Timári, I.; Schmidts, V.; Adams, R. W.; Nilsson, M.; Kövér, K. E.; Morris, G. A.; Thiele, C. M. *Chem. Commun.* **2014**, *50*, 2512−2514. (d) Timári, I.; Kaltschnee, L.; Raics, M. H.; Roth, F.; Bell, N. G. A.; Adams, R. W.; Nilsson, M.; Uhrín, D.; Morris, G. A.; Thiele, C. M.; Kövér, K. E. *RSC Adv.* **2016**, *6*, 87848−87855.

(4) (a) Liu, M.; Farrant, R. D.; Gillam, J. M.; Nicholson, J. K.; Lindon, J. C. *J. Magn. Reson., Ser. B* **1995**, *109*, 275−283. (b) Fehér, K.; Berger, S.; Kövér, K. E. *J. Magn. Reson.* **2003**, *163*, 340−346. (c) Kövér, K. E.; Fehér, K. *J. Magn. Reson.* **2004**, *168*, 307−313. (d) Thiele, C. M.; Bermel, W. *J. Magn. Reson.* **2012**, *216*, 134−143. (e) Saurí, J.; Castañar, L.; Nolis, P.; Virgili, A.; Parella, T. *J. Magn. Reson.* **2014**, *242*, 33−40. (f) Snider, J. D.; Troche-Pesqueira, E.; Woodruff, S. R.; Gayathri, C.; Tsarevsky, N. V.; Gil, R. R. *Magn. Reson. Chem.* **2012**, *50*, S86−S91. (g) Castañar, L.; García, M.; Hellemann, E.; Nolis, P.; Gil, R. R.; Parella, T. *J. Org. Chem.* **2016**, *81*, 11126−11131. (h) Furrer, J.; John, M.; Kessler, H.; Luy, B. *J. Biomol. NMR* **2007**, *37*, 231−243.

(5) (a) Yu, B.; van Ingen, H.; Vivekanandan, S.; Rademacher, C.; Norris, S. E.; Freedberg, D. I. *J. Magn. Reson.* **2012**, *215*, 10−22. (b) Yu, B.; van Ingen, H.; Freedberg, D. I. *J. Magn. Reson.* **2013**, *228*, 159−165.

(6) Johnson, C. S., Jr *Prog. Nucl. Magn. Reson. Spectrosc.* **1999**, *34*, 203−256.

(7) Boyer, R. D.; Johnson, R.; Krishnamurthy, K. *J. Magn. Reson.* **2003**, *165*, 253−259.

(8) Thrippleton, M. J.; Keeler, J. *Angew. Chem., Int. Ed.* **2003**, *42*, 3938−3941.

(9) (a) Perlin, A. S.; Casu, B. *Tetrahedron Lett.* **1969**, *10*, 2921−2924. (b) Bock, K.; Wiebe, L. *Acta Chem. Scand.* **1973**, *27*, 2676−2678. (c) Juaristi, E.; Cuevas, G. *Acc. Chem. Res.* **2007**, *40*, 961−970.

(10) Thiele, C. M. *J. Org. Chem.* **2004**, *69*, 7403−7413.

(11) (a) Williamson, R. T.; Buevich, A. V.; Martin, G. E.; Parella, T. *J. Org. Chem.* **2014**, *79*, 3887−3894. (b) Kutateladze, A. G.; Mukhina, O. A. *J. Org. Chem.* **2015**, *80*, 10838−10848. (c) Venkata, C.; Forster, M. J.; Howe, P. W. A.; Steinbeck, C. *PLoS One* **2014**, *9*, e111576. (d) Helgaker, T.; Jaszunski, M.; Swider, P. *J. Org. Chem.* **2016**, *81*, 11496−11500.

(12) Fernández, M.; Ferré, M.; Pla-Quintana, A.; Parella, T.; Pleixats, R.; Roglans, A. *Eur. J. Org. Chem.* **2014**, *2014*, 6242−6251.

■ NOTE ADDED AFTER ASAP PUBLICATION

Reference 9c was added on January 24, 2017.

DOI: 10.1021/acs.joc.6b02873
J. Org. Chem. 2017, 82, 2040−2044

Supporting Information

$^{1}J_{CH}$ NMR Profile: Identification of key structural features and functionalities by visual observation and direct measurement of one-bond proton-carbon coupling constants.

Núria Marcó,[a] Alexandre A. Souza,[a,d] Pau Nolis,[a] Carlos Cobas,[b] Roberto R. Gil,[c] and Teodor Parella[a,*]

[a]Servei de Ressonància Magnètica Nuclear, Universitat Autònoma de Barcelona, E-08193 Bellaterra (Barcelona) Catalonia, Spain; [b]Mestrelab Research, Santiago de Compostela, E-15706 A Coruña, Spain; [c]Department of Chemistry, Carnegie Mellon University, Pittsburgh, Pennsylvania 15213, United States; [d] Departamento de Química, Universidade Federal do Piauí, 64049-550, Teresina, PI, Brazil.

Table of contents

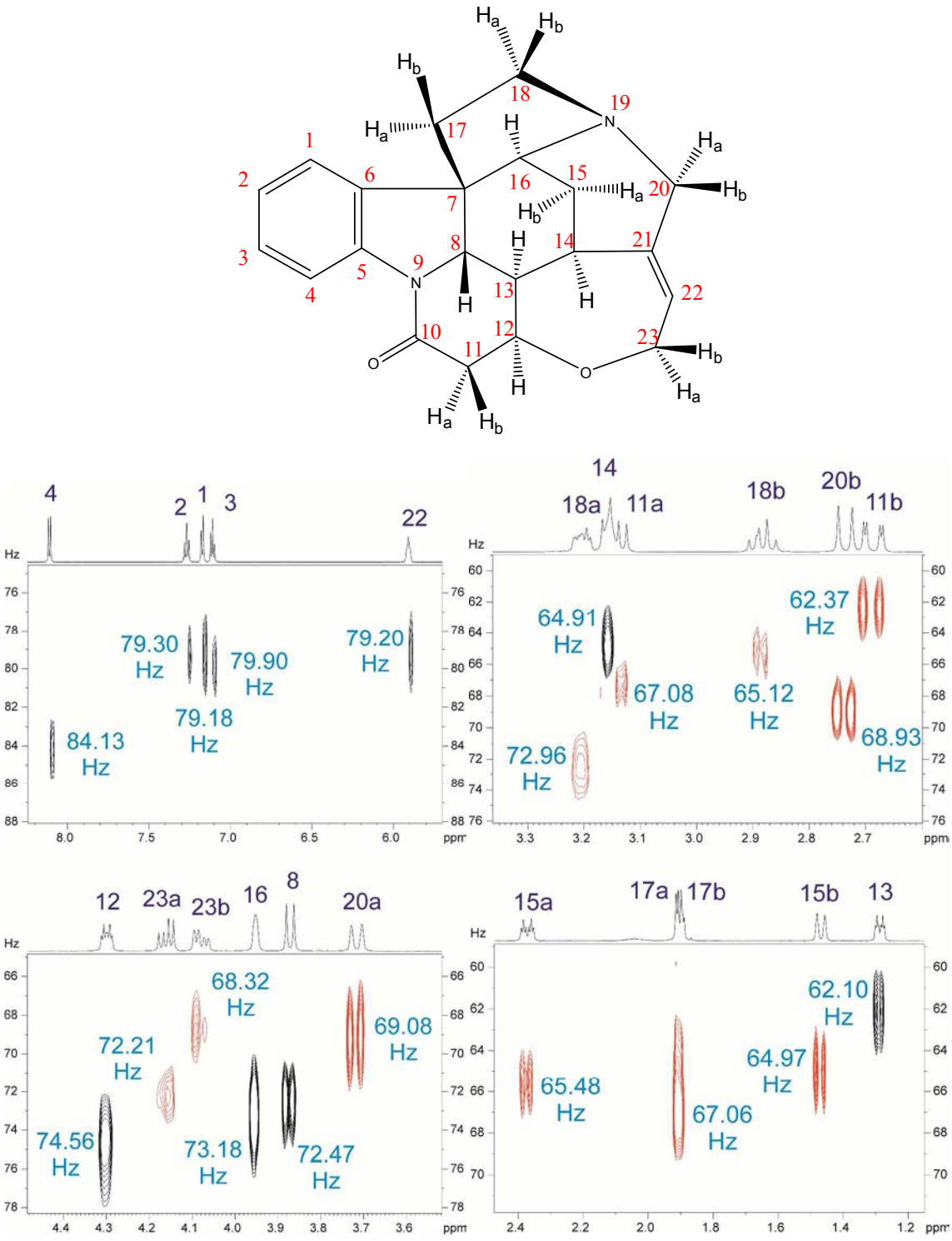

Figure S1: Expansions of the $^{1}J_{CH}$ NMR profile of strychnine (**1**) (see Fig. 2B in the main manuscript) for the direct determination of $^{1}J_{CH}/2$ (in Hz) of all ^{1}H signals from their F1 coordinates. Black and red cross-peaks are CH and CH_2, respectively.

Table S1: Experimental and theoretical scalar $^1J_{CH}$ coupling constants (in Hz) of strychnine in $CDCl_3$.

		Ref. 10	PIP-HSQC (Ref. 2c)	DFT (ref 11a)	Manual [a] $^1J_{CH}$ (this work)	Automatic [a] $^1J_{CH}$ (this work)	Manual J-Profile [a] ($^1J_{CH}$/2) (this work)	Automatic J-Profile [a] ($^1J_{CH}$/2) (this work)
H13	1.29	124.38	124.80	130	124.17	124.14	62.10	62.01
H15b	1.47	130.36	129.90	135.06	129.95	130.00	64.97	64.94
H17a/b	1.90	132.93	133.20	135.82	134.29	134.28	67.06	67.14
H15a	2.37	129.93	130.90	134.92	131.11	130.99	65.48	65.44
H11b	2.69	126.08	125.50	131.86	125.03	124.75	62.37	62.25
H20b	2.74	138.91	138.70	142.25	138.06	137.94	68.93	69.09
H18b	2.88	131.20	131.70	134.37	129.95	130.13	65.12	64.70
H11a	3.14	135.06	135.40	141.77	134.87	134.65	67.08	67.14
H14	3.15	130.36	131.30	135.28	129.66	128.88	64.91	64.94
H18a	3.21	146.17	146.30	150.57	145.29	145.03	72.96	72.51
H20a	3.72	138.91	138.80	143.2	138.06	138.42	69.08	69.33
H8	3.87	144.89	144.90	150.02	144.71	144.91	72.47	72.51
H16	3.96	146.60	146.70	153.09	146.74	146.48	73.18	73.24
H23b	4.08	137.20	137.20	139.57	137.48	137.45	68.32	68.85
H23a	4.16	145.74	145.50	149.99	144.14	144.27	72.21	72.26
H12	4.30	149.17	150.00	151.88	149.35	149.16	74.55	74.70
H22	5.91	159.43	158.80	165.4	158.61	158.19	79.20	79.09
H2	7.11	161.56	160.80	166.86	159.48	159.91	79.90	80.08
H1	7.17	159.00	158.30	162.83	158.90	158.45	79.18	79.35
H3	7.27	159.85	159.20	165.55	159.19	158.70	79.30	79.35
H4	8.11	168.40	168.40	178.62	168.24	168.33	84.13	83.98

[a] Digital resolution of 0.24 Hz in the F1 dimension.

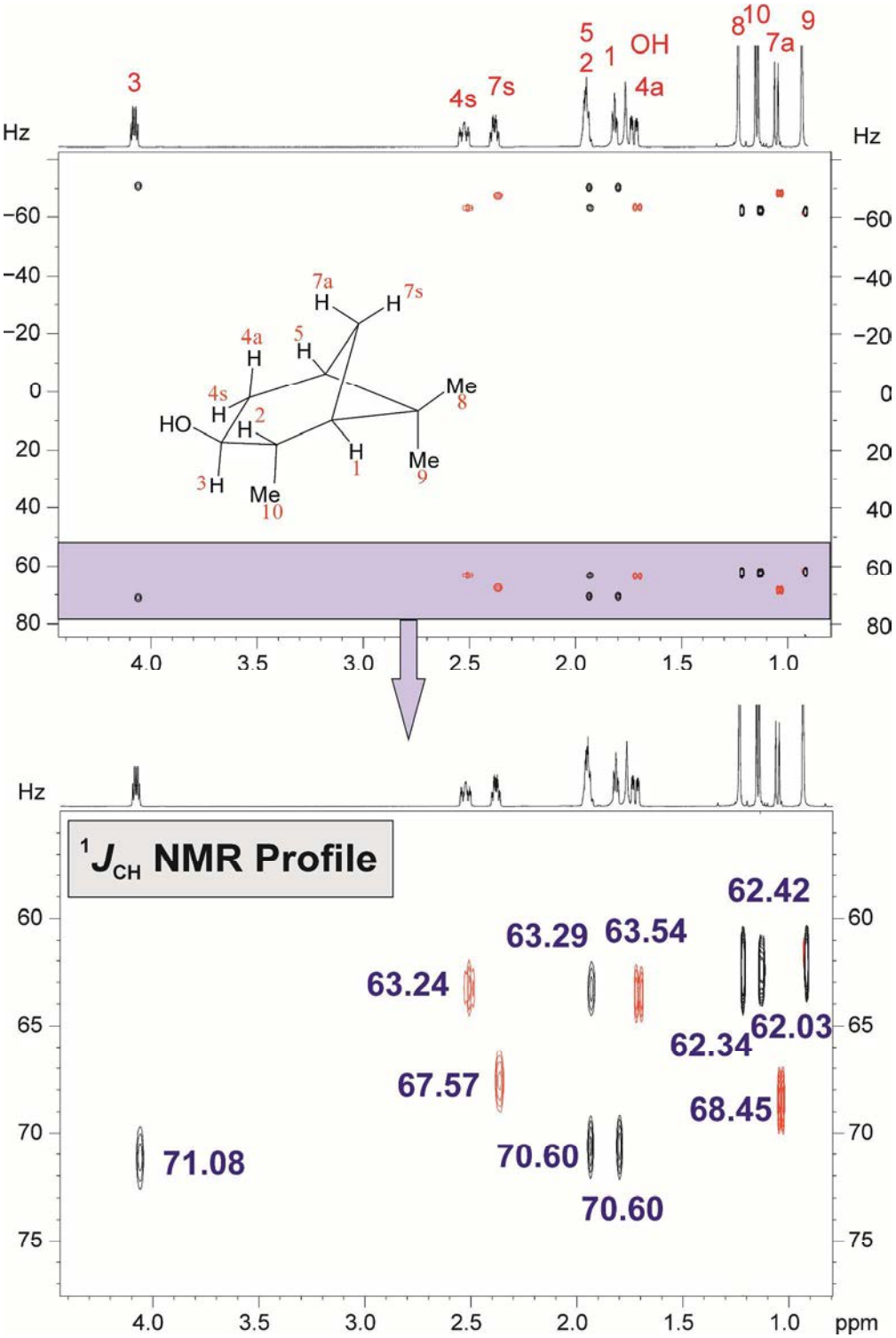

Figure S2: 600.13 MHz (top) 2D HSQC-$^1J_{CH}$ spectrum and (bottom) $^1J_{CH}$ NMR profile of isopinocampheol (**2**) in $CDCl_3$. In the later, $^1J_{CH}/2$ (in Hz) can be directly obtained from the F1 coordinate of each cross-peak.

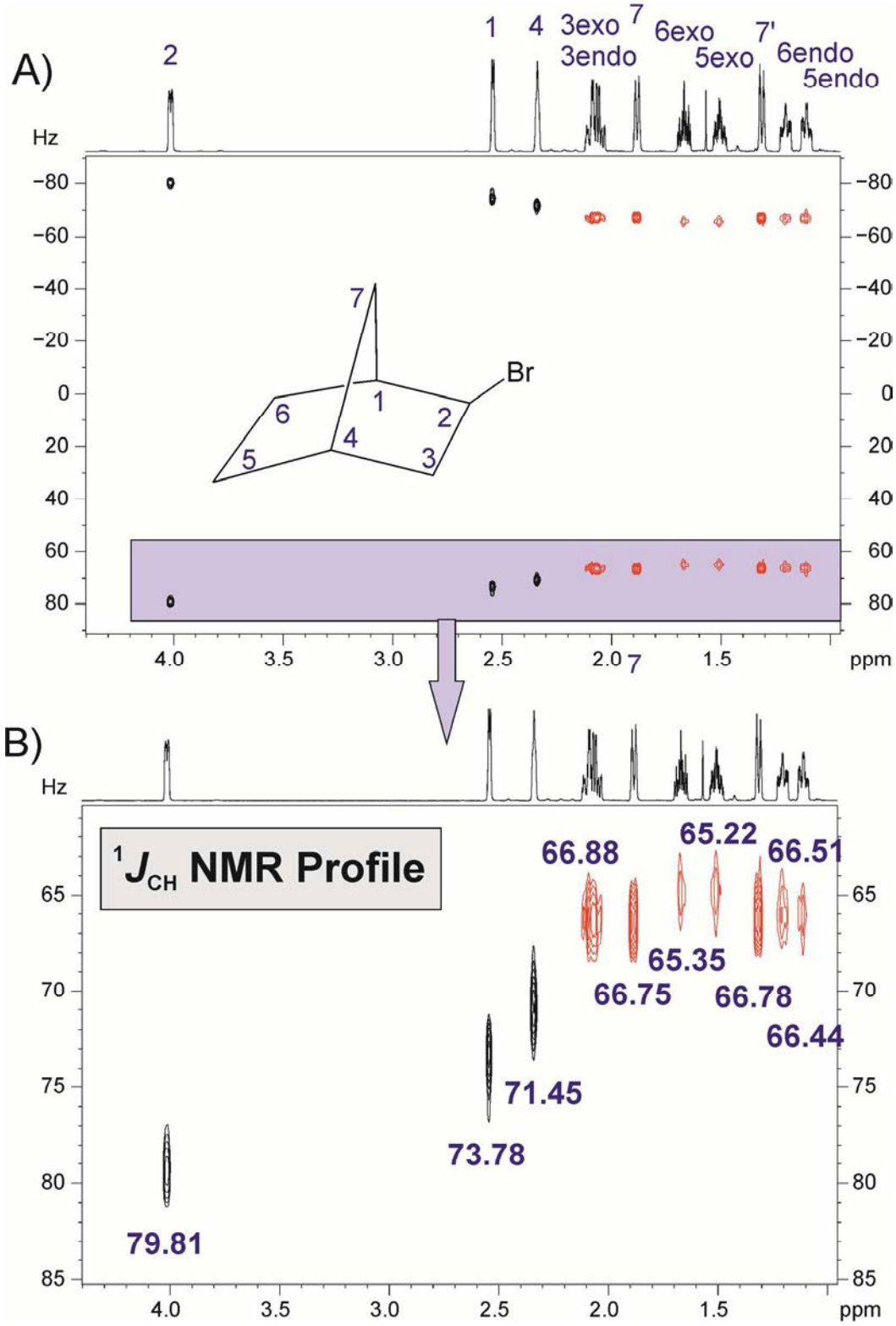

Figure S3: 600.13 MHz (A) 2D HSQC-$^1J_{CH}$ spectrum and (B) $^1J_{CH}$ NMR profile of 2-bromonorbornane (**3**) in $CDCl_3$. In the later, $^1J_{CH}/2$ (in Hz) can be directly obtained from the F1 coordinate of each cross-peak.

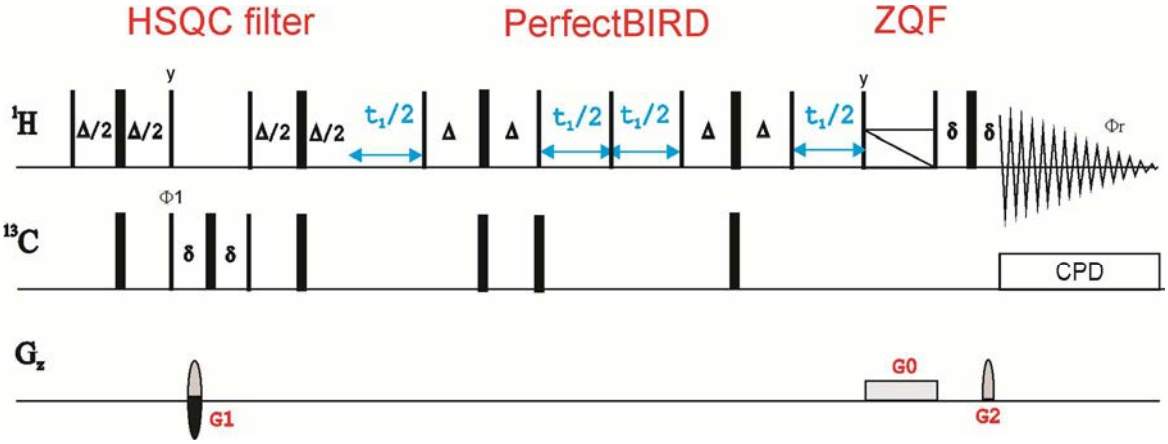

Figure S4: Pulse sequence diagram corresponding to the non-edited version of the HSQC-$^{1}J_{CH}$ experiment. See Fig. 1 in the main manuscript and experimental section for complete details.

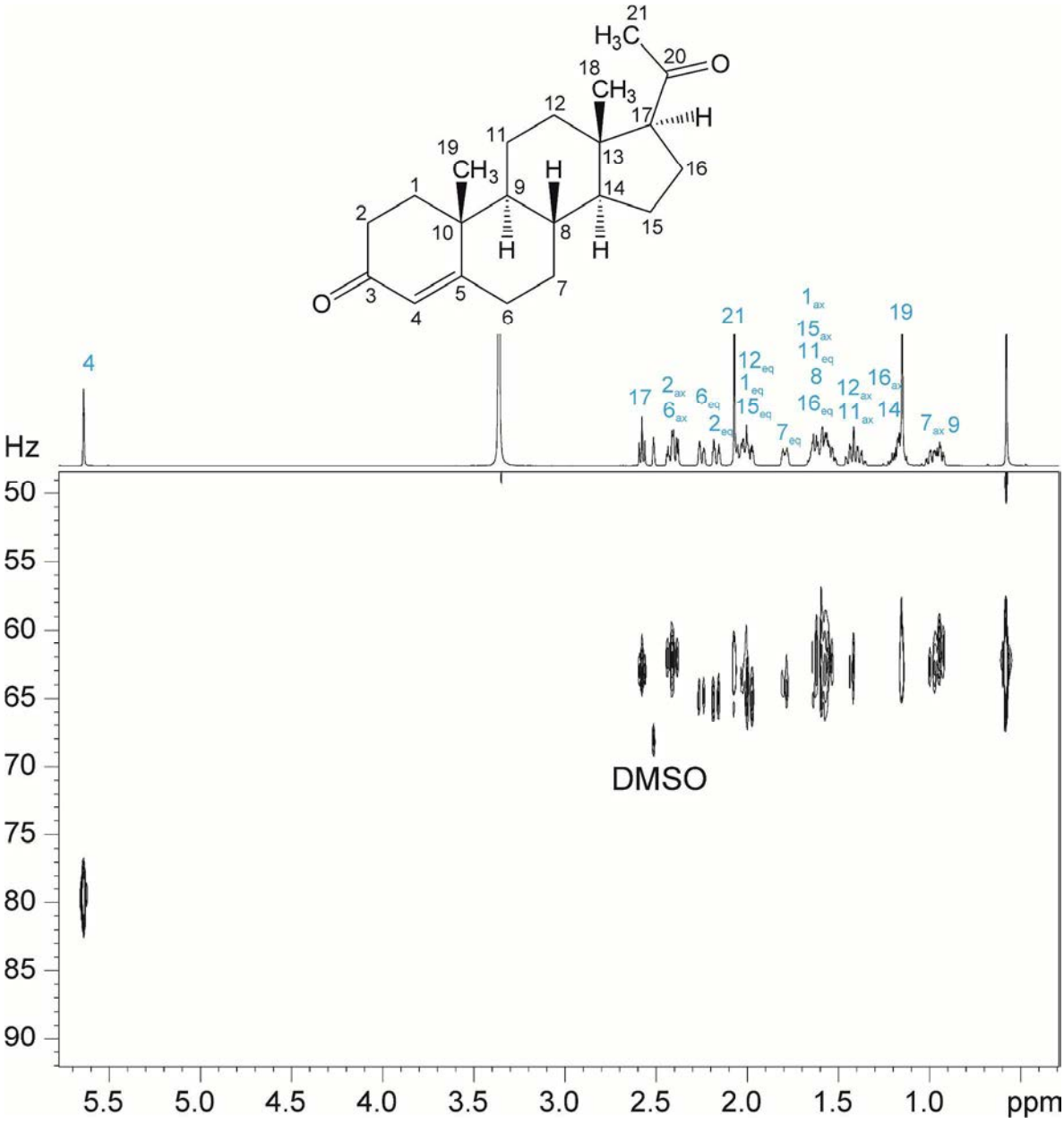

Figure S5: $^{1}J_{CH}$ NMR profile of progesterone (**6**) in DMSO-d_6 recorded at 600.13 MHz with the non-edited HSQC-$^{1}J_{CH}$ version. $^{1}J_{CH}/2$ (in Hz) can be directly obtained from the F1 coordinate of each cross-peak.

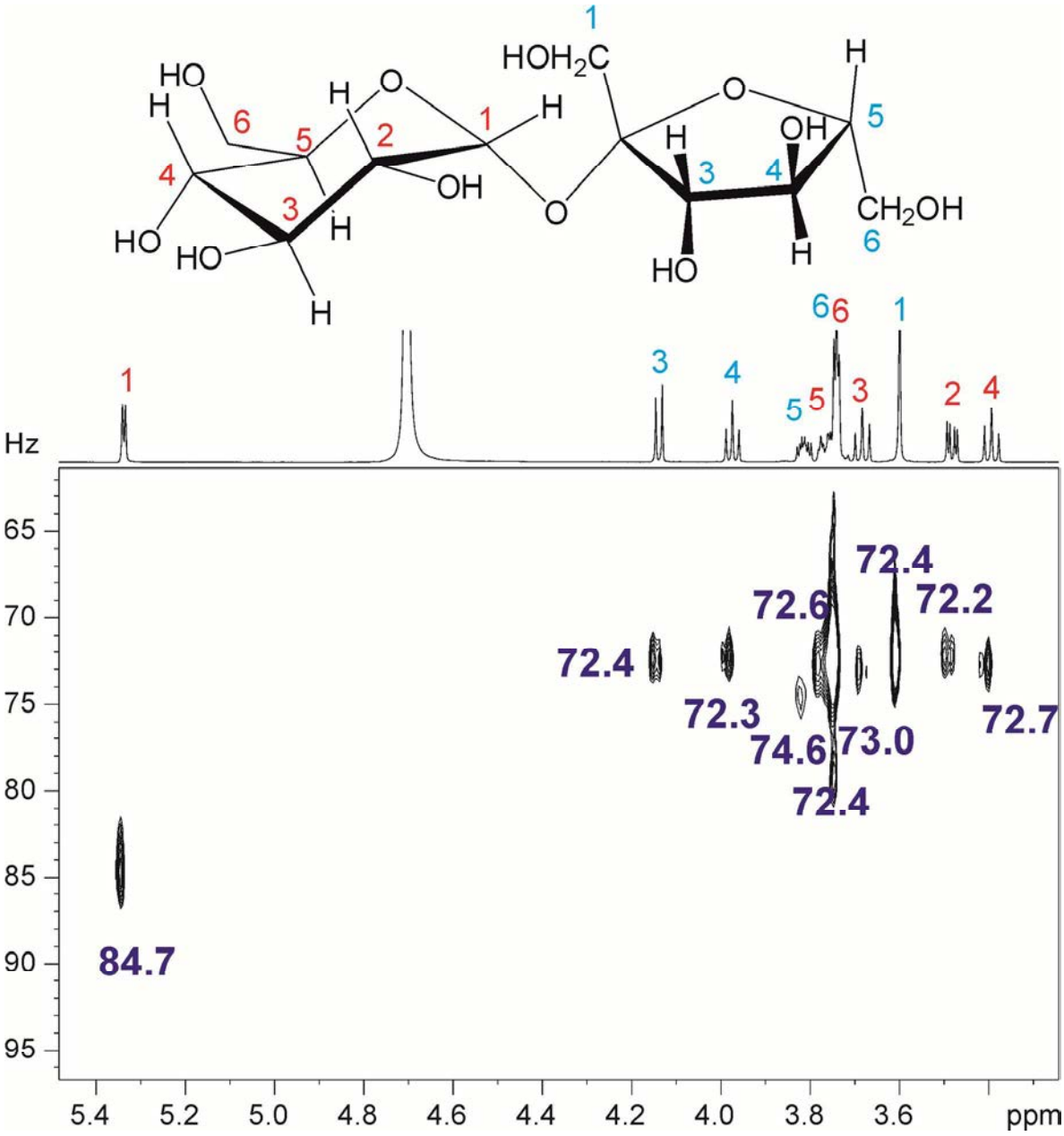

Figure S6: $^{1}J_{CH}$ NMR profile of sucrose (**5**) in D_2O recorded at 600.13 MHz with the non-edited HSQC-$^{1}J_{CH}$ version. $^{1}J_{CH}/2$ (in Hz) can be directly obtained from the F1 coordinate of each cross-peak.

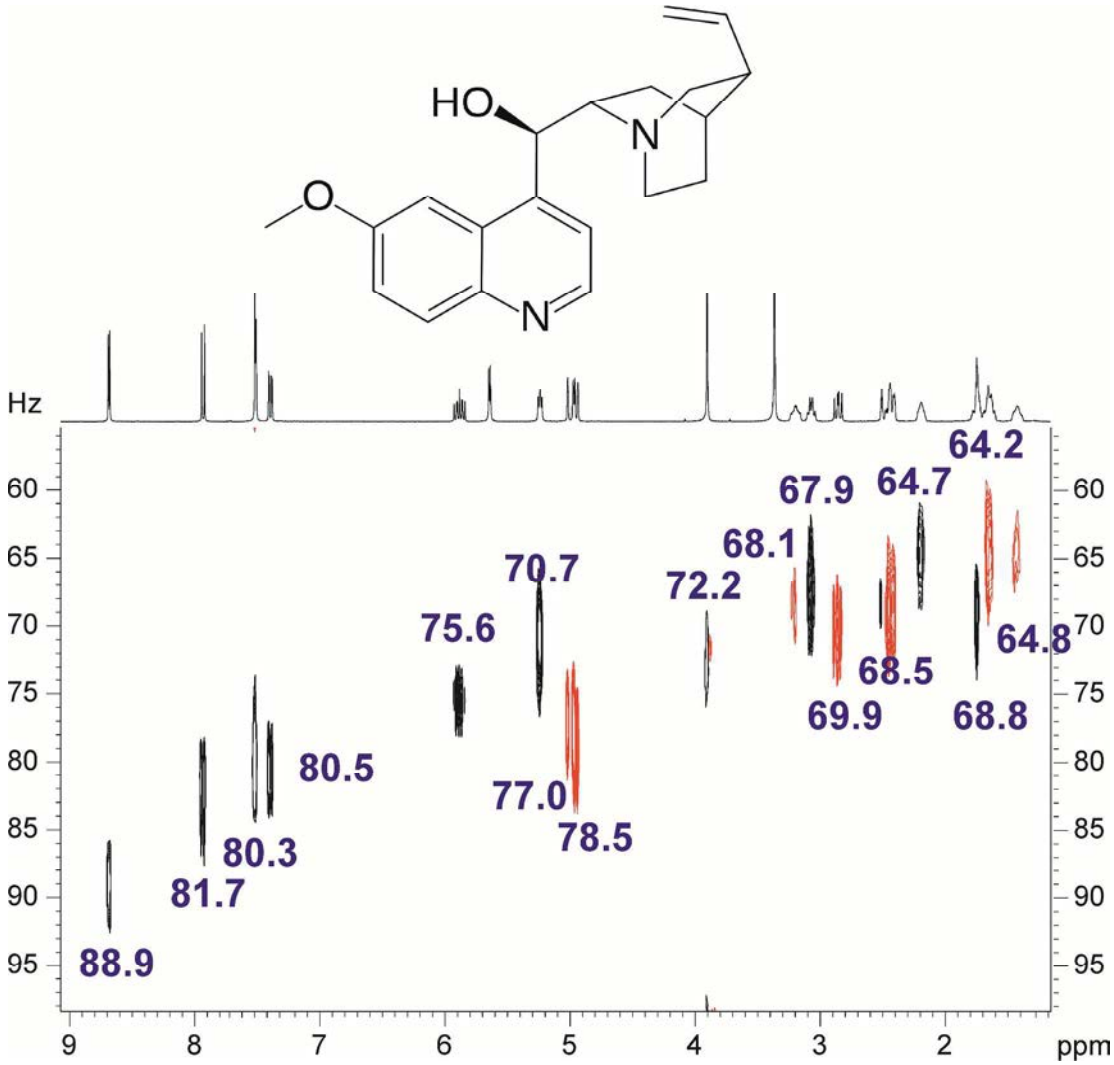

Figure S7: $^{1}J_{CH}$ NMR profile of quinine (**7**) in DMSO-d_6 recorded at 400.13 MHz. $^{1}J_{CH}/2$ (in Hz) can be directly obtained from the y coordinate of each cross-peak.

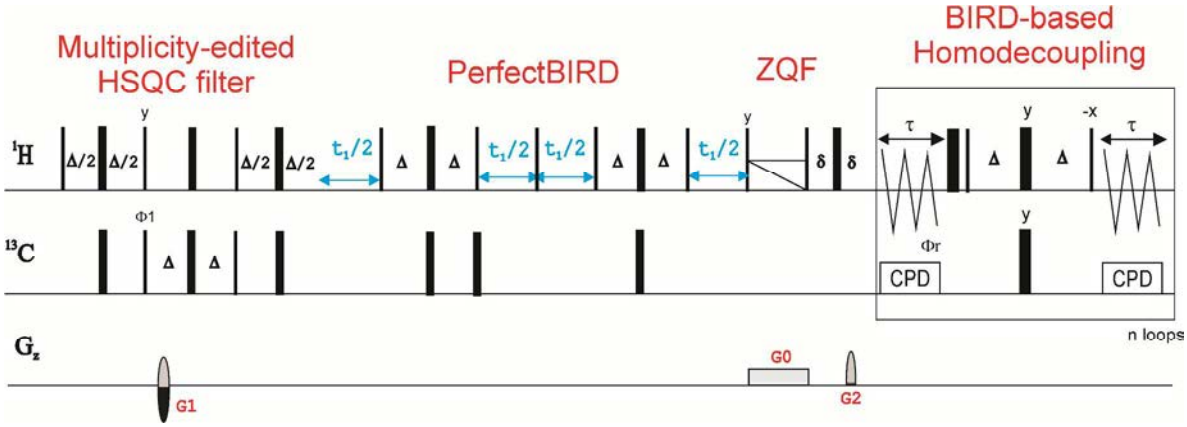

Figure S8: Pulse sequence diagram corresponding to the F2-broadband homodeocupled version of the HSQC-$^{1}J_{CH}$ experiment. See Fig. 1 in the main manuscript and experimental section for complete details.

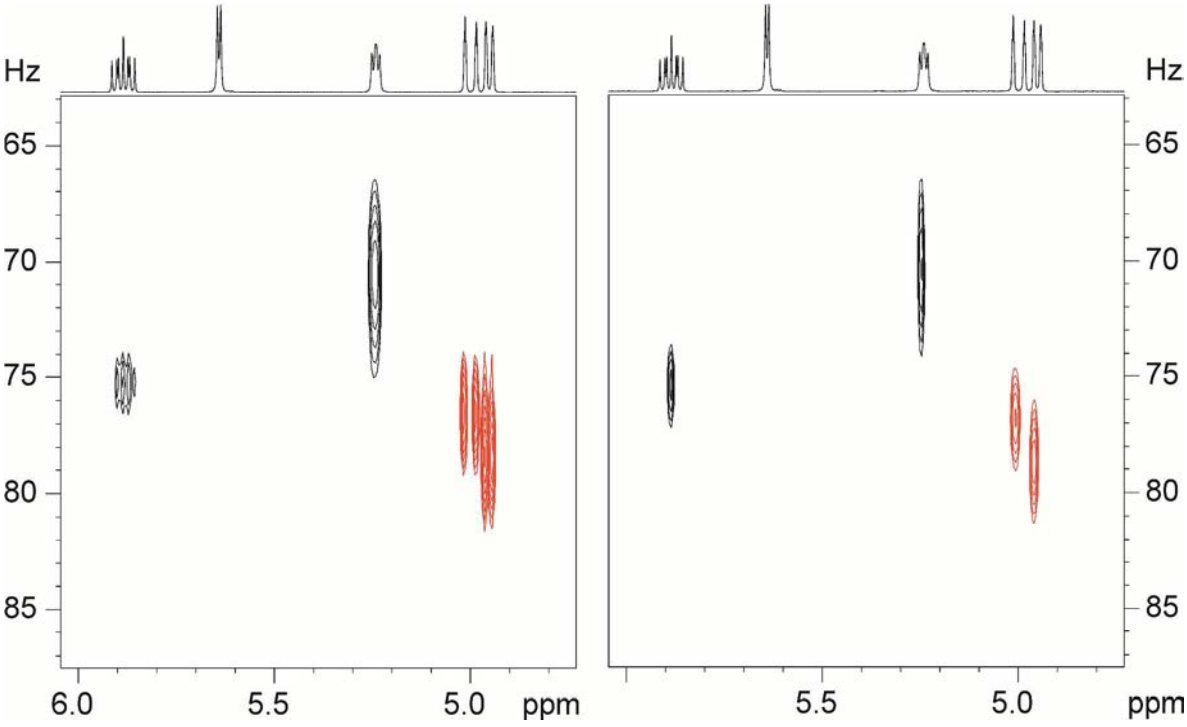

Figure S9: Comparison between the conventional and broadband homodecoupled $^{1}J_{CH}$ NMR profiles in quinine.

BRUKER Pulse program:

```
;teo_hsqc_jres.9
#include <Avance.incl>
#include <Grad.incl>
#include <Delay.incl>
#include <De.incl>

"p2=p1*2"
"d0=3u"
"d2=1s/(cnst2*2)"
"d4=1s/(cnst2*4)"
"in0=inf1/2"
"DELTA=p16+d16+p2+d13*2-4u"
"DELTA2=d4-p14/2-4u"
"DELTA5=d2-larger(p2,p14)/2"
"DELTA3=d2-p2+p3*2/PI"
"DELTA6=d2-p16-d16-p2-d13*2-p3*2/PI"
"acqt0=0"
baseopt_echo

1 ze
2 d1 do:f2
  d12 pl1:f1
3 (p1 ph1)
  DELTA2 pl0:f2
  4u
  (center (p2 ph1) (p14:sp3 ph6):f2 )
  4u
  DELTA2 pl2:f2 UNBLKGRAD
  (center (p1 ph2) (p3 ph3):f2 )

if "cnst24==0"
      {
  d13
  (p2 ph7)
  d13
  p16:gp1*EA
  d16
  DELTA6 pl0:f2
  (p31:sp18 ph1):f2
  (p2 ph1)
  DELTA3
  4u
  (p31:sp18 ph1):f2
  2u
  2u pl2:f2
}
      else
      {
  d13
  (p2 ph1)
  d13
  p16:gp1*EA
```

```
  d16 pl0:f2
  (p24:sp7 ph4):f2
  4u
  DELTA pl2:f2
}
  (center (p1 ph1) (p3 ph4):f2 )
  DELTA2 pl0:f2
  4u
  (center (p2 ph1) (p14:sp3 ph1):f2 )
  4u
  DELTA2

  d0
  (p1 ph1)
  DELTA5 pl0:f2
  (center (p2 ph1) (p14:sp3 ph1):f2 )
  DELTA5 pl2:f2
  (p1 ph1)
  (p4 ph1):f2
  d0

  p1 ph1

  d0
  (p1 ph1)
  DELTA5 pl0:f2
  (center (p2 ph1) (p14:sp3 ph1):f2 )
  DELTA5 pl2:f2
  (p1 ph1)
  d0

  p1 ph2
  d12 pl0:f1
  300u gron0
  p32:sp29:f1 ph1
  100u groff
  d16
  d12 pl1:f1
  p1 ph1

  DELTA
  p2 ph1
  p16:gp2
  d16 BLKGRAD


d12 pl12:f2
go=2 ph31 cpd2:f2
  d1 do:f2 mc #0 to 2
     F1EA(calgrad(EA), caldel(d0, +in0))
exit

ph1=0
ph2=1
```

```
ph3=0 2
ph4=0
ph6=0
ph7=2
ph31=0 2

;pl0 : 120dB
;pl1 : f1 channel - power level for pulse (default)
;pl2 : f2 channel - power level for pulse (default)
;pl10: f1 channel - power level for TOCSY-spinlock
;sp3: f2 channel - shaped pulse 180 degree
;spnam3: Crp60,0.5,20.1
;sp7: f2 channel - shaped pulse (180degree refocussing)
;spnam7: Crp60comp.4
;p1 : f1 channel -  90 degree high power pulse
;p2 : f1 channel - 180 degree high power pulse
;p3 : f2 channel -  90 degree high power pulse
;p14: f2 channel - 180 degree shaped pulse for inversion
;     = 500usec for Crp60,0.5,20.1
;p16: homospoil/gradient pulse                          [1 msec]
;p24: f2 channel - 180 degree shaped pulse for refocussing
;     = 2msec for Crp60comp.4
;d0 : incremented delay (2D)                            [3 usec]
;d1 : relaxation delay; 1-5 * T1
;d2 : 1/(2J(XH))
;d4 : 1/(4J(XH))
;d16: delay for homospoil/gradient recovery
;cnst2: = J(XH)
;cnst15: = conventional(0)/pure shift(1)
;cnst14: = conventional(0)/2JHH-resolved(1)
;cnst17: = -0.5 for Crp60comp.4
;in0: 1/(2 * SW(X)) = DW(X)
;nd0: 2
;NS: 2 * n
;DS: >= 16
;td1: number of experiments
;FnMODE: echo-antiecho


;use gradient ratio:   gp 1 : gp 2 : gp 0
;                   80 : 20.1 :   11   for C-13

;for z-only gradients:
;gpz1: 80%
;gpz2: 20.1% for C-13
;gpz0: 11%

;use gradient files:
;gpnam1: SINE.100
;gpnam2: SINE.100
```

PUBLICATION 7

Title: $^{2}J_{HH}$ -resolved HSQC: Exclusive determination of geminal proton-proton coupling constants[1]

Authors: Marcó, N.; Nolis, P.; Gil, R. R.; Parella, T.

Reference: *J. Magn. Reson.* **2017**, *282*, 18–26.

DOI: 10.1016/j.jmr.2017.06.014

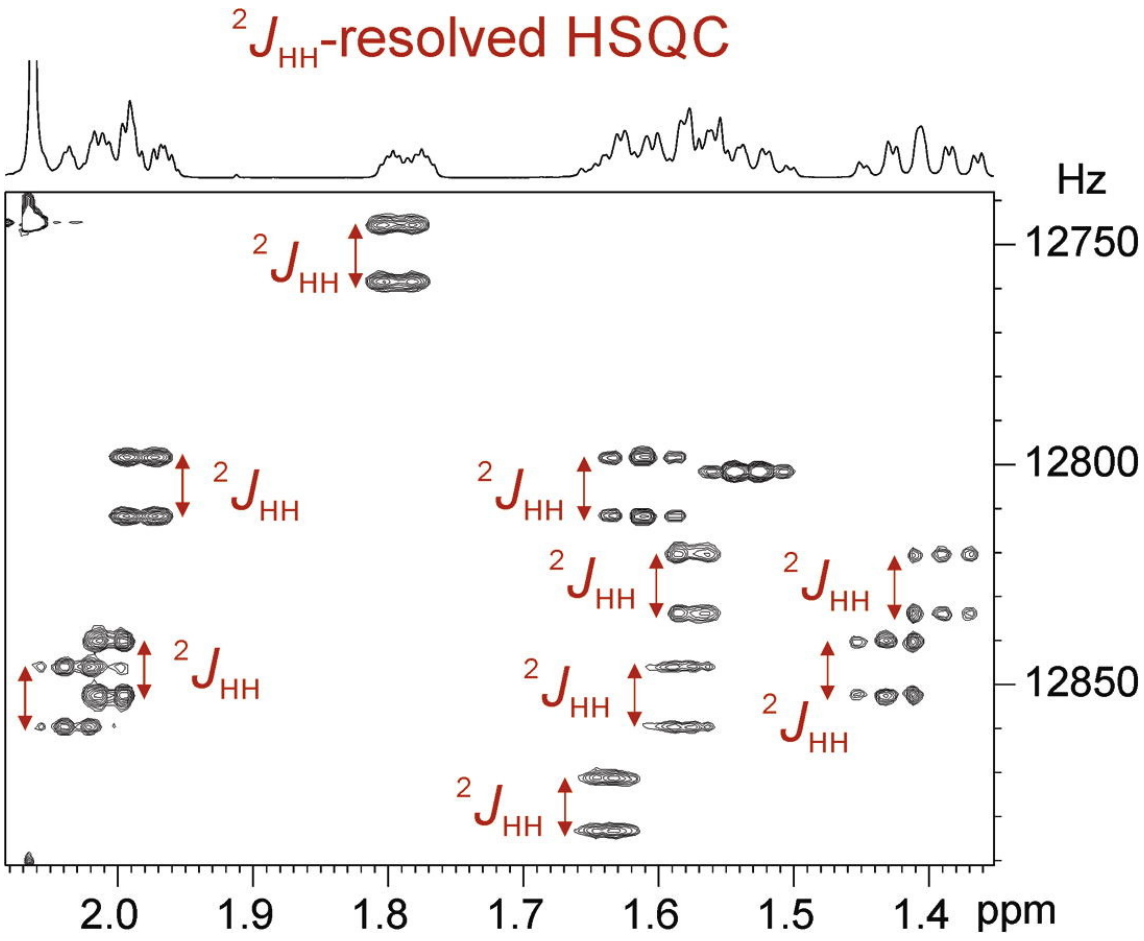

SUMMARY

Despite the interest in the measurement of $^2J_{HH}$ coupling constants in prochiral CH_2 groups, existing NMR experiments show many drawbacks due to extensive line broadening or the presence of complex multiplet patterns and strong coupling effects. These problems can be solved by the measurement of the $^2J_{HH}$ coupling constants along the F1 dimension. In this publication, a novel $^2J_{HH}$ resolved-HSQC experiment and the generation of a visual $^2J_{HH}$ NMR profile that correlates $\delta(^1H)$ in F2 with $^2J_{HH}$ in F1 are reported.

The basic pulse sequence contains a ^{13}C evolution and a BIRD based t_1 period, and both can be successfully scaled to simplify overlapped spectra. A ZQF is included to avoid unwanted dispersive contributions.

The experiment has also been applied to anisotropic samples to get exclusively $^2D_{HH}$ residual dipolar couplings. Its effectiveness is compared with other existing methods devoted to this purpose, such as P.E.HSQC, *J*SB-HSQC-E.COSY and $J_{CH}/^2J_{HH}$-resolved HSQC experiments.

Journal of Magnetic Resonance 282 (2017) 18–26

Contents lists available at ScienceDirect

Journal of Magnetic Resonance

journal homepage: www.elsevier.com/locate/jmr

$^2J_{HH}$-resolved HSQC: Exclusive determination of geminal proton-proton coupling constants

Núria Marcó [a], Pau Nolis [a], Roberto R. Gil [b], Teodor Parella [a,*]

[a] Servei de Ressonància Magnètica Nuclear, Universitat Autònoma de Barcelona, E-08193 Bellaterra, Barcelona, Catalonia, Spain
[b] Department of Chemistry, Carnegie Mellon University, Pittsburgh, PA, USA

ARTICLE INFO

Article history:
Received 19 May 2017
Revised 21 June 2017
Accepted 22 June 2017
Available online 23 June 2017

Keywords:
Two-bond proton-proton coupling constants
J-resolved
J-resolved HSQC
BIRD
Residual dipolar couplings

ABSTRACT

The measurement of two-bond proton-proton coupling constants ($^2J_{HH}$) in prochiral CH_2 groups from the F2 dimension of 2D spectra is not easy due to the usual presence of complex multiplet *J* patterns, line broadening effects and strong coupling artifacts. These drawbacks are particularly pronounced and frequent in AB spin systems, as those normally exhibited by the pair of diastereotopic CH_2 protons. Here, a novel $^2J_{HH}$-resolved HSQC experiment for the exclusive and accurate determination of the magnitude of $^2J_{HH}$ from the doublet displayed along the highly-resolved indirect F1 dimension is described. A pragmatic $^2J_{HH}$ NMR profile affords a fast overview of the full range of existing $^2J_{HH}$ values. In addition, a $^2J_{HH}/\delta(^{13}C)$-scaled version proves to be an efficient solution when severe signal overlapping complicate a rigorous analysis. The performance of the method is compared with other current techniques and illustrated by the determination of challenging residual dipolar $^2D_{HH}$ coupling constants of small molecules dissolved in weakly orienting media.

1. Introduction

Two dimensional *J*-resolved NMR experiments were originally developed to separate J_{HH} and $\delta(^1H)$ contributions in the two orthogonal dimensions of a 2D NMR spectrum [1]. The method has been extensively used to disentangle multiplet *J* patterns in overlapped regions, to extract quantitative proton-proton (J_{HH}) coupling values or to obtain internal F2 projections which are of interest in the analysis of complex mixtures and particularly in metabonomic studies [2]. *J*-resolved spectra are widely used thanks to their robustness and simplicity. Peaks appear symmetrical around the horizontal F1 = 0 axis and high levels of resolution are achieved along the indirect F1 dimension by using small spectral widths. The original homonuclear *J*-resolved method has been modified in different ways to improve its efficiency: (i) by obtaining phase sensitive data with improved signal lineshapes and resolution [3]; (ii) by designing more sophisticated methods to measure specific J_{HH} values, highlighting the family of SERF experiments [4]; (iii) by developing heteronuclear versions mainly based on *J*-resolved HSQC pulse schemes which have been used to determine one-bond ($^1J_{CH}$) or long-range proton-carbon coupling constants ($^nJ_{CH}$) [5] and to separate signals from non-racemic mixtures of enantiomers in chiral alignment media [6].

On the other hand, the extraction of individual $^1J_{CH}$ and two-bond proton-proton ($^2J_{HH}$) coupling constants in diastereotopic Ha-C-Hb spin systems has not been always straightforward. The subject has been studied from different perspectives and several HSQC-like methods are currently available for the simultaneous measurement of $^1J_{CH}$ and $^2J_{HH}$ [5g,7]. Available coupling patterns are schematized in Fig. 1. For instance, the P.E.HSQC experiment is a simple fully F1,F2-heterocoupled HSQC where the corresponding C-Ha cross-peak affords $^1J_{CHa}$ in the direct F2 dimension and a triplet with a characteristic 1:0:1 coupling pattern resulting from the sum of $^1J_{CHa} + {}^1J_{CHb}$ is observed in the F1 dimension [7a]. As the more relevant feature, a small flip ^1H pulse angle is applied to generate E.COSY patterns due to the passive Hb spin (Fig. 1A). This method provides the sign of $^2J_{HH}$ but, as a major drawback, there are a large number of splittings for each observed cross-peak. A related JSB-HSQC-E.COSY experiment was developed later to simplify the multiplet structure along F2, by inserting a refocusing period and broadband ^{13}C decoupling during acquisition (Fig. 1B) [5f]. The extraction of the magnitude and sign of $^2J_{HH}$ is made in the same way as described for the P.E.HSQC and the measurement of $^1J_{CHa} + {}^1J_{CHb}$ along F1 was improved by inserting a BIRD element into the t_1 period. Other techniques based on the generation of particular spin-state-selection in different NMR spectra were also designed but applied preferentially to proteins (CH_2-TROSY [7b],

* Corresponding author.
E-mail address: teodor.parella@uab.cat (T. Parella).

http://dx.doi.org/10.1016/j.jmr.2017.06.014
1090-7807/

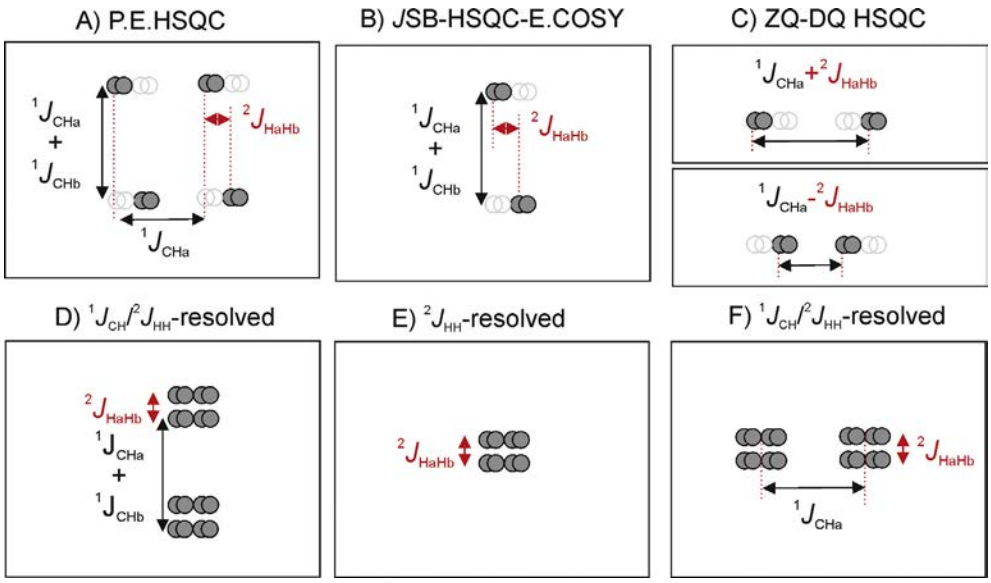

Fig. 1. Several coupling patterns obtained from different HSQC-type experiments to measure $^2J_{HH}$ in diastereotopic Ha-C-Hb spin systems. In (A–C) $^2J_{HH}$ is measured along the detected F2 dimension, whereas in (D–F) they are obtained from the indirect F1 dimension. Schemes E and F make reference to the novel $^2J_{HH}$-resolved experiment described in this work.

SPITZE [7b], ZQ-DQ HSQC [7d,7f,7g]). For instance, the ZQ-DQ HSQC method was based on the collection of two separate in-phase (IP) and *anti*-phase (AP) F2-coupled HSQC datasets followed by the subsequent IP ± AP data combination to give the ZQ and DQ components in two separate spectra (Fig. 1C). The biggest drawback of all these methods is that the *J* measurement is carried out along the F2 dimension where interference may also occur due to the presence of both homo- and heteronuclear couplings in the same dimension. In addition, the analysis can be further complicated by phase and multiplet signal distortions as a consequence of strong coupling effects and J_{HH} modulation that take place during INEPT blocks. Such modulations can be more pronounced in anisotropic media where typical J_{HH} values of 30–50 Hz can generate strong anti-phase components which severely distort multiplet splittings. As an alternative to avoid such drawbacks, *J*-resolved HSQC experiments can perform the same measurements of both $^1J_{CHa}$ and $^2J_{HH}$ from characteristic doublet of doublets revealed along the highly-resolved F1 dimension, as sketched in Fig. 1D [5g]. Based on this last concept, a pulse scheme for the exclusive and reliable determination of geminal $^2J_{HH}$ coupling constants is here presented. This new $^2J_{HH}$-resolved experiment generates a novel coupling pattern from which the magnitude of $^2J_{HH}$ can be extracted by simple analysis of the doublet generated along F1 (Fig. 1E). Although it is not treated in this article, the same sequence applied without heteronuclear decoupling during acquisition could also be used for the simultaneous measurement of $^1J_{CH}$ and $^2J_{HH}$ from the different F2 and F1 dimensions, respectively (Figs. 1F and S2). The different features of the new experiment are described by measuring accurate $^2J_{HH}$ in two target molecules presenting different spectral complexity, the alkaloid strychnine (**1**) and the more challenging steroid progesterone (**2**). In addition, the potential offered by the $^2J_{HH}$-resolved experiment for the in-situ determination of $^2D_{HH}$ residual dipolar couplings (RDCs) and the importance of $^2D_{HH}$ in the structural discrimination of small molecules will be illustrated by using **1** dissolved in a weakly aligned PMMA-$CDCl_3$ medium.

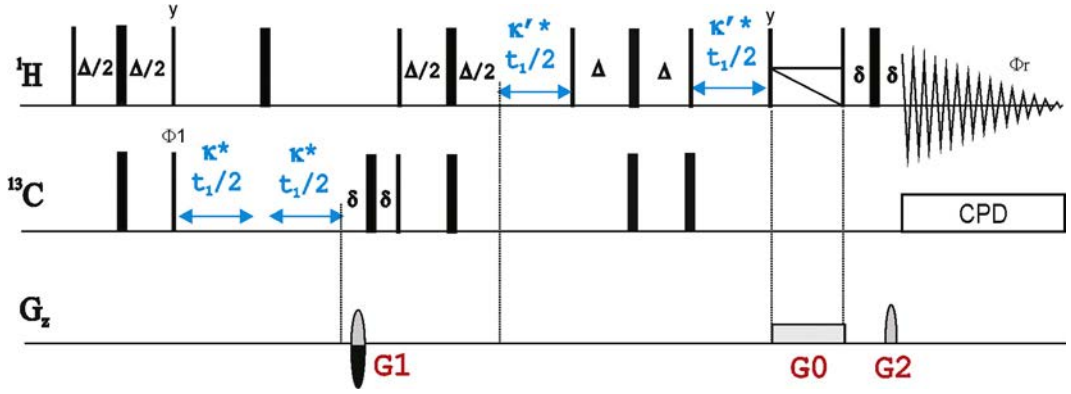

Fig. 2. (A) General pulse scheme to record $^2J_{HH}$-resolved HSQC experiments. Thin and thick rectangles represent 90° and 180° rectangular pulses, respectively, applied along the x axis unless indicated differently. A basic two-step phase cycling is applied: ϕ_1 = x,-x; ϕ_{rec} = x,-x. Inversion and refocusing 180° ^{13}C pulses can be applied as adiabatic pulses. Two independent blocks define the indirect F1 dimension. Whereas δ(^{13}C) evolves as usual (defined by a δ-scaling κ factor), $^2J_{HH}$ evolves in a separate incrementable period including a central BIRD^d inversion cluster (defined by a *J*-scaling κ′ factor). The inter-pulse delays in INEPT and BIRD^d elements are optimized according to $\Delta = 1/(2 * {}^1J_{CH})$. The ratio between gradients G1:G2 were 80:20.1 and the final zero-quantum filter (ZQF) contains a chirped adiabatic pulse applied simultaneously to a weak rectangular gradient (G0). More details can be found in the experimental section.

2. Results and discussion

Fig. 2 shows the general pulse scheme for the $^2J_{HH}$/δ-scaled HSQC experiment designed to measure $^2J_{HH}$. It contains the typical δ(^{13}C) evolution period (scaled by a κ factor) and a separate BIRD-based incrementable period (scaled by a κ' factor) after the regular HSQC pulse timing. The key point relies on the properties of the central BIRD^d cluster that exclusively inverts $^2J_{HH}$ whereas the evolution of $^1J_{CH}$ is doubly inverted, therefore unaffected [8]. The subsequent zero-quantum filter (ZQF) is mandatory to remove any existing dispersive contribution prior to acquisition, affording pure IP multiplets with absorption lineshapes that facilitate very much the realization of accurate measurements [9]. The nature of the resulting HSQC spectrum will depend of the values and proportion-

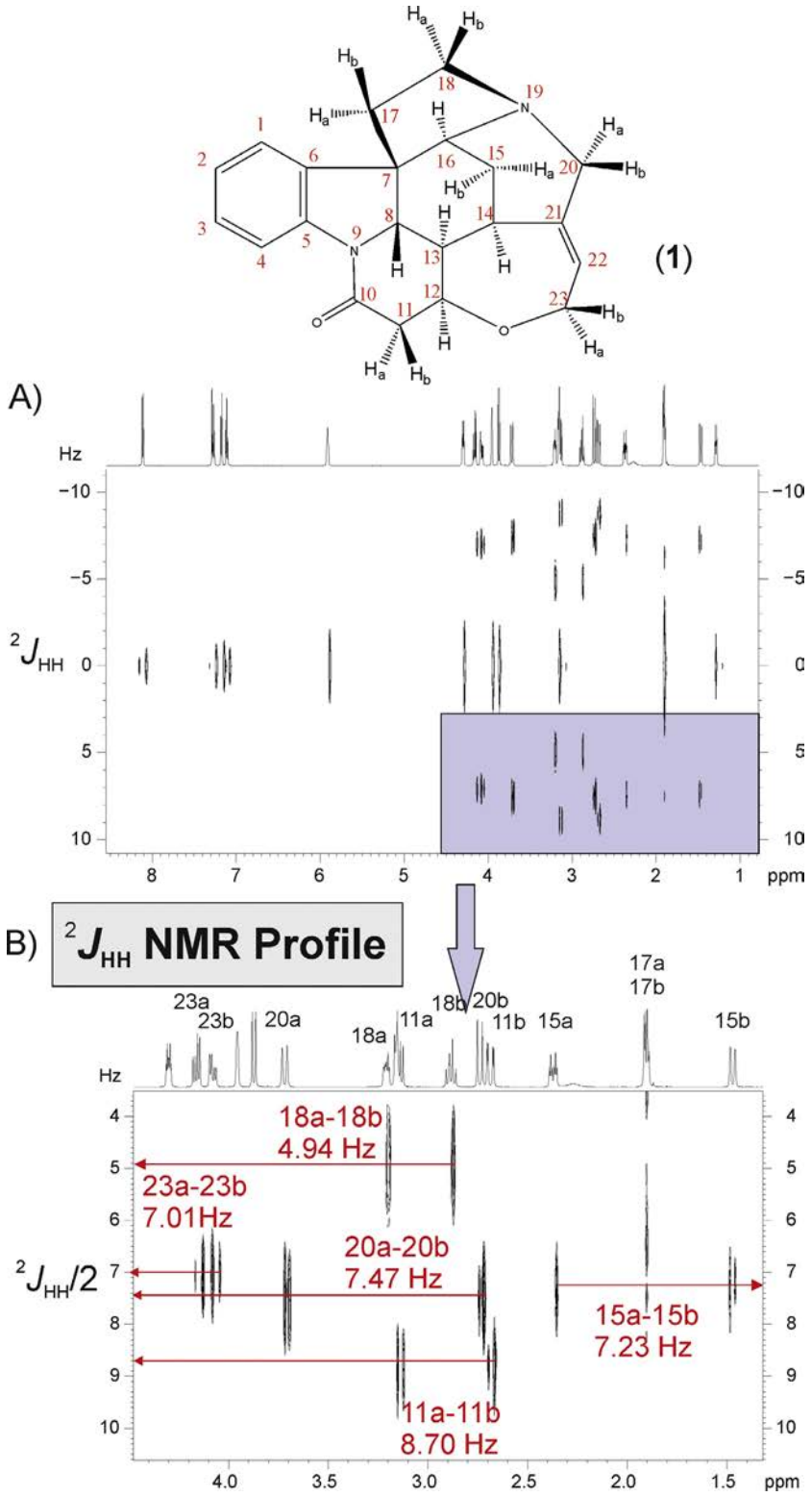

Fig. 3. (A) 600.13 MHz $^2J_{HH}$-resolved HSQC spectrum of **1**. The magnitude of $^2J_{HH}$ is extracted with accuracy from the clean doublet displayed in F1 for each individual 1H signal belonging to a CH_2 group; (B) $^2J_{HH}$ NMR profile from which the magnitude of $^2J_{HH}/2$ (in Hz) can be obtained directly from the F1 coordinate of each cross-peak.

Table 1
Scalar ($^2J_{HH}$), total ($^2T_{HH}$) and residual dipolar ($^2D_{HH}$) two-bond proton-proton coupling constants (in Hz) of strychnine measured from $^2J_{HH}$-resolved HSQC experiments in isotropic ($CDCl_3$) and anisotropic conditions ($CDCl_3$-PMMA gel at $\Delta\nu_Q$ ($CDCl_3$) = 49 Hz).

Geminal protons	$^2J_{HH}$[a]	$^2J_{HH}$[b]	$^2T_{HH}$[b]	$^2D_{HH}$[b,c] Experimental	$^2D_{HH}$[d] Predicted
H20a-H20b	15.0	15.0	46.2	−31.2	−27.0
H18a-H18b	9.9	9.9	11.3	−1.4 or +20.4?	+21.6
H11a-H11b	17.4	17.4	36.3	−18.9	−21.6
H15a-H15b	14.4	14.4	6.7	+7.7 or +21.1??	+20.4
H23a-H23b	14.4	14.4	35.9	−21.5	−22.9

[a] Experimental values extracted from the isotropic sample. They are assumed to be negative.
[b] Experimental values extracted from the anisotropic sample. The sign of $^2T_{HH}$ is unknown a priori.
[c] Calculated according to $^2D_{HH} = {}^2T_{HH} - {}^2J_{HH}$
[d] Predicted values obtained after alignment tensor calculation using experimental $^1D_{CH}$.

ality between κ and κ' factors. Thus, experiments recorded with κ = 0 will show a characteristic *J*-resolved format, whereas those using κ ≠ 0 will have a δ-correlation representation. As a proof of concept, Fig. 3A shows the symmetrical $^2J_{HH}$-resolved spectrum of **1** from which the very accurate measurement of $^2J_{HH}$ in almost all the diastereotopic CH_2 protons can be performed. The experiment was acquired without δ(^{13}C) evolution (κ = 0 and κ' = 1) and a short spectral width in F1 (SW(F1)) of 50 Hz, giving an excellent digital F1 resolution before zero-filling of 0.39 Hz/pt. It can be observed that all diastereotopic CH_2 signals show clean doublets in F1 (except the H17a/H17b pair which resonate practically at the same position) whereas all methine (CH) and methyl (CH_3) protons appear as singlets in F1 at the central position F1 = 0. Alternatively and in terms of practical visualization, a characteristic $^2J_{HH}$ NMR profile only showing part of the spectrum can be amenable for a more intuitive representation about the overall distribution of $^2J_{HH}$ values (Fig. 3B). This user-friendly fingerprint is fully complementary to the recent $^1J_{CH}$ NMR profile [5h], where all ^{1}H signals are efficiently dispersed as a function of the $^2J_{HH}$ magnitude, which can be directly determined from the F1 coordinate or from a simple peak picking. As a general trend, the magnitude of $^2J_{HH}$ depends mainly on hybridization of the directly-attached carbon atom, the H—C—H bond angle and the nature and electronegativity of substituents. For instance, if the bond angle is increased, the ring size in cyclic systems is decreased so that $^2J_{HH}$ becomes more positive. Typical ranges of $^2J_{HH}$ fall within the range between −20 to +40 Hz in isotropic conditions and it is established that in conventional five- and six membered rings, $^2J_{HH}$ are usually large in magnitude and negative. The proposed $^2J_{HH}$-resolved experiment does not provide the sign but in the case of **1**, it can be assumed that accurate $^2J_{HH}$ values in the range between −10.9 and −17.4 Hz are precisely determined (Table 1).

A major challenge of the $^2J_{HH}$-resolved experiment is the unequivocal determination of similar $^2J_{HH}$ sizes in overcrowded areas. This is the situation found for **2,** which contains eight different prochiral CH_2 groups, most of them resonating in very narrow frequency bands. Note that large $^2J_{HH}$ can be easily measured in the $^2J_{HH}$-resolved spectrum for some isolated signals such as H_{6eq} (14.6 Hz) and H_{2eq} (16.8 Hz), but considerable errors would be incurred when measuring them in overlapped signals having similar $^2J_{HH}$ and δ(^{1}H) (Fig. 4A). This is evidenced when analyzing the overcrowded areas around 2.0 and 1.6 ppm where three and five different ^{1}H resonances, respectively, are completely indistinguishable (expansions shown in Fig. 5A). Although tentative measurements could be made, errors above 1–1.5 Hz would be easily occurring. In such cases, the activation of the δ(^{13}C) dispersion by setting the κ scaling factor different from zero in the sequence of Fig. 1 can efficiently separate all ^{1}H signals. Fig. 4B shows the equivalent $^2J_{HH}$/δ-scaled HSQC spectrum of **2** acquired with κ = 0.1, κ′ = 1 and SW(F1) = 250 Hz, with a digital F1 resolution of 1.88 Hz/pt before zero-filling. In these conditions, all the aliased signals appear as well defined and very easy to analyze doublets. The corresponding expansions shown in Fig. 5B allow the clear differentiation of $^2J_{HH}$ values between 12.0 and 13.7 Hz, in addition to the unambiguous assignment of proton pairs and the dual measurement of the same $^2J_{HH}$ at each diastereotopic signal site (Table 2 and Fig. S1). Although the sign is not provided, it is assumed that all $^2J_{HH}$ couplings in **2** are negative.

The proposed $^2J_{HH}$-resolved experiment competes with other recently reported methods, such as P.E.HSQC [7a], *J*SB-HSQC-E.COSY [5c] and $^1J_{CH}$/$^2J_{HH}$-resolved HSQC [5g] experiments. It has been shown that the main advantage of the $^2J_{HH}$-resolved experiment lie in its simplicity, accuracy and general applicability, whereas the logical drawback of not measuring the absolute positive/negative sign can be solved by other means that will be discussed later in dealing the RDCs. In the *J*SB-HSQC-E.COSY experiment, both the magnitude and the sign of $^2J_{HH}$ are extracted from the relative displacement of each E.COSY component from F2. However, signal artifacts due to strong coupling effects in the form of distorted ^{1}H multiplets along F2 can become a real problem, as it is typically observed in prochiral CH_2 groups defining AB spin systems (small chemical shift differences and large *J* values, as well as showing similar chemical shifts with other coupled protons). Figs. S3 and S4 compares the *J*SB-HSQC-E.COSY and $^2J_{HH}$/δ-scaled HSQC spectra of **2**. It is shown that the non-symmetry between E.COSY components in *J*SB-HSQC-E.COSY can introduce a large source of errors in the extraction of the $^2J_{HH}$ magnitude and although it provides the sign, the method should be used with great caution to study such systems as clearly shown for H16e, H16a, H15a, H11e or H11a protons (Figs. S5 and S6). The potential impact of strong coupling effects on $^2J_{HH}$ were already noticed in the analysis by the P.E. HSQC experiment of the steroids cholesterol and 5-α-cholestan-3-one dissolved in stretched PDMS/$CDCl_3$ gels [11e]. On the other hand, a doublet of doublets is obtained for each diastereotopic CH_2 proton signal in the F1 dimension of the $^1J_{CH}$/$^2J_{HH}$-resolved HSQC spectrum, but the presence of four components for each cross-peak increases the probability of signal overlap and hinders the accurate measurement of both $^1J_{CH}$ and $^2J_{HH}$ when they present similar sizes, as shown in Fig. S7. Some additional spectra including other CH_2-containing molecules such as estradiol (**3**) (Figs. S8–S10) and quinine (**4**) (Fig. S11) are available in the SI to compare spectra or to show the presence of strong coupling artifacts when measuring couplings from the F2 dimension. In particular, quinine is a good example showing the limits of detection of the $^2J_{HH}$-resolved experiment. The exocyclic CH_2 system presents an absolute $^2J_{HH}$ value of 1.7 Hz which is not evident from the conventional 1D multiplet but that can be accurately measured from both the $^2J_{HH}$-resolved and the $^2J_{HH}$/δ-scaled spectra.

2.1. Dipolar $^2D_{HH}$ couplings

The CH_2 diastereotopic proton systems have been of interest since the first studies on the use RDCs in small molecules [10].

Of great importance, $^{1}D_{CH}$ plays a key role in the automatic assignment of diastereotopic protons without need of scalar J_{HH} or NOE information [11] and the relevance to use complementary $^{2}D_{HH}$ restraints to the habitual $^{1}D_{CH}$ in RDC-assisted structural discrimination studies between isomers and/or related chemical structures has been recognized. A comparative study analyzing the positive effects of $^{2}D_{HH}$ to increase the efficient discrimination between the different possible isomers of **1** has been reported [5g]. The incorporation of $^{2}D_{HH}$ in the alignment tensor calculation corrects possible errors in experimental $^{1}D_{CH}$ values, complements the subset of useful RDCs when insufficient data is available, worsens the calculated quality factors of the wrong structures and facilitate the analysis on the discrimination between the correct structure and all the wrong ones. Although

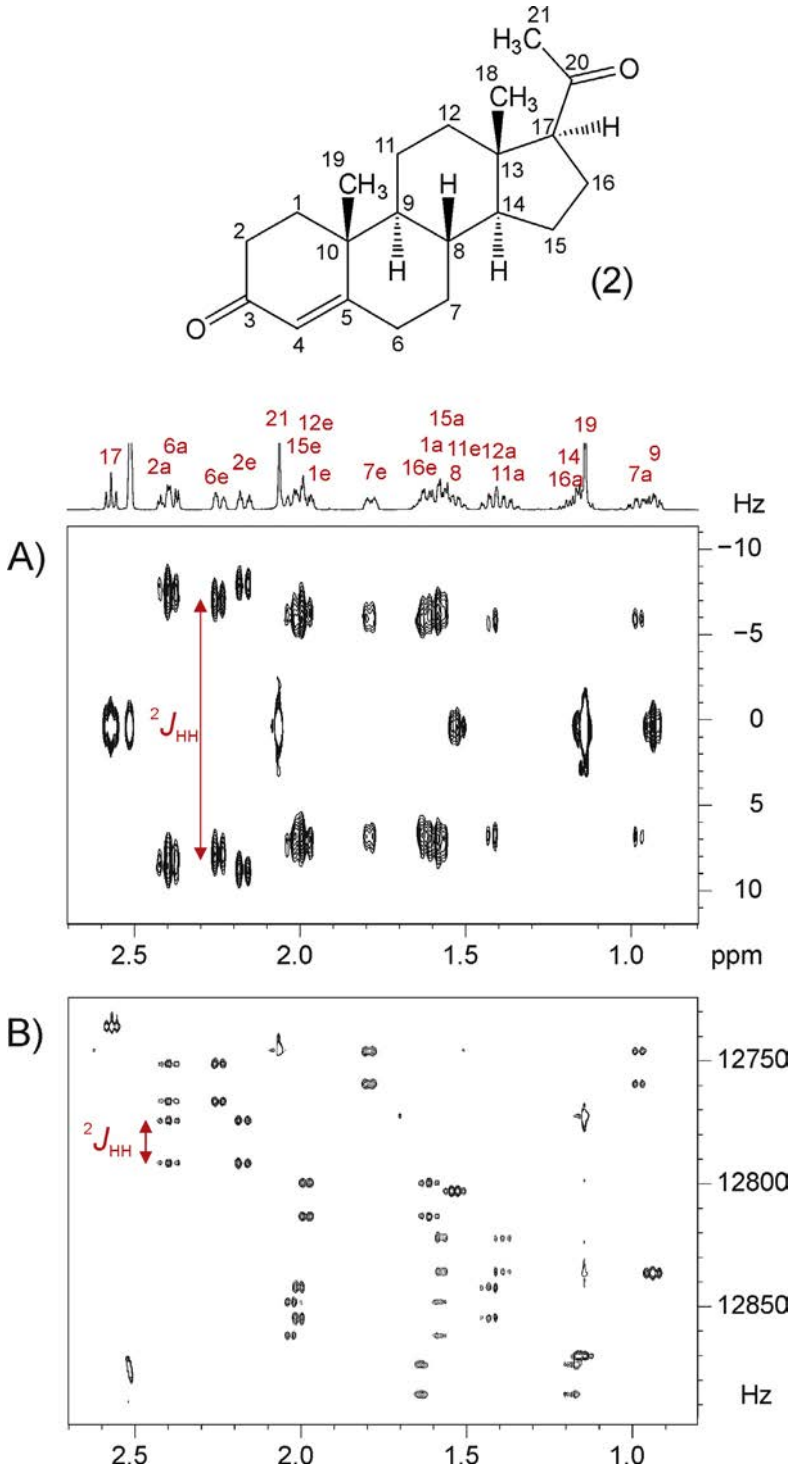

Fig. 4. Two different spectral representations of the $^{2}J_{HH}$-resolved HSQC spectra of **2** acquired (A) without δ-scaling (κ = 0, κ′ = 1, SW(F1) = 50 Hz), and (B) with δ-scaling (κ = 0.1, κ′ = 1; SW(F1) = 1.6 ppm (240 Hz)). Both data were acquired with a matrix of 2048(F2) * 256(F1) and the F1 resolution before zero-filling was 0.39 and 1.88 Hz/pt, respectively. Data were processed using zero-filling to 2048(F2) * 1024(F1) giving a final resolution in F1 of 0.05 and 0.24 Hz/pt, respectively. In (B) signals appear aliased in the F1 dimension but pairs of diastereotopic signals are automatically assigned at the same ω_1 frequency. Expansions of some overlapped regions areas are shown in Fig. 5.

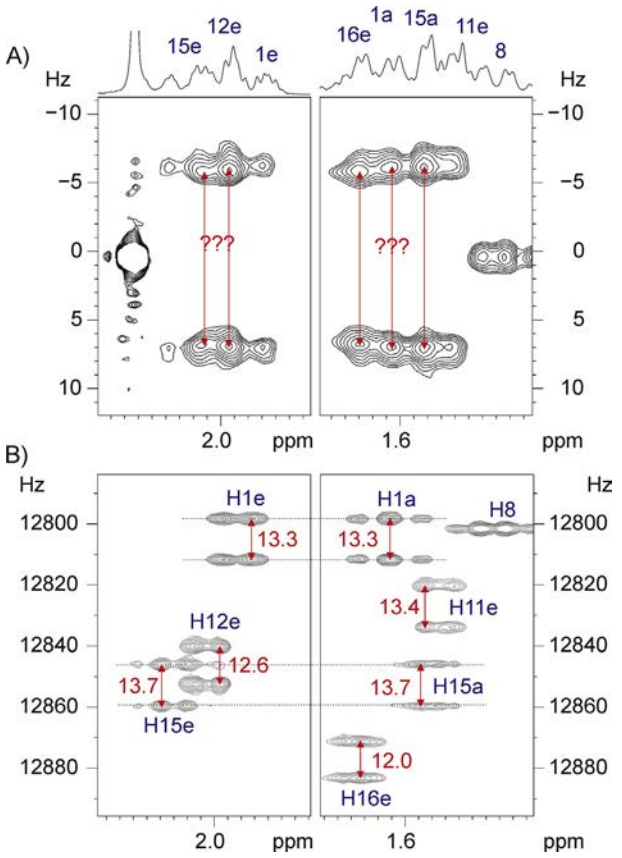

Fig. 5. Expansions extracted from two overcrowded areas of the spectra shown in Fig. 4A and B, respectively. Note that the magnitude of $^2J_{HH}$ (in Hz) can be accurately measured for each signal in B, irrespective of multiplet complexity along the F2 dimension.

that the simultaneous measurement of $^1J_{CH}/^1D_{CH}$ and $^2J_{HH}/^2D_{HH}$ is always advantageous in terms of spectrometer time, the probability to increase signal overlap and therefore to obtain inaccurate values when similar coupling sizes are present can advise to measure them in two separate experiments.

On the other hand, the use of mechanically compressed PMMA gels as orienting media in $CDCl_3$-soluble conditions is supported by several reasons [12]: (i) simple and fast sample preparation, (ii) the sample can be ready for NMR measurement in less than 24 h, (iii) the gel can be cleaned and recovered for later use, (iv) reversible compression allows collect complementary NMR experiments at different alignment degrees with the same NMR tube, (v) isotropic and anisotropic environments can be visualized and measured simultaneously [12c,12d], (vi) optimum lineshapes are achievable for the anisotropic components even at maximum compressions, and (vii) measurable $^1D_{CH}$ and $^2J_{HH}$ of similar magnitudes are available for alignments around $\Delta\nu_Q(^2H) = 30–50$ Hz. Thus, the combination of weakly aligned PMMA media and $^2J_{HH}$-resolved experiments are fully compatible for the simultaneous, in-situ measurement of $^2J_{HH}$ and $^2T_{HH}$ components from a single NMR spectrum, and therefore for the direct determination of $^2D_{HH}$ (Table 1 and Fig. S12) [5g]. Fig. 6 compares some cross-peaks extracted from the $^2J_{HH}$-resolved spectra of **1** in isotropic ($CDCl_3$) and anisotropic ($CDCl_3$-PMMA gel) conditions. For instance, H20a and H20b protons present clear and easy measurable doublets in the conventional isotropic 1D ^{1}H spectrum ($^2J_{H20a-H20b} = 15.0$ Hz) whereas broad, complex and non-interpretable resonances are available in its anisotropic 1D ^{1}H-CPMG spectrum (compare F2 projection in Fig. 6A *vs.* 6B). The same value of $^2J_{HH}$ is measured in the $^2J_{HH}$-resolved spectrum (as a reference, see the clean doublet along F1 and the F2 projection corresponding to the H20a expansion in Fig. 6A). On the other hand, note that both isotropic ($^2J_{H20a-H20b}$) and anisotropic ($^2T_{H20a-H20b}$) contributions can be simultaneously visualized and successfully determined as 15.0 and 46.2 Hz, respectively, in the PMMA gel (Fig. 6B). Assuming that both values are negative, the direct measurement between isotropic and anisotropic signals allows the precise measurement of $^2D_{H20a-H20b}$ as -31.2 Hz. A similar analysis can be performed for the negative value of $^2D_{H11a-H11b}$ (−18.9 Hz) (compare Fig. 6D and F).

It is noteworthy to discuss the cases of the diastereotopic H18a/H18b and H15a/H15b proton pairs where values of $^2J_{H18a-H18b} = -9.9$ Hz (not obvious from the conventional 1D multiplets) and $^2J_{H18a-H18b} = -14.4$ Hz, respectively, are accurately measured from the isotropic $^2J_{HH}$-resolved spectrum. For instance, in the case of H18a/H18b, the isotropic and anisotropic signals appear almost overlapped in the PMMA gel at $\Delta\nu_Q = 49$ Hz (see Fig. 6D and F), assuming an absolute value of $^2T_{H18a-H18b}$ around 11 Hz. Since signs cannot be determined by this method, a first indecision would arise on whether the resulting $^2D_{H18a-H18b}$ value is ∼ −1 Hz or ∼ +20 Hz. In practice this is not a problem because they can be determined by using the strategy outlined in Fig. 7. First and related to the $^2J_{HH}$-resolved experiment, we propose the determination of $^1D_{CH}$ for all CH, each individual diastereotopic CH_2 and CH_3 proton signals from the doublets obtained in the F1 dimension of an equivalent $^1J_{CH}$-resolved HSQC spectrum [5h,5i]. Once the tensor alignment is calculated by using a basic set including only the experimental $^1D_{CH}$ restraints for CH groups, the orientation of all H—C—H internuclear vectors and therefore the size (and also the sign) of diastereotopic $^1D_{CHa}$ and $^1D_{CHb}$ as well as $^2D_{HH}$ are theoretically predicted (see Tables 1 and S1). Thus, the ambiguity about the real value of $^2D_{H18a-H18b}$ can be quickly and safely solved, as similarly reasoned for $^2D_{H15a-H15b}$.

On the other hand, protons H17a/H17b resonating at 1.90 ppm are a good example to illustrate and discuss the possible measurement of $^2J_{HH}/^2D_{HH}$ in equivalent CH_2 protons. While the splitting due to $^2J_{H17aH17b}$ is not observed in isotropic conditions (Fig. 3A),

Table 2
Scalar ($^2J_{HH}$) two-bond proton-proton coupling constants (in Hz) of progesterone in DMSO-d_6 measured from different NMR spectra.

Geminal proton pairs	Chemical Shifts (ppm)	$^2J_{HH}$ from ^{1}H spectrum[b]	$^2J_{HH}$ from $^2J_{HH}$-resolved[b]	$^2J_{HH}$ from $^2J_{HH}/\delta$-scaled[b]
H1e/H1a	1.96/1.59	[a]	[a]	13.4
H2e/H2a	2.15/2.38	16.8	16.8	17.0
H6e/H6a	2.23/2.38	14.6	14.7	14.9
H7e/H7a	1.77/0.96	12.7	12.8	12.9
H11e/H11a	1.56/1.37	[a]	[a]	13.5
H12e/H12a	1.99/1.41	[a]	[a]	12.4
H15e/H15a	2.02/1.56	[a]	[a]	13.8
H16e/H16a	1.62/1.17	[a]	[a]	12.0

[a] Not measured.
[b] Values assumed to be negative.

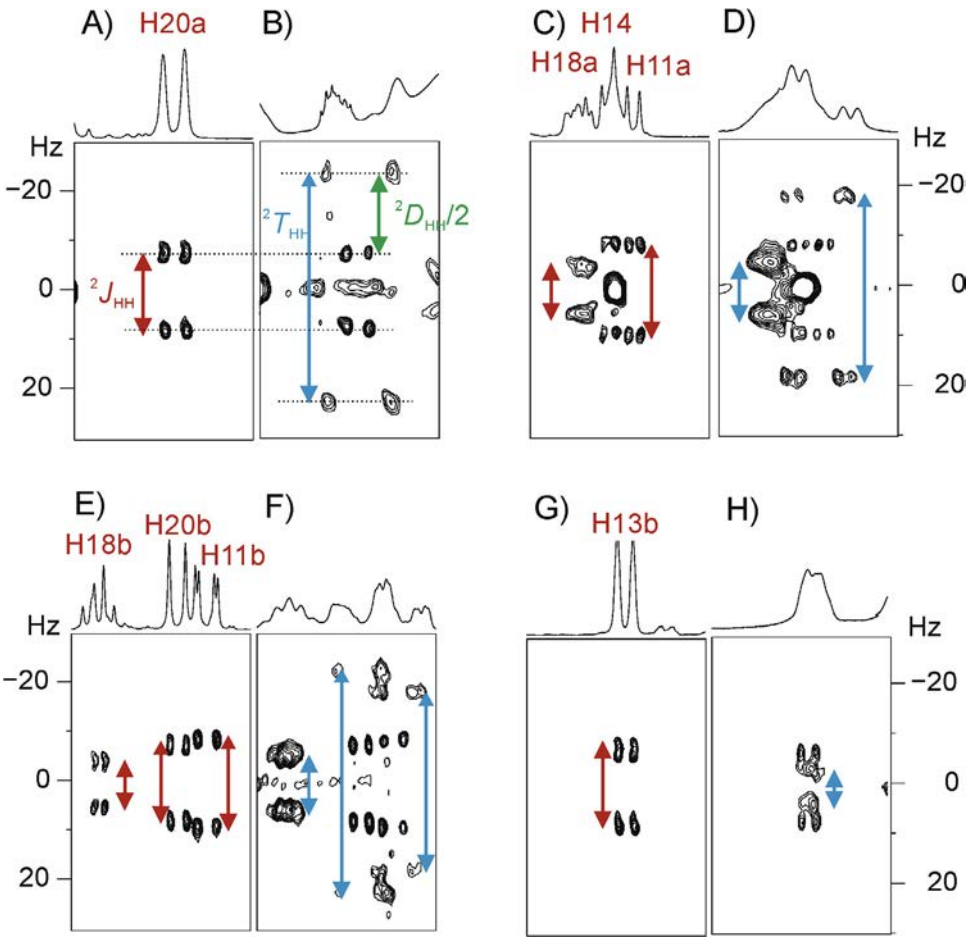

Fig. 6. Expansions corresponding to the $^2J_{HH}$-resolved spectra of **1** acquired in (left) isotropic ($CDCl_3$) and (right) anisotropic (PMMA/ $CDCl_3$ gel) conditions. In the anisotropic spectrum (B,D,F and H), note how both isotropic (red arrow) and anisotropic (blue arrow) components can be observed for each individual CH_2 signal, allowing the in-situ determination of scalar $^2J_{HH}$, total $^2T_{HH}$ and residual dipolar $^2D_{HH}$ coupling constants in a single spectrum according to $^2T_{HH} = {}^2J_{HH} + {}^2D_{HH}$. (For interpretation of the references to colour in this figure legend, the reader is referred to the web version of this article.)

in the anisotropic medium can be observed the isotropic component at F1 = 0 and the anisotropic component as an additional large doublet of 33.3 Hz that corresponds to the direct measurement of $^2D_{H17aH17b}$ according to $1.5 * {}^2D_{HH}$. This is because *J* coupling is not observed for chemically equivalent nuclei, while *D* couplings does [14]. This experimental value of 22.2 Hz is in accordance with the theoretically predicted value of +21.7 Hz (Table S1). Thus, the $^2J_{HH}$-resolved experiment allows the direct and selective measurement of $^2D_{HH}$ in equivalent CH_2 systems, even in the case that the existence of many other long-range $^nD_{HH}$ (n > 2) can complicate the conventional multiplet ^1H signal structure.

Table 3 summarizes the best quality factors (Q) obtained for some possible thirteen stereoisomers of **1**. Thus, the use of only 10 $^1D_{CH}$ of methine CH affords a poor discrimination of the correct structure (0.048 vs 0.079). The discrimination is largely improved by adding 5 $^2D_{HH}$ (0.058 vs 0.183), 8 $^1D_{CH}$ of diastereotopic CH_2 protons (0.076 vs 0.288) or 5 $^2D_{HH}$ + 8 $^1D_{CH}$ of diastereotopic CH_2 protons (0.079 vs 0.303). The logical doubts about the sign of $^2T_{HH}$ could also be resolved by two additional approaches. Experimentally, by measuring $^2T_{HH}$ values at two different alignment degrees and check their behavior (Fig. S13). Alternatively, correct and wrong $^2D_{HH}$ values can be discerned by performing and comparing different calculations (Q factors for correct $^2D_{HH}$ values: 0.079 vs 0.303, and wrong $^2D_{HH}$ values: 0.240 vs 0.394).

The importance of betting on $^2J_{HH}/^2D_{HH}$ as useful NMR restraints in RDC-assisted studies is confirmed by their easy measurement, the optimum size that allows minimizing errors in their measurement as well as their tremendous sensitivity to structural changes under anisotropic conditions. Although in isotropic conditions $1J_{CH}$ is about one order of magnitude larger than $^2J_{HH}$, $^2T_{HH}$ is much more sensitive than $^1T_{CH}$ ($^2T_{HH}$ values can reach maximum values of 30 Hz with $\Delta\nu_Q = 26$ Hz and 45 Hz if $\Delta\nu_Q = 49$ Hz). This is confirmed by the fact that, in the case of **1**, $^1D_{CH}$ and $^2D_{HH}$ present similar sizes.

3. Conclusions

Attempts to measure accurate $^2J_{HH}/^2D_{HH}$ for diastereotopic protons of prochiral CH_2 groups from the F2 dimension of 2D spectra can suffer of the usual presence of complex multiplet *J* patterns, line broadening effects and above all strong coupling artifacts. To avoid them, a new $^2J_{HH}$-resolved experiment has been proposed for simple and accurate measurement of the magnitude of $^2J_{HH}$ from a clean doublet obtained in F1, irrespective of multiplet complexity and strong coupling effects. The method performs a dual measurement where the same $^2J_{HH}$ value can be obtained in two different cross-peaks, reinforcing potential uncertainties. It accepts several implementations according to the degree of signal overlapping. A *J*/δ-scaled version is very useful in highly congested areas where $^2J_{HH}$ and $\delta(^1H)$ are very similar. On the other hand, it has been shown that a visual $^2J_{HH}$ NMR profile can be created and also the fast determination of relevant $^2D_{HH}$ RDCs in small molecules

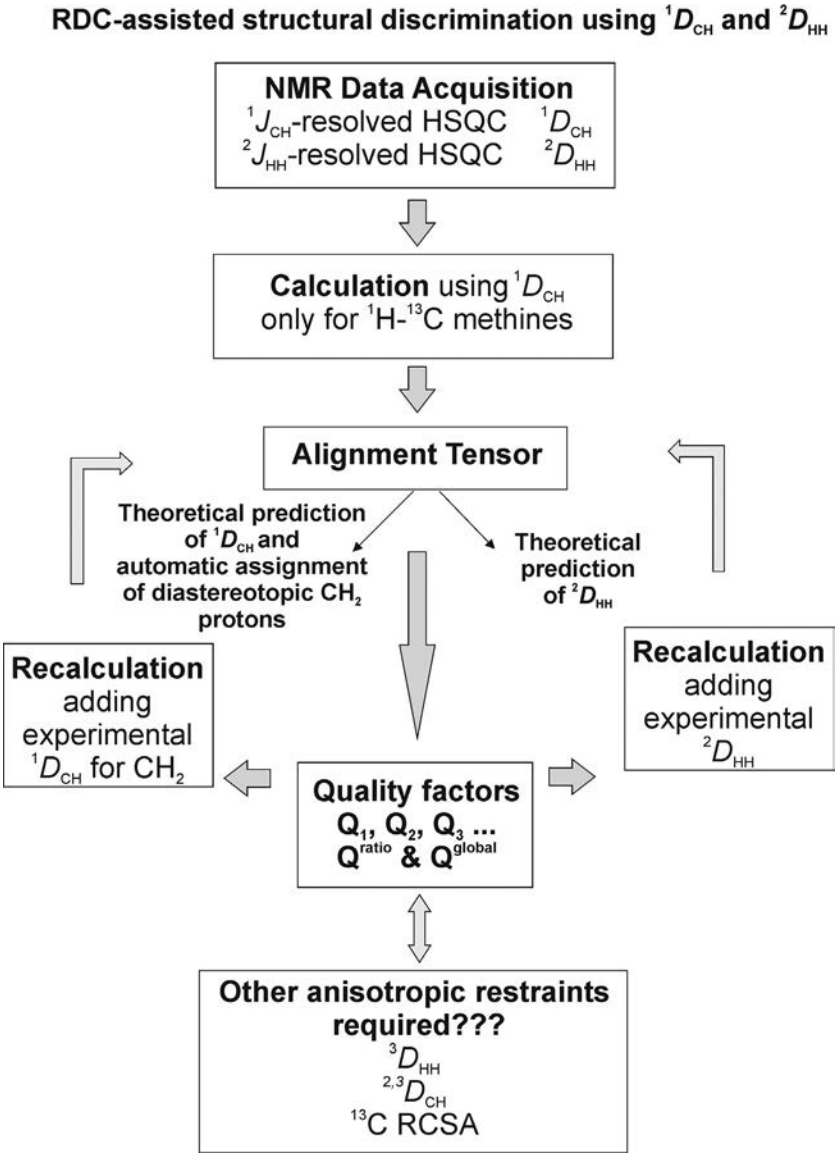

Fig. 7. General strategy for the RDC-assisted structural discrimination of small molecules involving experimental $^1D_{CH}$ and $^2D_{HH}$.

Table 3
Quality factors (Q) of the three best structures of **1** (13 isomeric structures were calculated) using different set of RDCs restraints in the calculation.

Isomer	Only CH[a]	CH[a] + $^2D_{HH}$[c]	CH[a] + CH_2[b]	CH[a] + CH_2[b] + $^2D_{HH}$[c]	CH[a] + CH_2[b] + $^2D_{HH}$[d]
1 (correct structure)	0.048	0.058	0.076	0.079	0.240
4	0.079	0.183	0.535	0.512	0.582
5	0.153	0.274	0.288	0.303	0.394
...					
Q^{ratio}	0607	0317	0.264	0.260	0.609

[a] 10 $^1D_{CH}$ values measured from a $^1J_{CH}$-resolved HSQC.
[b] 8 $^1D_{CH}$ values measured from a $^1J_{CH}$-resolved HSQC. C15 and C17 not included.
[c] 5 $^2D_{HH}$ values measured from a $^2J_{HH}$-resolved HSQC. H17a/H17b not included.
[d] As c, but using 3 correct values and 2 wrong $^2D_{HH}$ values (for H18a/H18b and H15a/H15b) according to Table 1.

dissolved in weakly anisotropic media is not compromised by the presence of overlapping and broad ^{1}H multiplets. Although the method does not provide the sign of $^2D_{HH}$, it can be predicted theoretically from the tensor alignment calculation in a straightforward way or deduced experimentally by measuring at two different degrees of alignment. It has been also shown that the size of $^2D_{HH}$ can be directly obtained for equivalent CH_2 systems. Definitively, the concerted use of experimental $^1D_{CH}$ and $^2D_{HH}$ data is strongly recommended in RDC-assisted structural discrimination studies of small molecules containing CH_2 protons.

4. Experimental section

NMR experiments were recorded on a 600 MHz spectrometer equipped with a triple-resonance ^{1}H/^{13}C/BB inverse probe. The temperature for all measurements was set to 298 K. The isotropic

samples were similarly prepared by dissolving 20 mg of **1** in $CDCl_3$ and 20 mg of **2** in DMSO-d_6. The anisotropic sample consisted of 20 mg of **1** aligned in a poly(methylmethacrylate) (PMMA) gel swollen in $CDCl_3$ using the reversible compression/relaxation method [12a,12b]. The ^2H quadrupolar splitting ($\Delta\ \nu_Q$) for the $CDCl_3$ signal was set to 49 Hz.

All NMR spectra were recorded with proton 90° pulses of 8.5 μs and carbon 90° pulses of 10.5 μs. For broadband carbon inversion and refocusing, 0.5 ms smoothed Chirp pulses sweeping over a frequency band of 60 kHz and a 1:2:1 composite adiabatic pulse with an overall duration of 2 ms duration were used, respectively. The interpulse Δ delays in INEPT and BIRD elements were set to 3.5 ms ($\Delta = 1/(2 * {}^1J_{CH})$; optimized to $^1J_{CH}$ = 145 Hz) and the recycle delay to 1 s. Gradient ratios for G1:G2 were set to 80:20.1, measured as percentage of the absolute gradient strength of 53.5 G/cm. The zero-quantum filter (ZQF) consists of a chirped adiabatic pulse applied simultaneously to a weak rectangular gradient (G0 = 11%) of the same duration (20 ms). Sine bell shaped gradients had 1 ms of duration and were followed by a recovery delay of 100 μs (δ). All experiments were acquired and processed using the echo/anti-echo protocol where the gradient G1 was inverted for every second FID.

General conditions for the $^2J_{HH}$-resolved HSQC experiment: Two scans were accumulated for each one of the 256 t_1 increments and the number of complex data points in t_2 was set to 2048. Spectra were acquired with an spectral window of 6000 Hz in F_2 and 50 Hz in F_1 ($\kappa = 0$ and $\kappa' = 1$), giving a FID resolution of 5.8 (F2) and 0.39 (F1) Hz/pt, respectively, prior to processing. In J/δ-scaled experiments, κ was set to 0.1 and SW(F1) to 250 Hz (1.6 ppm), giving a FID resolution of 1.9 Hz/pt in F1 prior to processing. Zero filling to 1024 in F_1 and a π/2-shifted squared cosine window function (QSINE, SSB: 2) in both dimensions were applied. After processing, the digital resolution in F1 was 0.05 Hz/pt and 0.23 Hz/pt in $^2J_{HH}$-resolved and J/δ-scaled spectra, respectively. The $^2J_{HH}$-resolved HSQC experiment of the anisotropic sample was acquired with the same parameters but using eight scans for each of the 128 t_1 increments and processed as described above. The F1 resolution before zero-filling was 0.78 Hz/pt.

Alignment tensor calculations were performed on a basis of 13 diastereoisomeric structures of **1** calculated at a DFT level. Fitting of RDC data to structures was performed using the MSpin software package (Mestrelab Research SL, Santiago de Compostela, Spain); http://www.mestrelab.com [13]. Other similar details can be found in Ref. [5g].

Acknowledgment

Financial support for this research provided by Spanish MINECO (project CTQ2015-64436-P) is gratefully acknowledged. We also thank to the Servei de Ressonància Magnètica Nuclear, Universitat Autònoma de Barcelona, for allocating instrument time to this project. NMR instrumentation at Carnegie Mellon University was partially supported by the NSF (CHE-0130903 and CHE-1039870). RRG gratefully acknowledges support from the NSF (CHE-1111684).

Appendix A. Supplementary material

NMR spectra of several compounds, comparison of different NMR methods and pulse program. Supplementary data associated with this article can be found, in the online version, at http://dx.doi.org/10.1016/j.jmr.2017.06.014.

References

[1] W.P. Aue, J. Karhan, R.R. Ernst, J. Chem. Phys. 64 (1976) 4226–4227.
[2] C. Ludwig, M.R. Viant, Phytochem. Anal. 21 (2010) 22–32.
[3] (a) M.J. Thrippleton, R.A.E. Edden, J. Keeler, J. Magn. Reson. 174 (2005) 97–109;
(b) A.J. Pell, J. Keeler, J. Magn. Reson. 189 (2007) 293–299;
(c) B. Luy, J. Magn. Reson. 201 (2009) 18–24;
(d) M. Foroozandeh, R.W. Adams, P. Kiraly, M. Nilsson, G.A. Morris, Chem. Commun. 51 (2015) 15410–15413.
[4] N. Giraud, L. Beguin, J. Courtieu, D. Merlet, Angew. Chem. Int. Ed. 49 (2010) 3481–3484.
[5] (a) A. Bax, R. Freeman, J. Am. Chem. Soc. 104 (1982) 1099–1100;
(b) M. Liu, R.D. Farrant, J.M. Gillam, J.K. Nicholson, J.C. Lindon, J. Magn. Reson. B 109 (1995) 275–283;
(c) K. Fehér, S. Berger, K.E. Kövér, J. Magn. Reson. 163 (2003) 340–346;
(d) K.E. Kövér, K. Fehér, J. Magn. Reson. 168 (2004) 307–313;
(e) J. Saurí, L. Castañar, P. Nolis, A. Virgili, T. Parella, J. Magn. Reson. 216 (2014) 33–40;
(f) L. Castañar, M. García, E. Hellemann, P. Nolis, R.R. Gil, T. Parella, J. Org. Chem. 81 (2016) 11126–11131;
(g) N. Marcó, R.R. Gil, T. Parella, Magn. Reson. Chem. 55 (2017) 540–545;
(h) N. Marcó, A.A. Souza, P. Nolis, C. Cobas, R.R. Gil, T. Parella, J. Org. Chem. 82 (2017) 2040–2044;
(i) N. Marcó, A.A. Souza, P. Nolis, R.R. Gil, T. Parella, J. Magn. Reson. 276 (2017) 37–42;
(j) J. Furrer, M. John, H. Kessler, B. Luy, J. Biomol. NMR 37 (2007) 231–243.
[6] (a) L. Ziani, J. Courtieu, D. Merlet, J. Magn. Reson. 183 (2006) 60–67;
(b) U.R. Prabhu, S.R. Chaudhari, N. Suryaprakash, Chem. Phys. Lett. (2010) 334–341;
(c) K. Kobzar, H. Kessler, B. Luy, Angew. Chem. Intl. Ed. 44 (2005) 3145–3147.
[7] (a) P. Tzvetkova, S. Simova, B. Luy, J. Magn. Reson. 186 (2007) 193–200;
(b) T. Carlomagno, W. Peti, C. Griesinger, J. Biomol. NMR 17 (2000) 99–109;
(c) P. Permi, J. Biomol. NMR 22 (2002) 27–35;
(d) E. Miclet, D.C. Williams Jr., G.M. Clore, D.L. Bryce, J. Boisbouvier, A. Bax, J. Am. Chem. Soc. 126 (2004) 10560–10570;
(e) H. Schwalbe, W. Smastag, J.W. Engels, W. Bermel, C. Griesinger, J. Biomol. NMR 3 (1993) 479–486;
(f) A. Rexroth, P. Schmidt, S. Szalma, T. Geppert, H. Schwalbe, C. Griesinger, J. Am. Chem. Soc. 117 (1995) 10389–10390;
(g) T. Carlomagno, H. Schwalb, A. Rexroth, O.W. Sorensen, C. Griesinger, J. Magn. Reson. 135 (1998) 216–226.
[8] (a) J.R. Garbow, D.P. Weitekamp, A. Pines, Chem. Phys. Lett. 93 (1982) 504–509;
(b) D. Uhrin, T. Liptaj, K.E. Kover, J. Magn. Reson. A 101 (1993) 41–46.
[9] M.J. Thrippleton, J. Keeler, Angew. Chem. Intl. Ed. 42 (2003) 3938–3941.
[10] (a) C.M. Thiele, Eur. J. Org. Chem. (2008) 5673–5685;
(b) G. Kummerlöwe, B. Luy, Annu. Rep. NMR Spectroscop. 68 (2009) 193–230;
(c) G. Kummerlöwe, B. Luy, Trend.Anal. Chem. 28 (2009) 483–493.
[11] (a) C.M. Thiele, S. Berger, Org. Lett. 5 (2003) 705–708;
(b) C.M. Thiele, J. Org. Chem. 69 (2004) 7403–7413;
(c) J.D. Snider, E. Troche-Pesqueira, S.R. Woodruff, C. Gayathri, N.V. Tsarevsky, R.R. Gil, Magn. Reson. Chem. 5 (2012) S86–S91;
(d) L. Verdier, P. Sakhaii, M. Zweckstetter, C. Griesinger, J. Magn. Reson. 163 (2003) 353–359;
(e) G. Kummerlöwe, S. Schmitt, B. Luy, Open Spectrosc. J. 4 (2010) 16–27.
[12] (a) R.R. Gil, C. Gayathri, N.V. Tsarevsky, K. Matyjaszewski, J. Org. Chem. 73 (2008) 840–848;
(b) C. Gayathri, N.V. Tsarevsky, R.R. Gil, Chem. Eur. J. 16 (2010) 3622–3626;
(c) L.F. Gil-Silva, R. Santamaría-Fernández, A. Navarro-Vázquez, R.R. Gil, Chem. Eur. J. 22 (2016) 472–476;
(d) E. Hellemann, R.R. Teles, H. Hallwass, W. Barros Jr., A. Navarro-Vázquez, R. R. Gil, Chem. Eur. J. 22 (2016) 16632–16635.
[13] A. Navarro-Vázquez, Magn. Reson. Chem. 50 (2012) S73–S79.
[14] (a) A. Saupe, G. Englert, Phys. Rev. Lett 11 (11) (1963) 462–464;
(b) L.C. Snyder, E.W. Anderson, J. Am. Chem. Soc. 86 (1964) 5023–5024;
(c) M.H. Levitt, Spin Dynamics. Basics of Nuclear Magnetic Resonance, second ed., Wiley, 2008, p. 620.

Supporting Information

$^2J_{HH}$-resolved HSQC: Exclusive determination of geminal proton-proton coupling constants

Núria Marcó,[1] Pau Nolis,[1] Roberto R. Gil[2] and Teodor Parella[1,*]

[1]Servei de Ressonància Magnètica Nuclear, Universitat Autònoma de Barcelona, E-08193 Bellaterra (Barcelona), Catalonia, Spain;
[2]Department of Chemistry, Carnegie Mellon University, Pittsburgh, PA, USA.

Table of contents:

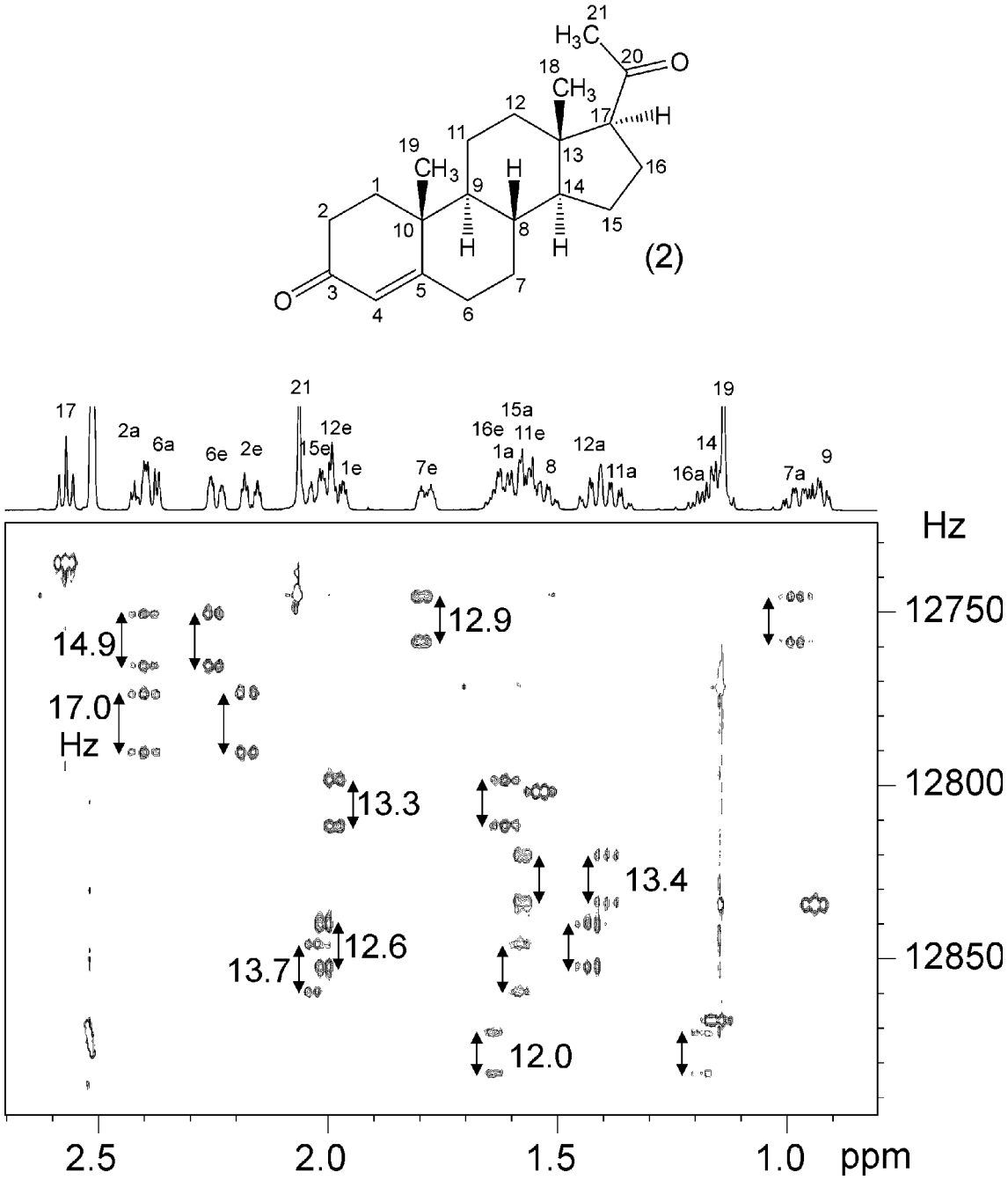

Figure S1: $^{2}J_{HH}$/δ-scaled HSQC spectrum of progesterone (**2**) with all experimental $^{2}J_{HH}$ values (in Hz) for each diastereotopic CH_2 cross-peak. Data were acquired using the pulse sequence of Fig. 1 with κ = 0.1, κ' = 1; SW(F1) = 1.6 ppm (250 Hz). After processing, digital F1 resolution was of 0.23 Hz/pt. Note that pairs of aliased diastereotopic signals are automatically assigned at the same F_1 frequency.

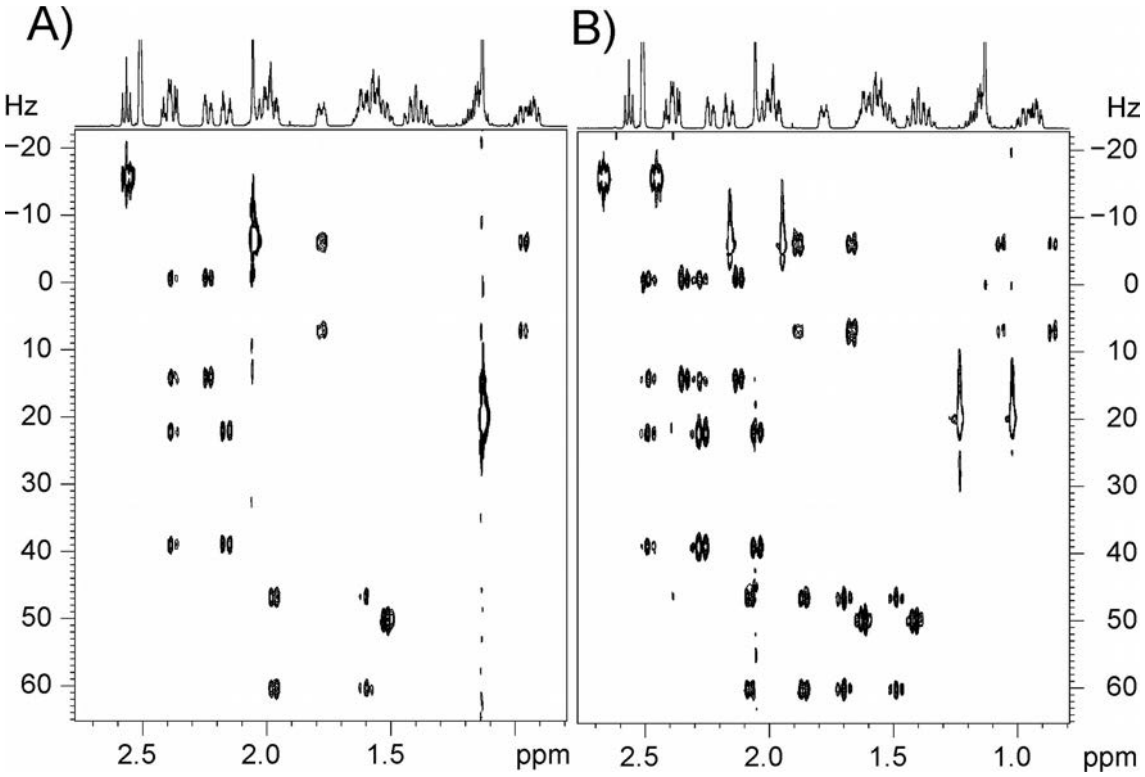

Figure S2: Expanded area corresponding to the $^{2}J_{HH}$/δ-scaled HSQC spectra of progesterone acquired (A) with and (B) without broadband ^{13}C decoupling during acquisition, respectively. The coupling patterns displayed in Fig. 1E and 1E, respectively, are obtained for diastereotopic CH_2 protons.

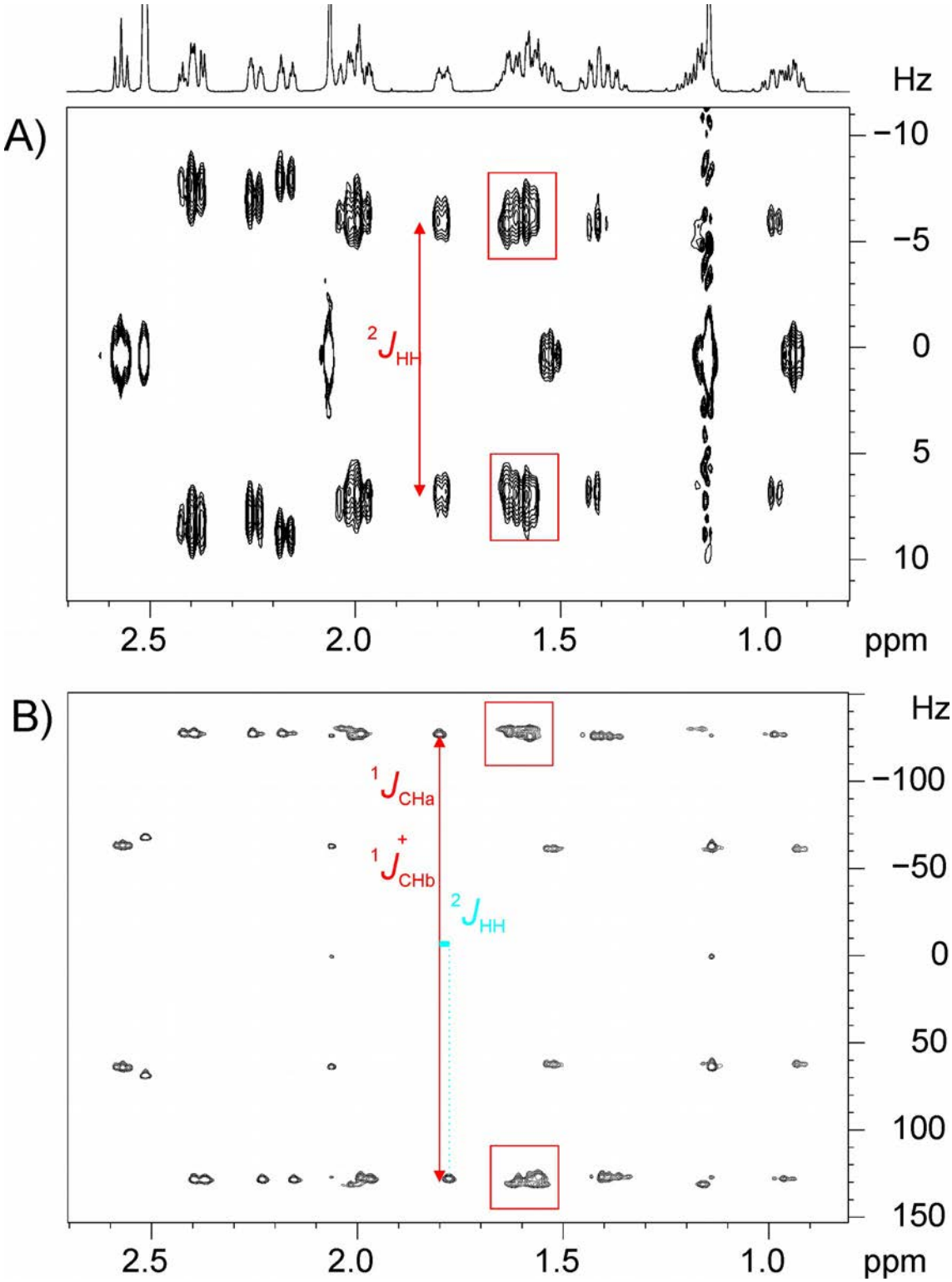

Figure S3: Comparison between the A) $^2J_{HH}$-resolved and B) *J*SB-HSQC-E.COSY spectra of progesterone. Note that isolated signals allow the accurate determination of $^2J_{HH}$ and/or $^1J_{CH}$, whereas overlapping precludes any attempt of success (see red boxes).

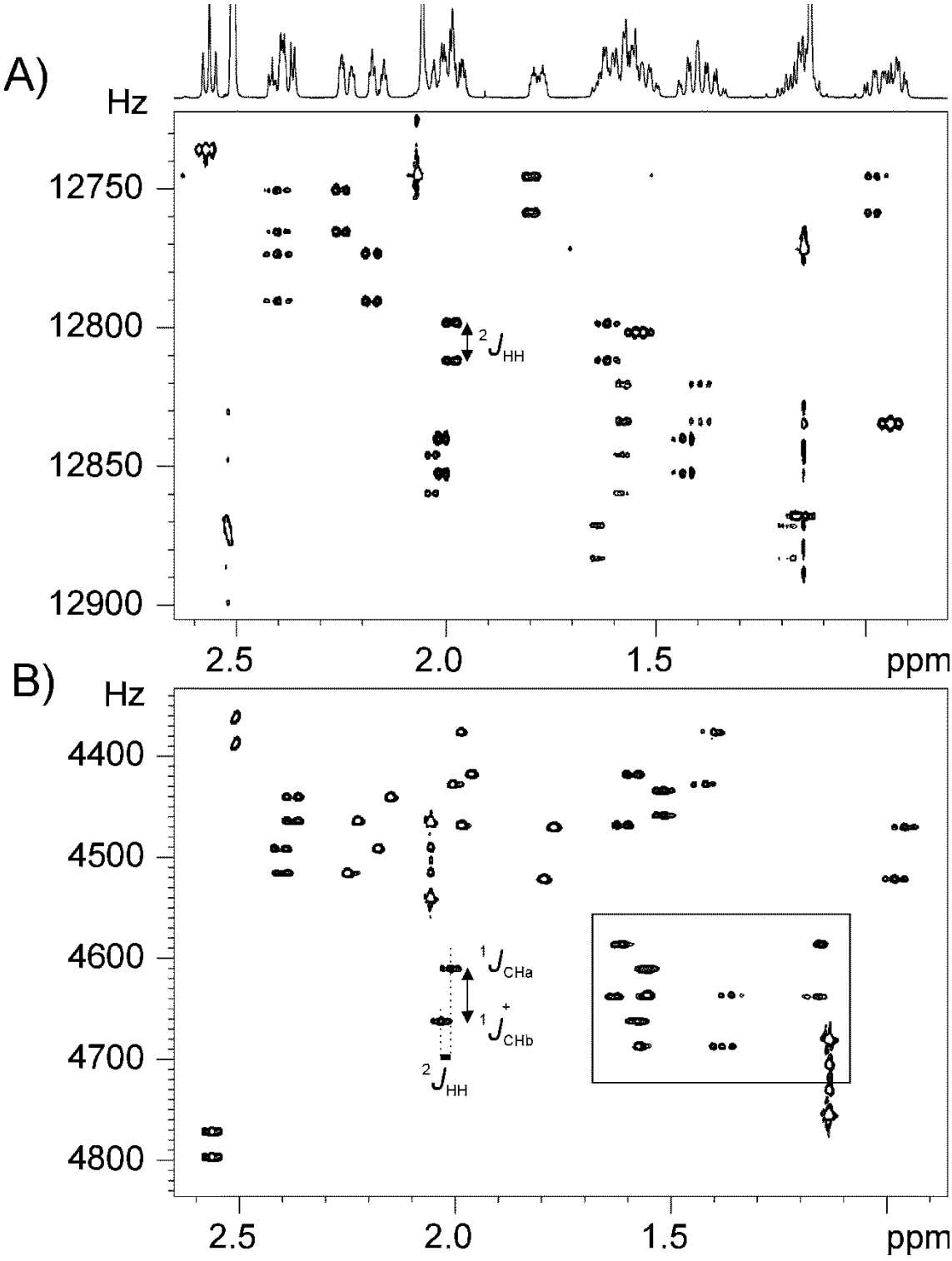

Figure S4: Comparison between the *J*/δ-scaled versions of the A) $^2J_{HH}$-resolved and B) *J*SB-HSQC-E.COSY spectra of progesterone. Apparently, the sign of both $^1J_{CHa}$+$^1J_{CHb}$ and $^2J_{HH}$ can be measured in B. However, strong coupling effects can introduce important errors in the measurement (marked box), as shown in the expansions of Fig. S5.

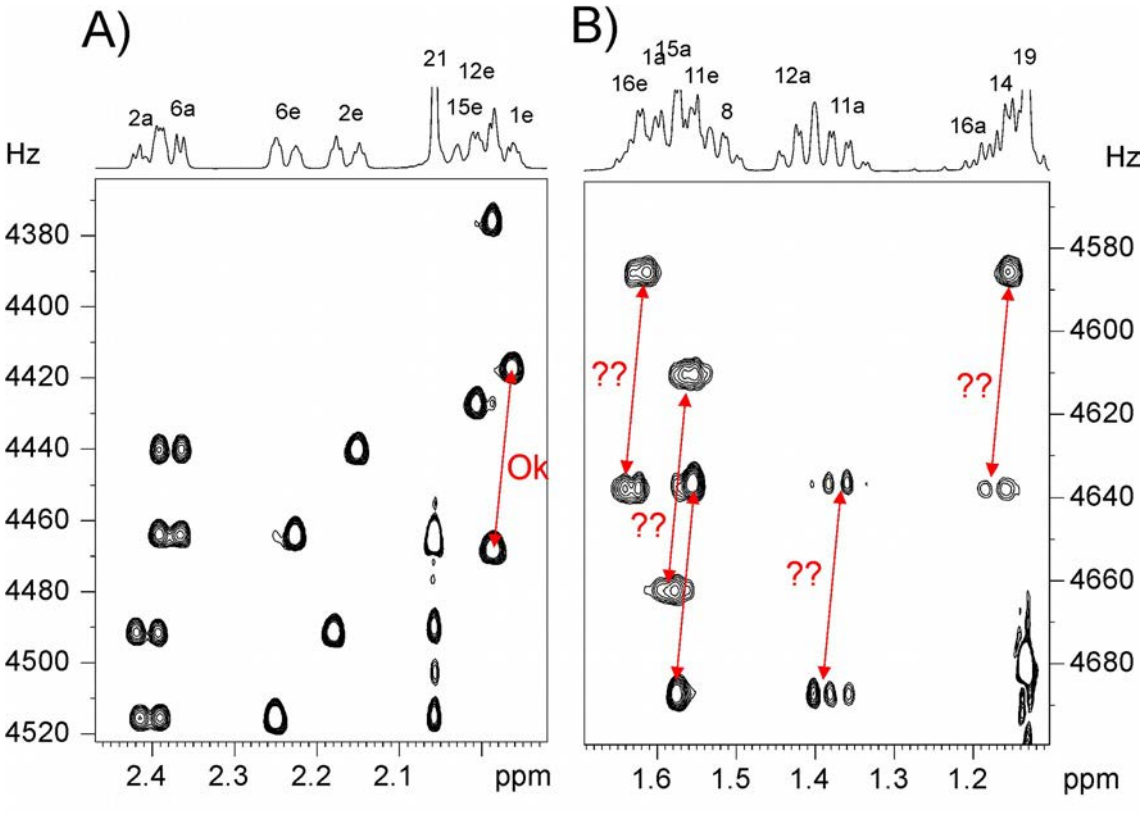

Figure S5: Expanded areas of the *J*SB-HSQC-E.COSY spectrum of progesterone displayed in Fig. S4B. On the left, $^{2}J_{HH}$ can be measured for all cross-peaks which show imperceptible signal distortions. However, evident strong coupling effects severely affects the different E.COSY components in the cross-peaks shown in the right panel, hindering the accurate extraction of $^{2}J_{HH}$.

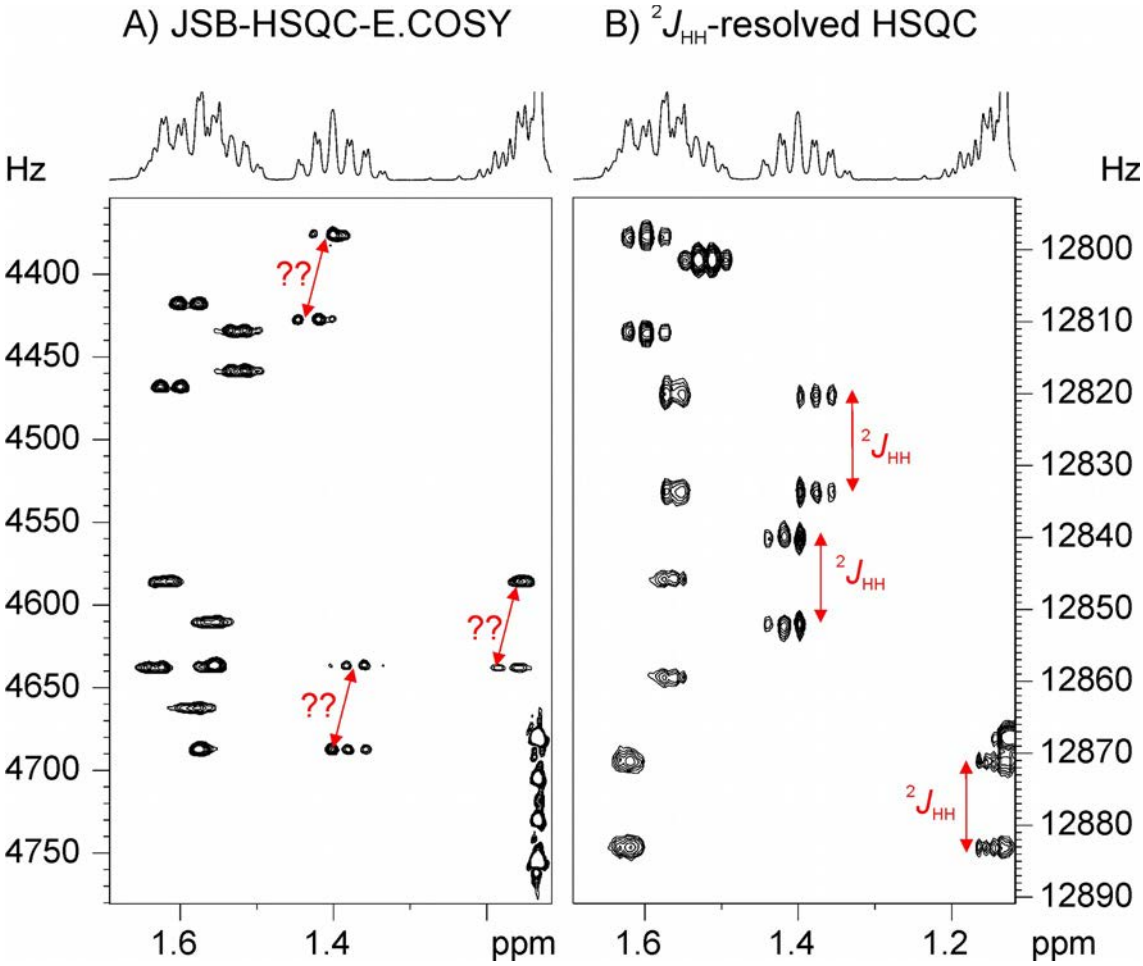

Figure S6: Comparison between the A) *J*SB-HSQC-E.COSY and B) $^2J_{HH}$ -resolved HSQC spectra of progesterone. Although the sign is available, note that strong coupling effects generate non-symmetrical cross-peaks along the direct dimension in A), hindering an accurate and reliable determination of the magnitude of $^2J_{HH}$. On the other hand, simple and precise measurement of $^2J_{HH}$ is performed from the clean doublets along F1 in B for all cross-peaks.

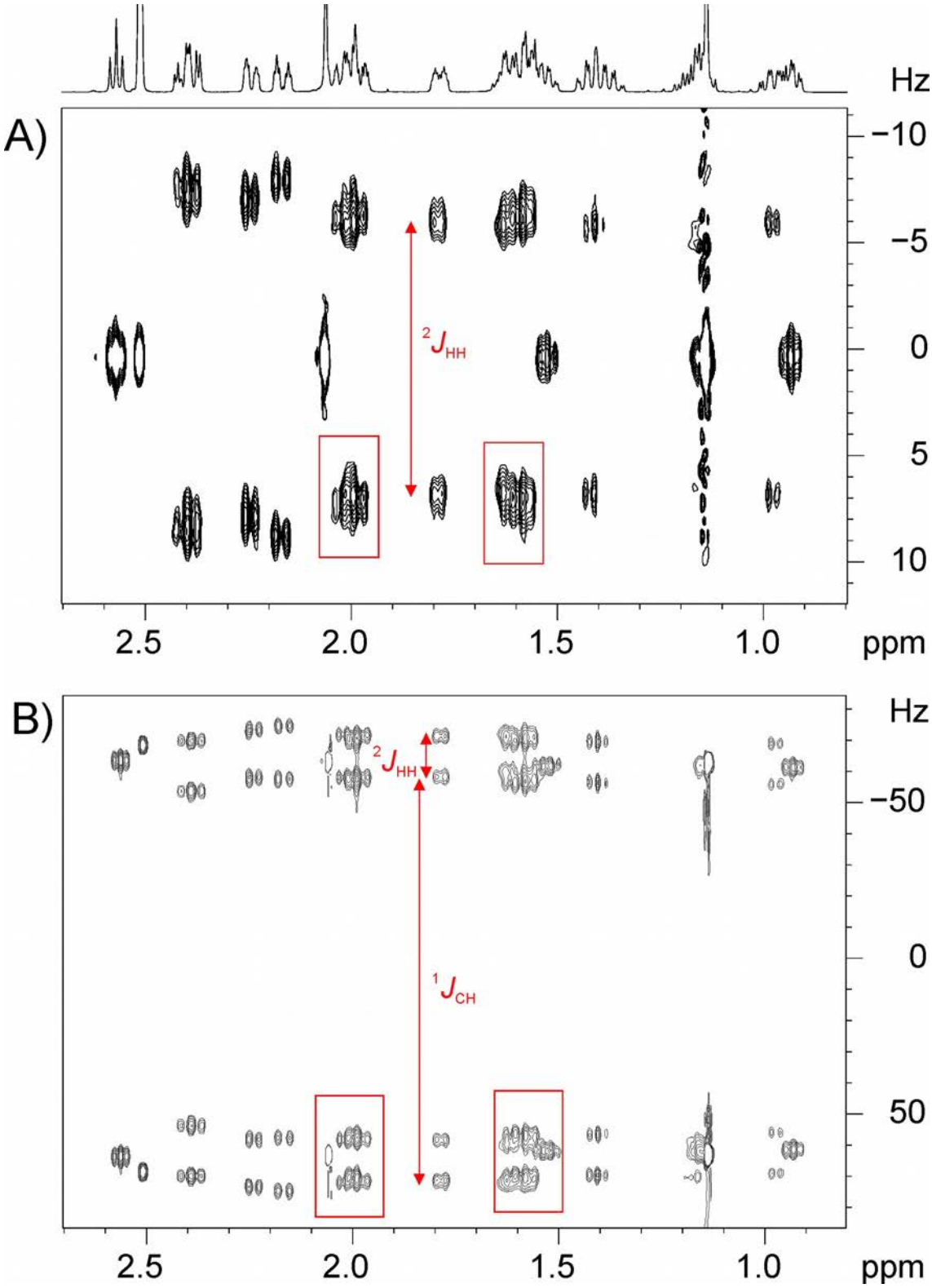

Figure S7: Comparison between the A) $^2J_{HH}$-resolved and B) $^2J_{HH}/^1J_{CH}$-resolved spectra of progesterone. Note that isolated signals allow the accurate determination of $^2J_{HH}$ and/or $^1J_{CH}$, whereas overlapping precludes any attempt of success (see red boxes).

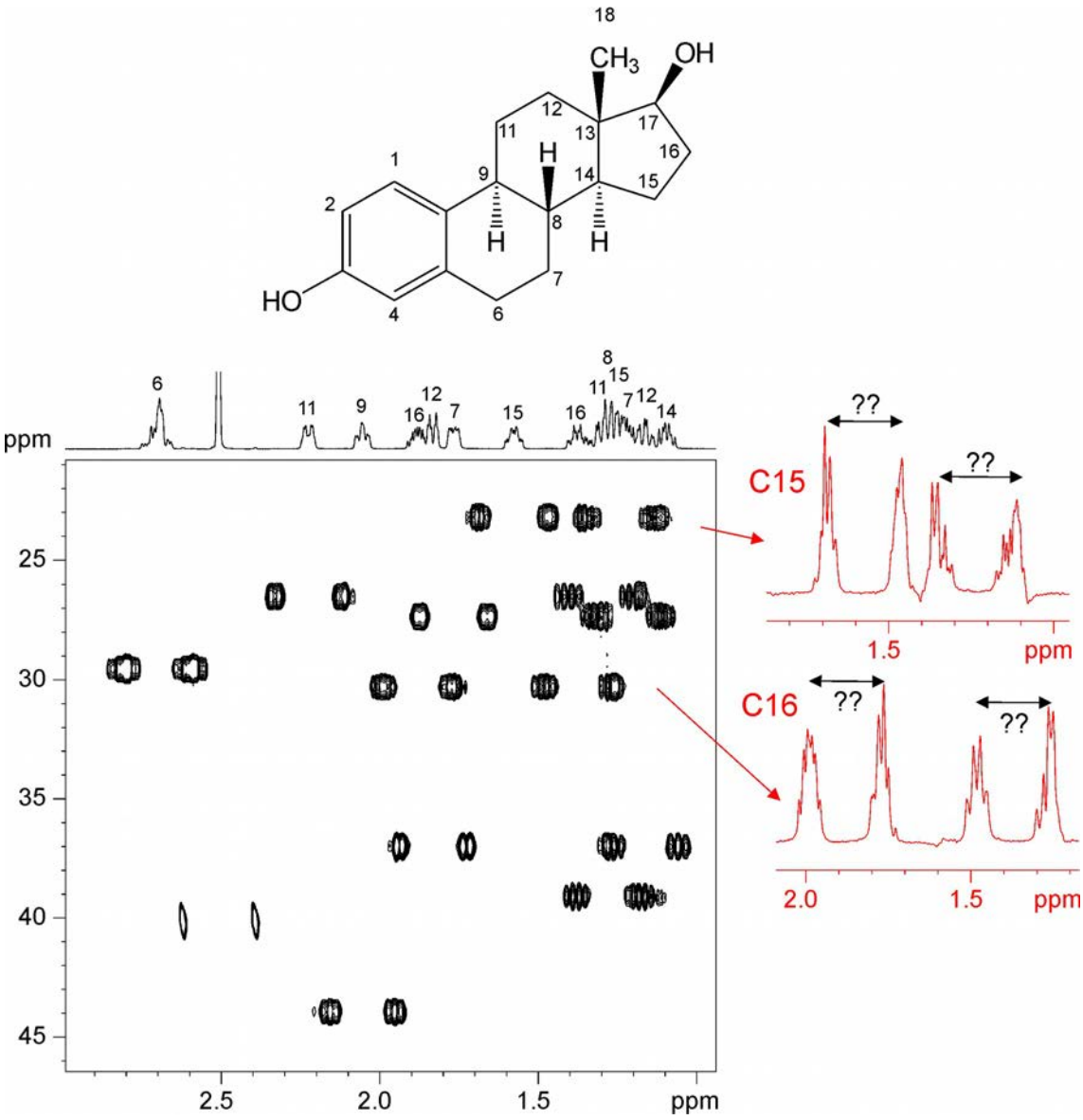

Figure S8: 2D CLIP-HSQC spectrum of estradiol (**3**) in DMSO-d_6. Note that the measurement of coupling constants along the F2 dimension can be severely affected by the presence of distorted, unsymmetrical peaks due to strong coupling effects.

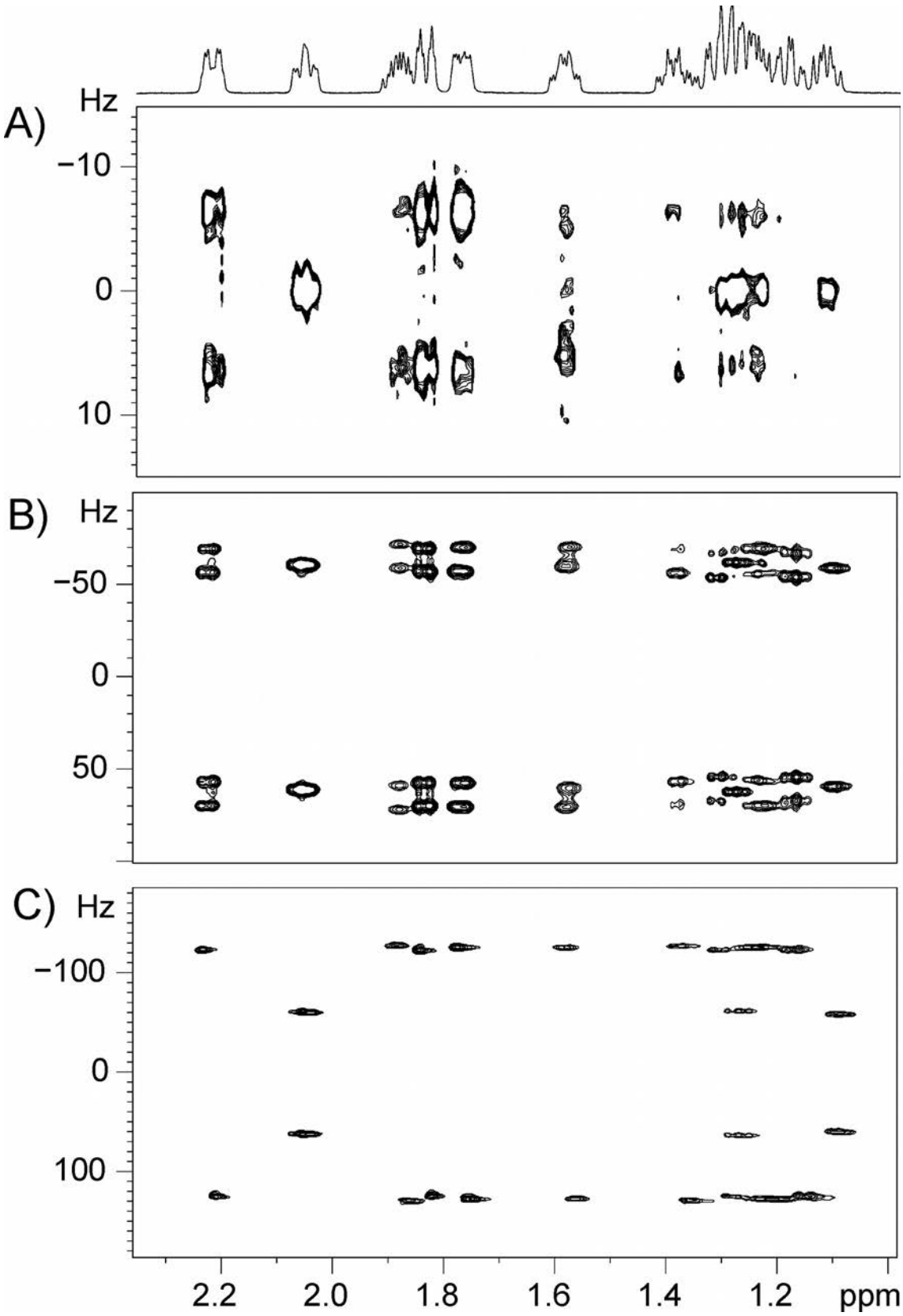

Figure S9: Comparison between the A) $^{2}J_{HH}$-resolved, B) $^{2}J_{HH}/^{1}J_{CH}$-resolved and C) *J*SB-HSQC-E.COSY spectra of estradiol.

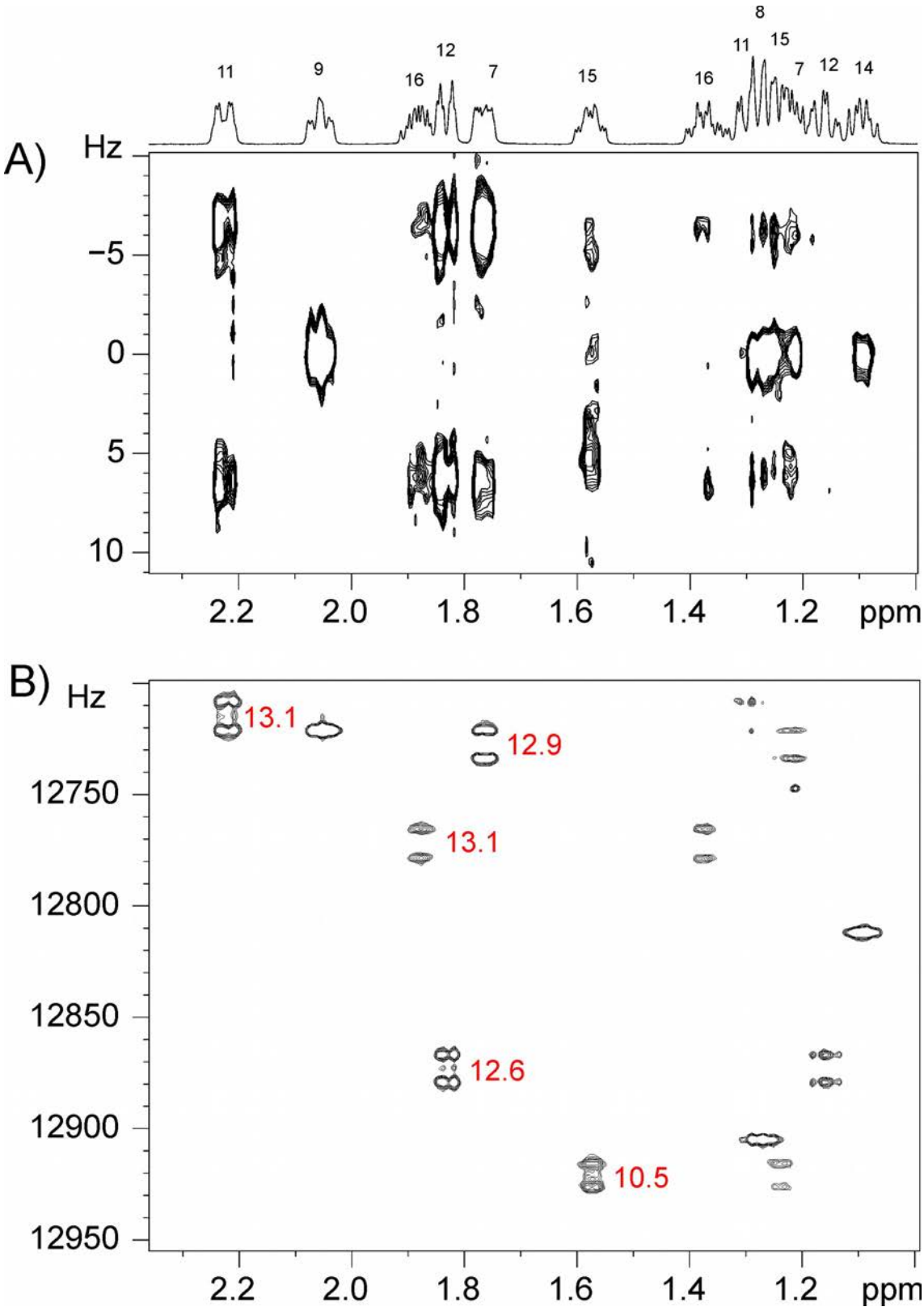

Figure S10: A) $^{2}J_{HH}$-resolved and B) $^{2}J_{HH}$/δ-scaled HSQC spectra of estradiol.

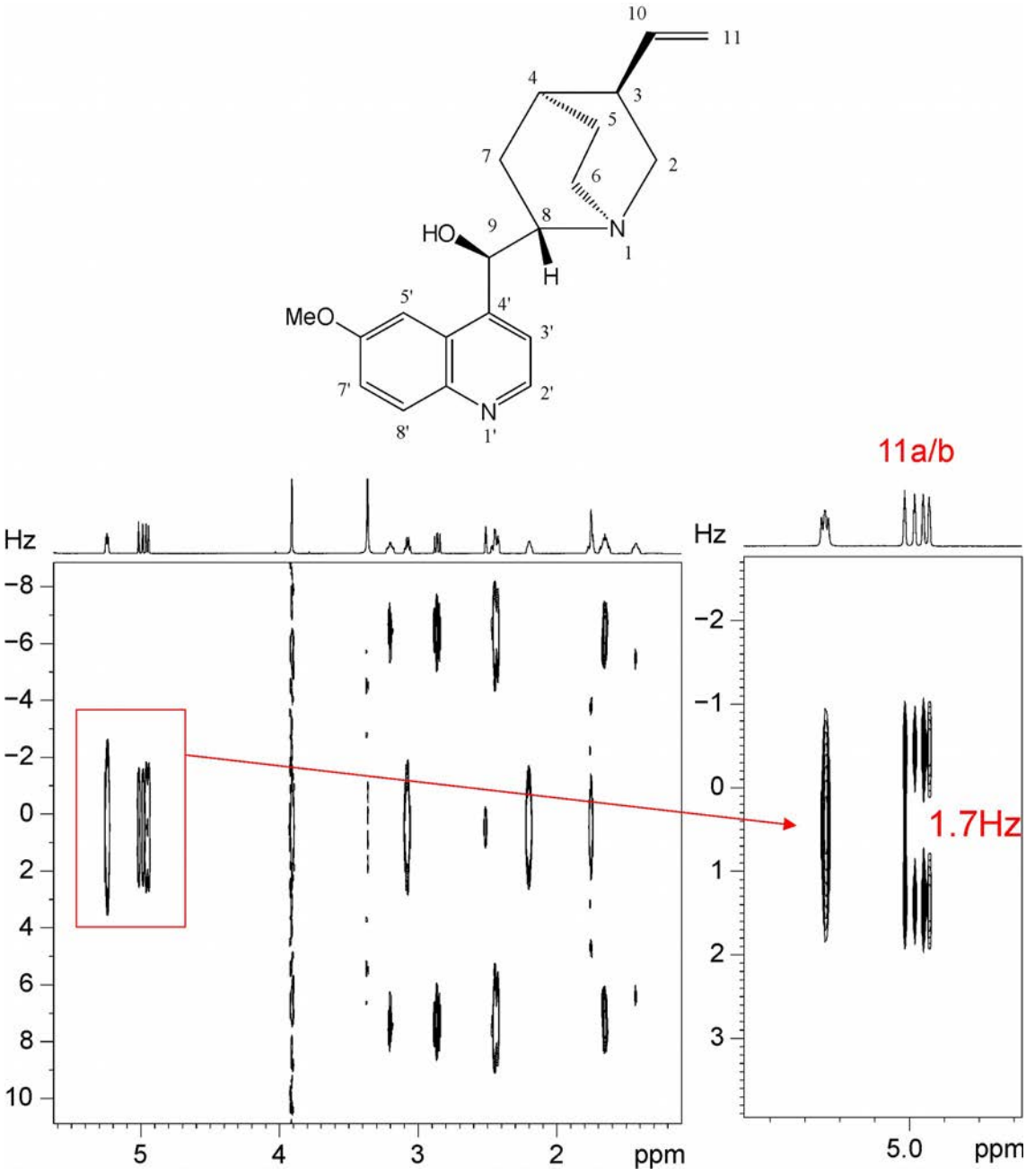

Figure S11: On the left, $^{2}J_{HH}$-resolved of quinine (**4**) in DMSO-d_6. On the right, it is shown that the small $^{2}J_{HH}$ value of 1.7 Hz corresponding to the exocyclic double bond can be accurately measured.

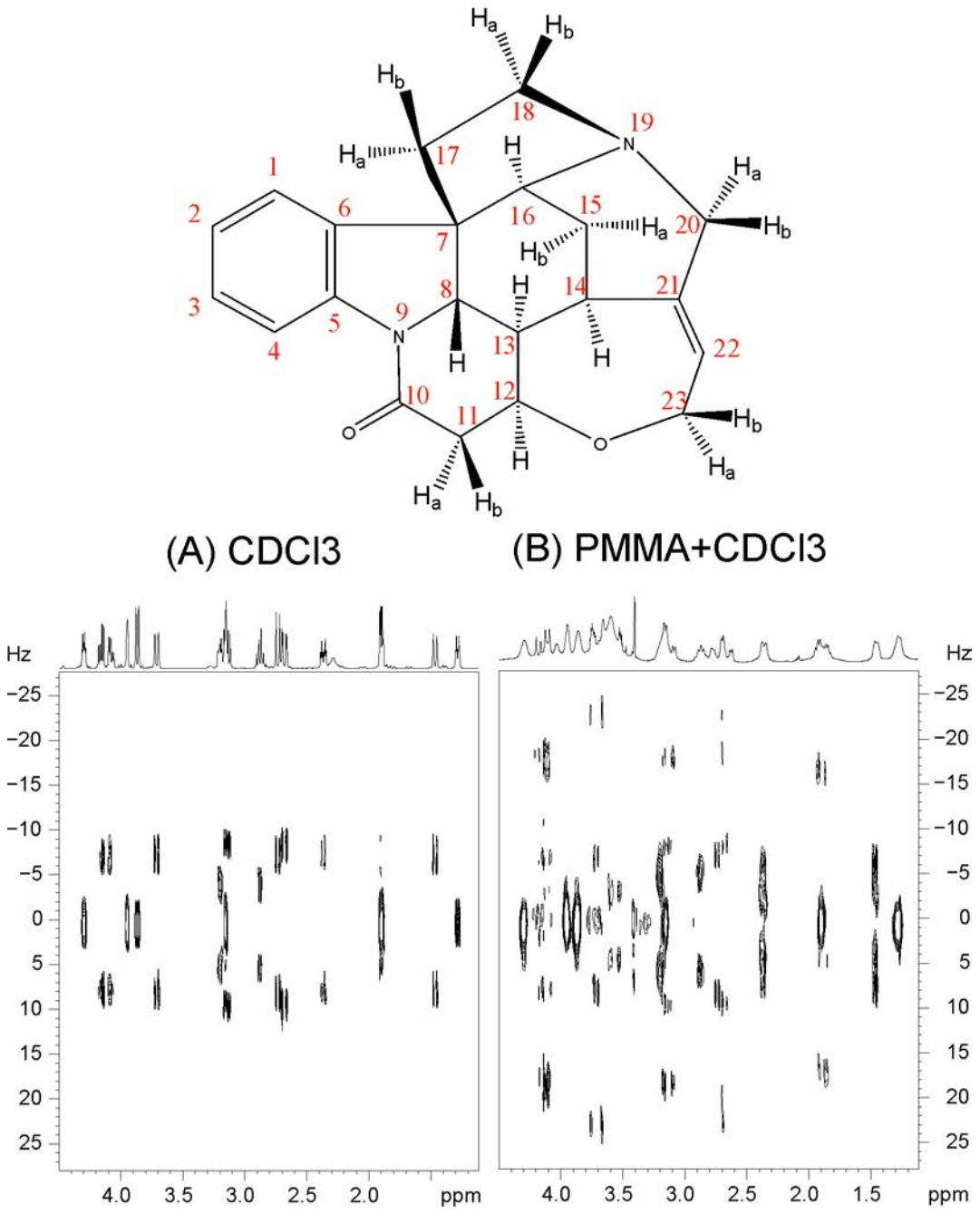

Figure S12: 2D $^{2}J_{HH}$-resolved spectrum of strychnine in A) isotropic ($CDCl_3$) and B) anisotropic (PMMA/ $CDCl_3$ gel) conditions. Some expanded areas are shown in the Fig. 6 of the main manuscript.

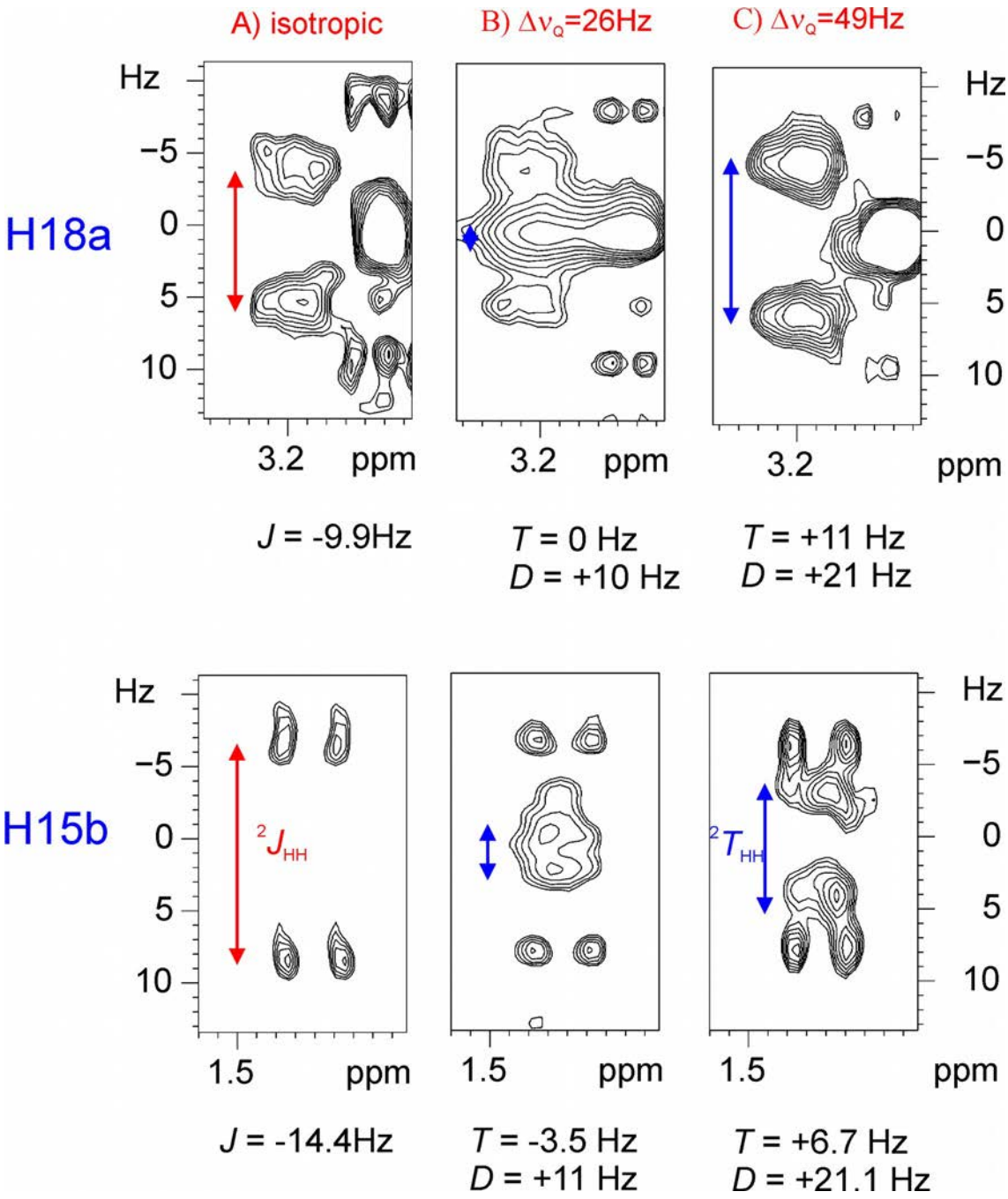

Figure S13: Expansions corresponding to the H18a and H15b protons in the $^2J_{HH}$-resolved spectra of strychnine acquired in (A) isotropic and (B and C) anisotropic (26 and 49 Hz, respectively) conditions. Although the sign of $^2T_{HH}$ (and therefore of $^2D_{HH}$) is not obtained from a single dataset, it can be experimentally deduced comparing the tendency at two different alignments. Assuming that $^2J_{HH}$ is negative, if $^2D_{HH}$ is positive the magnitude of $^2T_{HH} < {}^2J_{HH}$ (a smaller splitting is observed in the anisotropic sample). If $^2D_{HH}$ is negative, the magnitude of $^2T_{HH} > {}^2J_{HH}$ (a larger splitting is observed in the anisotropic sample). The results are confirmed with those predicted from the alignment tensor calculation.

Table S1: Experimental and calculated RDCs ($\Delta\nu_Q$ = 49 Hz) obtained for the DFT-based correct structure of strychnine:[5h]

	Exp	Calc
C1H1	34.1	32.5
C2H2	19.8	22.4
C3H3	14.22	16.3
C4H4	34.8	32.9
C8H8	-15.9	-12. 9
C12H12	-34.2	-35.0
C13H13	-4.3	-5.7
C14H14	-35	-35.4
C16H16	24	24.0
C22H22	0	1.9
C11H11a	15.2	17.0
C11H11b	-27	-29.1
C15H15a	8.6	5.3
C15H15b	0.4	3.8
C17H17a	-	-11.0
C17H17b	-	20.7
C18H18a	-1	0.7
C18H18b	22.8	23.1
C20H20a	-15.6	-15.9
C20H20b	-8.8	-5.0
C23H23a	15.1	12.1
C23H23b	-44.6	-43.2
H11aH11b	-18.9	-20.8
H15aH15b	21.1	21.0
H17ah17b	-	21,7
H18aH18b	20.4	22.0
H20aH20b	-32.1	-27.9
H23ah23b	-21.5	-22.4

Bruker pulse program:

```
;2jhh-res
;2JHH-resolved HSQC

#include <Avance.incl>
#include <Grad.incl>
#include <Delay.incl>
#include <De.incl>

"d22=d2-larger(p2,p14)/2"

"p2=p1*2"
"d0=3u"
"d20=3u"
"d21=3u"
"d2=1s/(cnst2*2)"
"d4=1s/(cnst2*4)"

"in0=inf1/2"
"in20=in0*cnst20"
"in21=in0*cnst21"

"DELTA=p16+d16+p2+d21*2-4u"
"DELTA2=d4-p14/2-4u"
"DELTA3=p16+d16+50u"
"DELTA4=d4-p14/2-4u-p16-d16"
"DELTA5=d2-larger(p2,p14)/2"

"count=(aq/d19)-1"
"acqt0=0"
baseopt_echo

1 ze
2 d1 do:f2
  d12 pl1:f1
3 (p1 ph1)
  DELTA2 pl0:f2
  4u
  (center (p2 ph1) (p14:sp3 ph6):f2 )
  4u
  p28 ph1
  DELTA2 pl2:f2 UNBLKGRAD
  (center (p1 ph2) (p3 ph3):f2 )
  d21
  (p2 ph1)
  d21


  p16:gp1*EA
  d16 pl0:f2
  (p24:sp7 ph4):f2
  4u
  DELTA pl2:f2

  (center (p1 ph1) (p3 ph4):f2 )
  DELTA2 pl0:f2
  4u
```

```
  (center (p2 ph1) (p14:sp3 ph1):f2 )
  4u
  DELTA2

  d20
  p1 ph1
  DELTA5 pl0:f2
  (center (p2 ph1) (p14:sp3 ph6):f2 )
  DELTA5 pl2:f2
  p1 ph1
  (p4 ph1):f2    ;OPTIONAL for specific 2JHH-J-resolved spectrum
  d20

  p1 ph2
  d12 pl5:f1
  300u gron0
  p32:sp29:f1 ph1
  100u groff
  d16
  d12 pl1:f1
  p1 ph1

  DELTA3
  p2 ph1
  50u
  p16:gp2
  d16 BLKGRAD

d12 pl12:f2
go=2 ph31 cpd2:f2


  d1 do:f2 mc #0 to 2
   F1EA(calgrad(EA), caldel(d0, +in0) & caldel(d20, +in20) &
caldel(d21, +in21))
exit



ph1=0
ph2=1
ph3=0 2
ph4=0
ph6=0
ph7=2

ph15=1
ph16=2
ph17=3

ph25=2
ph26=3
ph27=0

ph30=0
ph31=0 2
```

```
;pl0 : 120dB
;pl1 : f1 channel - power level for pulse (default)
;pl2 : f2 channel - power level for pulse (default)
;pl10: f1 channel - power level for TOCSY-spinlock
;sp3: f2 channel - shaped pulse 180 degree
;spnam3: Crp60,0.5,20.1
;sp7: f2 channel - shaped pulse (180degree refocussing)
;spnam7: Crp60comp.4
;p1 : f1 channel -  90 degree high power pulse
;p2 : f1 channel - 180 degree high power pulse
;p3 : f2 channel -  90 degree high power pulse
;p14: f2 channel - 180 degree shaped pulse for inversion
;     = 500usec for Crp60,0.5,20.1
;p16: homospoil/gradient pulse                          [1 msec]
;p24: f2 channel - 180 degree shaped pulse for refocussing
;     = 2msec for Crp60comp.4
;d0 : incremented delay (2D)                            [3 usec]
;d1 : relaxation delay; 1-5 * T1
;d2 : 1/(2J(XH))
;d4 : 1/(4J(XH))
;d16: delay for homospoil/gradient recovery
;cnst2: = J(XH)
;cnst15: = conventional(0)/pure shift(1)
;cnst14: = conventional(0)/2JHH-resolved(1)
;cnst17: = -0.5 for Crp60comp.4
;cnst20: = J(scale) factor
;cnst21: = Correlation factor
;in0: 1/(2 * SW(X)) = DW(X)
;nd0: 2
;NS: 2 * n
;DS: >= 16
;td1: number of experiments
;FnMODE: echo-antiecho


;use gradient ratio:   gp 1 : gp 2 : gp 0
;                   80 : 20.1 :   11   for C-13

;for z-only gradients:
;gpz1: 80%
;gpz2: 20.1% for C-13
;gpz0: 11%

;use gradient files:
;gpnam1: SINE.100
;gpnam2: SINE.100
```

4. CONCLUSIONS

♦ Two novel experiments have been designed, HSQMBC-COSY and HSQMBC-TOCSY, to be a valuable and complementary tool to existing NMR experiments for obtaining longer-range heteronuclear connectivities (publication 1). Compared with other currently available alternatives, these experiments are particularly able to reach smaller couplings constants under good SNR conditions. These long-range connectivities can provide fundamental information in structure elucidation of small molecules and natural products.

♦ New strategies have been developed to improve the accurate determination of homo- and heteronuclear coupling constants achieved thanks to the concerted use of resolution-enhanced methods such as spectral aliasing, NUS, and broadband homodecoupling techniques (publications 2 and 3).

♦ A novel ultra-high resolved HSQC experiment has been used for the general and efficient measurement of the magnitude and the sign of heteronuclear coupling constants J_{XH}, being X= ^{19}F, ^{31}P or ^{2}H from an HSQC (publication 2). Also, the method has been used to measure simultaneously isotropic and anisotropic NMR parameters with an outstanding precision (publication 3).

♦ Novel NMR methods have been developed to determine NMR anisotropic parameters in samples dissolved in PMMA/$CDCl_3$ as an alignment media (publications 3, 4, 5, 6 and 7).

♦ Isotropic and anisotropic interactions can be simultaneously measured in a single NMR measurement (publications 3, 4 and 7). In particular, a robust sign-sensitive spectral-aliased PIP-HSQC experiment allows the simultaneous determination of ^{1}H-^{13}C RDCs, $\Delta\delta^{iso\text{-}aniso}(^{1}H)$ and $\Delta\delta^{iso\text{-}aniso}(^{13}C)$ in a single measurement (Publication 3).

♦ Perfect BIRD NMR building blocks have been implemented in HSQC-type experiments (publications 5 and 6)

♦ A complete family of BIRD-based *J*-resolved HSQC experiments has been designed and successfully applied in the measurement of both homo- and heteronuclear

scalar and residual dipolar couplings in F1 dimension (publication 4, 5, 6 and 7). Related *J*/δ-scaled methods can be used to avoid signal overlap.

♦ Novel methods have been developed to study prochiral CH_2 groups, allowing the determination of each $^1J_{CHa}$ and $^1J_{CHb}$ (publication 5 and 6) and $^2J_{HH}$ (publication 7). These improvements enable the assignment and identification of all pairs of diastereotopic protons, helping in the determination of the correct structure.

♦ Novel graphical interfaces to obtain $^1J_{CH}$ (publication 6) and $^2J_{HH}$ (publication 7) NMR profiles have been designed. The method allows the automated determination of coupling constants by simple peak-picking.

♦ New strategies for the efficient structural discrimination of small molecules and natural products have been evaluated, using both $^1D_{CH}$ and $^2D_{HH}$ (publication 4 and 7). The use of $^2D_{HH}$ improves the quality factors in molecules containing prochiral CH_2 groups.

5. *BIBLIOGRAPHY*

(1) Rabi, I. I.; Zacharias, J. R.; Millman, S.; Kusch, P. *Phys. Rev.* **1938**, *53* (4), 318–318.
(2) Piantini, U.; Sorensen, O. W.; Ernst, R. R. *J. Am. Chem. Soc.* **1982**, *104* (24), 6800–6801.
(3) Braunschweiler, L.; Ernst, R. . *J. Magn. Reson.* **1983**, *53* (3), 521–528.
(4) Bax, A.; Griffey, R. H.; Hawkins, B. L. *J. Magn. Reson.* **1983**, *55* (2), 301–315.
(5) Bodenhausen, G.; Ruben, D. J. *Chem. Phys. Lett.* **1980**, *69* (1), 185–189.
(6) Morris, G. A.; Freeman, R. *J. Am. Chem. Soc.* **1979**, *101* (3), 760–762.
(7) Parella, T. *Magn. Reson. Chem.* **1998**, *36* (7), 467–495.
(8) Boyer, R. D.; Johnson, R.; Krishnamurthy, K. *J. Magn. Reson.* **2003**, *165* (2), 253–259.
(9) Schulze-Sünninghausen, D.; Becker, J.; Luy, B. *J. Am. Chem. Soc.* **2014**, *136* (4), 1242–1245.
(10) Herrera, A.; Fernández-Valle, E.; Martínez-Álvarez, R.; Molero, D.; Pardo, Z. D.; Sáez, E.; Gal, M. *Angew. Chemie Int. Ed.* **2009**, *48* (34), 6274–6277.
(11) Pardo, Z. D.; Olsen, G. L.; Fernández-Valle, M. E.; Frydman, L.; Martínez-Álvarez, R.; Herrera, A. *J. Am. Chem. Soc.* **2012**, *134* (5), 2706–2715.
(12) Fernández, I.; Fernández-Valle, M. E.; Martínez-Álvarez, R.; Molero-Vílchez, D.; Pardo, Z. D.; Sáez-Barajas, E.; Sánchez, Á.; Herrera, A. *J. Org. Chem.* **2014**, *79* (17), 8086–8093.
(13) Tvaroska, I.; Taravel, F. R. *Carbohydr. Res.* **1991**, *221* (1), 83–94.
(14) Uhrínova, S.; Uhrían, D.; Liptaj, T.; Bella, J.; Hirsch, J. *Magn. Reson. Chem.* **1991**, *29* (9), 912–922.
(15) Nakul C. Maiti, †; Yuping Zhu, ‡; Ian Carmichael, §; Anthony S. Serianni, ‡ and; Vernon E. Anderson*, †. **2006**.
(16) Enthart, A.; Freudenberger, J. C.; Furrer, J.; Kessler, H.; Luy, B. *J. Magn. Reson.* **2008**, *192* (2), 314–322.
(17) Castañar, L.; Sistaré, E.; Virgili, A.; Williamson, R. T.; Parella, T. *Magn. Reson. Chem.* **2015**, *53* (2), 115–119.
(18) Castañar, L.; Saurí, J.; Williamson, R. T.; Virgili, A.; Parella, T. *Angew. Chemie - Int. Ed.* **2014**, *53* (32), 8379–8382.
(19) Takegoshi, K.; Ogura, K.; Hikichi, K. *J. Magn. Reson.* **1989**, *84* (3), 611–615.
(20) Baishya, B.; Khetrapal, C. L. *J. Magn. Reson.* **2014**, *242*, 143–154.
(21) Torres, A. M.; Zheng, G.; Price, W. S. *Magn. Reson. Chem.* **2009**, *48* (2), n/a-n/a.
(22) Pell, A. J.; Edden, R. A. E.; Keeler, J. *Magn. Reson. Chem.* **2007**, *45* (4), 296–316.
(23) Luy, B. *J. Magn. Reson.* **2009**, *201* (1), 18–24.
(24) Torres, A. M.; Cruz, R. Dela; Price, W. S. *J. Magn. Reson.* **2008**, *193* (2), 311–316.
(25) Thrippleton, M. J.; Keeler, J. *Angew. Chemie - Int. Ed.* **2003**, *42* (33), 3938–3941.
(26) Saurí, J.; Espinosa, J. F.; Parella, T. *Angew. Chemie - Int. Ed.* **2012**, *51* (16), 3919–3922.
(27) Gil, S.; Espinosa, J. F.; Parella, T. *J. Magn. Reson.* **2010**, *207* (2), 312–321.
(28) Gil, S.; Espinosa, J. F.; Parella, T. *J. Magn. Reson.* **2011**, *213* (1), 145–150.
(29) Thiele, C. M. *J. Org. Chem.* **2004**, *69* (22), 7403–7413.
(30) Tolman, J. R.; Prestegard, J. H. *J. Magn. Reson. Ser. B* **1996**, *112* (3), 269–274.
(31) Thiele, C. M.; Bermel, W. *J. Magn. Reson.* **2012**, *216*, 134–143.
(32) Fehér, K.; Berger, S.; Kövér, K. E. *J. Magn. Reson.* **2003**, *163* (2), 340–346.
(33) Saurí, J.; Castañar, L.; Nolis, P.; Virgili, A.; Parella, T. *J. Magn. Reson.* **2014**,

242, 33–40.
(34) Aue, W. P.; Bartholdi, E.; Ernst, R. R. *J. Chem. Phys.* **1976**, *64* (5), 2229–2246.
(35) Castañar, L.; Garcia, M.; Hellemann, E.; Nolis, P.; Gil, R. R.; Parella, T. *J. Org. Chem.* **2016**, *81* (22), 11126–11131.
(36) Williamson, R. T.; Márquez, B. L.; Gerwick, W. H.; Kövér, K. E. *Magn. Reson. Chem.* **2000**, *38* (4), 265–273.
(37) Kövér, K. E.; Batta, G.; Fehér, K. *J. Magn. Reson.* **2006**, *181* (1), 89–97.
(38) Lacerda, V.; da Silva, G. V. J.; Tormena, C. F.; Williamson, R. T.; Marquez, B. L. *Magn. Reson. Chem.* **2007**, *45* (1), 82–86.
(39) Saurí, J.; Parella, T.; Espinosa, J. F. *Org. Biomol. Chem.* **2013**, *11* (27), 4473.
(40) Cicero, D. O.; Barbato, G.; Bazzo, R. *J. Magn. Reson.* **2001**, *148* (1), 209–213.
(41) Kobzar, K.; Luy, B. *J. Magn. Reson.* **2007**, *186* (1), 131–141.
(42) Edden, R. A. E.; Keeler, J. *J. Magn. Reson.* **2004**, *166* (1), 53–68.
(43) Verdier, L.; Sakhaii, P.; Zweckstetter, M.; Griesinger, C. *J. Magn. Reson.* **2003**, *163* (2), 353–359.
(44) Williamson, R. T.; Buevich, A. V.; Martin, G. E.; Parella, T. *J. Org. Chem.* **2014**, *79* (9), 3887–3894.
(45) Williamson, R. T.; Buevich, A. V.; Martin, G. E. *Tetrahedron Lett.* **2014**, *55* (22), 3365–3366.
(46) Blinov, K. A.; Buevich, A. V.; Williamson, R. T.; Martin, G. E. *Org. Biomol. Chem.* **2014**, *12* (47), 9505–9509.
(47) Lerner, L.; Bax, A. *J. Magn. Reson.* **1986**, *69* (2), 375–380.
(48) Koźmiński, W. *J. Magn. Reson.* **1999**, *137* (2), 408–412.
(49) Nolis, P.; Espinosa, J. F.; Parella, T. *J. Magn. Reson.* **2006**, *180* (1), 39–50.
(50) Sørensen, M. D.; Meissner, A.; Sørensen, O. W. *J. Magn. Reson.* **1999**, *137* (1), 237–242.
(51) Reif, B.; Köck, M.; Kerssebaum, R.; Schleucher, J.; Griesinger, C. *J. Magn. Reson. Ser. B* **1996**, *112* (3), 295–301.
(52) Martin, G. E. *Annu. Reports NMR Spectrosc.* **2011**, *74*, 215–291.
(53) Anderson, W. A.; Freeman, R. *J. Chem. Phys.* **1962**, *37* (1), 85–103.
(54) Zangger, K.; Sterk, H. *J. Magn. Reson.* **1997**, *124* (2), 486–489.
(55) Lupulescu, A.; Olsen, G. L.; Frydman, L. *J. Magn. Reson.* **2012**, *218*, 141–146.
(56) Sathyamoorthy, B.; Parish, D. M.; Montelione, G. T.; Xiao, R.; Szyperski, T. *ChemPhysChem* **2014**, *15* (9), 1872–1879.
(57) Foroozandeh, M.; Giraudeau, P.; Jeannerat, D. *Magn. Reson. Chem.* **2013**, *51* (12), 808–814.
(58) Lokesh, L.; Suryaprakash, N. *Chem. Commun.* **2014**, *50* (62), 8550–8553.
(59) Kupče, E.; Freeman, R. *Magn. Reson. Chem.* **2007**, *45* (1), 2–4.
(60) Castañar, L.; Nolis, P.; Virgili, A.; Parella, T. *Chem. - A Eur. J.* **2013**, *19* (46), 15472–15475.
(61) Meyer, N. H.; Zangger, K. *Angew. Chemie Int. Ed.* **2013**, *52* (28), 7143–7146.
(62) Kiraly, P.; Adams, R. W.; Paudel, L.; Foroozandeh, M.; Aguilar, J. A.; Timári, I.; Cliff, M. J.; Nilsson, M.; Sándor, P.; Batta, G.; Waltho, J. P.; Kövér, K. E.; Morris, G. A. *J. Biomol. NMR* **2015**, *62* (1), 43–52.
(63) Aguilar, J. A.; Morris, G. A.; Kenwright, A. M. *RSC Adv.* **2014**, *4* (16), 8278–8282.
(64) Chaudhari, S. R.; Suryaprakash, N. *RSC Adv.* **2014**, *4* (29), 15018–15021.
(65) Timári, I. I.; Illyés, T. Z.; Adams, R. W.; Nilsson, M.; Szilágyi, L.; Kövér, K. E.; Szilágyi, L.; Morris, G. A.; Kövér, K. E. *Chem. - A Eur. J.* **2015**, *21* (8), 3472–3479.

(66) Adams, R. W.; Byrne, L.; Király, P.; Foroozandeh, M.; Paudel, L.; Nilsson, M.; Clayden, J.; Morris, G. A. *Chem. Commun.* **2014**, *50* (19), 2512–2514.
(67) Ying, J.; Roche, J.; Bax, A. *J. Magn. Reson.* **2014**, *241*, 97–102.
(68) Castañar, L.; Nolis, P.; Virgili, A.; Parella, T. *Chem. - A Eur. J.* **2013**, *19* (51), 17283–17286.
(69) Garbow, J. R.; Weitekamp, D. P.; Pines, A. *Chem. Phys. Lett.* **1982**, *93* (5), 504–509.
(70) Aguilar, J. A.; Nilsson, M.; Morris, G. A. *Angew. Chemie Int. Ed.* **2011**, *50* (41), 9716–9717.
(71) Jeannerat, D. *Magn. Reson. Chem.* **2003**, *41* (1), 3–17.
(72) Vitorge, B.; Bieri, S.; Humam, M.; Christen, P.; Hostettmann, K.; Muñoz, O.; Loss, S.; Jeannerat, D. *Chem. Commun.* **2009**, *0* (8), 950.
(73) Jeannerat, D. *Magn. Reson. Chem.* **2000**, *38* (6), 415–422.
(74) Gómez-Reyes, J. F.; Ariza-Castolo, A. *J. Math. Chem.* **2013**, *51* (8), 1961–1980.
(75) Jeannerat, D. *J. Magn. Reson.* **2007**, *186* (1), 112–122.
(76) Baskyr, I.; Brand, T.; Findeisen, M.; Berger, S. *Angew. Chemie Int. Ed.* **2006**, *45* (46), 7821–7824.
(77) Cotte, A.; Foroozandeh, M.; Jeannerat, D. *Chim. Int. J. Chem.* **2012**, *66* (10), 764–769.
(78) Njock, G. B. B.; Pegnyemb, D. E.; Bartholomeusz, T. A.; Christen, P.; Vitorge, B.; Nuzillard, J.-M.; Shivapurkar, R.; Foroozandeh, M.; Jeannerat, D. *Chim. Int. J. Chem.* **2010**, *64* (4), 235–240.
(79) Kazimierczuk, K.; Lafon, O.; Lesot, P. *Analyst* **2014**, *139* (11), 2702.
(80) Kazimierczuk, K.; Orekhov, V. Y. *Angew. Chemie Int. Ed.* **2011**, *50* (24), 5556–5559.
(81) Orekhov, V. Y.; Jaravine, V. A. *Prog. Nucl. Magn. Reson. Spectrosc.* **2011**, *59* (3), 271–292.
(82) Holland, D. J.; Bostock, M. J.; Gladden, L. F.; Nietlispach, D. *Angew. Chemie* **2011**, *123* (29), 6678–6681.
(83) Le Guennec, A.; Dumez, J. N.; Giraudeau, P.; Caldarelli, S. *Magn. Reson. Chem.* **2015**, *53* (11), 913–920.
(84) Karplus, M. *J. Chem. Phys.* **1959**, *30* (1), 11–15.
(85) Anet, F. A. L.; Bourn, A. J. R. *J. Am. Chem. Soc.* **1965**, *87* (22), 5250–5251.
(86) Neuhaus, N.; Williamson, M. P. *The Nuclear Overhauser Effect in Structural and Conformational Analysis, Second Edition*,; 2000.
(87) Gil, R. R.; Griesinger, C.; Navarro-Vázquez, A.; Sun, H. *Struct. Elucidation Org. Chem. Search Right Tools* **2015**, 279–324.
(88) Thiele, C. M. *Use of RDCs in Rigid Organic Compounds and Some Practical Considerations Concerning Alignment Media*; 2007; Vol. 30A.
(89) Gil, R. R. *Reference Module in Chemistry, Molecular Sciences and Chemical Engineering*, Elsevier.; 2016.
(90) Gil, R. R. *Modern NMR Approaches To The Structure Elucidation of Natural Products Volume 1: Instrumentation and Software*; 2017; Vol. 1.
(91) Saupe, A.; Englert, G. *Phys. Rev. Lett.* **1963**, *11* (10), 462–464.
(92) Mangoni, A.; Esposito, V.; Randazzo, A. *Chem. Commun. (Camb).* **2003**, No. 1, 154–155.
(93) Yan, J.; Kline, A. D.; Mo, H.; Shapiro, M. J.; Zartler, E. R. *J. Org. Chem.* **2003**, *68* (5), 1786–1795.
(94) Mueller, L. *J. Magn. Reson.* **1987**, *72* (1), 191–196.
(95) Griesinger, C.; Soerensen, O. W.; Ernst, R. R. *J. Am. Chem. Soc.* **1985**, *107* (22),

6394–6396.
(96) Thiele, C. M.; Marx, A.; Berger, R.; Fischer, J.; Biel, M.; Giannis, A. *Angew. Chemie - Int. Ed.* **2006**, *45* (27), 4455–4460.
(97) Gil, R. R. *Angew. Chemie - Int. Ed.* **2011**, *50* (32), 7222–7224.
(98) Gil, R. R.; Gayathri, C.; Tsarevsky, N. V.; Matyjaszewski, K. *J. Org. Chem.* **2008**, *73* (3), 840–848.
(99) Kummerlöwe, G.; Crone, B.; Kretschmer, M.; Kirsch, S. F.; Luy, B. *Angew. Chemie - Int. Ed.* **2011**, *50* (11), 2643–2645.
(100) Pérez-Trujillo, M.; Castañar, L.; Monteagudo, E.; Kuhn, L. T.; Nolis, P.; Virgili, A.; Williamson, R. T.; Parella, T. *Chem. Commun.* **2014**, *50* (71), 10214.
(101) Snider, J. D.; Troche-Pesqueira, E.; Woodruff, S. R.; Gayathri, C.; Tsarevsky, N. V.; Gil, R. R. *Magn. Reson. Chem.* **2012**, *50 Suppl 1* (September).
(102) Furrer, J.; John, M.; Kessler, H.; Luy, B. *J. Biomol. NMR* **2007**, *37* (3), 231–243.
(103) Kramer, F.; Deshmukh, M. V.; Kessler, H.; Glaser, S. J. 2004, pp 10–21.
(104) Saupe, A. *Angew. Chemie - Int. Ed.* **1968**, *7*, 97112.
(105) Losonczi, J. A.; Andrec, M.; Fischer, M. W. F.; Prestegard, J. H. *J. Magn. Reson.* **1999**, *342*, 334–342.
(106) Azurmendi, H. F.; Bush, C. A. *J. Am. Chem. Soc.* **2002**, *124* (11), 2426–2427.
(107) Almond, A.; Axelsen, J. B. *J. Am. Chem. Soc.* **2002**, *124* (34), 9986–9987.
(108) Zweckstetter, M. *Nat. Protoc.* **2008**, *3*, 679–690.
(109) Navarro-Vázquez, A. *Magn. Reson. Chem.* **2012**, *50* (May), S73–S79.
(110) Hallwass, F.; Schmidt, M.; Sun, H.; Mazur, A.; Kummerlöwe, G.; Luy, B.; Navarro-Vázquez, A.; Griesinger, C.; Reinscheid, U. M. *Angew. Chemie - Int. Ed.* **2011**, *50* (40), 9487–9490.
(111) Nath, N.; Schmidt, M.; Gil, R. R.; Williamson, R. T.; Martin, G. E.; Navarro-Vázquez, A.; Griesinger, C.; Liu, Y. *J. Am. Chem. Soc.* **2016**, *138* (30), 9548–9556.
(112) Gil, R. R.; Hellemann, E. **2018**.
(113) Courtieu, J.; Bayle, J. P.; Fung, B. M. *Prog. Nucl. Magn. Reson. Spectrosc.* **1994**, *26*, 141–169.
(114) Grishaev, a; Yao, L. S.; Ying, J. F.; Pardi, a; Bax, a. *J. Am. Chem. Soc.* **2009**, *131*, 9490–+.
(115) Kummerlöwe, G.; Grage, S. L.; Thiele, C. M.; Kuprov, I.; Ulrich, A. S.; Luy, B. *J. Magn. Reson.* **2011**, *209* (1), 19–30.
(116) Kuchel, P. W.; Chapman, B. E.; Müller, N.; Bubb, W. A.; Philp, D. J.; Torres, A. M. *J. Magn. Reson.* **2006**, *180* (2), 256–265.
(117) Kummerlöwe, G.; McCord, E. F.; Cheatham, S. F.; Niss, S.; Schnell, R. W.; Luy, B. *Chem. - A Eur. J.* **2010**, *16* (24), 7087–7089.
(118) Gayathri, C.; Tsarevsky, N. V.; Gil, R. R. *Chem. - A Eur. J.* **2010**, *16* (12), 3622–3626.
(119) Aroulanda, C.; Boucard, V.; Guibe, F.; Courtieu, J.; Merlet, D. *Chem. - A Eur. J.* **2003**, *9* (18), 4536–4539.
(120) Thiele, C. M.; Berger, S. *Org. Lett.* **2003**, *5* (5), 705–708.
(121) Aroulanda, C.; Sarfati, M.; Courtieu, J.; Lesot, P. *Enantiomer* **2001**, *6* (5), 281–287.
(122) Aroulanda, C.; Lesot, P.; Merlet, D.; Courtieu, J. *J. Phys. Chem. A* **2003**, *107* (50), 10911–10918.
(123) Lesot, P.; Sarfati, M.; Courtieu, J. *Chem. - A Eur. J.* **2003**, *9* (8), 1724–1745.
(124) Sarfati, M.; Lesot, P.; Merlet, D.; Courtieu, J. *Chem. Commun.* **2000**, No. 21, 2069–2081.

(125) Arnold, L.; Marx, A.; Thiele, C. M.; Reggelin, M. *Chem. - A Eur. J.* **2010**, *16* (34), 10342–10346.
(126) Thiele, C. M.; Pomerantz, W. C.; Abbott, N. L.; Gellman, S. H. *Chem. Commun.* **2011**, *47* (1), 502–504.
(127) Mayer, S.; Zentel, R. *Chiral polyisocyanates, a special class of helical polymers*; 2001; Vol. 26.
(128) Meyer, N. C.; Krupp, A.; Schmidts, V.; Thiele, C. M.; Reggelin, M. *Angew. Chemie - Int. Ed.* **2012**, *51* (33), 8334–8338.
(129) Yu, L. J.; Saupe, A. *Mol. Cryst. Liq. Cryst.* **1982**, *80*, 129–134.
(130) Prosser, R. S.; Losonczi, J. A.; Shiyanovskaya, I. V. *J. Am. Chem. Soc.* **1998**, *120* (42), 11010–11011.
(131) Pham, T. N.; Hinchley, S. L.; Rankin, D. W. H.; Liptaj, T.; Uhrín, D. *J. Am. Chem. Soc.* **2004**, *126* (40), 13100–13110.
(132) Bertini, I.; Luchinat, C.; Parigi, G.; Pierattelli, R. *Dalt. Trans.* **2008**, No. 29, 3782.
(133) Wöhnert, J.; Franz, K. J.; Nitz, M.; Imperiali, B.; Schwalbe, H. *J. Am. Chem. Soc.* **2003**, *125* (44), 13338–13339.
(134) Haberz, P.; Rodriguez-Castañeda, F.; Junker, J.; Becker, S.; Leonov, A.; Griesinger, C. *Org. Lett.* **2006**, *8* (7), 1275–1278.
(135) Deloche, B.; Samulski, E. T. *Macromolecules* **1981**, *14* (3), 575–581.
(136) Tycko, R.; Blanco, F. J.; Ishii, Y. *J. Am. Chem. Soc.* **2000**, *122* (38), 9340–9341.
(137) Sass, H. J.; Musco, G.; J. Stahl, S.; T. Wingfield, P.; Grzesiek, S. *J. Biomol. NMR* **2000**, *18* (4), 303–309.
(138) Liu, Y.; Prestegard, J. H. *Natl. Inst. Heal.* **2010**, *47* (4), 249–258.
(139) Chou, J. J.; Gaemers, S.; Howder, B.; Louis, J. M.; Bax, A. *J. Biomol. NMR* **2001**, *21*, 377–382.
(140) New Era Enterprise. *Inc. Vineland, NJ, USA*.
(141) Haberz, P.; Farjon, J.; Griesinger, C. *Angew. Chemie - Int. Ed.* **2005**, *44* (3), 427–429.
(142) Meier, S.; Häussinger, D.; Grzesiek, S. *J. Biomol. NMR* **2002**, *24* (4), 351–356.
(143) Kummerlöwe, G.; Auernheimer, J.; Lendlein, A.; Luy, B. *J. Am. Chem. Soc.* **2007**, *129* (19), 6080–6081.
(144) Kummerlöwe, G.; Behl, M.; Lendlein, A.; Luy, B. *Chem. Commun.* **2010**, *46* (43), 8273.
(145) Freudenberger, J. C.; Knör, S.; Kobzar, K.; Heckmann, D.; Paululat, T.; Kessler, H.; Luy, B. *Angew. Chemie - Int. Ed.* **2005**, *44* (3), 423–426.
(146) Luy, B.; Kobzar, K.; Kessler, H. *Angew. Chemie - Int. Ed.* **2004**, *43* (9), 1092–1094.
(147) Luy, B.; Kobzar, K.; Knör, S.; Furrer, J.; Heckmann, D.; Kessler, H. *J. Am. Chem. Soc.* **2005**, *127* (17), 6459–6465.
(148) Freudenberger, J. C.; Spiteller, P.; Bauer, R.; Kessler, H.; Luy, B. *J. Am. Chem. Soc.* **2004**, *126* (45), 14690–14691.
(149) Kobzar, K.; Kessler, H.; Luy, B. *Angew. Chemie - Int. Ed.* **2005**, *44* (20), 3145–3147.
(150) Kummerlöwe, G.; Kiran, M. U.; Luy, B. *Chem. - A Eur. J.* **2009**, *15* (45), 12192–12195.